Modeling and Simulation of Resistive Switching Devices

Von der Fakultät für Elektrotechnik und Informationstechnik der Rheinisch-Westfälischen Technischen Hochschule Aachen zur Erlangung des akademischen Grades eines Doktors der Ingenieurwissenschaften genehmigte Dissertation

vorgelegt von

Diplom-Ingenieur Elektrotechnik

Stephan Jan-Martin Menzel

aus Bremen

Berichter: Univ.-Prof. Dr.-Ing. Rainer Waser
Univ.-Prof. Dr.-Ing. Christoph Jungemann

Tag der mündlichen Prüfung: 29.06.2012

Bibliografische Information der Deutschen Nationalbibliothek
Die Deutsche Nationalbibliothek verzeichnet diese Publikation in der Deutschen Nationalbibliografie; detaillierte bibliografische Daten sind im Internet über
http://dnb.d-nb.de abrufbar.

ISBN 978-3-8439-0964-8

Sternstr. 18, 80538 München
Tel.: 089/66060798
www.dr.hut-verlag.de

1. Auflage 2013

Abstract

As conventional memory concepts are approaching their physical scaling limits, novel memory device concepts for highly scalable, ultrafast, energy efficient, nonvolatile memory are demanded. Resistive switching devices, which rely on nanoionic redox phenomena, are potential candidates for the use in resistive random access memories (ReRAMs) or logic applications. By applying appropriate electrical stimuli they can be switched back and forth between different resistance states, which encode the digital information. Based on their physical nature three different resistive switching mechanisms can be distinguished: the electrochemical mechanism (ECM), the valence-change mechanism (VCM) and the thermochemical mechanism (TCM). While the basic principles of the switching processes are well understood, many details are still unknown or under discussion. Especially, the origin of the switching kinetics in VCM cells and the physical origin of the multilevel programming capability in ECM cells need to be clarified. To address these open questions simulation models can be employed. However, until now there are no simulation models available that can answer these questions.

In this thesis, physics-based simulation models of ECM and VCM devices are developed to address these questions. For this, the corresponding simulation results are compared to experimental data.

A physics-based dynamic 1D compact model for resistive switching in ECM cells is presented. Simulations based on this model were performed to investigate fundamental phenomena as the multilevel switching capabilities and the nonlinear switching kinetics. The former is realized by modulation of a tunneling gap between one electrode and a growing filament within the insulating layer. By comparison to experimental data, this model was validated. Further simulations were performed to investigate the material impact on the resistive switching properties. This model was further simplified to an analytical one. Analytical expressions were derived, which allow predicting switching times and currents. Finally, the 1D model is extended to a 2D finite elements simulation model. With this approach polyfilamentary growth and the unipolar switching phenomenon in ECM cells at very low resistances were investigated and discussed.

Regarding the VCM cell, an electro-thermal finite elements simulation model was developed to explain the origin of the nonlinear switching kinetics. While it is widely accepted that the resistive switching is triggered by the migration of oxygen vacancies in the insulating layer, it is yet unclear whether the motion is temperature- or field-enhanced. A comparison of the model and the experimental data revealed that the nonlinear switching kinetics is predominantly caused by temperature-accelerated drift of oxygen vacancies. Further simulations were performed to investigate the scaling potential of VCM cells. It could be demonstrated that the VCM memory concept allows cell sizes in the low nanometer regime. In addition, the derived model provides essential rules for an optimized cell design.

Kurzfassung

Weil herkömmliche Speicherkonzepte an ihre physikalischen Skalierungsgrenzen stoßen, entsteht der Bedarf nach neuartigen Speicherkonzepten für hochskalierbare, ultraschnelle, energieeffiziente nichtflüchtige Speicher. Resistiv schaltende Bauelemente, die auf nanoionische Redoxprozessen beruhen, gelten als potentielle Kandidaten für den Einsatz in resistiven Speichern mit wahlfreien Zugriff (ReRAMs) oder in Logikanwendungen. Durch geeignete elektrische Anregung können ReRAMs zwischen verschiedenen Widerstandszuständen hin und her geschaltet werden. Durch diese Widerstandszustände wird die digitale Information abgebildet. Basierend auf ihrer physikalischen Natur kann zwischen drei verschiedenen resistiven Schaltmechanismen unterschieden werden: dem elektrochemischen Mechanismus (ECM), dem Valenzwechselmechanismus (VCM) und dem thermochemischen Mechanismus (TCM). Während das grundlegende Prinzip dieser Schaltmechanismen verstanden ist, sind viele Details noch unbekannt oder momentan in der Diskussion. Insbesondere der Ursprung der nichtlinearen Schaltkinetik in VCM Speicherzellen und die physikalische Ursache der Multilevel-Speicherfähigkeit in ECM Zellen müssen geklärt werden. Zur Klärung dieser offenen Fragen, können Simulationsmodelle eingesetzt werden. Es existieren bisher nur einige wenige Simulationsmodelle und diese können die Fragestellungen nicht hinreichend beantworten.
In dieser Dissertation wurden physikalisch motivierte Simulationsmodelle für ECM und VCM Zellen entwickelt, um diese Fragen zu untersuchen. Die Simulationsresultate wurden dazu mit experimentellen Ergebnissen verglichen.
Im Detail wurde ein physikalisch motiviertes, numerisches, eindimensionales (1D) Kompaktmodell von ECM Zellen hergeleitet. Auf Basis dieses Modells wurden Simulationen zur Untersuchung fundamentaler Phänomene wie der Multilevel-Speicherfähigkeit und der nichtlinearen Schaltkinetik durchgeführt. Dabei werden die unterschiedlichen Widerstandszustände (Multilevel) durch die Modulation der Weite der Tunnelbarriere zwischen Elektrode und wachsendem Filament im Isolator dargestellt. Durch den Vergleich mit experimentellen Daten konnte dieses Modell validiert werden. Weitere Simulationen dienten der Untersuchung des Einflusses der eingesetzten Materialien auf das Schaltverhalten. Das abgeleitete numerische 1D Modell wurde zu einem analytischen Modell weiter vereinfacht. Dabei wurden analytische Ausdrücke abgeleitet, mit denen Schaltzeiten und Schaltströme explizit berechnet werden können. Abschließend wurde das numerische 1D Modell zu einem 2D FEM Modell erweitert. Mit diesem Ansatz konnte sowohl das polyfilamentäre Wachstum als auch das unipolare Schaltphänomen bei niedrigen Widerstandswerten untersucht und diskutiert werden.
In Bezug auf VCM Speicherzellen wurde ein elektro-thermisches Finite-Elemente Simulationsmodell vorgestellt, mit dessen Hilfe der Ursprung der nichtlinearen Kinetik erklärt werden kann. Es ist weithin akzeptiert, dass das resistive Schalten durch die Bewegung von Sauerstoffleerstellen im Isolator ausgelöst wird. Trotzdem

ist bisher noch unklar, ob diese Ionenbewegungen durch das angelegte elektrische Feld oder durch Temperaturerwärmung beschleunigt werden. Durch Vergleich der Simulationsergebnisse mit experimentellen Daten konnte die Temperaturerhöhung als der dominante Beitrag zur Erklärung der nichtlinearen Kinetik identifiziert werden. Weitere Simulationen zielten auf die Untersuchung des Skalierungspotentials von VCM Zellen ab. Dabei konnte gezeigt werden, dass das VCM Speicherkonzept Zellgrößen im unteren Nanometerbereich ermöglicht. Mit Hilfe des VCM-Modells konnten außerdem grundlegende Regeln für ein optimiertes Zelldesign aufgestellt werden.

Acknowledgement

This dissertation was written during my doctoral research at the Institut für Werkstoffe der Elektrotechnik II (IWE II) of Rheinisch Westfälische Technische Hochschule Aachen (RWTH Aachen University), with regular stays at the Peter Grünberg Institut (PGI-7) of Forschungszentrum Jülich.

I would like to express my gratitude to Prof. Rainer Waser for giving me the opportunity to do research at the Institut für Werkstoffe der Elektrotechnik and at the Peter Grünberg Institut in the exciting field of resistive switches. I thank Prof. Rainer Waser for his support and guidance. I am also indebted to Prof. Christoph Jungemann who kindly agreed to be my co-examiner in the jury.

I would like to thank Dr. Ulrich Böttger for helpful discussions, his support and advice. I owe thanks to Dr. Ilia Valov and Dr. Georgi Staikov for the fruitful discussions on the topic of electrochemistry.

To Dr. Eike Linn and Astrid Marchewka, I am very grateful for many fruitful discussions on device modeling and collaboration on this topic.

I would like to thank Prof. Regina Dittmann for the collaboration on the switching kinetics of $SrTiO_3$-based ReRAMs. Moreover, I appreciate the collaboration with Dr. Christoph Hermes and Florian Lentz on the ultrafast switching of TiO_2 ReRAM cells.

To Udo Evertz, I am very grateful for the maintenance of the compute servers and his support with the software licensing. I would like to thank my student assistants Ada Wille, Juliana Müller and Nikolas Adler for their great work on implementing the ECM model using COMSOL Multiphysics.

Many thanks also to the following people: To Stefan Tappertzhofen, Jan van den Hurk and Sebastian Schmelzer for several discussions about the experimental behavior of resistive switches. To Astrid Marchewka, Juliana Müller and Dr. Eike Linn for efficient proofreading and helpful suggestions. To Thomas Pössinger and Dagmar Leisten for their help with graphics. To Carsten Dehoff, Andreas Burkert, Astrid Marchewka, Karsten Fleck and Dr. Deok-Yong Cho for being great office mates. I thank all co-workers from IWE and PGI for their support and the pleasant work climate.

Contents

1 Introduction

As conventional memory concepts are approaching their physical scaling limits, resistive switching device concepts based on nanoionic redox phenomena have attracted great attention for their potential use in highly scalable nonvolatile resistive random access memories (ReRAMs) and crossbar logic [1]. Today, dynamic random access memories (DRAM), flash memory and static random access memory (SRAM) are the dominating memory concepts. DRAMs enables fast read and write operation and exhibit a very high endurance. Due to the charge-based memory concept, however, their scaling potential is limited. Moreover, DRAMs are volatile. In contrast, flash memories are non-volatile but suffer from limited endurance and slow write access times. The SRAM exhibits the fastest read and write operation. Therefore, it is mainly used as fast cache. A single memory cell, however, consists of several transistors and is thus very large. ReRAMs show the potential to combine the advantages of these different memory cell types. ReRAM cells with an endurance of more than 10^{12} cycles [2] and ultrafast switching in the ps-range [3] have been demonstrated. Due to their simple metal/insulator/metal (MIM) structure ReRAMs can be easily integrated into solid state circuits and are fully CMOS compatible. Furthermore, experimental studies showed that switching elements of a few nanometers size are conceivable [4, 5], demonstrating the high scaling potential of ReRAMs. The binary information is decoded as different resistance states of the ReRAM cell. By applying appropriate electrical stimuli it can be switched back and forth between different resistance states. It has been demonstrated that more than two resistance states can be programmed (multilevel switching) allowing for storing multiple bits in a single ReRAM cell. Apart from the memory application, ReRAMs can be used in crossbar logic devices [6, 7].

First publications on resistive switching were published in the 1960s, which have been comprehensively reviewed by Dearnaley et al. [8], Oxley [9] and Pagnia [10]. This research activity faded in the 1980s due to the advantages of Si semiconductor based memories at that time. In the late 1990s a new period of research activity started, triggered by the publications of Asamitsu et al. [11], Kozicki et al. [12], and Beck et al. [13]. Up to now the research activity in this topic has increased immensely driven by the demand of low cost high performance memory.

The understanding of the basic resistive switching mechanisms has been developed in recent years. In general, three different major switching mechanisms could be identified: the electrochemical mechanism (ECM), the valence change mechanism (VCM), and the thermochemical mechanism (TCM). Nevertheless, many details remain or are under discussion such as the origin of the nonlinear switching kinetics or the physical origin of the multilevel switching in ECM cells. As one possibility to address these open questions computer simulations can be employed. Using computer simulations different physical switching models can be investigated and proven by comparison of the simulation results with experimental data. In addition, they can provide information about scaling projections, the choice of the most suited materials and the best geometry. Moreover, the development of dynamic simulation models for resistive switching is crucial for the development of integrated logic circuits consisting of several different electronic devices including ReRAMs. But, despite the huge research activity only a few publications deal with the physical modeling. Moreover, the published models cannot answer these questions sufficiently.

In this thesis novel physics-based simulation models of resistive switching devices of ECM and VCM cells are developed. In detail, a dynamic model of the switching process in ECM is presented. Simulations based on this model are performed to investigate fundamental phenomena as the switching kinetics and the multilevel switching capabilities. The latter is realized by a modulation of a tunneling gap between one electrode and a growing filament within the insulating layer. By comparison of the simulation results to experimental data this model is verified. Regarding the VCM cell, the simulations aim for understanding the nonlinear switching kinetics. For this, a static simulation model including electro-thermal coupling is set up. Again, the simulation results are compared to experimental data. Furthermore, the model enables to address the scaling of VCM cells. The switching in TCM cells is briefly discussed based on the simulation results of the ECM and VCM modeling.

Chapter 2 gives a brief overview the classification of ReRAMs, the memory architecture and requirements as well as the physical fundamentals required for modeling resistive switching. In Chapter 3 the used simulation methods are presented. The modeling and simulation of resistive switching in ECM cells is covered in Chapter 4, whereas Chapter 5 addresses the VCM switching. Finally, the results of this thesis are summarized and the similarities of the ECM and VCM cells are elaborated in Chapter 6. In addition, an outlook on further model improvements and developments as well as an outlook on further simulation studies are given.

2 Fundamentals

2.1 Classification of ReRAMs

A ReRAM cell generally consists of an insulating material 'I' sandwiched between two (often different) electron conductors 'M'. In order to repeatedly switch between a high resistive state (HRS) and a low resistive state (LRS) an initial electroforming process is typically required. In a number of systems also more than two different resistance states can be programmed, which offers the possibility of storing more than one bit in a single cell.

Two different switching schemes have to be distinguished: bipolar and unipolar switching. If the switching does not depend on the voltage polarity, the switching operation is called unipolar. During the SET operation into the LRS a current compliance is used to prevent permanent breakdown of the device and an immediate RESET (see **Figure 2.1(a)**). To reset the device to the HRS a higher current than for the SET operation is required. The RESET operation typically occurs at lower applied voltages, whereas the voltage polarity is irrelevant. In contrast, a reversal of the voltage polarity is required for the RESET operation in bipolar switching cells. Here, the SET operation is obtained by applying a voltage with a distinct polarity and the RESET occurs by applying a voltage with reversed polarity (see Figure 2.1(b)). A ReRAM cell which shows bipolar switching needs to have some asymmetry. This can be different electrode materials or it can be induced during the initial electroforming process.

The resistive switching mechanism in ReRAMs can be divided into three subclasses: the electrochemical mechanism (ECM), the valence change mechanism (VCM) and the thermochemical mechanism (TCM) [14]. In ECM cells one of the electrodes consists of Ag or Cu and is electrochemically active. The resistive switching is attributed to an electrochemical growth and a dissolution of a Ag or Cu filament within the I-layer. Due to their electrochemical nature ECM cells show a bipolar operation scheme [15]. The valence change mechanism relies on the migration of oxygen vacancies within the applied electric field and thus exhibits bipolar operation. The subsequent change in stoichiometry leads to a valence change in the cation sublattice and a change in the electronic conductivity. In addition, the oxygen

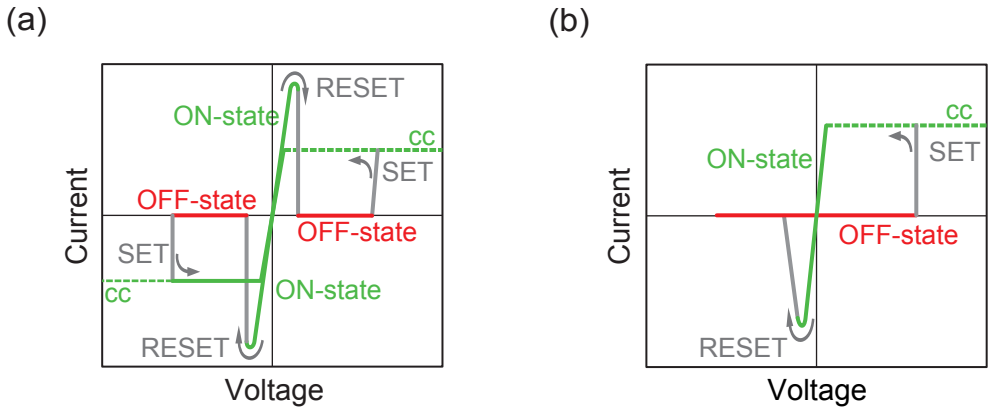

Figure 2.1: The two basic switching schemes (a) unipolar and (b) bipolar switching (redrawn from [14]). The I-V curves are displayed for a triangular voltage sweep as excitation. The current compliance is denoted as cc. Within cc the measured voltage drop deviates from the control voltage.

vacancies act as mobile dopants and can therefore modulate the electronic barriers at the interfaces (cf. Section 2.4) [14]. The third mechanism (TCM) shows an inherently unipolar switching operation, since the thermochemical effect dominates over the electrochemical effects. Here, thermally induced stoichiometry variations and redox reactions lead to a variation of the local conductivity [16]. The state of the art and the physical mechanisms have been extensively reviewed by Valov et al. [15], Waser et al. [14] and Ielmini et al. [16] for ECM, VCM and TCM cells, respectively.

In order to model the resistive switching in ReRAMs one needs to identify the governing physical processes within the MIM structure. After a short overview on memory architecture and requirements in Section 2.2, these processes are described. Firstly, in Section 2.3 the electronic and ionic transport within the I-layer is discussed. The barrier-related transport process at the MI interface or across the whole MIM structure are presented in Section 2.4. Due to the mixed ionic and electronic transport in the I-layer redox reactions occur at the MI interfaces, which can result in a formation of a new phase (cf. Section 2.5). In these sections the leading questions are which processes account for the switching kinetics and how the resistance change can be explained.

2.2 Memory Architecture and Requirements

A ReRAM is organized in an array structure (see **Figure 2.2**), where the columns are called bit lines and the rows word lines. At each node (crosspoint) a resistive

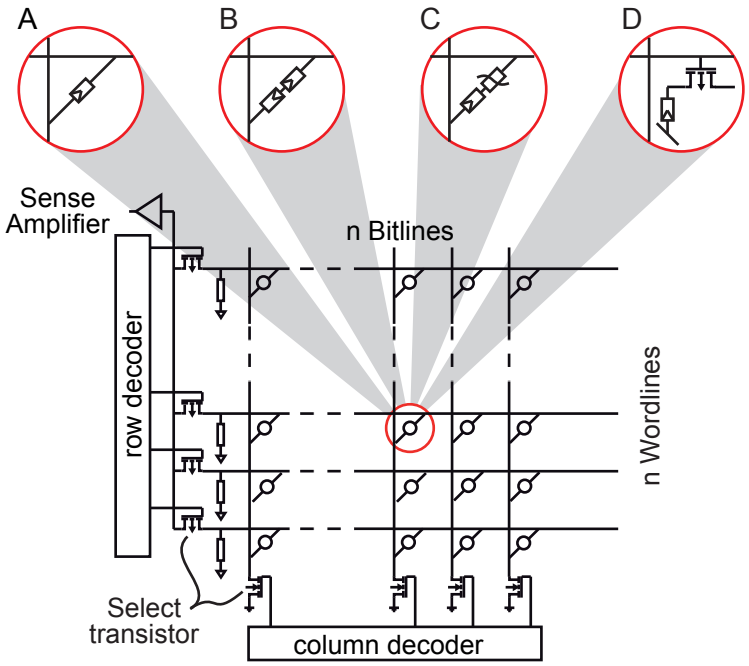

Figure 2.2: Schematic of a memory array with ReRAMs at each node (crosspoint). The nodes can consist of (A) a single ReRAM cell, (B) a CRS cell (two bipolar ReRAM cells anti-serially connected), (C) a diode in series to a ReRAM cell or (D) a transistor in series to a ReRAM cell.

switching memory cell is located. The word lines are used to access all bit lines in a specific row to write or read information. Thus, always a complete word can be processed in parallel. During a write operation the bit lines contain the information ('0' or '1') that is to be stored. For read-out the bit lines are connected to a sense amplifier which interprets the stored information. The simplest case of such a memory array is a passive crossbar array where only the ReRAM cell connects bit and word line (A). This design is favorable with respect to complexity and scalability. But, a single ReRAM cell in LRS can lead to short circuits within the array, which limits the memory functionality. Recently, a solution of this sneak path obstacle has been given by Linn et al. [17]. Instead of having one ReRAM cell a configuration of two anti-serially connected bipolar resistive switches is proposed (B). One of these cells is always in the HRS whereas the other one is in the LRS. Thus, sneak paths are avoided. This concept enables large passive arrays whereas it is restricted to bipolar ReRAMs. Sneak paths can also be avoided by using selector diodes in connection with the ReRAM cell at each node (C). Due to the strongly rectifying behavior of a diode, this memory concept is well suited for unipolar devices. For bipolar devices, however, it is very challenging to achieve sufficiently

high current levels with both polarities. The most common concept is to use a select transistor at each node (D). Its gate contact is connected to the word line, while the source is connected to the bit line and the drain contact to the ReRAM cell. Hence, the ReRAM cell can be accessed by applying a voltage to the word line. The ReRAM cell has to be connected to either ground in case of a unipolar cell or an additional plate line for a bipolar cell. In contrast, the memory designs A-C can be all implemented within a simple crossbar array requiring less integration complexity.

This memory architecture imposes some constraints on the ReRAM cell. By scaling the cross section of the bit and word lines, their resistance increases. In addition, electron scattering occurs at the boundaries when the dimensions of the line gets smaller than the electron mean free path [18]. This leads to an additional increase in line resistance. According to [19] the resistance of a Cu bit line with 128 memory elements is approximately $R_{\mathrm{BL}} = 4\,\mathrm{k\Omega}$ for a cross section of $5 \times 5\,\mathrm{nm}$. To enable a secure, low power RESET operation the LRS resistance is restricted to $R_{\mathrm{LRS}} \gg R_{\mathrm{BL}}$. In addition, the select transistor as well as the word line select transistor constrain the maximum current during switching to approximately $10\,\mu\mathrm{A}$. Further constraints are given by the sense amplifier that should be reasonably small and highly efficient. A resistance ratio $R_{\mathrm{HRS}}/R_{\mathrm{LRS}} \geq 10$ is preferable and secondly the read current in the LRS should be more than $1\,\mu\mathrm{A}$ to allow for a fast detection [14].

Besides the constraints given by the memory architecture further requirements apply to outperform FLASH or even DRAM. The number of successful write cycles (endurance) should exceed 10^7, if compared to FLASH, and 10^{15} to be competitive with DRAM. The switching speed at voltages of a few volts should be less than 100 ns or even 10 ns to compete with SRAM [14]. In contrast, a data retention time of more than 10 years at 85°C is required for a universal non-volatile memory. This retention time should also be kept under constant read pulse trains. This combination of fast switching time and long retention time is called the voltage-time dilemma [14]. A suitable memory material should show a nonlinearity in the switching kinetics of approximately 16 orders of magnitude to overcome this dilemma. This nonlinearity needs to be achieved by a ratio of write to read voltage of 10.

2.3 Electronic and Ionic Transport in Solids

The I-layer in the ReRAM cell exhibits electronic as well as ionic conduction. Such materials are called mixed ionic electronic conductors. Depending on the material

system the ionic partial conductivity can be only a small fraction or the majority of the total conductivity.

In general, the electronic conduction mechanism in the I-layer can be described by a wide band gap semiconductor model. In the absence of dopants the conductivity is very low due to the wide band gap ΔW_g and the resulting high activation energy. In transition metal oxides, however, oxygen vacancies are incorporated during fabrication and the electroforming step. Basically, these vacancies act as shallow donors in most transition metal oxides and thus the electronic conductivity is given by

$$\sigma\left(T\right) = 2ec_{\mathrm{V\ddot{O}}}\mu_n\left(T\right) = 2ec_{\mathrm{V\ddot{O}}}\mu_\mathrm{n}\left(300\,\mathrm{K}\right)\left(\frac{T}{300\,\mathrm{K}}\right)^{-\beta}. \tag{2.1}$$

In Eq. (2.1) $c_{\mathrm{V\ddot{O}}}$ denotes the concentration of the oxygen vacancies, μ_n the electron mobility, e the electron charge and β a temperature coefficient, which depends on the underlying scattering mechanism within the semiconductor. The factor of 2 in Eq. (2.1) results since oxygen vacancies are doubly charged and donate two electrons to the lattice in the conduction band. The local electronic conductivity of the material can therefore be strongly modulated when the oxygen vacancies move within an applied electric field. In addition, there is a slight temperature dependence of the electronic conductivity.

On an atomistic level the ionic transport corresponds to ions hopping from site to site in the insulating layer. An ion must hop to a vacant site, which can be either an interstitial or a vacancy. In an energy diagram these vacant sites represent energy minima and an activation energy ΔW_a is required to overcome the potential barrier between two sites (cf. **Figure 2.3**). The mean distance between these two sites is called hopping distance a. Due to the intrinsic energy landscape of ionic crystals this hopping distance lies within interatomic distances [20]. In the special case of a vacancy a hopping ion causes a vacancy moving through the solid. Without an applied electric field the hopping process occurs randomly induced by thermal fluctuations with a net flux of zero. If an electric field E is applied, a net ion flux occurs (cf. Figure 2.3). This ionic transport and its related ionic current density J can be mathematically described by the Mott-Gurney law of ion hopping [21]:

$$J = 2zeca\nu\exp\left(-\frac{\Delta W_\mathrm{a}}{k_\mathrm{B}T}\right)\sinh\left(\frac{aze}{2k_\mathrm{B}T}E\right). \tag{2.2}$$

Here, z is the ionic charge number, c the concentration of the ions and ν the attempt frequency. According to this equation a significant increase in ionic current is expected for an increase in temperature. On the other hand the ionic current

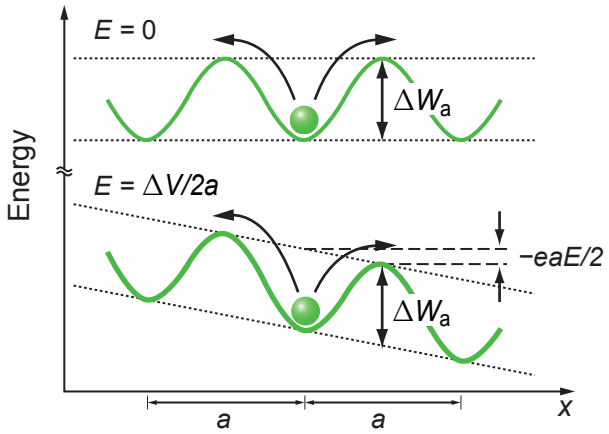

Figure 2.3: Schematic presentation of a random ion hopping event without (upper figure) and with (lower figure) an externally applied electric field E. The ion has to overcome a barrier ΔW_a to jump to a vacant site within the hopping distance a. With applied field the energy barrier for a jump to the right is reduced by $\Delta W = -eaE/2$ (redrawn from [22]).

becomes exponentially dependent on the electric field for $E \gg 2k_\mathrm{B}T/aze$, whereas it is linearly dependent for low electric fields ($E \ll 2k_\mathrm{B}T/aze$). Thus, the ionic transport can be temperature and electric field enhanced.

2.4 Electronic Transport across Interfaces

2.4.1 Electronic Transport across an MI Interface

The resistive switching in VCM cells is attributed to a modulation of the electrostatic barrier at the MI interface. This barrier is formed due to different work functions of the M-layer and the I-layer. The structure is called a Schottky junction and reveals a current rectification. In forward direction the junction is conducting and in reverse direction the current is suppressed. If two Schottky junctions are anti-serially connected as in an MIM structure, at least one interface is polarized in reverse direction. Thus, the MIM device is in general initially highly insulating. The electronic transport for high barriers and low doping levels can be described by the thermionic emission (TE) theory derived by Bethe [23]. The derivation for the $J-V$ characteristic yields

$$J_\mathrm{TE} = A^* T^2 \exp\left(-\frac{e\phi_\mathrm{Bn}}{k_\mathrm{B}T}\right)\left[\exp\left(\frac{eV}{k_\mathrm{B}T}\right) - 1\right] \tag{2.3}$$

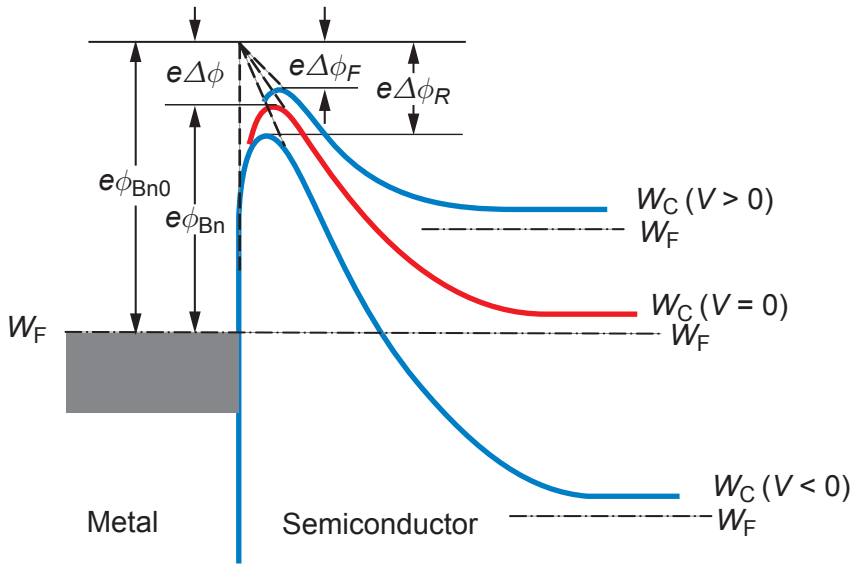

Figure 2.4: Energy-band diagram for a metal n-type semiconductor under forward bias ($V_\mathrm{F} > 0$), reverse bias ($V_\mathrm{R} > 0$) (in blue) and zero bias (red line) taking into account the Schottky effect. The intrinsic barrier is denoted $e\phi_\mathrm{Bn0}$ and the lowered barrier under thermal equilibrium $e\phi_\mathrm{Bn}$. The barrier lowering under forward bias $e\Delta\phi_\mathrm{F}$ is less than under reverse bias $e\Delta\phi_\mathrm{R}$.

where

$$A^* = \frac{4\pi e m_\mathrm{eff} k_\mathrm{B}^2}{h^3} \tag{2.4}$$

is the effective Richardson constant, k_B the Boltzmann constant, e the elementary electric charge, m_eff the effective electron mass and h the Planck constant. The barrier height $e\phi_\mathrm{Bn}$ is decreased for charge carrier emission due to image-force barrier lowering in the presence of an electric field. This effect is called the Schottky effect [24, 25]. In fact, the barrier lowering is polarity dependent and is less in forward direction than in reverse direction as illustrated in **Figure 2.4**. Mathematically, this lowering can be expressed as [24]

$$e\phi_\mathrm{Bn} = e\phi_\mathrm{Bn0} - e\Delta\phi = e\phi_\mathrm{Bn0} - e\sqrt{\frac{eE}{4\pi\varepsilon_\mathrm{is}}} = e\phi_\mathrm{Bn0} - e\left[\frac{e^3 N\,|\psi_s|}{8\pi^2\varepsilon_\mathrm{is}^3}\right]^{\frac{1}{4}}. \tag{2.5}$$

Here, ε_is is the dielectric permittivity of the insulator, E the maximum electric field at the MI interface, $e\phi_\mathrm{Bn0}$ the barrier height without barrier lowering and N the dopant concentration. The surface potential ψ_s is given by

$$\psi_\mathrm{s} = \phi_\mathrm{Bn0} - \phi_\mathrm{n} - V \approx \phi_\mathrm{Bn0} - \left(\frac{e\Delta W_\mathrm{g}}{2} - \frac{k_\mathrm{B}T}{e}\ln\left(\frac{N}{n_\mathrm{i}}\right)\right) - V \tag{2.6}$$

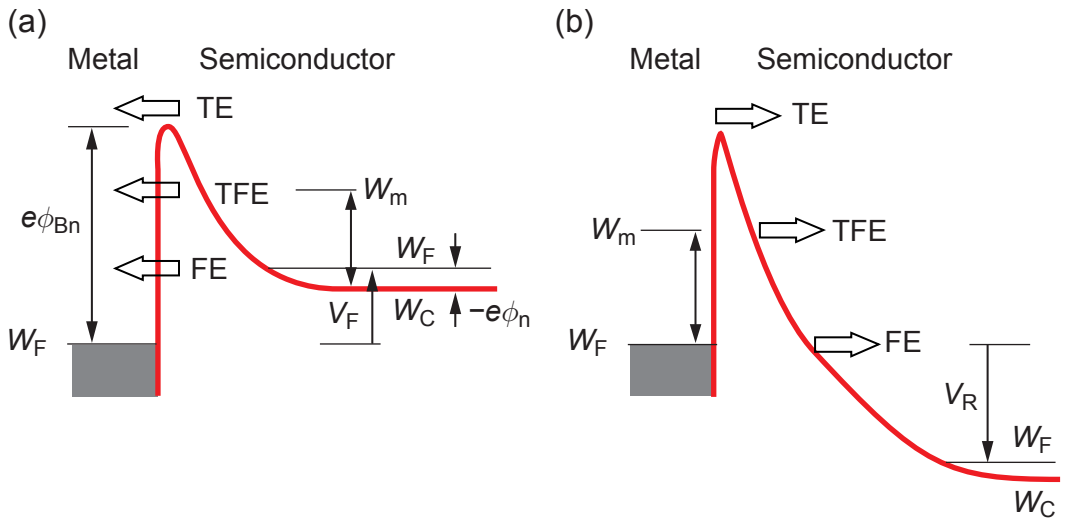

Figure 2.5: Schematic of the energy-band diagram for a metal n-type degenerate semiconductor interface illustrating tunneling currents under (a) forward bias V_F and (b) reverse bias V_R. The abbreviations are TE = thermionic emission, TFE = thermionic field emission, and FE = field emission.

where n_i is the intrinsic carrier concentration and ΔW_g the band gap of the insulator. According to Eq. (2.5) the barrier lowering is proportional to $N^{\frac{1}{4}}$. Thus, by increasing the doping concentration at the interface the electronic current will increase. Due to the polarity dependence of the barrier lowering this modulation of the current density is more pronounced in reverse direction. In a VCM cell oxygen vacancies are driven towards the active electrode and can hence modulate the electronic current across the interface accompanied by a resistance change.

At very high doping concentrations at the interface the width of the barrier becomes very narrow, which enables electron tunneling. Thus, additional current contributions have to be considered which leads to even higher currents than in the pure thermionic case. These different electronic transfer processes are illustrated in **Figure 2.5** for forward and reverse direction. Apart from the thermionic emission (TE) over the barrier, field emission (FE) near the Fermi level W_F of the emitting material and thermionic-field emission (TFE) at energies between TE and FE emerge. For TFE thermally exited carriers see a thinner barrier as they tunnel through it at a higher energy level W_m. In contrast, for FE only carriers at the Fermi level contribute. Analytical expressions for these contributions are based on the work of Padovani and Stratton [26] and outlined in the textbook of Sze and Ng [24]. These processes have in common that an exponential relation between current density and voltage results. Depending on temperature and doping level one of the

above processes dominates. A rough criterion for this arises from the comparison of the thermal energy $k_\mathrm{B}T$ to a characteristic energy E_{00} which is defined as [24]

$$E_{00} = \frac{e\hbar}{2}\sqrt{\frac{N}{m_\mathrm{eff}\varepsilon_\mathrm{is}}}. \tag{2.7}$$

TE dominates if $k_\mathrm{B}T \gg E_{00}$ and the equations derived above describe the barrier transport. When $k_\mathrm{B}T \approx E_{00}$ TFE dominates, whereas FE prevails when $k_\mathrm{B}T \ll E_{00}$ [24]. Especially, for the latter case the reverse direction becomes also well conducting, which is a prerequisite for resistive switching in VCM cells. Otherwise an MIM structure would always be insulating. In terms of the doping concentration N the above criteria can be rewritten to:

$$\text{TE: } N \ll \left(\frac{2k_\mathrm{B}T}{e\hbar}\right)^2 m_\mathrm{eff}\varepsilon_\mathrm{is}, \tag{2.8}$$

$$\text{TFE: } N \approx \left(\frac{2k_\mathrm{B}T}{e\hbar}\right)^2 m_\mathrm{eff}\varepsilon_\mathrm{is}, \tag{2.9}$$

$$\text{FE: } N \gg \left(\frac{2k_\mathrm{B}T}{e\hbar}\right)^2 m_\mathrm{eff}\varepsilon_\mathrm{is}. \tag{2.10}$$

The doping concentration needed to achieve the TFE regime is thus linearly dependent on the effective mass and the effective permittivity of the I-layer. Assuming a relative effective mass of $m_\mathrm{r} = 1$, a relative permittivity $\varepsilon_\mathrm{r} = 10$ and $T = 300\,\mathrm{K}$ a doping concentration of $N \approx 2 \cdot 10^{25}\,\mathrm{m}^{-3}$ is required to reach the TFE regime. With regard to VCM switching a corresponding amount of oxygen vacancies has to be moved to the interface to result in a significant modulation of the barrier transport in both directions.

2.4.2 Electronic Transport across an MIM Structure

When the I-layer is very thin, e.g. in the low nanometer regime, direct tunneling from metal to metal through the I-layer occurs. Besides tunneling through an as-deposited thin layer also tunneling between one metal electrode and a growing metallic filament in ECM cells or a virtual cathode in VCM cells is possible. The resulting current-voltage relation has been derived by Simmons for similar [27] and dissimilar electrodes [28]. In the simplest approximation the shape of the tunneling barrier is rectangular as illustrated in **Figure 2.6**. For the derivation of the $J - V$ characteristic three different voltage regimes need to be distinguished: the low, intermediate and high voltage regime. In the low voltage regime $eV \approx 0$ holds and

the barrier can be regarded as rectangular (cf. Figure 2.6(a)). The current density J in this regime is calculated according to Simmons [27] using

$$J = \frac{3\sqrt{2m_{\text{eff}}\Delta W_0}}{2g}\left(\frac{e}{h}\right)^2 \exp\left(-\frac{4\pi g}{h}\sqrt{2m_{\text{eff}}\Delta W_0}\right) V. \tag{2.11}$$

Here, ΔW_0 denotes the tunneling barrier height and g the tunneling gap. In this voltage regime a linear current-voltage relation is observed. If a higher voltage is applied, a trapezoidal barrier shape results. According to Figure 2.6(b) the mean barrier height is reduced by $eV/2$. This leads to [27]

$$\begin{aligned} J =& \frac{e}{2\pi h g^2}\left(\Delta W_0 - \frac{eV}{2}\right)\exp\left(-\frac{4\pi g}{h}\sqrt{2m_{\text{eff}}}\sqrt{\Delta W_0 - \frac{eV}{2}}\right) \\ &- \frac{e}{2\pi h g^2}\left(\Delta W_0 + \frac{eV}{2}\right)\exp\left(-\frac{4\pi g}{h}\sqrt{2m_{\text{eff}}}\sqrt{\Delta W_0 + \frac{eV}{2}}\right). \end{aligned} \tag{2.12}$$

When $eV \ll \Delta W_0$ Eq. (2.12) reduces to Eq. (2.11).
The third regime applies for voltages $eV \geq \Delta W_0$. In this regime the shape of the barrier becomes triangular and the effective tunneling gap is reduced as illustrated in Figure 2.6(c). From this figure the mean barrier height is $\Delta W_0/2$ and the effective tunneling gap is $\Delta g = g\Delta W_0/eV$. The current-voltage relation now reads [27]

$$\begin{aligned} J =& \frac{2.2e^3V^2}{8\pi h\Delta W_0 g^2}\exp\left(-\frac{8\pi g}{2.96heV}\sqrt{2m_{\text{eff}}}\Delta W_0^{\frac{3}{2}}\right) \\ &- \frac{2.2e^3V^2}{8\pi h\Delta W_0 g^2}\left(1+\frac{2eV}{\Delta W_0}\right)\exp\left(-\frac{8\pi g}{2.96heV}\sqrt{2m^*}\Delta W_0^{\frac{3}{2}}\left(1+\frac{2eV}{\Delta W_0}\right)^{\frac{1}{2}}\right). \end{aligned} \tag{2.13}$$

In all three regimes the current density depends exponentially on the tunneling gap. Thus, a dramatic resistance change is achieved if a metal filament grows towards the counter electrode and electron tunneling becomes the dominating conduction mechanism. Especially, for high electronic barriers the tunnel current dominates over the thermionic emission current.
In the foregoing discussion an ideal barrier has been assumed. A real barrier, however, has a different shape due to image-force barrier lowering. The image force leads to a reduction of the barrier thickness and the barrier height, which results in a more parabolic shape. Regarding the $J-V$ characteristic an increase in current density follows but the general shape is preserved [27]. In addition, the tunnel characteristics become dependent on the dielectric constant of the I-layer due to the image force. The smaller the permittivity, the higher is the tunneling current [27].

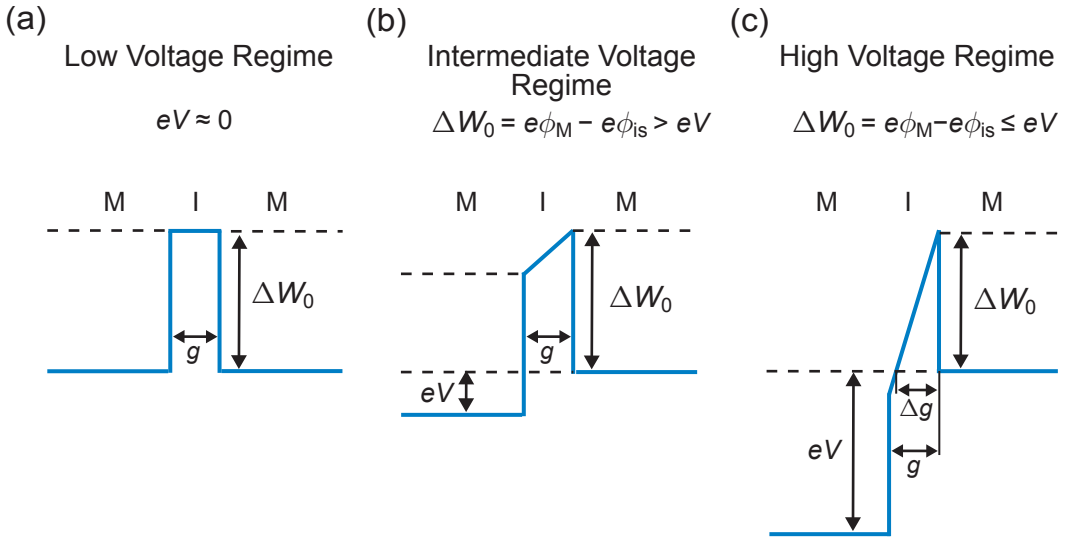

Figure 2.6: Energy-band diagram of a symmetric MIM structure with barrier height ΔW_0 in the (a) low (b) intermediate and (c) high voltage regime. The work functions for the metal and the insulator are denoted ϕ_{M} and ϕ_{is}, respectively.

2.5 Electrodeposition and Phase Formation

The M-layers are typically not ion conducting but even ion blocking. Thus, the ions in the I-layer can only contribute to the overall current if electron transfer reactions occur at both MI interfaces. This means that an oxidation takes place at one electrode and a reduction at the opposite electrode. The energy diagram of such an electron transfer process with and without applied voltage is shown in **Figure 2.7**. The left potential well describes the potential energy of a metal atom at the metal surface. In contrast, the right potential well is attributed to a metal ion in the insulator close to the metal surface. To oxidize a surface metal atom a free activation energy ΔG_{ox} is required, whereas for the reduction and succeeding deposition the free activation energy ΔG_{red} is required. If a positive potential is applied to the metal electrode, its Fermi energy is decreased by $ze\eta$. Here, z is the number of exchanged electrons and η represents the electrochemical overpotential. Thus, the activation energies for oxidation and reduction are changed and the oxidation process is favored over the reduction process. Figure 2.7 shows that the change of the activation energy is proportional to the applied overpotential. The involved proportionality factor α is called charge transfer coefficient and represents that part of the overpotential being used for lowering the activation energy for the

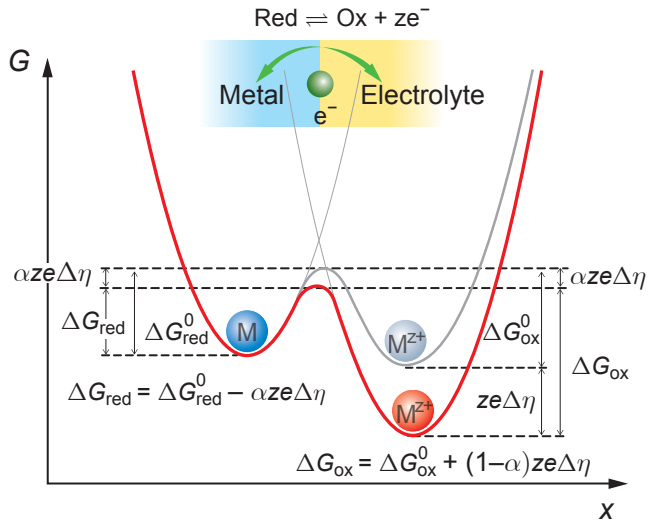

Figure 2.7: Schematic of the energy profile of an electron transfer reaction between a metal electrode and a corresponding cation within the electrolyte close to the metal surface. The profiles are shown for the equilibrium case (grey line) and under an applied voltage (red line) (redrawn from [22]).

particular process. Based on these considerations the electron transfer process can be described mathematically by the Butler-Volmer equation [29]

$$J = j_0 \left[\exp\left(\frac{(1-\alpha)\, ze}{k_\mathrm{B}T} \eta \right) - \exp\left(-\frac{\alpha ze}{k_\mathrm{B}T} \eta \right) \right]. \tag{2.14}$$

Here, j_0 is the exchange current density, which is strongly temperature dependent according to $j_0 \propto \exp\left(-\Delta W_\mathrm{a}/k_\mathrm{B}T\right)$. The left term of Eq. (2.14) describes the oxidation, whereas the right term corresponds to the reduction reaction. For low overpotentials $\eta \ll k_\mathrm{B}T/ze$ the current becomes linearly dependent on η, whereas it becomes exponentially dependent for high overpotentials $\eta \gg k_\mathrm{B}T/ze$.

In case of ECM cells metal cations are reduced at the inert cathode which leads to the formation of a filament by electrocrystallization. This process starts with a nucleation of the new metal phase. The formed nucleus, which consists of a number metal atoms N, has to achieve a critical cluster size of N_crit atoms in order to permit further growth. Therefore, a characteristic threshold overpotential η_crit exists for the nucleation process, below which the nucleation rate is practically zero and above which it increases exponentially. According to these considerations the nucleation rate can be expressed by

$$J = K(Z_0, N_\mathrm{crit}) \exp\left(\frac{(N_\mathrm{crit} + \alpha) ze}{k_\mathrm{B}T} \eta \right), \tag{2.15}$$

where the pre-exponential term $K(Z_0, N_{\text{crit}})$ depends on the number density Z_0 of available nucleation sites and on the number N_{crit} of metal atoms constituting the critical nucleus. Note that the nucleation process limits the switching speed only if a critical nucleus has to be formed.

A nucleation process is also necessary if a phase transformation occurs in the I-layer upon induced chemical or thermal gradients as in VCM or TCM systems. For instance, a phase transition from TiO_2 to a Magnéli phase as Ti_4O_7 can occur if oxygen vacancies move within a TiO_2 layer [30]. In a first stage a critical nucleus is formed, from which the new phase grows.

3 Simulation Methods

In general, the mathematical modeling of physical problems leads to a system of coupled differential equations, which are solved for their dependent variables. The latter represent physical properties as the electric potential or the local temperature. The differential equations contain either a single or several independent variables. In the former case the differential equation is called ordinary differential equation (ODE) and in the latter case partial differential equation (PDE). An example for an ordinary differential equation is the one dimensional Laplace equation $\Delta\varphi = \partial^2\varphi/\partial x^2 = 0$, which is solved for the electric potential φ. In a three dimensional description the Laplace equation depends on three space dimensions and is thus a partial differential equation. A time dependent physical problem involves additional time derivatives. A differential equation can be either linear or nonlinear. It is linear if the dependent variable and its derivative appear to the power of 1 and nonlinear otherwise. Analytical solutions of differential equations only exist for some special cases. They are particularly rare for partial differential equations, for nonlinear differential equations or for a system of coupled differential equations. In these cases, numerical methods have to be applied.
In order to solve the differential equations appropriate boundary conditions and/or initial values have to be defined. Three different kinds of boundary conditions can be distinguished. If the value of the dependent variable is defined at the boundary, it is called a Dirichlet boundary condition. It is called a Neumann boundary condition if the normal derivative of the dependent variable is given at the boundary. In contrast, a Cauchy boundary condition specifies both the value of the normal derivative and the dependent variable itself at the boundary. For time dependent problems initial values have to be defined in the whole solution domain.

In this chapter the different numerical methods used in this work are presented. Partial differential equations are covered in Section 3.1 and ordinary differential equations in Section 3.2. Regarding the modeling of ReRAMs in this work, all multidimensional models are mathematically described by a set of partial differential equations. This concerns the modeling and simulation of ECM cells in Section 4.4 and of VCM cells in Chapter 5. On the other hand, the derivation of a compact

model for ECM cells in Section 4.2 leads to a system of ordinary differential equations.

3.1 Partial Differential Equations

Within this thesis the commercial software COMSOL Multiphysics™ (Version 3.5a) is employed to solve the governing partial differential equations. The COMSOL software uses the finite element method (FEM) to discretize the corresponding equations. Thereby the solution domain is divided into small segments in one dimension (1D), triangles in two dimensions (2D) and tetrahedra in three dimensions in (3D): the finite elements. Note that the FEM is not restricted to segments, triangles and tetrahedra. Yet, these kinds of finite elements are used in this study. COMSOL provides different numerical solvers to solve the discretized equation system, which are described in [31]. To model the filamentary growth in ECM cells a moving mesh mode is applied. This mode is explained in more detail in Section 4.4 along with the corresponding partial differential equations. Further details of the finite element method are given in the textbook of Bathe [32].

3.2 Ordinary Differential Equations

In Section 4.2 a compact model for ECM cells is derived. In this model the equation system is reduced to a first order ordinary differential equation with only one state variable which describes the behavior of the ECM cell. This time-dependent linear differential equation reads

$$\frac{\mathrm{d}x}{\mathrm{d}t} = f(x,t). \tag{3.1}$$

Here, t is the time and $f(x,t)$ is an implicit function so that the equation has to be solved numerically. For this, one-step methods (e.g. Euler, advanced Euler or one-step Runge-Kutta) or multiple-step methods (e.g. Adams-Bashforth or Adams-Moulton) can be employed [33].

In the system in Section 4.2 an implicit equation has to be solved in every time step. The solution of this equation is the most time-critical step while solving the ordinary differential equation. Thus, a one-step method, i. e. the advanced Euler method, is applied to minimize the number of implicit equations that need to be solved. Here, MATLAB is used to implement the advanced Euler method. In the

considered systems an initial solution at time step j is given. The solution j+1 for the next time step can then be calculated using an intermediate time step at j+$\frac{1}{2}$ as

$$t_{\mathrm{j}+1} = t_{\mathrm{j}} + h, \tag{3.2}$$

$$x^{\mathrm{j}+\frac{1}{2}} = x^{\mathrm{j}} + \frac{h}{2} f\left(t_{\mathrm{j}}, x^{\mathrm{j}}\right), \tag{3.3}$$

$$x^{\mathrm{j}+1} = x^{\mathrm{j}} + h f\left(t_{\mathrm{j}} + \frac{1}{2}, x^{\mathrm{j}+\frac{1}{2}}\right). \tag{3.4}$$

The deviation of the numerical solution $x^{\mathrm{j}+1}$ from the exact solution $x(\mathrm{j}+1)$ after a single step is called the local truncation error $\tau_{\mathrm{j},h}$. Since the exact solution is not known, $\tau_{\mathrm{j},h}$ is estimated. For the advanced Euler method this yields

$$\|\tau_{\mathrm{j},h}\| = \frac{2^{p+1}}{2^{p+1}-1}\left(x^{\mathrm{j}+1} - x^{\mathrm{j}} - h f\left(t_{\mathrm{j}}, x^{\mathrm{j}}\right)\right). \tag{3.5}$$

Here, p is termed the consistency, which is 2 for the advanced Euler method. By estimation of the local truncation error the time step length h can be adapted correspondingly in every time step. The advantage of such a time step control is the optimization of the simulation speed. The time step control, which is employed, operates as follows. After calculating $x^{\mathrm{j}+1}$ using Eqs. (3.2) – (3.4) the local truncation error is estimated according to Eq. (3.5). The solution is accepted if either $\|\tau_{\mathrm{j},h}\| \leq h\epsilon$, where ϵ is a chosen tolerance, or the time step length equals a predefined minimum time step length $h_{\min}$. Otherwise the solution is abandoned and the time step is reduced to the maximum of $h/2$ and $h_{\min}$. If the solution is accepted, the time step is adjusted according to the height of the estimated error. If $\|\tau_{\mathrm{j},h}\| \leq 2^{-p-1}h\epsilon$, the time step is increased to the minimum of $2h$ or a predefined value $h_{\max}$, otherwise the time step remains unchanged. The next time step length is then calculated using the same procedure.

4 Modeling and Simulation of Resistive Switching in ECM Cells

4.1 Resistive Switching Mechanism

The resistive switching in ECM cells is attributed to the electrochemical growth and dissolution of Cu or Ag nanosized filament. Typically, ECM cells consist of a Cu or Ag active electrode, an ion conducting switching layer (SL) and an inert electrode. The switching layer can be a solid electrolyte (e.g. Ag_2S or Cu-doped $GeSe_2$) or an insulator (e.g. SiO_2, Ta_2O_5). In addition, ECM switching has been observed in cells comprising organic thin films like Cu:TCNQ or Ag:TCNQ [34, 35, 36]. In these cells the actual switching takes place in an oxide layer at one electrode, whereas the organic layer serves as ion source. Switching times in the nanosecond regime have been demonstrated [37, 38]. Furthermore, the ECM memory concept offers scaling potential down to atomic dimensions [5]. Excellent overviews of the state of the art of ECM cells have been given by Valov et al. [15] and Aono [39].
Here, the discussion will be focused on the resistive switching mechanism in ECM cells. The filamentary nature of the switching mechanism has been clearly observed in lateral cells [40, 41]. For vertical ECM cells a silver rich filamentary region has been observed using spectroscopical analysis for a LRS of $20\,\Omega$ [42]. The metallic filament might grow within nanopores in the hosting switching layer [15]. These nanopores might act as preferred ionic drift paths resulting in the filamentary growth. In addition, mechanical stress within the switching layer is avoided if the filament grows along these pores. It should be noted that the initial switching cycle typically shows different characteristics than the following switching cycles [15, 43]. This can be considered as an electroforming process. During this initial cycle nanopores for the further switching are possibly formed due to mechanical stress.

Figure 4.1 shows a typical $I - V$ characteristic of an ECM cell along with a sketch of the operation principle. During the SET switching the following processes

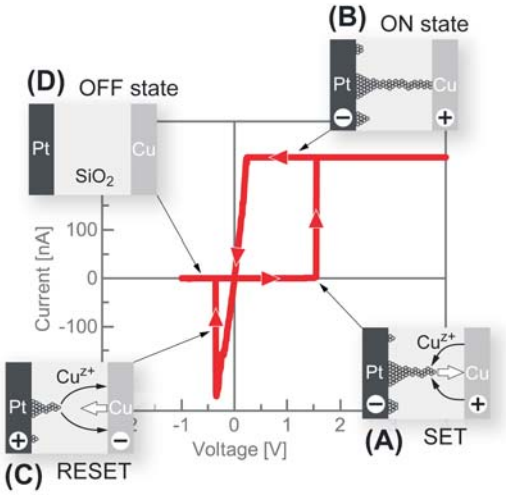

Figure 4.1: $I - V$ characteristic of a $Cu/SiO_2/Pt$ ECM cell using a triangular voltage sweep. The insets show the different stages of the switching process [43].

occur. By applying a positive voltage at the active electrode (e. g. a Cu electrode) Cu is oxidized according to the following reaction

$$Cu \rightarrow Cu^{z+} + ze^{-}$$

where z is the charge number. The Cu ions are driven out of the Cu anode and migrate towards the cathode due to the applied electric field. At the cathode an electrochemical reduction and an electro-crystallization of Cu according to

$$Cu^{z+} + ze^{-} \rightarrow Cu$$

occurs. This electro-crystallization process results in the formation of a Cu filament, which grows towards the active electrode. Finally, the filament has grown so far that an electrical contact can be established, which defines the LRS. To reset the cell a voltage with opposite polarity needs to be applied. Now, the processes are reversed, which leads to a dissolution of the filament.

The switching speed of the ECM cells is determined by the kinetics of the described process. In detail, the electrode reactions are limited by the electron-transfer process which can be well described by the Butler-Volmer equation (cf. Eq. (2.14) in Section 2.5). Secondly, the ionic motion within the switching layer, which follows the Mott-Gurney law for ion hopping (cf. Eq. (2.2) in Section 2.3), can limit the switching speed. And thirdly, the nucleation process can be the limiting factor (cf. Eq. (2.15) in Section 2.5). All these processes would lead to a highly nonlinear

exponential relation between switching time and applied voltage which has been observed in experiments [38, 44, 45]. In former studies the origin of this nonlinear switching dynamic has been modeled by ion hopping at high electric fields [44, 46], injection of ions into the switching layer [47] or to electron transfer reactions at the electrodes [43, 48]. Using ion hopping, however, leads to unrealistic high hopping distances in the nanometer regime in order to fit the switching kinetics [43, 46]. It has been assumed that the dissolution of the active electrode during the SET operation does not influence the switching kinetics [15]. In a recent study, however, the influence of the oxidation process has been demonstrated experimentally [49]. ECM cells show multilevel programming capabilities. The LRS can be modulated by an external current compliance (cc) or a load resistor over several orders of magnitude with values above GΩ and below kΩ [45, 50, 51, 52]. The possibility of the LRS control by a set current compliance is connected to the nonlinear dependency between switching voltage and time. As soon as the current compliance is reached the cell voltage will drop. This drop will dramatically decrease the driving force for the switching due to the nonlinear kinetics of the switching process. This excludes nucleation to be the rate limiting step during the final stages of SET switching and during RESET switching, since the nucleation overpotential is zero as soon as a stable nucleus is formed. Nucleation, however, can limit the process during the initial forming cycle or the first step during the SET switching. Multilevel programming is often explained as a variation in the width of the conductive filament resulting in different LRS [44, 46, 45]. For a more detailed discussion the achievable resistance range for this variable-width hypothesis is calculated in the following. Here, it has to be considered that the metal resistivity ρ_0 deviates from its bulk value, if the diameter d is smaller than the electron mean free path λ_0. The Fuchs-Sondheimer approximation [18] for cylindrical wires can be used to calculate the resistivity ρ^* in the limit $d \ll \lambda_0$:

$$\rho^* = \rho_0 \frac{1-p}{1+p} \cdot \frac{\lambda_0}{d}. \tag{4.1}$$

Here, p is the surface reflectivity for scattering events. For $p = 0$ the resistivity achieves its maximum value. The overall maximum resistance of a metallic bridge R_{Bridge} of length L is calculated by the sum of the contact resistance $R_{\mathrm{c}} = \rho_0/d$ and the filament series resistance R_{s} [53]

$$R_{\mathrm{Bridge}} = R_{\mathrm{c}} + R_{\mathrm{s}} = \frac{\rho_0}{d} + \rho^* \frac{4L}{\pi d^2} = \frac{\rho_0}{d}\left(1 + \frac{4L\lambda_0}{\pi d^2}\right). \tag{4.2}$$

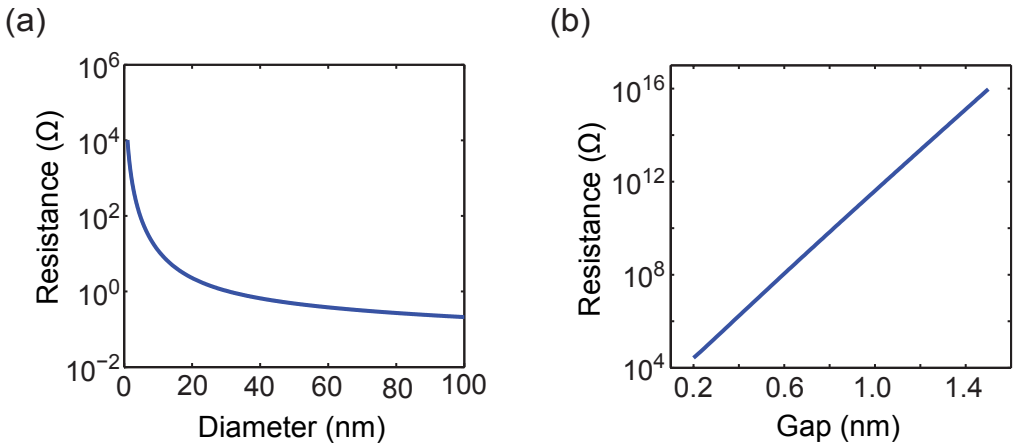

Figure 4.2: (a) Resistance vs. filament diameter calculated according to Eq. (4.2) whith $L = 10\,\text{nm}$, $\lambda_0 = 40\,\text{nm}$ and $\rho_0 = 2 \cdot 10^{-8}\,\Omega\text{m}$. (b) Resistance vs. tunneling gap calculated according to Eq. (2.12) in Section 2.4 with $m_\text{r} = 1$, $d = 4\,\text{nm}$, $\Delta W_0 = 3.6\,\text{eV}$ and $V_\text{read} = 0.2\,\text{V}$.

The resistances calculated according to Eq. (4.2) are plotted against the diameter in **Figure 4.2(a)**. Obviously, the variable width case leads to resistances $R \leq 10\,\text{k}\Omega$, which are lower than those experimentally observed. In addition, it only accounts for five orders of magnitude. For this, however, the filament diameter has to be changed by two orders of magnitude, which seems to be rather unlikely. Especially, the amount of Cu atoms to build up such a large filament might consume a huge part of the active electrode. In addition, this large variation in diameter might be accompanied by huge mechanical stress. If one considers only a moderate maximum diameter of 10 nm, the change in resistance is only three orders of magnitude. It is therefore hard to explain the whole range of multilevel states by a variation of the filament diameter. A second big issue is connected to the proposed RESET mechanism based on a combination of Joule heating and an electrochemical dissolution of the filament [54]. To achieve significant Joule heating in thin filaments for typical RESET voltages in ECM cells below 0.5 V, RESET currents higher than 1 µA are expected [55, 56]. For high LRS, however, RESET currents can be lower than µA [57, 43, 45, 51] excluding Joule heating.

In an alternative scenario the different LRS can be explained by a variation of the tunneling gap between filament and active electrode as proposed by Menzel et al. [58]. The resistance in this scenario is correlated to the tunneling current (cf. Section 2.4) if the applied voltage is significantly lower than the barrier height. The calculated resistances plotted against the tunneling gap are shown in Figure 4.2(b) for a filament of 4 nm diameter. Apparently, the resistance can be potentially

modulated over more than 10 orders of magnitude by varying the gap by 1 nm. The gap width in this model is controlled by the set current compliance. This kind of control method has been used to fabricate electrode pairs with distinct angstrom-sized gaps [59]. The RESET switching in this picture is simply the reversed SET process, since the electrochemical cell is not shortened. The quantum resistance of a single-atom metallic contact is about $R_0 = 12.9\,\mathrm{k\Omega}$ [60], which lies in between the resistance values of the variable-width and the proposed variable-gap resistances. Thus, there might be a possible transition between these two cases. In a recent study a step-wise resistance decrease has been observed using an STM tip as the inert electrode in tunneling distance to a Cu_2S substrate [61]. This has been attributed to the transition from a tunneling gap region to a quantum contact, which supports the proposed model. In addition, also unipolar switching modes have been demonstrated, where the LRS is below $20\,\mathrm{k\Omega}$ [54, 62, 63]. Using a tunneling based model, the occurrence of unipolar switching modes can be attributed to a filament that has established a galvanic contact. In this case a low LRS results and significant Joule heating might give rise to a unipolar switching behavior.
Based on these considerations an ECM model has been derived in this work in which the electron-transfer reaction limits the switching speed and the variation of a tunneling gap accounts for the multilevel switching capabilities. It is assumed that nanopores are present within the switching layer as well as copper/silver nuclei at the inert electrode. Thus, a nucleation overpotential can be neglected. This restricts the model to the switching case and the forming process is not covered. In addition, copper gradients are neglected, resulting in zero space charge. Based on this physical model a 1D compact model, an analytical model and a multidimensional FEM model are derived in Sections 4.2, 4.3 and 4.4, respectively. The corresponding simulation results are discussed with respect to experimental data.

4.2 1D Physical Compact Model

Figure 4.3 shows a schematic of the simulation model. The metallic cylindrical filament grows from the inert bottom electrode through the SL and modulates the tunneling gap x. Within the SL ionic and electronic tunneling currents are present. The ionic current path is modeled by two voltage controlled current sources, which represent the electron-transfer reactions at the boundaries (see explanation below), and the resistance due to ionic drift $R_{\mathrm{ion}}(x)$. The electronic current path is attributed to electronic tunneling, represented by one voltage controlled current source. The LRS is reached as the tunneling gap is small enough to enable significant

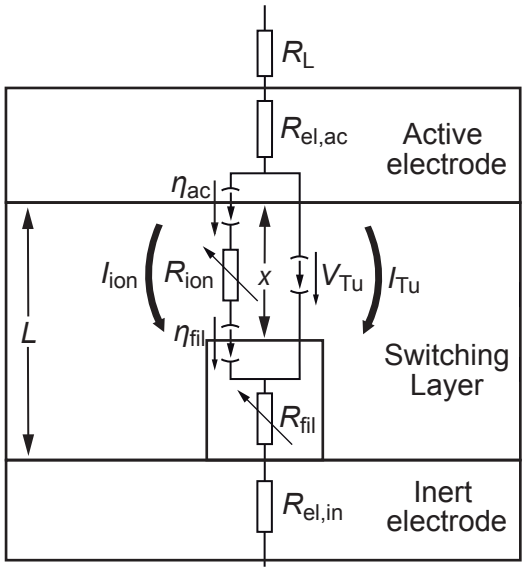

Figure 4.3: Schematic of the switching model with equivalent circuit diagram. The switching layer of thickness L is sandwiched between the active top electrode and the inert bottom electrode. A cylindrical filament growth within the SL and modulates the tunneling gap x between filament and active electrode. The elements of the equivalent circuit are an optional load resistor R_{L}, the electrode resistors $R_{\mathrm{el,ac}}$ and $R_{\mathrm{el,in}}$ and the filament resistor $R_{\mathrm{fil}}(x)$. In the switching layer the ionic current path (left path) is represented by two voltage controlled current sources with controlling voltages η_{ac} and η_{fil}, and the ionic resistance $R_{\mathrm{ion}}(x)$. The electronic current path (right path) within the SL is given by one voltage controlled current source with controlling voltage V_{Tu} (redrawn from Menzel et al. [58]).

tunneling current. The filament growth/dissolution and thus the change of x can be described using Faraday's law [29, 64]

$$\frac{\mathrm{d}x}{\mathrm{d}t} = -\frac{M_{\mathrm{Me}}}{ze\rho_{\mathrm{m,Me}}} J_{\mathrm{Me}^{z+}}. \tag{4.3}$$

where $J_{\mathrm{Me}^{z+}}$ is the ionic current density, z the charge transfer number, M_{Me} the atomic mass and ρ_{Me} the mass density of deposited metal. To simplify the model dissolution/growth of the active electrode is neglected, since its active volume is large compared to the volume of the filament. The redox reactions at the electrodes involve an electron transfer reaction. The resulting current density due to this charge transfer is described by the Butler-Volmer equation

$$J_{\mathrm{Me}^{z+}} = J_{\mathrm{BV}}(\eta) = j_0 \left\{ \exp\left(\frac{(1-\alpha)\, ze}{k_{\mathrm{B}}T} \eta \right) - \exp\left(-\frac{\alpha ze}{k_{\mathrm{B}}T} \eta \right) \right\} \tag{4.4}$$

and defines the ionic current. Here, j_0 is the exchange current density, α the charge transfer coefficient and η the overpotential. If η is positive, the first term describing the oxidation process dominates, whereas the second term describing the reduction process prevails for negative η. In this form the Butler-Volmer equation leads to severe numerical problems in determining the overpotentials at both electrodes. For better numerical stability it is further simplified using two different approaches. In each simplification an explicit expression for the overpotential at the active electrode/SL interface η_{ac} as a function of the filament/SL overpotential η_{fil} is derived.

In the first approach the charge transfer coefficient is set to $\alpha = 0.5$ and thus Eq. (4.4) reduces to

$$J_{\mathrm{BV}}(\eta) = 2j_0 \sinh\left(\frac{ze}{2k_{\mathrm{B}}T}\eta\right). \tag{4.5}$$

For $\eta \gg 2k_{\mathrm{B}}T/ze$ Eq. (4.5) becomes exponentially dependent on η and linear at very low η. Due to charge neutrality the ionic currents at the active and the inert electrode are equal. Therefore, η_{ac} can be expressed by η_{fil}

$$\begin{aligned} I_{\mathrm{ion}} &= I_{\mathrm{BV}}(\eta_{\mathrm{fil}}) = I_{\mathrm{BV}}(\eta_{\mathrm{ac}}) \\ \Leftrightarrow -2j_0 A_{\mathrm{fil}} \sinh\left(\frac{ze}{2k_{\mathrm{B}}T}\eta_{\mathrm{fil}}\right) &= 2j_0 A_{\mathrm{ac}} \sinh\left(\frac{ze}{2k_{\mathrm{B}}T}\eta_{\mathrm{ac}}\right) \\ \Rightarrow \eta_{\mathrm{ac}} &= \frac{2k_{\mathrm{B}}T}{ze} \sinh^{-1}\left(-\frac{A_{\mathrm{fil}}}{A_{\mathrm{ac}}} \sinh\left(\frac{ze}{2k_{\mathrm{B}}T}\eta_{\mathrm{fil}}\right)\right), \end{aligned} \tag{4.6}$$

where A_{ac} is the area of the active electrode involved in the redox reaction and A_{fil} the filament area. Note that the algebraic signs of the Butler-Volmer currents in Eq. (4.6) are different due to the inverse redox reactions occurring at the interfaces. This first approach is restricted to simulations for $\alpha = 0.5$. In order to model the system for variable α the following second approach is used. For $\eta \gg kT/2ze$ the first term in Eq. (4.4) dominates and the second can be neglected and vice-versa for negative η. This approximation is valid for $|\eta| \gg 2k_{\mathrm{B}}T/ze\,(= 51.4/z\,\mathrm{mV}$ at $T = 300\,\mathrm{K})$. The resulting error using this approximation is negligible, since the ionic current density for $|\eta| \leq 25.7\,\mathrm{mV}$ is too low to result in a significant filamentary dissolution or growth. Using this approximation, however, leads to different equation systems for SET and RESET operation.

During SET operation the Butler-Volmer current at the filament/SL boundary is expressed by

$$I_{\mathrm{BV,SET}}(\eta_{\mathrm{fil}}) = j_0 A_{\mathrm{fil}} \exp\left(-\frac{\alpha ze}{k_{\mathrm{B}}T}\eta_{\mathrm{fil}}\right) \tag{4.7}$$

and at the active electrode/SL boundary by

$$I_{\mathrm{BV,SET}}\left(\eta_{\mathrm{ac}}\right) = j_0 A_{\mathrm{ac}} \exp\left(\frac{(1-\alpha)\, ze}{k_{\mathrm{B}}T}\eta_{\mathrm{ac}}\right). \tag{4.8}$$

As in the first approach η_{ac} can be expressed with η_{fil} using

$$\begin{aligned} I_{\mathrm{BV,SET}}\left(\eta_{\mathrm{fil}}\right) &= I_{\mathrm{BV,SET}}\left(\eta_{\mathrm{ac}}\right) \\ \Leftrightarrow j_0 A_{\mathrm{fil}} \exp\left(-\frac{\alpha ze}{k_{\mathrm{B}}T}\eta_{\mathrm{fil}}\right) &= j_0 A_{\mathrm{ac}} \exp\left(\frac{(1-\alpha)\, ze}{k_{\mathrm{B}}T}\eta_{\mathrm{ac}}\right) \\ \Rightarrow \eta_{\mathrm{ac}} &= -\frac{\alpha}{(1-\alpha)}\eta_{\mathrm{fil}} + \frac{k_{\mathrm{B}}T}{ze\,(1-\alpha)} \ln\left(\frac{A_{\mathrm{fil}}}{A_{\mathrm{ac}}}\right). \end{aligned} \tag{4.9}$$

Again the algebraic signs of the Butler-Volmer currents are different in Eq. (4.9) due to the inverse redox reactions occurring at the interfaces. For the RESET operation the algebraic signs of the overpotentials are reversed. Therefore the resulting Butler-Volmer currents are

$$I_{\mathrm{BV,RESET}}\left(\eta_{\mathrm{fil}}\right) = -j_0 A_{\mathrm{fil}} \exp\left(\frac{(1-\alpha)\, ze}{k_{\mathrm{B}}T}\eta_{\mathrm{fil}}\right), \tag{4.10}$$

$$I_{\mathrm{BV,RESET}}\left(\eta_{\mathrm{ac}}\right) = -j_0 A_{\mathrm{ac}} \exp\left(-\frac{\alpha ze}{k_{\mathrm{B}}T}\eta_{\mathrm{ac}}\right). \tag{4.11}$$

Now, η_{ac} can be derived as follows:

$$\begin{aligned} I_{\mathrm{BV,RESET}}\left(\eta_{\mathrm{fil}}\right) &= I_{\mathrm{BV,RESET}}\left(\eta_{\mathrm{ac}}\right) \\ \Leftrightarrow j_0 A_{\mathrm{fil}} \exp\left(\frac{(1-\alpha)\, ze}{k_{\mathrm{B}}T}\eta_{\mathrm{fil}}\right) &= j_0 A_{\mathrm{ac}} \exp\left(-\frac{\alpha ze}{k_{\mathrm{B}}T}\eta_{\mathrm{ac}}\right) \\ \Rightarrow \eta_{\mathrm{ac}} &= -\frac{(1-\alpha)}{\alpha}\eta_{\mathrm{fil}} - \frac{k_{\mathrm{B}}T}{ze\alpha} \ln\left(\frac{A_{\mathrm{fil}}}{A_{\mathrm{ac}}}\right). \end{aligned} \tag{4.12}$$

Using Kirchhoff's first law the cell current for both cases ($\alpha = 0.5$ and $\alpha \neq 0.5$) is calculated as the sum of the ionic and the tunnel current I_{Tu} in the switching layer to

$$I_{\mathrm{cell}} = I_{\mathrm{Tu}}\left(V_{\mathrm{Tu}}\right) + I_{\mathrm{ion}} = I_{\mathrm{Tu}}\left(V_{\mathrm{Tu}}\right) + I_{\mathrm{BV}}\left(\eta_{\mathrm{fil}}\right). \tag{4.13}$$

The tunnel voltage V_{Tu} is equal to the voltage drop across the ionic current path according to Kirchhoff's second law. It can be calculated as the sum of η_{fil}, η_{ac} and the voltage drop due to the ionic transport in the insulating layer according to

$$V_{\mathrm{Tu}} = \eta_{\mathrm{ac}} - \eta_{\mathrm{fil}} + I_{\mathrm{BV}}\left(\eta_{\mathrm{fil}}\right) R_{\mathrm{ion}}\left(x\right) = f\left(\eta_{\mathrm{fil}}, x\right). \tag{4.14}$$

The ionic resistance is calculated as $R_{\text{ion}} = \rho_{\text{ion}} x / A_{\text{ion}}$ with the ionic resistivity ρ_{ion} and the effective area of ionic transport within the insulator A_{ion}. For an intermediate voltage range and a trapezoidal barrier I_{Tu} is calculated according to Simmons [27]

$$I_{\text{Tu}} = \frac{eA_{\text{fil}}}{2\pi h x^2}\left(\Delta W_0 - \frac{eV_{\text{Tu}}}{2}\right)\exp\left(-\frac{4\pi x}{h}\sqrt{2m_{\text{eff}}}\sqrt{\Delta W_0 - \frac{eV_{\text{Tu}}}{2}}\right) - \frac{eA_{\text{fil}}}{2\pi h x^2}\left(\Delta W_0 + \frac{eV_{\text{Tu}}}{2}\right)\exp\left(-\frac{4\pi x}{h}\sqrt{2m_{\text{eff}}}\sqrt{\Delta W_0 + \frac{eV_{\text{Tu}}}{2}}\right), \tag{4.15}$$

where ΔW_0 is the tunneling barrier height and $m_{\text{eff}} = m_r m_0$ the electron effective mass of the insulating material. In the equivalent circuit diagram Eq. (4.15) is represented by a voltage controlled current source, whereas the controlling voltage is V_{Tu} (cf. Figure 4.3). Due to the exponential dependence of I_{Tu} on x, the LRS is very sensitive to small variations in x. For small voltages V_{Tu} the tunnel junction shows an ohmic behavior, which is consistent with the experimentally observed characteristic of LRS in ECM cells. Note that a real tunnel barrier has a more parabolic shape and a shorter effective gap [27]. Both effects lead to higher currents than predicted using Eq. (4.15). The real gaps should thus be larger than in the simulations. Using Eq. (4.14) with Eq. (4.15) the tunneling voltage can be expressed as a function of η_{fil} and x. With Eq. (4.13), Eq. (4.14) and Eq. (4.15) the cell voltage V_{cell} can be calculated using

$$V_{\text{cell}} = V_{\text{Tu}} + I_{\text{cell}}\left(R_{\text{fil}}(x) + R_{\text{el}} + R_{\text{L}}\right) = f\left(\eta_{\text{fil}}, x\right). \tag{4.16}$$

Here, the filament resistance is calculated using $R_{\text{fil}} = \rho_{\text{fil}}(L - x)/A_{\text{fil}}$, whereas L is the SL thickness. V_{cell} is thus a function of η_{fil} and x. The resistances R_{el} and R_{L} correspond to the added resistance of both electrodes and an optional load resistor, respectively. With this set of equations the switching behavior of ECM can be simulated and it describes an implicit memristive system [65].

For a given cell voltage V_{cell} Eq. (4.3) is solved along with Eq. (4.16) and in current compliance Eq. (4.3) is solved along with Eq. (4.13). An advanced Euler method is used to solve this ordinary differential equation (see Section 3.2 for details). In each time step η_{fil} is calculated using the implicit equation Eq. (4.13) in voltage control or Eq. (4.16) in current control. The overpotential η_{ac} is replaced by either Eq. (4.6), Eq. (4.9) or Eq. (4.12) depending on the choice of α and SET or RESET operation. While simulating the SET operation, Eq. (4.3) is solved along with Eq. (4.16) as long as the cell current is lower than the current compliance. As soon as the set

Table 4.1: Standard simulation parameter

Parameter	Symbol	Value	Parameter	Symbol	Value
Electrode resistance	$R_{\mathrm{el}}\,(\Omega)$	$76 \cdot 10^{-3}$	Exchange current density	$j_0\,(\mathrm{A/m^2})$	$1 \cdot 10^{-2}$
Ionic resistivity	$\rho_{\mathrm{ion}}\,(\Omega\,\mathrm{m})$	$1 \cdot 10^{-2}$	Filament radius	$r_{\mathrm{fil}}\,(\mathrm{nm})$	2
Filament resistivity	$\rho_{\mathrm{fil}}\,(\Omega\,\mathrm{m})$	$2 \cdot 10^{-8}$	Active electrode radius	$r_{\mathrm{ac}}\,(\mathrm{nm})$	2
Effective electron mass SiO_2	$m_{\mathrm{r,SiO_2}}$	0.86	Ionic area radius	$r_{\mathrm{ion}}\,(\mathrm{nm})$	2
Barrier height	$\Delta W_0\,(\mathrm{eV})$	3.6	Switching layer thickness	$L\,(\mathrm{nm})$	20
Copper mass density	$\rho_{\mathrm{m,Cu}}$ $(\mathrm{g/cm^3})$	8.95	Electrode thickness	$t_{\mathrm{el}}\,(\mathrm{nm})$	20
Copper atomic mass	$M_{\mathrm{Cu}}\,(\mathrm{g})$	$63.546/N_{\mathrm{A}}$	Tempera-ture	$T\,(\mathrm{K})$	300
Charge transfer coefficient	α	0.5	Electron mass	$m_0\,(\mathrm{kg})$	$9.1 \cdot 10^{-31}$
Charge number	z	2	Planck constant	$h\,(\mathrm{Js})$	$6.626{\cdot}10^{-34}$

current compliance is reached, Eq. (4.3) is solved along with Eq. (4.13) until the end of the SET operation. This differs from a real current compliance, which turns back to voltage control as the cell current drops below the set current value. If the tunneling gap x drops below 1.42 Å, it is set to zero and a metallic galvanic contact is achieved. In this case the derived model is not applicable anymore and the filament is assumed to remain intact.

As a model system for the 1D simulations a cylindrical Cu/SL/Pt structure is used. Both electrodes have a thickness of 20 nm and a 100 nm radius, which leads to an added electrode resistance of $R_{\mathrm{el}} = 76\,\Omega$. The SL thickness is $L = 20$ nm. Further parameters are $\rho_{\mathrm{m,Cu}} = 8.95$ g/cm^3, $M_{\mathrm{Cu}} = 1.06 \cdot 10^{-22}$ g and $T = 300$ K. The remaining open parameters ΔW_0, m_{r}, r_{fil}, σ_{ion} and j_0 depend on the electronic properties of the SL material, its microstructure and the solubility of Cu ions in

the SL. A set of standard values for these parameters is used and listed in **Table 4.1**. As reference material SiO_2 is used and thus $\Delta W_0 = e\phi_{Cu} - e\phi_{SiO_2} = (4.5 - 0.9)$ eV $= 3.6$ eV [24] and $m_{r,SiO_2} = 0.86$ [66]. For numerical simplicity it is set $A_{ion} = A_{ac} = A_{fil} = \pi r_{fil}^2$. These standard values for the open parameters are used, if not mentioned otherwise. In several simulation studies they are varied in order to investigate their influence on resistive switching.

4.2.1 Simulation of $I - V$ Sweeps

In this section the current-voltage characteristics of ECM cells are simulated using the derived physical 1D compact model and comparing it to experimental $I - V$ characteristics. These characteristics are typically obtained by applying a bipolar triangular voltage. To prevent a permanent breakdown of the ECM cell a current compliance is used in experiment. Alternatively, a series resistor can be used to limit the current. In an integrated memory cell the select transistor serves as a current compliance. In this case the drain source current of the transistor is controlled by the gate voltage. At very low feature sizes also the resistance of the bit line comes in the range of kΩ [19], which would also limit the current. For the simulations a compliance current of 10 µA or a series resistor of 100 kΩ is used. This resistance value leads to similar LRS values as in the case of a 10 µA current compliance.

$I - V$ Sweeps with Current Compliance

Figure 4.4(a) shows the simulated $I - V$ characteristic (red solid line) using a current compliance of 10 µA. The ECM cell is initially in HRS corresponding to $x = L$. As excitation a triangular voltage sweep with 1 V amplitude and 1 s rise time is used (cf. inset in Figure 4.4(a)). The first 2 s correspond to the SET operation and the following 2 s to the RESET operation. Obviously, the LRS exhibits an ohmic behavior as expected from Eq. (4.15) for low voltages. During SET operation the actual cell voltage V_{cell} is not equal to the applied voltage V_{ap} (cf. blue curve in Figure 4.4(a)). As soon as the set current compliance is reached, the cell voltage first drops abruptly. Afterwards it decreases gradually during the current control. This behavior can be explained by interpreting the transient data of I_{ion}, I_{Tu} and x during SET and RESET shown in **Figure 4.4(c)** and **Figure 4.4(d)**, respectively. While V_{ap} is raised, I_{ion} increases according to Eq. (4.5) and x starts decreasing. This leads to an increase of I_{Tu} (cf. Eq. (4.15)), and finally the set current compliance is reached. A further decrease of x is compensated by the abrupt drop of V_{cell}. In conclusion I_{ion} is reduced three orders of magnitude (cf. Figure 4.4(c)) and the

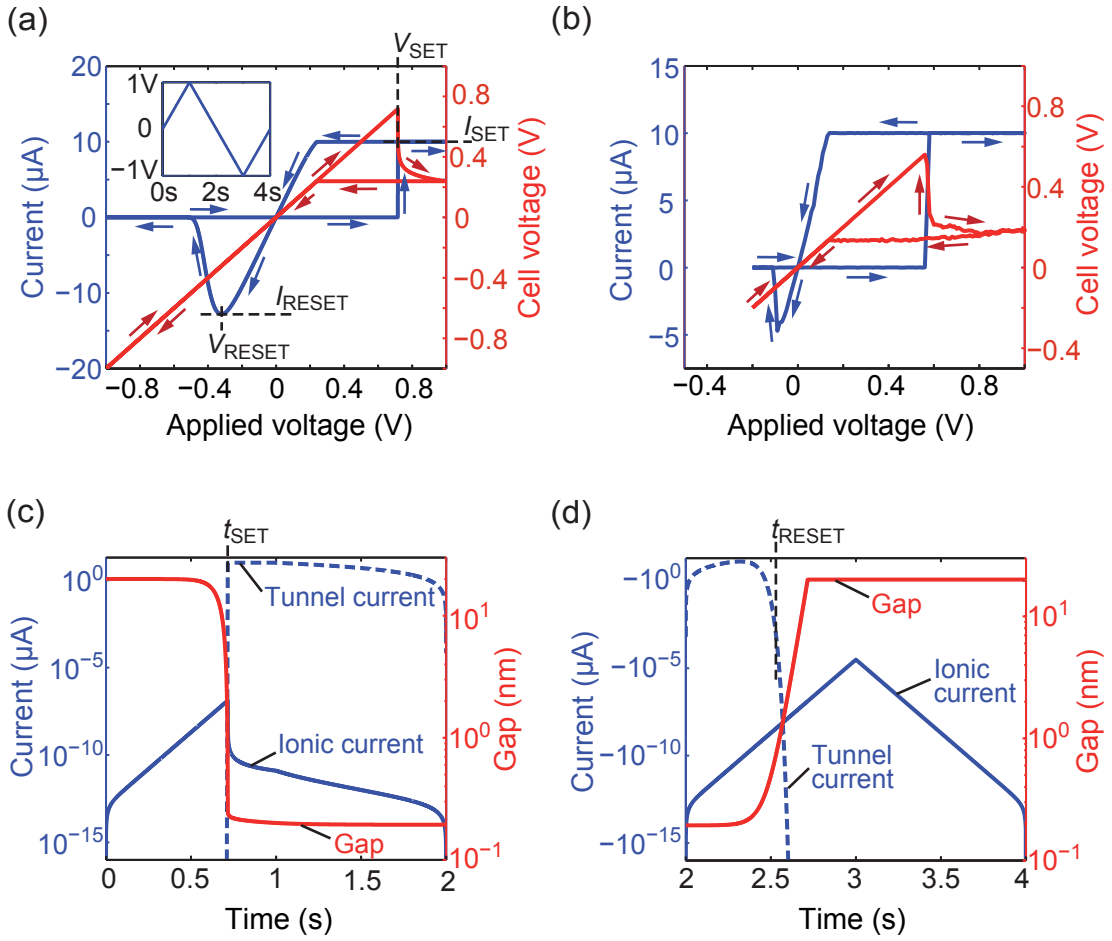

Figure 4.4: (a) Simulated $I-V$ curve (red) and corresponding relation between V_{cell} and V_{applied} (blue). The applied voltage vs. time is shown as inset. Corresponding simulated transient tunneling (dashed blue line) and ionic currents (blue solid line) and transient gap (red solid line) during (c) SET and (d) RESET. A gap of 0.19 nm remains after the SET operation. (b) Experimental $I-V$ characteristic for a Cu/SiO_2/Pt cell (preparation in [38]).

filament growth is suppressed. At the end of the SET pulse a gap of 0.19 nm remains. Note, that x still decreases in current compliance, which allows for a metallic contact at a longer timescale. During RESET I_{Tu} is orders of magnitude larger than I_{ion} (cf. Figure 4.4(d)). But, it is very sensitive to x. Thus, even a low ionic current is sufficient to RESET the cell. In the following I_{Tu} drops to zero and the filament dissolves completely. The simulated $I-V$ characteristics are in good agreement to experimental data shown in **Figure 4.4(b)**. The electronic charge Q_{el} and the ionic charge Q_{ion} involved in SET and RESET can be evaluated by integrating the corresponding currents over time. This yields $Q_{\text{ion,SET}} = Q_{\text{ion,RESET}} = 6.8\,\text{fC}$, $Q_{\text{el,SET}} = 7.8\,\mu\text{C}$ and $Q_{\text{el,RESET}} = 3.5\,\mu\text{C}$. Apparently, the electronic charge is orders

of magnitude higher than the ionic charge, which is directly connected to the volume of the generated metallic filament and thus limited. On the contrary, the electronic charge during SET switching strongly depends on the set current compliance and the time following the switching event. For RESET switching, the electronic charge accumulates as long as a tunneling current flows and then saturates. Therefore the electronic charge can be different for SET and RESET operation.
Based on the simulated $I-V$ curves the following characteristic values are introduced and defined (cf. Figure 4.4(a),(c) and (d)). These definitions will be used for all simulations with a current compliance. The first characteristic value is the SET voltage V_{SET}. For this voltage the set current compliance is reached. The same event also gives the SET time t_{SET}, whereas the SET current I_{SET} is equal to the set current compliance. Another important characteristic value is the LRS voltage, which is defined as $V_{\mathrm{LRS}} = I_{\mathrm{SET}} R_{\mathrm{LRS}}$. The current minimum during RESET operation gives the RESET current I_{RESET} and the RESET voltage V_{RESET}. As RESET time the point in time is chosen at which the absolute value of the cell current is three orders of magnitude lower, than its absolute maximum value during RESET. Thus, the RESET time is not identical to the point in time at which the RESET current is reached. This definition is chosen as it is applicable to voltage sweeps as well as voltage pulses. The previous simulation result indicate that a galvanic metallic contact is still possible at longer timescales. To verify this educated guess the $I-V$ characteristics are simulated for an excitation of a 1 V triangular voltage with a 40 ns rise time (see **Figure 4.5(a)**). As in the previous simulation, the gap x drops to a low value until the current compliance is reached and then decrease slowly afterwards. This further decrease finally leads to a value lower than the contact criteria and thus a metallic contact as indicated by the jump in **Figure 4.5(b)**. The resulting LRS is $R_{\mathrm{LRS}} = 31.9\,\Omega$, which is comparable to literature data [42, 67, 68, 69]. Comparing the simulated and experimental $I-V$ characteristics in Figure 4.4(a) and (b) with respect to the RESET current levels, it appears that the RESET current is higher in the simulation. Especially, it is higher than the SET current. This discrepancy can be attributed to the choice of $\alpha = 0.5$ and $r_{\mathrm{ac}} = r_{\mathrm{is}} = r_{\mathrm{fil}}$ in the simulation. If the charge transfer coefficient α is lower than 0.5, the oxidation process is preferred compared to the reduction process. This should yield in an easier filament dissolution than formation. In an ECM cell, however, the reverse process occurs at the active electrode and the ionic current is limited by the slower reaction. To achieve a higher RESET current, also the effective radius at the active electrode has to be changed. In a real device this area is supposed to be larger than the filament area. To investigate the interplay of these

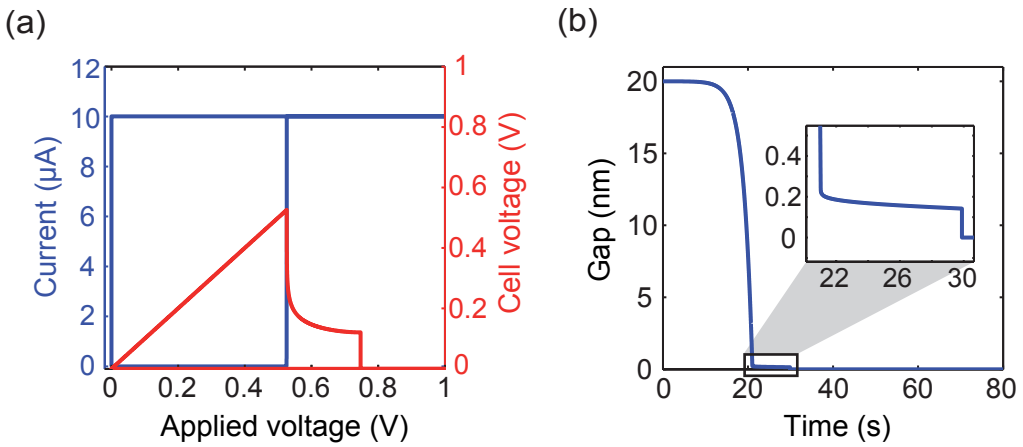

Figure 4.5: (a) Simulated $I-V$ curve (blue solid line) and corresponding cell voltage vs. applied voltage (red). The second voltage drop of the cell voltage corresponds to a metallic contact. (b) Corresponding transient gap vs. time. The inset shows a zoom into the time scale at which the metallic contact is achieved.

two parameters with respect to the switching behavior a simulation series is carried out. In this simulation study the active area of the active electrode $A_{\mathrm{ac}} = \pi r_{\mathrm{ac}}^2$ is varied while the filament area $A_{\mathrm{fil}} = \pi r_{\mathrm{fil}}^2$ is kept constant. The effective area of the ionic transport within the switching layer is set to $A_{\mathrm{is}} = \pi r_{\mathrm{is}}^2 = A_{\mathrm{ac}}$. This variation is conducted for $\alpha = 0.5$ and $\alpha = 0.1$. Since α also influence the switching kinetics (cf. Section 4.2.4) triangular voltages with different amplitudes and rise times are used. For $\alpha = 0.5$ the voltage amplitude V_{p} is set to 1 V and the rise time t_{rise} is 1 s, whereas for $\alpha = 0.1$ the amplitude is $V_{\mathrm{p}} = 2.5\,\mathrm{V}$ with a rise time of $t_{\mathrm{rise}} = 2.5\,\mathrm{s}$. The sweep rate, defined as $V_{\mathrm{p}}/t_{\mathrm{rise}}$, is constant for both charge transfer coefficient simulations.

In **Figure 4.6(a)** the $I-V$ characteristics for 3 different radii r_{ac} and $\alpha = 0.5$ are shown. The SET voltage decreases with increasing r_{ac} since the ionic current is raised for larger radii. Since the sweep rate is unaltered, also the SET time decreases. Thus the cell remains a longer time in current compliance leading to a lower LRS value. In general, the RESET current depends on the LRS value. The lower the LRS value the higher is the RESET current. Thus, increasing r_{ac} leads to an increase in RESET current. The overall trend of RESET current over the corresponding SET current as well as the SET and RESET voltage depending on r_{ac} are shown in 4.6(c). Here, the SET and RESET voltage are normalized to their value at $r_{\mathrm{ac}} = 2\,\mathrm{nm}$. These results clearly show that a mere change of r_{ac} does not lead to the low RESET currents demonstrated in experiment. If the charge transfer coefficient, however, is additionally changed to $\alpha = 0.1$, the RESET current can

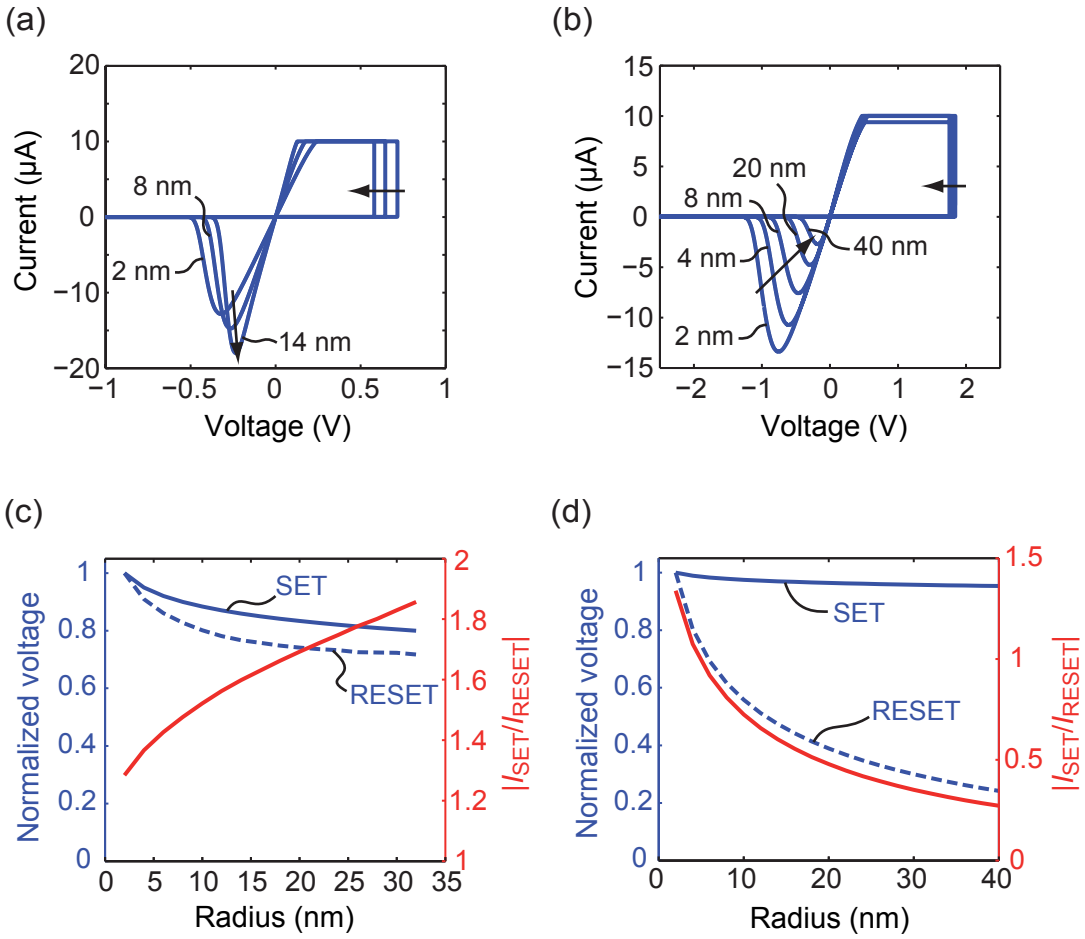

Figure 4.6: (a) Simulated $I-V$ characteristic for a charge transfer coefficient of $\alpha = 0.5$ for $r_{ac} = 2\,\text{nm}$, 8 nm and 14 nm. (b) Simulated $I-V$ characteristic for a charge transfer coefficient of $\alpha = 0.1$ for $r_{ac} = 2\,\text{nm}$, 4 nm, 8 nm, 20 nm and 40 nm. SET voltage (blue solid line), RESET voltage (blue dashed line) in relation to the values for $r_{ac} = 2\,\text{nm}$ and SET vs. RESET current ratio (red solid line) for (c) $\alpha = 0.5$ and (d) $\alpha = 0.1$.

be reduced as supposed (**Figure 4.6(b) and (d)**). Compared to the simulations with $\alpha = 0.5$ the SET voltages are considerably higher since the reduction process is suppressed for $\alpha = 0.1$. Thus, higher voltages are required to build up the same filament volume. Increasing r_{ac} leads to a decrease in SET voltage, but this trend is less pronounced than for $\alpha = 0.5$. On the contrary, the RESET current reduces drastically with increasing r_{ac}. Furthermore, it becomes lower than the SET current as it is the case in the experimental $I-V$ characteristics. This simulation study points to a charge transfer coefficient $\alpha < 0.5$.

Within the simulations a fixed value for the effective radius of the active electrode r_{ac} is assumed. In general, this area is supposed to decrease as the filament approaches the active electrode and vice versa. To get a better understanding of

this process 3D or at least axisymmetric simulations are necessary. Nevertheless, the simulations with the fixed radius (cf. Figure 4.6) gives a good hint towards the influence of the geometry on the switching properties.

$I-V$ Sweeps with a Load Resistor as Current Limiter

A load resistor of $R_\mathrm{L} = 100\,\mathrm{k\Omega}$ is used to limit the current in the following simulation. The charge transfer coefficient is set to $\alpha = 0.5$ and the standard values (cf. Table 4.1) are used. As in the simulation with a current compliance a triangular voltage of 1 V and 1 s rise time is used as excitation. Initially, the ECM cell is in the HRS. The simulated $I-V$ curve is shown as a blue solid line in **Figure 4.7(a)**. During SET operation the current first jumps and then converges to a slope, which is given by

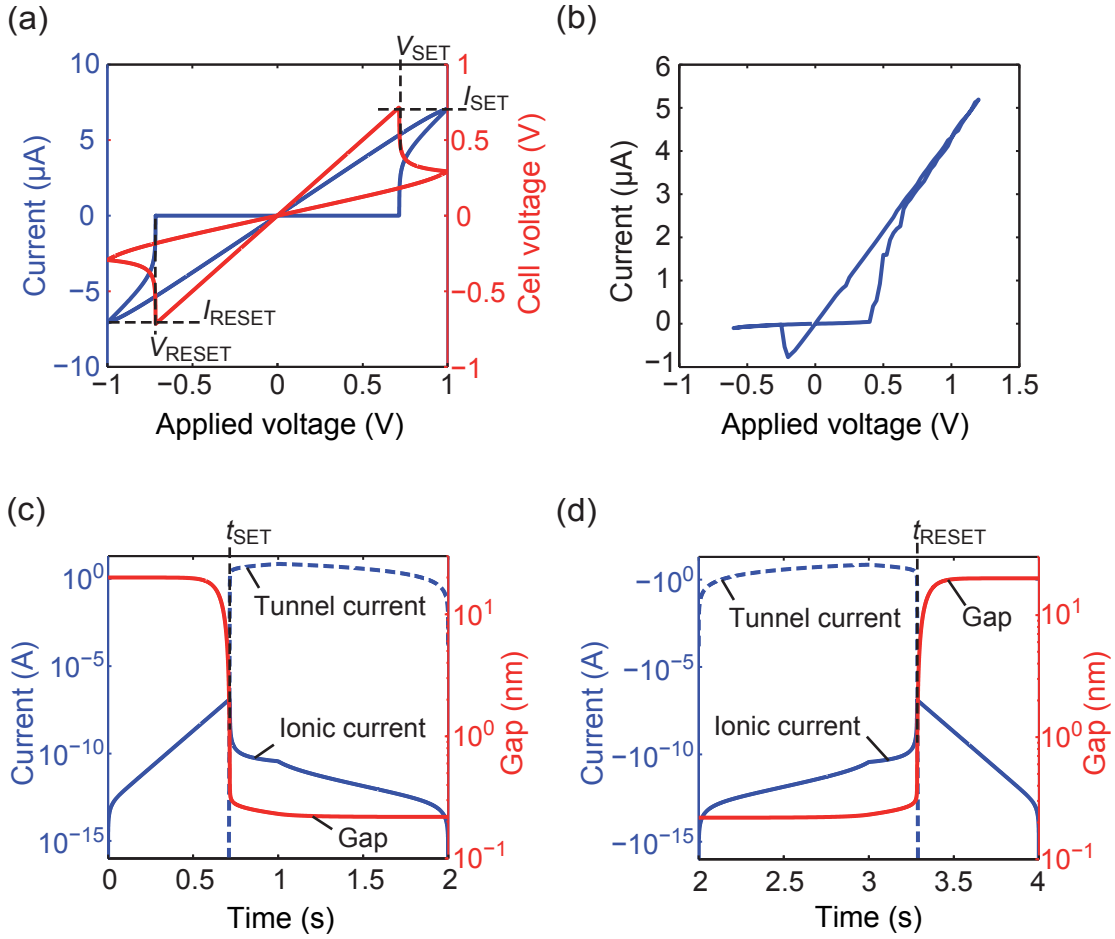

Figure 4.7: a) Simulated $I-V$ curve (blue) and corresponding relation between V_cell and V_applied (red) for $R_\mathrm{L} = 100\,\mathrm{k\Omega}$. (b) Corresponding simulated transient tunneling (dashed blue line) and ionic currents (blue solid line) and transient gap (red solid line) during (c) SET and (d) RESET. (b) Experimental $I-V$ characteristic for a $Cu/SiO_2/Pt$ cell [70].

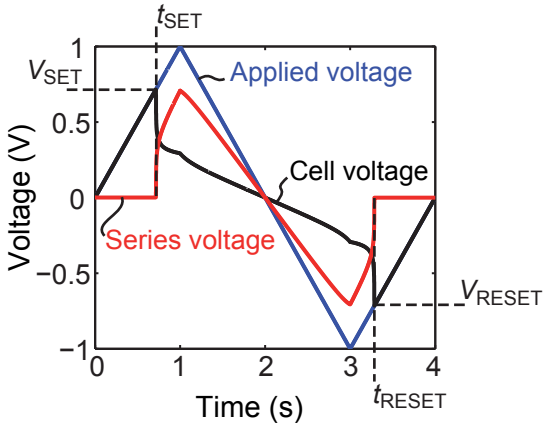

Figure 4.8: Transient applied voltage (blue) and resulting voltages across the load resistor (red) and the ECM cell only (black).

$R_{\mathrm{LRS}} + R_{\mathrm{L}}$. As the cell current increases due to the onset of electron tunneling the voltage drop over the load resistor increases according to Ohm's law. This results in a decrease of the cell voltage, which is shown as red curve in Figure 4.7(a). As for a set current compliance (cf. Figure 4.4(c)) this cell voltage drop leads to a reduction of the ionic current and thus the filament growth is suppressed (Figure 4.7(c)). But, the tunneling gap further decreases slowly in this regime allowing for a galvanic contact at longer timescales. Interestingly, the RESET branch of the $I - V$ curve is symmetric with respect to the point of origin. This symmetry is also visible in the transient data of the ionic current, the electronic current and the tunneling gap in Figure 4.7(c),(d). The simulated data is now compared to a measurement with a load resistor of $R_{\mathrm{L}} = 200\,\mathrm{k\Omega}$. For the SET operation the same characteristic shape of the $I - V$ curve is visible for the experimental data (Figure 4.7(b)). In contrast, the shape of the RESET branch differs strongly. A possible solution of this discrepancy is discussed below. First, some definitions of characteristic values are introduced, which shall be used for all simulations involving a load resistor as current limitation. The SET time is set to the point in time at which the current jump in the $I - V$ curve occurs. At this point also the ionic current reaches its maximum (see Figure 4.7(c)). The SET voltage is now defined as $V_{\mathrm{SET}} = V_{\mathrm{cell}}\,(t_{\mathrm{SET}})$. As SET current the maximum current during SET operation is defined. The definition of characteristic values for the RESET operation is not as straightforward. The RESET current is equal to the maximum absolute current during RESET. For the RESET time the same definition as in the case of a set current compliance is used. Thus, the RESET time is given by that point of time, at which the absolute cell current has dropped three orders of magnitude compared to its maximum absolute

value during RESET. Finally, the RESET voltage is given by the point in time at which the absolute voltage drop across the load resistor reaches its minimum (cf. **Figure 4.8**).

The last simulation result indicates that a galvanic contact can be achieved at longer timescales. Therefore a further simulation is carried out. Here, only the rise time is increased to $t_{\mathrm{rise}} = 200\,\mathrm{s}$, whereas all other parameters remain unchanged. In contrast to the previous simulated $I - V$ curve one additional current jump is observed (**Figure 4.9(a)**). The first current jump is connected to the onset of significant electron tunneling, whereas the second jump occurs as a galvanic contact is established (cf. Figure 4.9(b)). Hence, it is demonstrated that a galvanic contact can be achieved at longer timescales. These kind of jumps have been also found experimentally by Yang et. al. in Cu/TaO_x/Pt cells [67].

At this point the discrepancy in the RESET branches of the simulated and experimental data observed in Figure 4.7(a) and (b) will be discussed. In order to reduce the RESET current an increased ionic current during RESET is necessary. This can be achieved by a combination of geometric asymmetry and a charge transfer coefficient $\alpha < 0.5$ as for the case of a set current compliance discussed above. Therefore a similar simulation study is carried out. The radius r_{ac} is varied, whereas the filament radius is kept constant at $r_{\mathrm{fil}} = 2\,\mathrm{nm}$. This variation study is conducted for $\alpha = 0.5$ and $\alpha = 0.1$. Since the kinetics are strongly influenced by the choice of the charge transfer coefficient, the applied triangular voltages differ for both simulation series. For $\alpha = 0.5$ a peak voltage of $V_{\mathrm{p}} = 1\,\mathrm{V}$ and a rise time

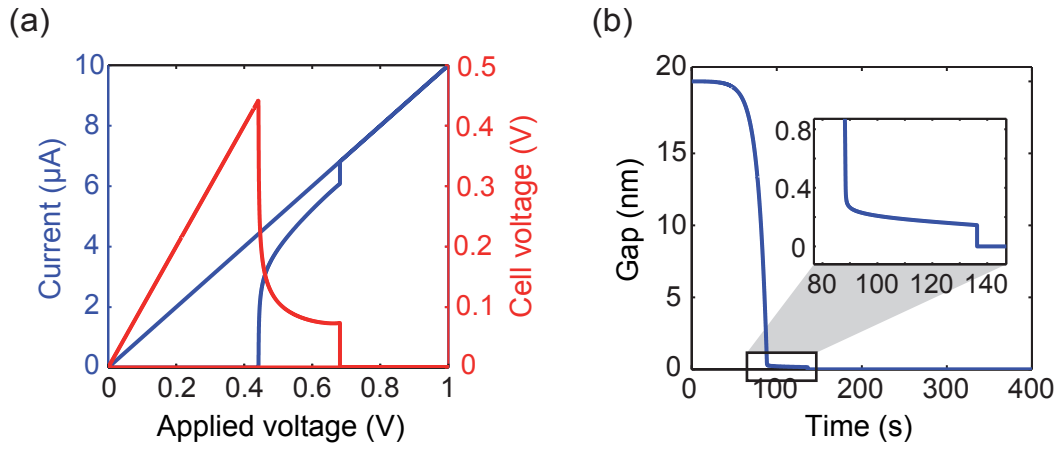

Figure 4.9: (a) Simulated $I - V$ curve (blue solid line) and corresponding cell voltage vs. applied voltage (red) for $R_{\mathrm{L}} = 100\,\mathrm{k\Omega}$. The second voltage drop of the cell voltage corresponds to a metallic contact. (b) Corresponding transient gap vs. time. The inset shows a zoom into the time scale at which the metallic contact is achieved.

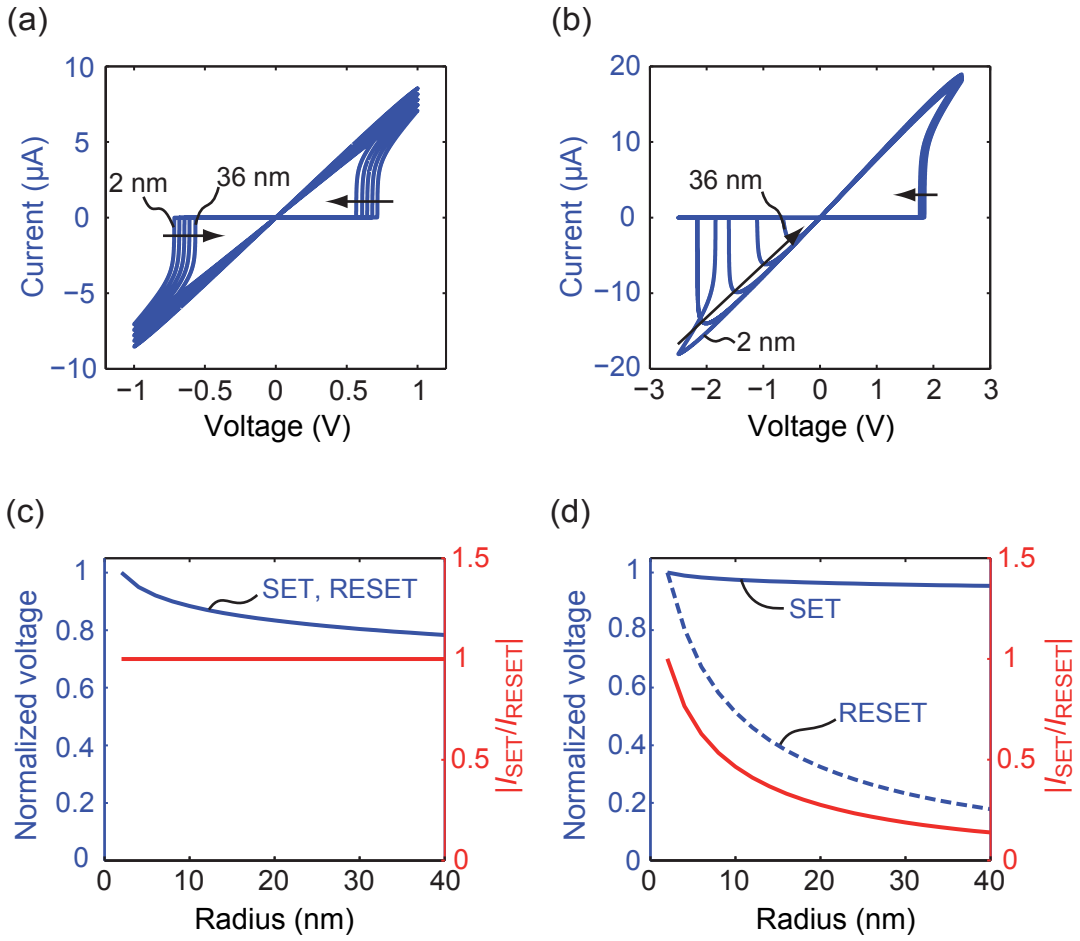

Figure 4.10: (a) Simulated $I-V$ characteristic for a charge transfer coefficient of $\alpha = 0.5$ for $r_{ac} = 2\,\text{nm}$, $4\,\text{nm}$, $8\,\text{nm}$, $16\,\text{nm}$ and $36\,\text{nm}$. (b) Simulated $I-V$ characteristic for a charge transfer coefficient of $\alpha = 0.1$ for $r_{ac} = 2\,\text{nm}$, $4\,\text{nm}$, $8\,\text{nm}$, $16\,\text{nm}$ and $36\,\text{nm}$. SET voltage (blue solid line), RESET voltage (blue dashed line) in relation to the values for $r_{ac} = 2\,\text{nm}$ and SET vs. RESET current ratio (red solid line) for (c) $\alpha = 0.5$ and (d) $\alpha = 0.1$. The load resistance is for $R_L = 100\,\text{k}\Omega$ in all simulations.

of $t_{rise} = 1\,\text{s}$ is used. The peak voltage and the rise time for $\alpha = 0.1$ are $V_p = 2.5\,\text{V}$ and $t_{rise} = 2.5\,\text{s}$, respectively.

Figure 4.10 shows the simulation results for $\alpha = 0.5$ in (a) and (c) and for $\alpha = 0.1$ in (b) and (d). Apparently, the $I-V$ curves for $\alpha = 0.5$ exhibit an odd symmetry for all values of r_{ac}. Hence, the ratio RESET to SET current equals one and the absolute SET and RESET voltages are also identical. With increasing r_{ac} the ionic current increases and thus the SET time and SET voltage decrease. This leads to the lower LRS visible as a higher slope in the $I-V$ curve. A different behavior is observed in the simulation study with $\alpha = 0.1$. Here, the $I-V$ characteristics become asymmetric for $r_{ac} > r_{fil} = 2\,\text{nm}$. Increasing r_{ac} result in decreasing RE-

SET currents and voltages. In this case the shape of the simulated $I-V$ curve coincides with the experimental data (cf. Figure 4.7(b)). With respect to the SET characteristics the SET voltages are higher than for $\alpha = 0.5$ since the oxidation is favored. Regarding the SET voltages the same trend is observed as in the case for $\alpha = 0.5$. But it is less pronounced. This simulation study indicates that the charge transfer coefficient is less than 0.5, which is consistent with the results of the simulations with a set current compliance.
In conclusion, the simulation results show that the derived compact model based on the proposed switching mechanism is capable of simulating ECM cells. It is further demonstrated that a tunneling gap can remain due to combination of a current limitation and the nonlinear ionic current behavior. The growth within the current limitation is suppressed. But, a metallic galvanic contact can still be achieved at longer timescales. An occuring asymmetry in the $I-V$ characteristics can be explained by a combination of an geometric asymmetry and and a charge transfer coefficient $\alpha \neq 0.5$. The simulation results also suggest that the charge transfer coefficient is $\alpha < 0.5$ in the experimental ECM cells.

4.2.2 Polyfilamentary Growth

In this section the growth of several parallel filaments is discussed and compared to the results of single filamentary growth. Especially, the question should be investigated if only one filament is responsible for the switching in ECM cells. Furthermore, the circumstances that may lead to a polyfilamentary mechanism are elucidated.
In order to simulate polyfilamentary growth of n parallel filaments, the derived equation system in Section 4.2 has to be extended. For each filament the ordinary differential equation (4.3) has to be solved. This leads to an equation system of n coupled differential equations:

$$\frac{\mathrm{d}x_1}{\mathrm{d}t} = -\frac{M_{\mathrm{Me}}}{ze\rho_{\mathrm{m,Me}}} J_{\mathrm{ion},1} \tag{4.17}$$

$$\frac{\mathrm{d}x_2}{\mathrm{d}t} = -\frac{M_{\mathrm{Me}}}{ze\rho_{\mathrm{m,Me}}} J_{\mathrm{ion},2} \tag{4.18}$$

$$\vdots$$

$$\frac{\mathrm{d}x_{\mathrm{n}}}{\mathrm{d}t} = -\frac{M_{\mathrm{Me}}}{ze\rho_{\mathrm{m,Me}}} J_{\mathrm{ion,n}}. \tag{4.19}$$

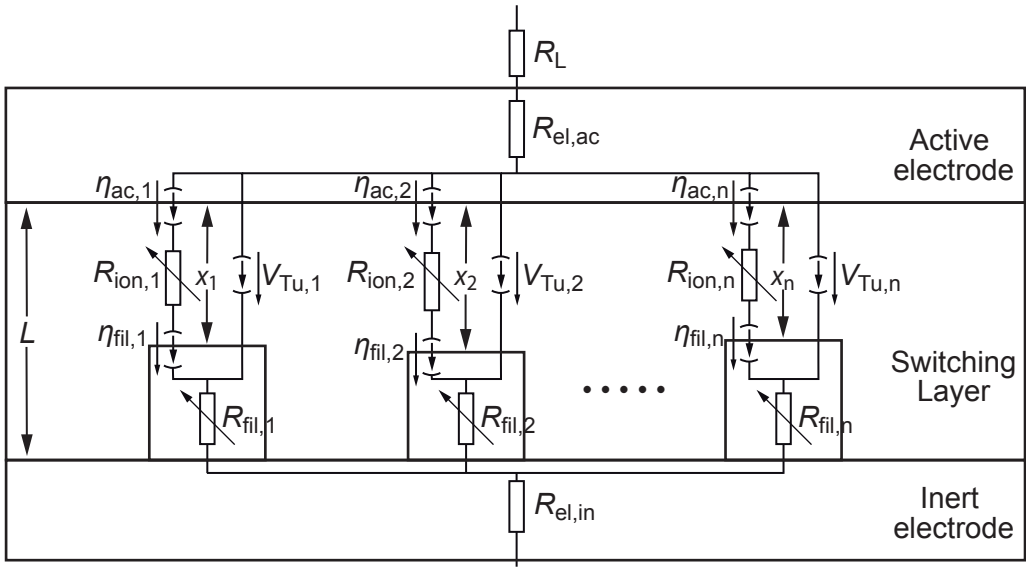

Figure 4.11: Equivalent circuit diagram for modeling polyfilamentary growth analog to the one for the single filament model in Figure 4.3.

The ionic currents at each filament are given by the Butler-Volmer currents

$$J_{\text{ion,1}} = J_{\text{BV,1}} = -2j_{0,1}\sinh\left(\frac{ze}{2k_{\text{B}}T}\eta_{\text{fil,1}}\right) \tag{4.20}$$

$$J_{\text{ion,2}} = J_{\text{BV,2}} = -2j_{0,2}\sinh\left(\frac{ze}{2k_{\text{B}}T}\eta_{\text{fil,2}}\right) \tag{4.21}$$

$$\vdots$$

$$J_{\text{ion,n}} = J_{\text{BV,2}} = -2j_{0,\text{n}}\sinh\left(\frac{ze}{2k_{\text{B}}T}\eta_{\text{fil,n}}\right). \tag{4.22}$$

For simplicity is $\alpha = 0.5$ and thus the Butler-Volmer equation can be expressed with a hyperbolic sine. The ionic current at each filament is now a function of the local overpotential. **Figure 4.11** shows the equivalent circuit diagram for n parallel filaments. Crosscurrents between different filaments are neglected. On a microscopic scale this correlates to the idea of parallel preferred ionic paths within the switching layer. The filamentary growth would then take place along these paths. Since ionic cross currents are neglected the charge neutrality condition has to be fulfilled for each paths separately. Thus, the active electrode/SL boundary overpotential in

the i-th path $\eta_{\mathrm{ac,i}}$ can be expressed by the corresponding filament/SL boundary overpotential $\eta_{\mathrm{fil,i}}$ according to

$$\eta_{\mathrm{ac,1}} = -\frac{2k_{\mathrm{B}}T}{ze}\mathrm{arsinh}\left(\frac{A_{\mathrm{fil,1}}}{A_{\mathrm{ac,1}}}\sinh\left(\frac{ze}{2k_{\mathrm{B}}T}\eta_{\mathrm{fil,1}}\right)\right) \tag{4.23}$$

$$\eta_{\mathrm{ac,2}} = -\frac{2k_{\mathrm{B}}T}{ze}\mathrm{arsinh}\left(\frac{A_{\mathrm{fil,2}}}{A_{\mathrm{ac,2}}}\sinh\left(\frac{ze}{2k_{\mathrm{B}}T}\eta_{\mathrm{fil,2}}\right)\right) \tag{4.24}$$

$$\vdots$$

$$\eta_{\mathrm{ac,n}} = -\frac{2k_{\mathrm{B}}T}{ze}\mathrm{arsinh}\left(\frac{A_{\mathrm{fil,n}}}{A_{\mathrm{ac,n}}}\sinh\left(\frac{ze}{2k_{\mathrm{B}}T}\eta_{\mathrm{fil,n}}\right)\right). \tag{4.25}$$

For each filamentary path the voltage drop is defined by

$$\begin{aligned} V_1 &= \eta_{\mathrm{ac,1}} - \eta_{\mathrm{fil,1}} + I_{\mathrm{BV,1}}R_{\mathrm{ion,1}} + \left(I_{\mathrm{Tu,1}} + I_{\mathrm{BV,1}}\right)R_{\mathrm{fil,1}} \\ &= V_{\mathrm{Tu,1}} + \left(I_{\mathrm{Tu,1}} + I_{\mathrm{BV,1}}\right)R_{\mathrm{fil,1}} = f\left(\eta_{\mathrm{fil,1}}, x_1\right) \end{aligned} \tag{4.26}$$

$$\begin{aligned} V_2 &= \eta_{\mathrm{ac,2}} - \eta_{\mathrm{fil,2}} + I_{\mathrm{BV,2}}R_{\mathrm{ion,2}} + \left(I_{\mathrm{Tu,2}} + I_{\mathrm{BV,2}}\right)R_{\mathrm{fil,2}} \\ &= V_{\mathrm{Tu,2}} + \left(I_{\mathrm{Tu,2}} + I_{\mathrm{BV,2}}\right)R_{\mathrm{fil,2}} = f\left(\eta_{\mathrm{fil,2}}, x_2\right) \end{aligned} \tag{4.27}$$

$$\vdots$$

$$\begin{aligned} V_n &= \eta_{\mathrm{ac,n}} - \eta_{\mathrm{fil,n}} + I_{\mathrm{BV,n}}R_{\mathrm{ion,n}} + \left(I_{\mathrm{Tu,n}} + I_{\mathrm{BV,n}}\right)R_{\mathrm{fil,n}} \\ &= V_{\mathrm{Tu,n}} + \left(I_{\mathrm{Tu,n}} + I_{\mathrm{BV,n}}\right)R_{\mathrm{fil,n}} = f\left(\eta_{\mathrm{fil,n}}, x_{\mathrm{n}}\right). \end{aligned} \tag{4.28}$$

The voltage drop along the i-th path V_{i} is thus an implicit function of the i-th tunneling gap x_{i} and the i-th filament/SL boundary overpotential $\eta_{\mathrm{fil,i}}$. It is straightforward that $V_1 = V_2 = \ldots = V_{\mathrm{n}}$. The overall cell current equals the sum of all ionic currents and tunneling currents

$$\begin{aligned} I_{\mathrm{cell}} &= I_{\mathrm{BV,1}} + I_{\mathrm{Tu,1}} + I_{\mathrm{BV,2}} + I_{\mathrm{Tu,2}} + \ldots + I_{\mathrm{BV,n}} + I_{\mathrm{Tu,n}} \\ &= f\left(\eta_{\mathrm{fil,1}}, x_1, \eta_{\mathrm{fil,2}}, x_2, \ldots, \eta_{\mathrm{fil,n}}, x_{\mathrm{n}}\right). \end{aligned} \tag{4.29}$$

It is thus a function of all n overpotentials and tunneling gaps. Using Kirchoff's voltage law, the cell voltage can be calculated in n different ways:

$$\begin{aligned} V_{\mathrm{cell}} &= V_1 + I_{\mathrm{cell}}\left(R_{\mathrm{el}} + R_{\mathrm{s}}\right) = V_2 + I_{\mathrm{cell}}\left(R_{\mathrm{el}} + R_{\mathrm{s}}\right) = \ldots = V_{\mathrm{n}} + I_{\mathrm{cell}}\left(R_{\mathrm{el}} + R_{\mathrm{s}}\right) \\ &\approx V_1 \approx V_2 \approx \ldots \approx V_{\mathrm{n}}. \end{aligned} \tag{4.30}$$

Due to the voltage drop over the electrodes and the optional load resistor, the cell voltage is coupled to the cell current. For a voltage controlled simulation Eq. (4.30)

and Eqs. (4.26) – (4.28) span a system of n coupled implicit equations. This equation system has to be solved in every time step. However, this is a critical numerical task. Hence, it is preferable to decouple these equations. This can be achieved, if the voltage drop over the electrodes and the load resistor become negligible. Since the resistance of the electrodes is very low the corresponding voltage drop can always be neglected. If the optional load resistor is set to R_L the preconditions for decoupling are fulfilled. In this case $V_\mathrm{cell} = V_\mathrm{i}$ holds and the growth of each filament can be treated separately within the voltage control. As soon as the set current compliance is reached Eq. (4.29) and Eqs. (4.26) – (4.28) span a system of n coupled implicit equations, which has to be solved in every time step. If the i-th filament establishes a galvanic metallic contact, the corresponding voltage drop and current are connected by Ohm's law: $V_\mathrm{i} = \rho_\mathrm{fil,i} L / A_\mathrm{fil,i} I_\mathrm{i}$. As consequence the number of coupled implicit equations is reduced by one.
Due to the complexity of the general case for n filaments, the discussion is now restricted to two parallel filaments, whereas five parallel filaments will be considered in Section 4.2.3 with respect to multilevel switching. The simulation results of two parallel filaments can be easily adopted to multiple filaments, so that this restriction does not lead to a loss of generality. In this case the resulting equation system in current compliance is given by Eq. (4.29) with n = 2 and

$$\begin{aligned} &\eta_\mathrm{ac,1} - \eta_\mathrm{fil,1} + I_\mathrm{BV,1} R_\mathrm{ion,1} + \left(I_\mathrm{Tu,1} + I_\mathrm{BV,1}\right) R_\mathrm{fil,1} \\ &= \eta_\mathrm{ac,2} - \eta_\mathrm{fil,2} + I_\mathrm{BV,2} R_\mathrm{ion,2} + \left(I_\mathrm{Tu,2} + I_\mathrm{BV,2}\right) R_\mathrm{fil,2}. \end{aligned} \tag{4.31}$$

During the SET operation one filament can achieve a galvanic contact. This event might occur during voltage control as well as current control. Let the first filament be in galvanic contact, then only the ordinary differential equation for the second filament has to be solved. To calculate the overpotential $\eta_\mathrm{fil,2}$ the implicit equations

$$V_1 = V_2 = \eta_\mathrm{ac,2} - \eta_\mathrm{fil,2} + I_\mathrm{BV,2} R_\mathrm{ion,2}\left(x_2\right) \approx V_\mathrm{cell} \tag{4.32}$$

$$I_\mathrm{cell} = V_2 / R_\mathrm{fil,1}\left(x_1 = L\right) + I_\mathrm{BV,2} + I_\mathrm{Tu,2} = f\left(\eta_\mathrm{fil,2}, x_2\right) \tag{4.33}$$

are used under voltage control and current control, respectively. Here, the current through the filament is given by Ohm's law $V_1 = (\rho_\mathrm{fil,1} L / A_\mathrm{fil,1}) I_1$.

There are two parameters in which the drift paths might differ. Firstly, the area of the ionic paths can be different. The second parameter is the concentration of cations in the ionic paths, which alters the exchange current density as well as the ionic resistivity. The former depends linearly on the concentration whereas the

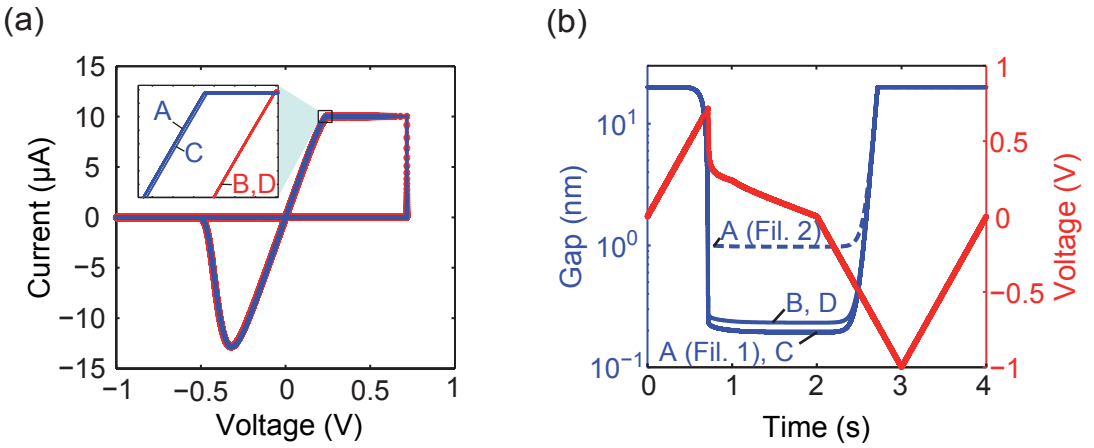

Figure 4.12: (a) Simulated $I-V$ characteristics for parallel growth of two filaments (case A and B) compared to single filamentary growth (C and D). In A two filaments with radii $r_{\mathrm{fil},1} = 2\,\mathrm{nm}$ and $r_{\mathrm{fil},2} = 1.96\,\mathrm{nm}$ are assumed. In B the radius is 2 nm for both filaments. In C a single filament with $r_{\mathrm{fil}} = 2\,\mathrm{nm}$ is used and in D the single filament has a radius of $r_{\mathrm{fil}} = \sqrt{2}\cdot 2\,\mathrm{nm}$. (b) Corresponding transient gap and voltage for the cases A, B, C and D.

latter is inversely proportional to it. Theoretically, the ionic drift paths does not necessarily connect the two electrodes directly. They might be twisted, and thus the paths lengths differ. In such a case the electric field distribution has to be calculated three-dimensionally rather than in one-dimension. Thus, this alternative is not considered. The effective mass and the barrier height are parameters of the switching layer. So, they are identical in each path. The same holds for the charge number and the charge transfer coefficient, which depends on the metal/SL interface. This leaves the concentration c and the area of the ionic drift paths $A_{\mathrm{ion}} = \pi r_{\mathrm{ion}}^2$ as free parameters. Certainly, there is also the possibility that the different paths are identical in all parameters.

At first, the polyfilamentary growth is studied conducting two different simulations. For both simulations $r_{\mathrm{ac,i}} = r_{\mathrm{fil,i}} = r_{\mathrm{ion,i}}$ and $\alpha = 0.5$ apply. In the first case (A) two filaments with different radii $r_{\mathrm{fil},1} = 2\,\mathrm{nm}$ and $r_{\mathrm{fil},2} = 1.96\,\mathrm{nm}$ are assumed. On the contrary, two identical filaments with $r_{\mathrm{fil},1} = r_{\mathrm{fil},2} = 2\,\mathrm{nm}$ are considered in case B. For all other parameters the standard values listed in 4.1 are used. These two simulations are compared to two single filament simulations with $r_{\mathrm{fil}} = 2\,\mathrm{nm}$ (C) and $r_{\mathrm{fil}} = \sqrt{2}\cdot 2\,\mathrm{nm}$ (case D), respectively. The cross-sectional area in D is thus identical to the cumulative area in B. As excitation a triangular voltage of $V_{\mathrm{p}} = 1\,V$ and $t_{\mathrm{rise}} = 1\,\mathrm{s}$ applies. The current compliance is set to $10\,\mu\mathrm{A}$.

Figure 4.12(a) shows the simulated $I-V$ characteristics for the cases A-D. At first sight no deviations are visible. But a zoom, shown as inset, reveals that the

simulated $I-V$ curves of A and C coincide as well as those of B and D. The LRS resistances are $R_{\mathrm{LRS,A}} = R_{\mathrm{LRS,C}} = 21.4\,\mathrm{k\Omega}$ and $R_{\mathrm{LRS,B}} = R_{\mathrm{LRS,D}} = 20\,\mathrm{k\Omega}$. If one takes a look at the transient voltage and gaps in Figure 4.12(b), this behavior can be understood. For all cases the transient voltages coincide, whereas the transient gaps differ. If both ionic paths are identical (case B), the gaps within these paths also evolve equally. Moreover, the reference simulation D shows the same transient behavior. This means on the one hand that it is impossible to distinguish between two or more parallel identical paths and one path with the same cumulative area. On the other hand it results that a single filamentary model is appropriate to obtain the correct $I-V$ characteristics. In contrast, the transient gaps evolve differently in simulation A. Here, the filament within the larger paths (filament 1) grows faster, since its ionic resistance is lower and thus the ionic current density can be higher. As soon as the current compliance is reached the voltage drops. Hence, the filamentary growth is suppressed in both paths. Interestingly, the remaining gaps can be well discriminated (1.94 Å compared to 9.78 Å) even though the radii $r_{\mathrm{fil},1}$ and $r_{\mathrm{fil},2}$ differ only slightly. In addition, the transient behavior of filament 1 coincides with the transient behavior of the filament in simulation C. The total ionic currents in A and C, which are equal to the total current prior to the switching event, differ according to the additional ionic current through the second path in A. But this does not influence the the characteristic values V_{SET}, V_{RESET}, t_{SET}, t_{RESET} and R_{LRS}. Thus, so far a single filament model seems to be appropriate to model ECM cells. Finally, the differences in R_{LRS} can be deduced from the transient gaps. For a larger filament radius the tunneling gap can be wider in order to obtain a tunneling current equal to the set current compliance. Here, it is $r_{\mathrm{fil,D}} = \sqrt{2} r_{\mathrm{fil,C}}$ and the corresponding gaps are $x_{\mathrm{D}} = 2.32\,\text{Å}$ and $x_{\mathrm{C}} = 1.94\,\text{Å}$. Thus, the current compliance is reached earlier for larger radii than for smaller radii, which finally results in a lower R_{LRS}.

Since filamentary growth is simply suppressed within the current compliance, a galvanic contact can be achieved at longer timescales. In case of polyfilamentary growth, the question rises, whether a galvanic contact of the first filament is reached before or after a second filament builds up a tunneling contact. To address this issue the previous simulation A is repeated, while changing only the rise time to $t_{\mathrm{rise}} = 40\,\mathrm{s}$. The simulation results are compared to the single filament case from the previous section (cf. Figure 4.5). As shown in **Figure 4.13** the transient voltages for the single and polyfilamentary simulations coincide. Thus, the simulated transient gaps of $x_{\mathrm{poly},1}$ and x_{single} exhibit the same characteristics. In both cases a first voltage drop occurs as the current compliance is reached. The second voltage drop

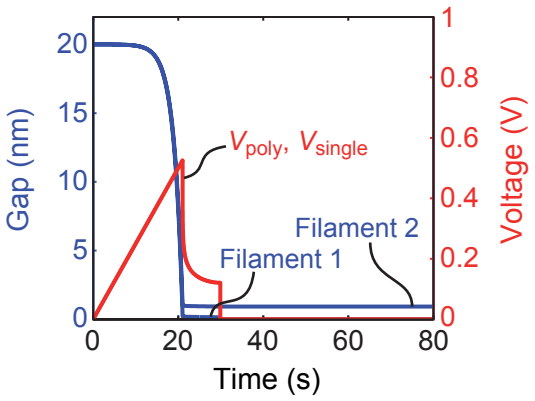

Figure 4.13: Simulated transient gaps (blue) and transient cell voltages (red) using a triangular voltage sweep. The filament radii are $r_{\mathrm{fil},1} = 2\,\mathrm{nm}$ and $r_{\mathrm{fil},2} = 1.96\,\mathrm{nm}$, respectively.

is connected to the galvanic contact. Apparently, the growth of the second filament is strongly suppressed such as a second tunneling contact cannot be achieved before the first filament builds up a galvanic contact.

In order to validate the foregoing simulation results, a parameter simulation study with two parallel filaments is carried out. The radius of the first filament is $r_{\mathrm{fil},1} = 2\,\mathrm{nm}$. Apart from that the standard values are used for the first filament. These parameters remain unchanged within the simulation studies whereas either the radius or the ion concentration of the second path is varied. In the first simulation study the second filament radius is varied within $1.5\,\mathrm{nm} \leq r_{\mathrm{fil},2} \leq 20\,\mathrm{nm}$, such as it is smaller or larger than the first one. Secondly, the concentration of the second filament is altered relatively to the first ones with a scaling factor C that is $0.1 \leq C \leq 10$. Hence, the ionic resistivity as well as the exchange current density are altered according to $\rho_{\mathrm{ion},2} = \rho_{\mathrm{ion},1}C$ and $j_{0,2} = j_{0,1}/C$, respectively. Again, a triangular voltage with $V_{\mathrm{p}} = 1\,\mathrm{V}$ and $t_{\mathrm{rise}} = 1\,\mathrm{s}$ is used as excitation. The simulated remaining gaps and the LRS resistance after SET operation are shown in **Figures 4.14(a) and (b)** in case of concentration and area variation, respectively. In both cases two distinct regimes can be identified. These regimes are associated with the prevailing filament. Regarding the area variation, the larger filament dominates and determine the SET operation as discussed above. Since the exchange current density is proportional to the concentration, the filament with the higher concentration will grow faster and thus determine the SET operation. Therefore, the first filament dominates for $r_{\mathrm{fil},2} < r_{\mathrm{fil},1} = 2\,\mathrm{nm}$ and $C > 1$. In these regimes, the LRS resistance and the remaining gap $x_{\mathrm{min},1}$ remain constant upon variation of the relevant parameter. Only the remaining gap of the second

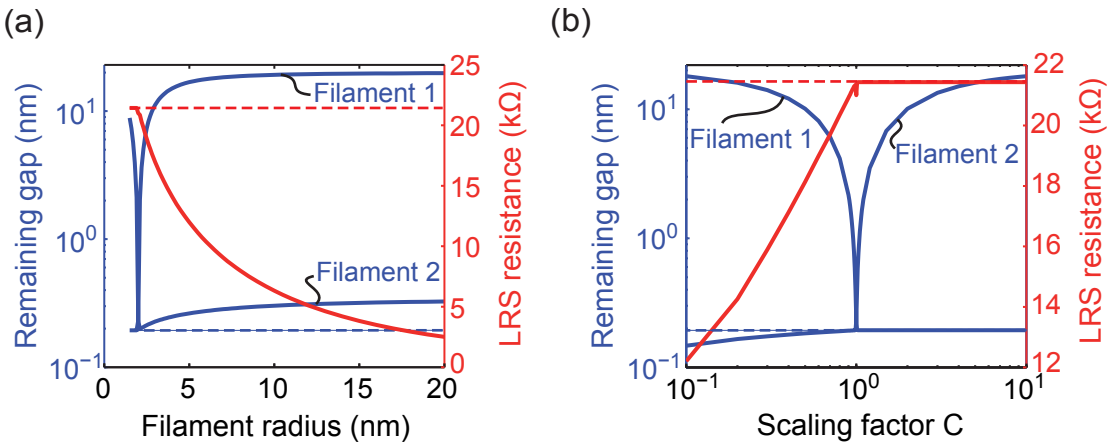

Figure 4.14: (a) Simulated remaining gaps (blue) and LRS resistance (red) for different radii of filament 2. For filament one $r_{\mathrm{fil},1} = 2\,\mathrm{nm}$ holds. The dashed lines are reference values for a single filament simulation with $r_{\mathrm{fil}} = 2\,\mathrm{nm}$. (b) Simulated remaining gaps (blue) and LRS resistance (red) for the different scaling factors of filament 2. The radius of both filaments is 2 nm. The dashed lines are reference values for a single filament simulation with $r_{\mathrm{fil}} = 2\,\mathrm{nm}$.

filament changes, but this does not affect the switching properties. In addition, the simulation results of a single filament simulation using the parameters of the first filament are identical to the polyfilamentary simulation results in this regime (see dashed lines in Figure 4.14). If $r_{\mathrm{fil},2} > r_{\mathrm{fil},1} = 2\,\mathrm{nm}$ and $C < 1$ applies the second filament determines the switching. Therefore, the remaining gap and the LRS resistance change according to the parameter variation. A special case yields for $r_{\mathrm{fil},2} = r_{\mathrm{fil},1} = 2\,\mathrm{nm}$ and $C = 1$, respectively. The switching characteristics of the polyfilamentary simulation are then equivalent to a single filament simulation with an effective cumulative area as discussed above. So one filament dominates the switching except both filamentary paths have identical properties.

In the following simulation study the influence of the set current compliance on polyfilamentary growth is investigated. For this purpose an ECM cell with two parallel filaments with radii $r_{\mathrm{fil},1} = 2\,\mathrm{nm}$ and $r_{\mathrm{fil},2} = 2.08\,\mathrm{nm}$ is considered. As excitation a voltage triangle with $V_{\mathrm{p}} = 1\,\mathrm{V}$ and $t_{\mathrm{rise}} = 1\,\mathrm{s}$ is used. The current compliance is set to $I_{\mathrm{cc}} = 1\,\mu\mathrm{A}, 10\,\mu\mathrm{A}, 100\,\mu\mathrm{A}, 1\,\mathrm{mA}, 10\,\mathrm{mA}$ and $0.1\,\mathrm{A}$, respectively. **Figure 4.15(a)** shows the remaining gaps and the LRS resistance after SET operation and in (b) three corresponding $I - V$ curves are illustrated. In all simulations the second filament grows faster due to its larger radius. For $I_{\mathrm{cc}} = 1\,\mu\mathrm{A}$ and $10\,\mu\mathrm{A}$ a tunneling gap remains after SET operation. Apparently, the one order of magnitude higher current compliance allows for a smaller remaining tunneling gap $x_{\mathrm{min},2}$ and thus a one order of magnitude lower LRS resistance. The remaining gap

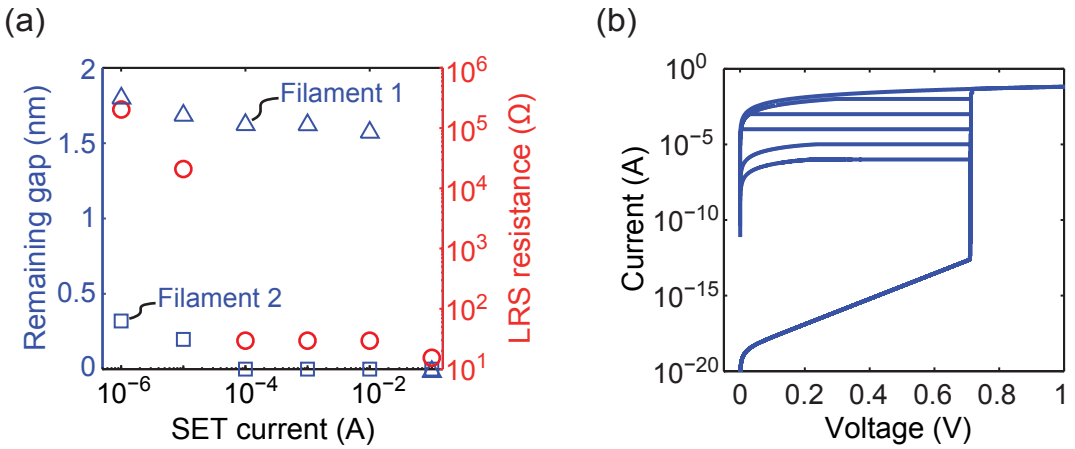

Figure 4.15: (a) Simulated remaining gaps (blue symbols) and LRS resistance (red circles) vs. set current compliance. (b) Corresponding $I-V$ characteristics. The filament radii are $r_{\mathrm{fil},1} = 2\,\mathrm{nm}$ and $r_{\mathrm{fil},2} = 2.08\,\mathrm{nm}$, respectively.

of the first filament adjusts accordingly. For $I_{\mathrm{cc}} = 100\,\mu\mathrm{A}$ the second filament builds up a galvanic contact and the LRS resistance drops to $R_{\mathrm{LRS}} = 29.4\,\Omega$. If the current compliance is further increased, the remaining gap $x_{\mathrm{min},1}$ decreases. In current compliance the cell voltage can be calculated according to $V = I_{\mathrm{cc}} R_{\mathrm{LRS}}$, whereas the LRS resistance is given by the galvanic contact of the second filament. So, a higher current compliance results in a higher cell voltage and thus a higher ionic current within the first drift paths. Thus, the growth speed is enhanced and a smaller remaining gap $x_{\mathrm{min},1}$ follows. Eventually, for $I_{\mathrm{cc}} = 100\,\mathrm{mA}$ filament one builds up a galvanic contact. This second contact corresponds to a second current jump in the $I-V$ curve (cf. Figure 4.15). Now, the LRS resistance is given by both filaments which results in $R_{\mathrm{LRS}} = 15.4\,\Omega$. To conclude, two distinct regimes with respect to the level of current compliance can be distinguished. If the current compliance is to low to allow for a galvanic contact, the filamentary growths of all filaments is suppressed equally within the current compliance. Moreover, the level of current compliance does not influence the growth speed. Only when a first filament builds up a galvanic contact, an increase in current compliance leads to an enhanced growth speed of further filaments. This could finally yield in additional galvanic contacts. In addition, this simulation study reveals two possibilities of multilevel switching. Firstly, a remaining tunneling gap can be controlled by a current compliance. On the other hand the number of filaments in galvanic contact can account for different LRS values. These two possibilities will be discussed in more detail in Section 4.2.3. So far a copper filament was considered using bulk resistivity values. For nanometer scale wires, however, the resistivity is increased due to scattering. Theoretically, the

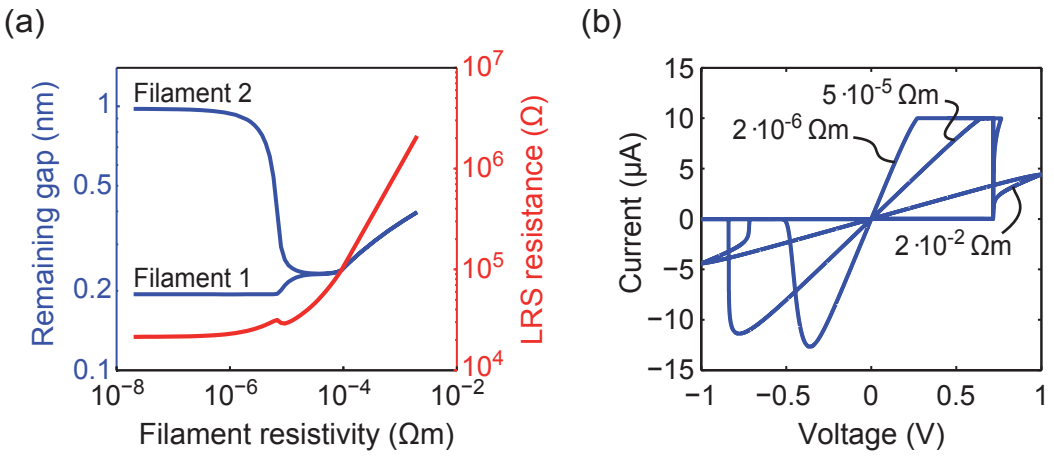

Figure 4.16: (a) Simulated remaining gaps and LRS resistances vs. filament resistivity. (b) Corresponding $I-V$ characteristics for filament resistivities of $\rho_{\text{fil}} = 2 \cdot 10^{-6}\,\Omega\text{m}$, $5.02 \cdot 10^{-5}\,\Omega\text{m}$ and $2 \cdot 10^{-2}\,\Omega\text{m}$.The filament radii are $r_{\text{fil},1} = 2\,\text{nm}$ and $r_{\text{fil},1} = 2.08\,\text{nm}$, respectively.

increased resistivity can be about 1-2 orders of magnitude higher [18]. To study its influence a series of simulations is conducted whereas the resistivity is increased up to five orders of magnitude. This leads to resistivity values considerably higher than expected and describes a rather hypothetical case. In each simulation two filaments are considered with radii $r_{\text{fil},1} = 2\,\text{nm}$ and $r_{\text{fil},2} = 1.96\,\text{nm}$. A triangular voltage with $V_{\text{p}} = 1\,\text{V}$ and $t_{\text{rise}} = 1\,\text{s}$ is applied. For all other parameters the standard values are used. **Figure 4.16(a)** illustrates the remaining gaps and the LRS resistance after SET operation. For resistivities $\rho_{\text{fil}} < 10^{-6}\,\Omega\text{m}$ the same behavior as in the previous simulation studies is observed. Here, filament one dominates due to the larger radius. If the resistivity is further increased, first the remaining gap $x_{\text{min},2}$ decreases and at about $\rho_{\text{fil}} \approx 10^{-6}\,\Omega\text{m}$ the remaining gap $x_{\text{min},1}$ starts increasing. Finally both converge and then increase for $\rho_{\text{fil}} \geq 10^{-4}\,\Omega\text{m}$. This behavior leads to the non-monotonic increase in LRS value. First, it increases according to an increased gap $x_{\text{min},1}$. As the second filament approaches the counter electrode significant tunneling current also flows through filament two, which leads to a minimum LRS at about $\rho_{\text{fil}} \approx 10^{-5}\,\Omega\text{m}$. For higher resistivities the LRS increases again according to the increasing gaps. In all previous simulations only one filament determined the resistive switching. Here, both filaments determine the LRS for high resistivities. This phenomenon can be understood by analyzing the corresponding $I-V$ curves. In Figure 4.16(b) three $I-V$ curves are shown, which illustrate the influence of the resistivity. For $\rho_{\text{fil}} = 2 \cdot 10^{-6}\,\Omega\text{m}$ the common $I-V$ characteristics are visible. But, at $\rho_{\text{fil}} = 5.02 \cdot 10^{-5}\Omega\text{m}$ an additional feature emerges. Here, the current

increases gradually and finally reaches the current compliance rather than it jumps. This gradual increase looks like the shape of a simulation with a series resistor (cf. Figure 4.7). In addition, at the highest resistivity the whole shape of the $I-V$ curve is similar to a simulation with a series resistor. Such as the set current compliance is not even reached. Here, the filaments themselves represent a series resistor and thus act as an intrinsic current compliance. The filament resistivity is simply calculated by $R_{\mathrm{fil}} = \rho_{\mathrm{fil}} l_{\mathrm{fil}}/\pi r_{\mathrm{fil}}^2$, such that $R_{\mathrm{fil}} = 1.6\,\mathrm{k\Omega}$ for $\rho_{\mathrm{fil}} = 1 \cdot 10^{-6}\,\Omega\mathrm{m}$. This value is only one order of magnitude lower than the LRS resistance in the low resistivity limit. Thus, the resistance of the filament starts to influence the switching behavior as shown in Figure 4.16(a). But it only affects its own growth speed. As long as the growth is self limiting due to the filament resistance, there is no mutual interaction not until the external current compliance sets in. In this case the growth of all filaments is suppressed. If the filament resistance is too high to reach the set external current compliance limit, the remaining gaps of the filaments are equal due the self limitation.
To conclude, it is demonstrated that only one filament is responsible for the SET state if an external current limitation is used except for very high current compliance levels $I_{\mathrm{cc}} \gg 1\,\mathrm{mA}$. Thus, in general the use of a single filament model is appropriate to investigate the switching behavior of ECM cells. Another exception unfolds for very high filament resistivities so that the filamentary growth becomes self-limited. But such a high resistivity value cannot be realized for copper or silver filaments even though it might be increased due to scattering.

4.2.3 Simulaton of Multilevel Switching

ECM cells show multilevel programming capabilities. This means that the LRS can be modulated by an external current compliance or a load resistor in series as current limitation over several orders of magnitude. This phenomenon has been demonstrated for different switching layer materials with similar LRS values. An appropriate model should cover this behavior. Particularly, the LRS resistance should be dominated by the current limitation rather than the switching layer properties. In the previous Section 4.2.2 two possibilities of multilevel switching were revealed. Firstly, the modulation of a tunneling gap and secondly several filaments that subsequently build up galvanic contacts. In this section both possibilities are investigated, whereas for the former one both, the current limitation by an external compliance and by a load resistor, are discussed.

Control by Current Compliance

In order to study the multilevel programming simulations with varying current compliance are performed, where $I_{cc} = I_{SET}$ holds. A voltage triangle of 1 V peak voltage with a rise time of 1 s is used and the filament radius is set to $r_{fil} = 8\,nm$. The simulated LRS values as a function of I_{SET} are shown in **Figure 4.17(a)** along with experimental data. Evidently, the proposed tunneling model is capable of explaining multilevel switching over the full range of SET currents. The remaining gap x_{min} is proportional to $\log\left(I_{SET}\right)^{-1}$ and changes from 1.18 nm at 1 pA to 0.17 nm at 251 µA. At higher SET currents the gap is closed completely resulting in a metallic galvanic contact. Also for the relation between RESET and SET current experimental data and simulation data are consistent (cf. **Figure 4.17(b)**). The simulated RESET currents are a little bit higher than the experimental data. This mismatch can be resolved by introducing an electron transfer coefficient $\alpha < 0.5$ and a geometric asymmetry as discussed in Section 4.2.1. Nevertheless, the RESET current shows a linear relation to the SET current as in experiment. More precisely, the RESET current depends on the LRS resistance, which is controlled by the SET current. This relation is very important with respect to power consumption. In order to keep the RESET current (and thus the power consumption) low the LRS resistance requires a lower limit. A maximum RESET current of 10 µA at an operation voltage of 2 V, for instance, demands an LRS not lower than $R_{LRS} \geq 200\,k\Omega$. So the SET current has to be adjusted accordingly to meet this requirement.

To identify which parameters control the LRS, simulation studies with varying

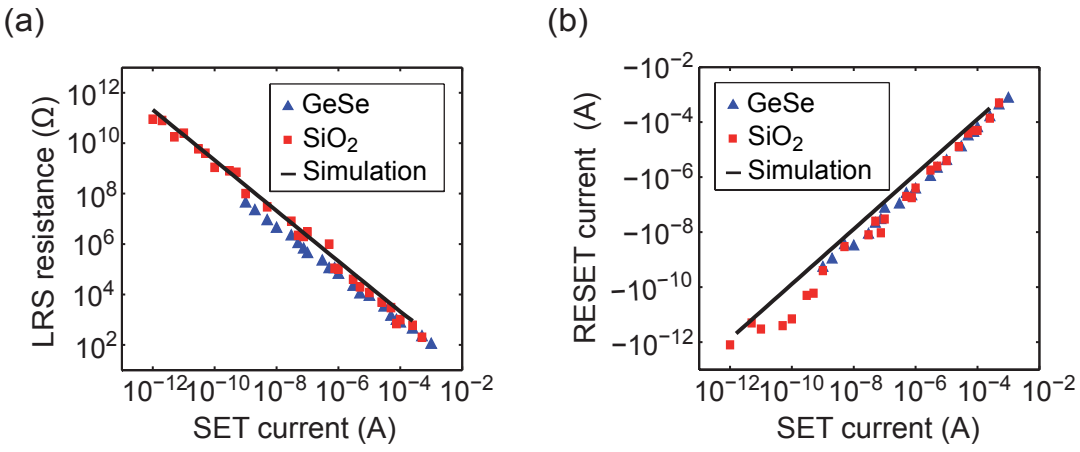

Figure 4.17: (a) LRS resistance vs. SET current and (b) corresponding RESET current vs. SET current. The simulation results for (a) and (b) are depicted as black solid lines. Experimental data is displayed as blue triangles for a Ag:GeSe system [38] and as red squares for a Cu:SiO_2 system [38]. The filament radius is $r_{fil} = 8\,nm$.

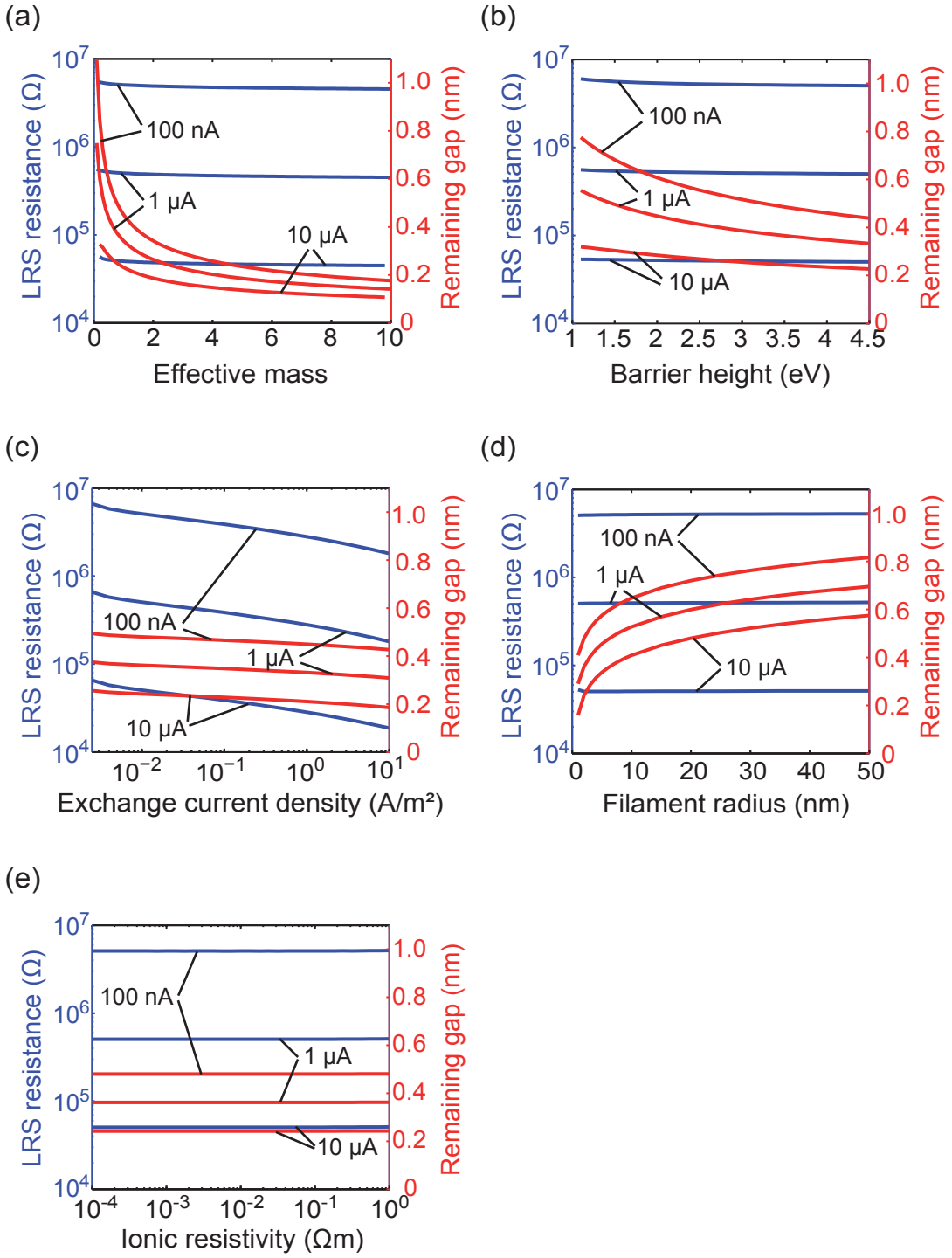

Figure 4.18: LRS resistance (blue lines) and corresponding remaining gap (red lines) vs. (a) effective mass (b) barrier height (c) exchange current density (d) filament radius and (e) ionic resistivity for SET current levels of 100 nA, 1 µA and 10 µA.

parameter values for $I_{\mathrm{SET}} = 100\,\mathrm{nA}$, $1\,\mu\mathrm{A}$ and $10\,\mu\mathrm{A}$ are performed. For each simulation study only one parameter value is varied, while the others are kept constant. As excitation a 1 ms long 1 V SET pulse with a rise and fall time of 10 ns is used. This ensures that SET switching occurs during the hold time. **Figure 4.18** shows that the LRS is virtually invariant to the barrier height ΔW_0, the effective mass m_{r} and the filament radius r_{fil}, whereas it is controlled by I_{SET}. ΔW_0, m_{r} and r_{fil} rather determine the remaining gap, as these parameters relate to the tunneling current according to Eq. (4.15). With the variation of the exchange current density j_0 over four orders of magnitude a small variation of LRS by way of comparison is observed (Figure 4.18(c)), whereas the remaining gap changes accordingly. This variation is directly related to Eq. (4.5) and Eq. (4.3). If the exchange current density is increased, the growth velocity increases analogous. Thus the current compliance is reached faster, and the filament can grow for a longer time under current control. This leads to a slightly lower LRS resistance. The independence of the LRS resistance on the filament area is a very surprising result. Typically, the invariance of the LRS with respect to cell area scaling has been regarded as proof for the filamentary nature of the switching mechanism. In this simulation study, however, it has been shown that only the current compliance controls the LRS rather than the filament area. Thus the invariance of the LRS against cell scaling cannot be taken as a proof for the filamentary nature of the switching. A variation of the ionic resistivity of the switching layer ρ_{ion} does not change the LRS resistance and the remaining gap at all (**Figure 4.18(e)**) in this simulation study. This result originates in the limitation of switching speed by the electron transfer reaction. Not until the ionic resistivity becomes equally limiting an influence on the LRS resistance and the remaining gap is anticipated.

In a further simulation study the amplitude of the voltage pulse is varied. The simulation results in **Figure 4.19(a)** clearly show that it has no influence on the LRS resistance and thus the remaining gap. This behavior can be understood by evaluating the transient gap and the cell resistance in Figure 4.19(b). Increasing the pulse voltage leads to faster switching, but finally the transient behavior is determined by the set current compliance, which is constant. Interestingly, the initial cell resistance after the switching event is higher for higher voltages. With respect to switching in the nanosecond regime, which is achieved at higher voltages (cf. Section 4.2.4), wider remaining gaps and higher LRS resistances are thus expected. In addition, a galvanic metallic contact is even more unlikely to occur for nanosecond switching.

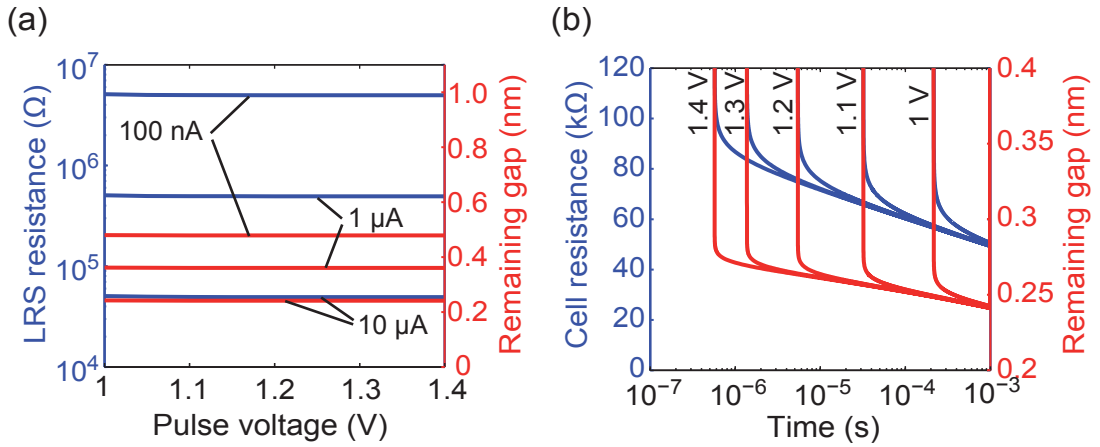

Figure 4.19: (a) LRS resistance (blue) and corresponding remaining gap (red) vs. pulse voltage at SET currents of 100 nA, 1 µA and 10 µA. (b) Transient cell resistance (blue) and gap (red) during the SET pulse for the 10 µA data in (a).

Control by Load Resistor

Multilevel switching can also be achieved, if a load resistor is used as current limitation. As shown in **Figure 4.20** the current during SET operation converges to a slope, which is given by $R_{\mathrm{LRS}} + R_{\mathrm{L}}$. So the maximum current is calculated by $I_{\mathrm{max}} = V_{\mathrm{p}}/R_{\mathrm{L}}$ and gives the current limit. The multilevel switching is simulated using the standard parameters and a triangular voltage of $V_{\mathrm{p}} = 1\,\mathrm{V}$ and $t_{\mathrm{rise}} = 1\,\mathrm{s}$, whereas the load resistance is varied from 1 kΩ to 1 TΩ. The simulated LRS values as well as the corresponding reset current with respect to the load resistance are

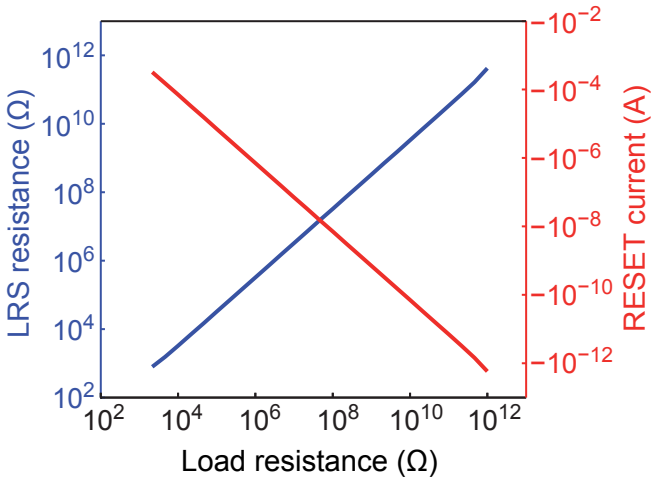

Figure 4.20: LRS resistance (blue) and corresponding RESET current (red) vs. load resistance.

illustrated in Figure 4.20. Here, $R_{\mathrm{LRS}} \propto R_{\mathrm{L}}$ and $I_{\mathrm{RESET}} \propto R_{\mathrm{L}}^{-1}$ applies, which is consistent with the simulated data of the current compliance control. The remaining gap x_{min} changes from 1.22 nm at 1 TΩ to 0.15 nm at 2.15 kΩ.

Multilevel Switching by Polyfilamentary Growth

The second possibility to obtain multilevel switching is attributed to a number of filaments, which successively build up galvanic contacts. To simulate this kind of multilevel switching five parallel filaments are considered. The ionic concentration in the corresponding drift paths differs with scaling coefficients $C_1 = 1$, $C_2 = 0.5$, $C_3 = 0.2$, $C_4 = 0.1$ and $C_5 = 0.05$, respectively. Therefore, filament 1 should build up the galvanic contact first followed by filaments 2, 3, 4 and 5 in ascending order. In this simulation the filament resistivity is $\rho_{\mathrm{fil}} = 2 \cdot 10^{-7}$. For all other parameters the standard values apply. Furthermore no external current limitation is used to enable the galvanic contact of each filament. **Figure 4.21(a)** depicts the simulated $I - V$ characteristic of the SET operation. Every single current jump corresponds to a filament achieving a galvanic contact. After each current jump the $I - V$ curve exhibits a different slope according to the resistance of the parallel filaments in galvanic contact. By setting the current compliance to a level between these slopes several resistance states can be adjusted. As demonstrated in Section 4.2.2 the growth of the remaining filaments is suppressed within the current control. Thus, these resistance states are stable. In Figure 4.21 their extracted LRS values (red filled squares) are plotted against the corresponding number of filaments in galvanic contact. Here, all filaments have the same resistance and thus the low resistance value is given by the number of filaments in galvanic contact as $R_{\mathrm{LRS}} = \rho_{\mathrm{fil}} l_{\mathrm{fil}} / A_{\mathrm{fil}} \cdot 1/n$. This relation is illustrated as dashed red line and open red squares. In general, the filaments differ in area and length. If scattering is considered the resistivity might also differ. So the above relation can be generalized to Eq. (4.34), whereas the resistivity, the area and the length are now mean values. The exact resistance values would then be dispersed about the mean. This simulation result is comparable to experimental data of a recent study [71].

$$R_{\mathrm{LRS}} = \langle \rho_{\mathrm{fil}} \rangle \frac{\langle l_{\mathrm{fil}} \rangle}{\langle A_{\mathrm{fil}} \rangle} n^{-1} \tag{4.34}$$

In summary, in this section it is demonstrated that the derived physical model exhibits multilevel switching as observed in experiment. The modulation of a tunneling gap controlled by current limitation causes resistance modulation over

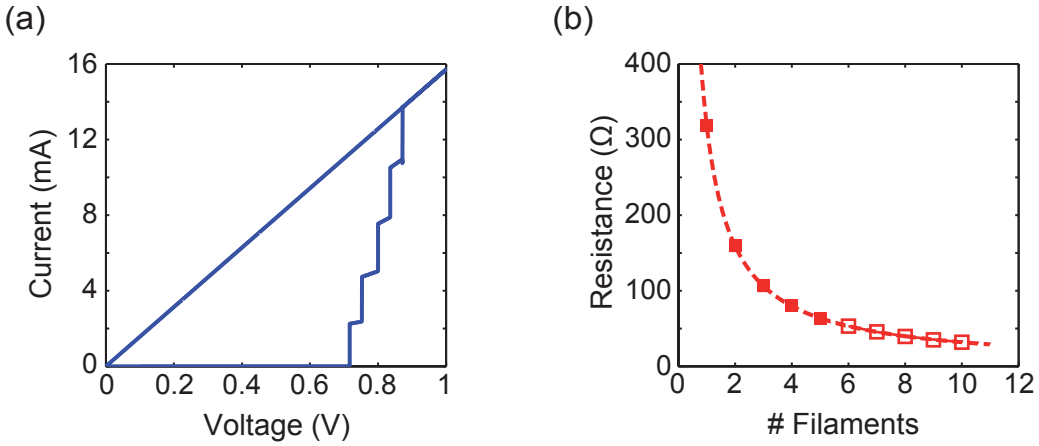

Figure 4.21: (a) Simulated $I-V$ characteristic for a simulation with 5 parallel filaments. Each jump corresponds to a further filament achieving a galvanic contact. The scaling coefficients of the filaments are $C_1 = 1$, $C_2 = 0.5$, $C_3 = 0.2$, $C_4 = 0.1$ and $C_5 = 0.05$. (b) Extracted resistance values (filled squares) against the number of filaments in galvanic contact. The open squares and the red solid line indicate the relation between the LRS value and the number of filaments in galvanic contact.

several orders of magnitude. Importantly, the LRS values are invariant against the material parameters of the switching layer. In other words, different materials show the same experimental multilevel behavior, which is consistent to the literature. Small differences in LRS are then attributed to the switching speed of the cell and hence longer growth times. This kind of multilevel switching is the dominating one for $R_{\mathrm{LRS}} \gg 1\,\mathrm{k\Omega}$. A second kind of multilevel switching is achieved if multiple filament build up galvanic contacts successively. Due to the galvanic contacts this kind of multilevel switching can only be observed at high current compliances. The corresponding LRS values are below $1\,\mathrm{k\Omega}$ and are inversely proportional to the number of filaments in galvanic contact. This kind of multilevel switching has also been observed experimentally in literature. due to the low resistance values, however, it is not relevant for application as ReRAM. To conclude, the derived physical model explains consistently multilevel switching as observed in experiment.

4.2.4 Simulation of Switching Kinetics

ECM cells exhibit nonlinear switching kinetics. Here, the electron transfer reaction described by the Butler-Volmer equation accounts for this nonlinearity. In this section the SET and RESET kinetics are studied with regard to the material parameters. Since the filamentary growth is defined by the Bulter-Volmer equation, the involved parameters are expected to affect the switching kinetics predominantly.

These parameters are the exchange current density j_0, the charge transfer coefficient α and the charge number z. For high voltages also the ionic transport might limit the switching speed. Thus, the ionic resistivity ρ_{ion} might become a decisive parameter at high voltages. In Section 4.2.3 it is demonstrated that the remaining gap x_{min} is determined by the filament area $A_{\mathrm{fil}} = \pi r_{\mathrm{fil}}^2$, the effective electron mass of the switching layer $m_{\mathrm{eff}} = m_{\mathrm{r}} m_0$ and the barrier height ΔW_0. So these parameters determine how long the filament will be and should thus also influence the kinetics slightly. Based on these preliminary considerations different simulations studies are carried out depending on the investigated parameter. The switching kinetics can be studied in two different ways. First, a voltage pulse with a fixed voltage is applied and the SET or RESET time is measured ('pulse mode'). In this mode switching during the rise time should be avoided. Thus, the rise time has to be very small compared to the SET or RESET time. Experimentally, this method is limited for fast switching due to the measurement equipment. For the second method a voltage ramp is used, whereas the ramp speed is varied. Now, both the SET/RESET voltage and the SET/RESET time are measured ('sweep mode'). In experiment often a staircase ramp is used rather than an analog one. If the step height is to large, the sweep mode can converge to a pulse mode for very slow sweep rates. Here, only the pulse mode is used since this is the operation mode for an integrated ReRAM.

SET Kinetics

To investigate the SET switching kinetics simulations with varying pulse amplitudes $0.05\,\mathrm{V} \leq V_{\mathrm{p}} \leq 3\,\mathrm{V}$ are performed. This variation is conducted for different values of the exchange current density j_0, the charge transfer coefficient α and the ionic resistivity ρ_{ion}. The charge number z is either 1 or 2. The standard values are used for the remaining parameters.

In **Figure 4.22(a)** the simulated SET switching kinetics are shown for different exchange current densities. Two different regimes are apparent. For switching times longer than $\Delta t_{\mathrm{SET}} > 100\,\mathrm{ns}$ (or low voltages) the switching time depends exponentially on the pulse amplitude. In this regime the switching speed is limited due to the electron transfer reaction at the boundaries. The ionic current is then given by the the Butler-Volmer equation, which depends exponentially on the overpotential. On the contrary, the switching time becomes inversely proportional to the pulse amplitude for sufficiently high voltages. In this regime the ionic drift within the switching layer limits the switching speed. Here, any additional voltage drops across the switching layer, whereas the overpotentials at the boundaries stay

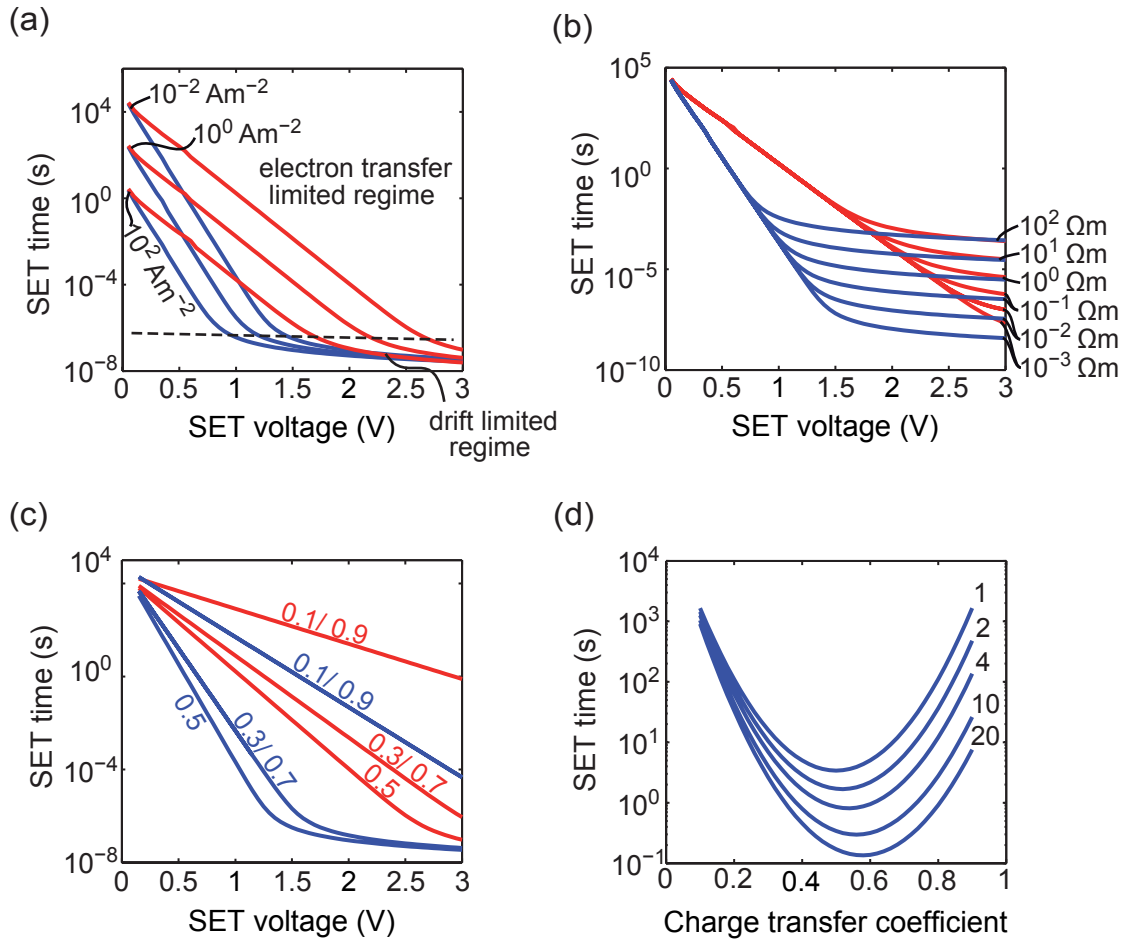

Figure 4.22: Simulated SET time vs. SET voltage using $z = 1$ (red) and $z = 2$ (blue) while varying (a) the exchange current density, (b) the ionic resistivity and (c) the charge transfer coefficient. (d) SET time vs. charge transfer coefficient for different radius ratios $r_{\mathrm{ac}}/r_{\mathrm{fil}}$.

almost constant. Since the resistance of the switching layer is ohmic, the ionic current increases only linearly with voltage in this regime. This leads to the observed inversely proportional relationship. Evidently, the charge number determines the slope in the electron-transfer limited regime, whereas the exchange current density leads to parallel shift of the SET time-voltage characteristics in the electron-transfer limited regime. The SET time is thus directly proportional to the exchange current density within this regime. In addition, the exchange current density also influences the voltage at which the drift limitation occurs. If it increases, the ionic current and thus the switching speed also increases. Thus a significant voltage drop across the switching layer occurs at lower voltages. Another interesting result is that the switching time for $z = 1, 2$ converges at low voltages and the exponential relation vanishes. This is attributed to the Butler-Volmer equation at low overpotentials

$\eta < ze/kT$. Rewriting the Butler-Volmer equation using the Taylor expansion and truncation after the linear term gives

$$\begin{aligned} J_{\mathrm{BV}}(\eta) &= j_0 \left\{ \exp\left(\frac{(1-\alpha)\, ze}{k_{\mathrm{B}}T} \eta \right) - \exp\left(-\frac{\alpha z e}{k_{\mathrm{B}}T} \eta \right) \right\} \\ \Leftrightarrow J_{\mathrm{BV}}(\eta) &= j_0 \left\{ 1 + \frac{(1-\alpha)\, ze}{k_{\mathrm{B}}T} \eta - \left(1 - \frac{\alpha z e}{k_{\mathrm{B}}T} \eta \right) \right\} \\ \Leftrightarrow J_{\mathrm{BV}}(\eta) &= j_0 \frac{ze}{k_{\mathrm{B}}T} \eta. \end{aligned} \tag{4.35}$$

So the ionic current depends linearly on the charge number and thus the ordinary differential equation (4.3) becomes charge-number-independent for low voltages. In addition, the exponential relation of the SET time vanishes and becomes inversely proportional.

The influence of the ionic resistivity on the SET switching kinetics is illustrated in Figure 4.22(b). This parameter only changes the SET kinetics in the drift limited regime. In this regime the SET time becomes linearly dependent on the resistivity. For higher ionic resistivities the transition to the drift limited regime occurs at lower voltages, since the switching layer resistance is increased. Comparing the data for $z = 1$ and $z = 2$ show that the corresponding SET time-pulse voltage characteristics converge in the drift limited regime.

The simulation results for different charge transfer coefficients reveal that the fastest switching is obtained for $\alpha = 0.5$ (cf. Figure 4.22(c)). In contrast to the previous simulations the switching times for $z = 1$ and $z = 2$ do not converge at low voltages for a specific charge transfer coefficient. This is caused by the use of Eq. (4.7) and Eq. (4.8), which deviate from the Butler-Volmer equation (4.4) at low voltages. Identical switching kinetics can be observed for pairs of $\alpha = 0.5 \pm X$, whereas $X < 0.5$. This behavior is attributed to the choice of $r_{\mathrm{ac}} = r_{\mathrm{is}} = r_{\mathrm{fil}}$. If $\alpha > 0.5$ the reduction process is preferred compared to the oxidation process. Thus at a first glance the SET switching should be enhanced. In an ECM cell, however, the reverse redox process occurs at the counter electrode and the switching speed is limited by the slower process. Therefore, the switching speed is identical for $\alpha = 0.5 \pm X$. By setting $r_{\mathrm{ac}} = r_{\mathrm{is}} > r_{\mathrm{fil}}$ this symmetry disappears as discussed in Section 4.2.1. The influence of this geometric asymmetry is simulated by varying the charge transfer coefficient for five different radius ratios $r_{\mathrm{ac}}/r_{\mathrm{fil}}$ and a pulse voltage amplitude $V_{\mathrm{p}} = 0.5\,\mathrm{V}$. As illustrated in Figure 4.22(d) the SET switching time shows an even symmetry with respect to $\alpha = 0.5$ for $r_{\mathrm{ac}} = r_{\mathrm{fil}}$ as discussed before. If the geometry asymmetry increases, this symmetry axis is shifted to charge transfer

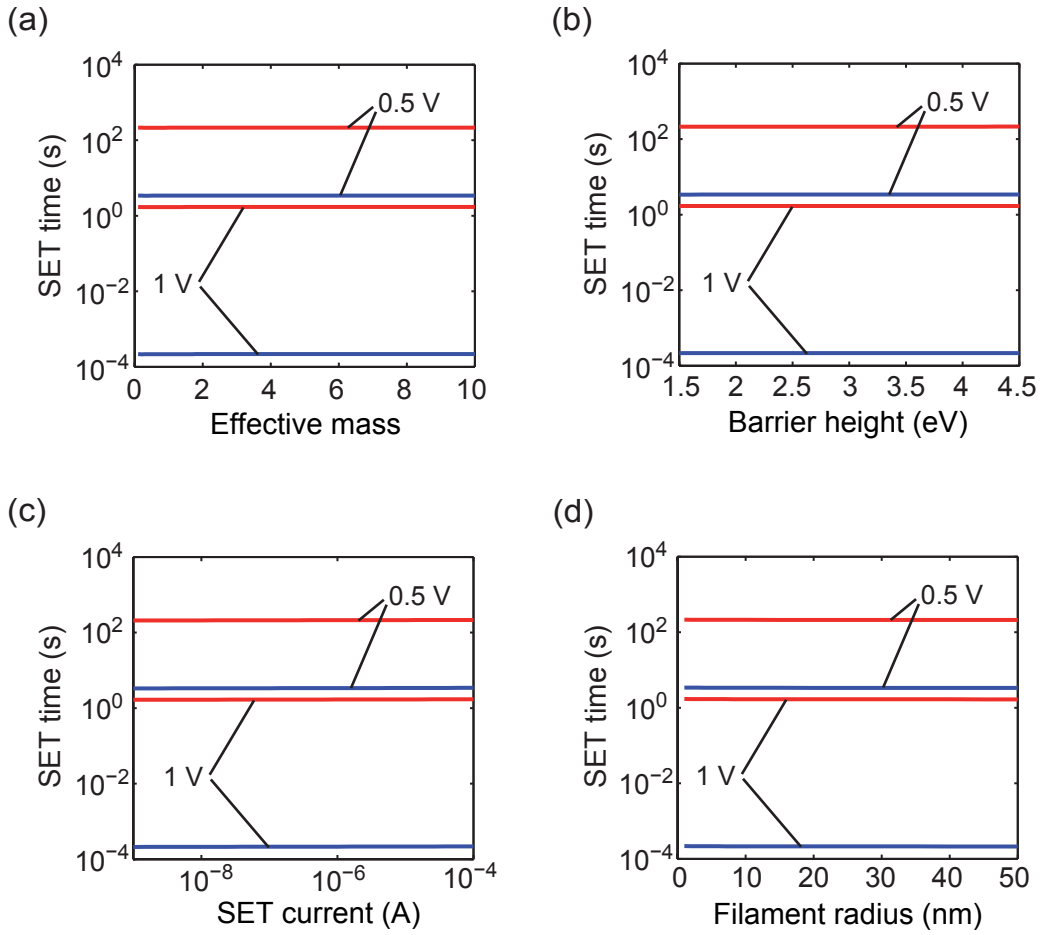

Figure 4.23: Simulated SET time vs. (a) the effective mass, (b) the effective barrier, (c) the SET current and (d) the filament radius using $z = 1$ (red) and $z = 2$ (blue) and a pulse voltage of 0.5 V and 1 V, respectively.

coefficients higher than 0.5. In addition the minimum switching time decreases.

In the following simulation studies the influence of the barrier height ΔW_0, the effective relative mass m_r, the filament radius r_fil and the set current compliance I_cc on the SET switching kinetics are investigated. For that purpose parameter simulations are performed for two different pulse amplitudes $V_\mathrm{p} = 0.5\,\mathrm{V}$ and $V_\mathrm{p} = 1\,\mathrm{V}$ and charge numbers $z = 1$ and $z = 2$. The above named material parameters are varied in the same ranges as in Section 4.2.3. The simulation results depicted in **Figure 4.23** clearly show that these parameters do not influence the SET switching time significantly on a logarithmic scale. As discussed above a slight influence is expected due to the different resulting length of the filament (cf. Section 4.2.3). This is only visible on a linear scale and will be discussed in detail in Section 4.3. To conclude, the SET switching kinetics are predominantly determined by the

charge transfer coefficient, the charge number, the exchange current density and the ionic resistivity. In contrast, the remaining material parameters does not show a significant contribution.

RESET Kinetics

The RESET switching kinetics are studied by conducting simulations with varying pulse amplitudes $-0.05\,\mathrm{V} \geq V_\mathrm{p} \geq -1.5\,\mathrm{V}$. As initial resistance value $R_\mathrm{LRS} = 100\,\mathrm{k\Omega}$ is used. The corresponding initial tunneling gap x_init is calculated according to the specific simulation parameters. The charge number z is either 1 or 2. The pulse modulation variation is conducted for different values of the exchange current density j_0 and the charge transfer coefficient α. The simulated RESET time-voltage characteristics are shown in **Figure 4.24(a), (b)**. The same trend is observed as for the SET kinetics. With increasing absolute voltage amplitude the RESET time decreases exponentially. In contrast to the SET kinetics only an exponential regime is visible, which is dominated by the electron-transfer reactions at the boundaries. For higher voltages and faster RESET times a drift limitation is expected. The simulations in this regime become numerical unstable and are not shown here. In the electron-transfer limited regime the RESET time depends linearly on the exchange current density. This coherence is revealed by the parallel shift of the voltage-RESET time characteristic in Figure 4.24(a). At low absolute voltage amplitudes the simulation results for $z = 1$ and $z = 2$ converge due to the low overpotential approximation of the Butler-Volmer equation (cf. Eq. (4.35)).
As for the SET kinetics the charge number and the charge transfer coefficient define the slope of these exponential characteristics. Again, the RESET voltage-RESET time characteristics are identical for values of $\alpha = 0.5 \pm \mathrm{X}$ since identical radii $r_\mathrm{fil} = r_\mathrm{is} = r_\mathrm{ac}$ are used. Thus, a simulation series is conducted with varying radius ratio $r_\mathrm{ac}/r_\mathrm{fil}$ and $V_\mathrm{p} = -0.5\,\mathrm{V}$. For $r_\mathrm{ac} = r_\mathrm{fil}$ the simulation results show an even symmetry with respect to $\alpha = 0.5$. At this charge transfer coefficient also the minimum RESET time is achieved. If the radius ratio increases, the symmetry axis shifts to lower values of α and the minimum RESET time decreases (cf. 4.24(d)). So for the RESET operation the symmetry axis shifts in the opposite direction as for the SET operation due to the inverse redox reactions occuring at the boundaries. This result is consistent to the simulation results of the $I - V$ sweeps with a real asymmetry (cf. Section 4.2.1).
In a further study the influence of the effective electron mass m_r, the barrier height ΔW_0, the filament area $A_\mathrm{fil} = \pi r_\mathrm{fil}^2$ and the initial LRS resistance R_LRS is simulated. The simulations are conducted for voltage pulses of $V_\mathrm{p} = -0.5\,\mathrm{V}$ and $V_\mathrm{p} = -1\,\mathrm{V}$,

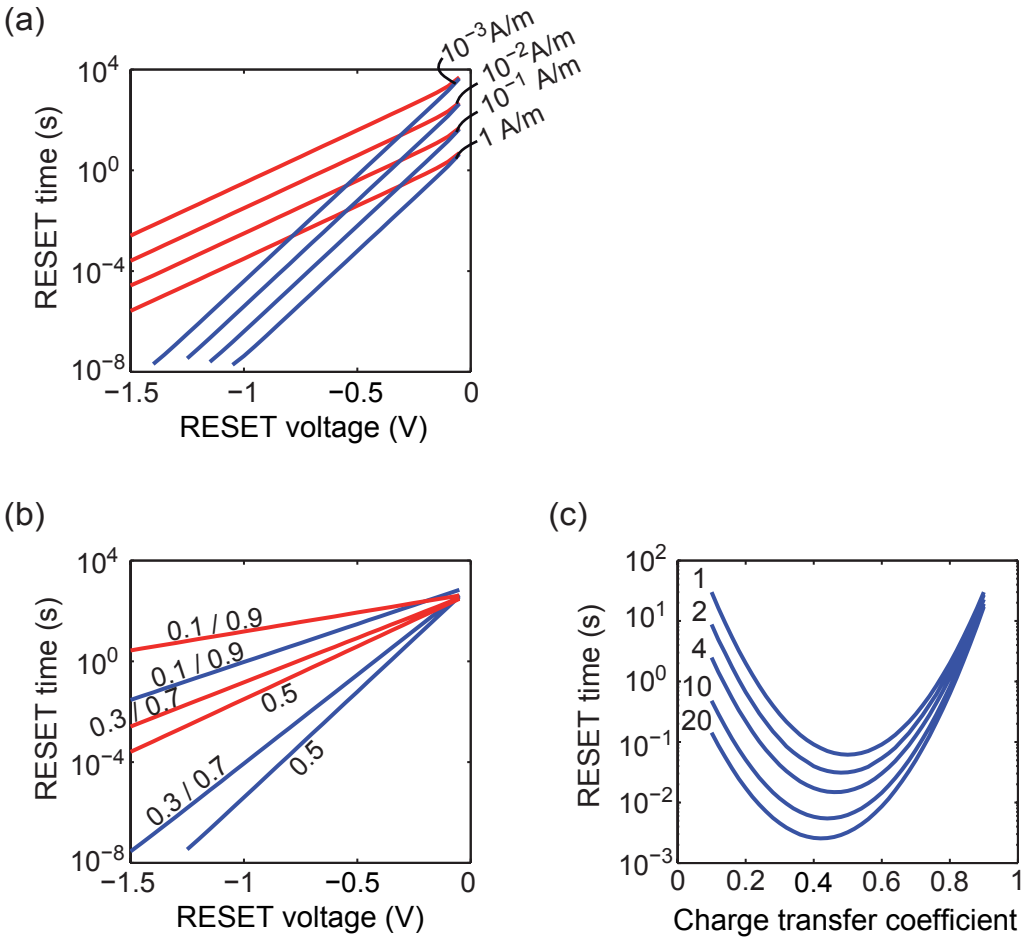

Figure 4.24: Simulated RESET time vs. RESET voltage using $z = 1$ (red) and $z = 2$ (blue) while varying (a) the exchange current density between and (b) the charge transfer coefficient. (c) RESET time vs. charge transfer coefficient for different radius ratios $r_{\mathrm{ac}}/r_{\mathrm{fil}}$.

while the above named parameters are varied. The charge number is either $z = 1$ or $z = 2$ and the initial resistance is $R_{\mathrm{LRS}} = 100\,\mathrm{k\Omega}$, while not varied. According to the specific parameters the initial tunneling gap has to be calculated for each simulation individually. In **Figure 4.25** the resulting simulated RESET times are shown. As illustrated in (a) and (b) the effective electron mass and the barrier height slightly influence the RESET time. As these parameters increase the RESET time decreases. In contrast, no influence is visible on the logarithmic scale by variation of the LRS resistance and the filament area (Figures 4.25(c) and (d)). On a linear scale the influence becomes visible and will be discussed in the analytic Section 4.3. In comparison, the influence of the effective electron mass and the barrier height is not visible for the SET kinetics (cf. Figure 4.23) on a logarithmic scale. This discrepancy is attributed to the SET and RESET criterion as defined in Section

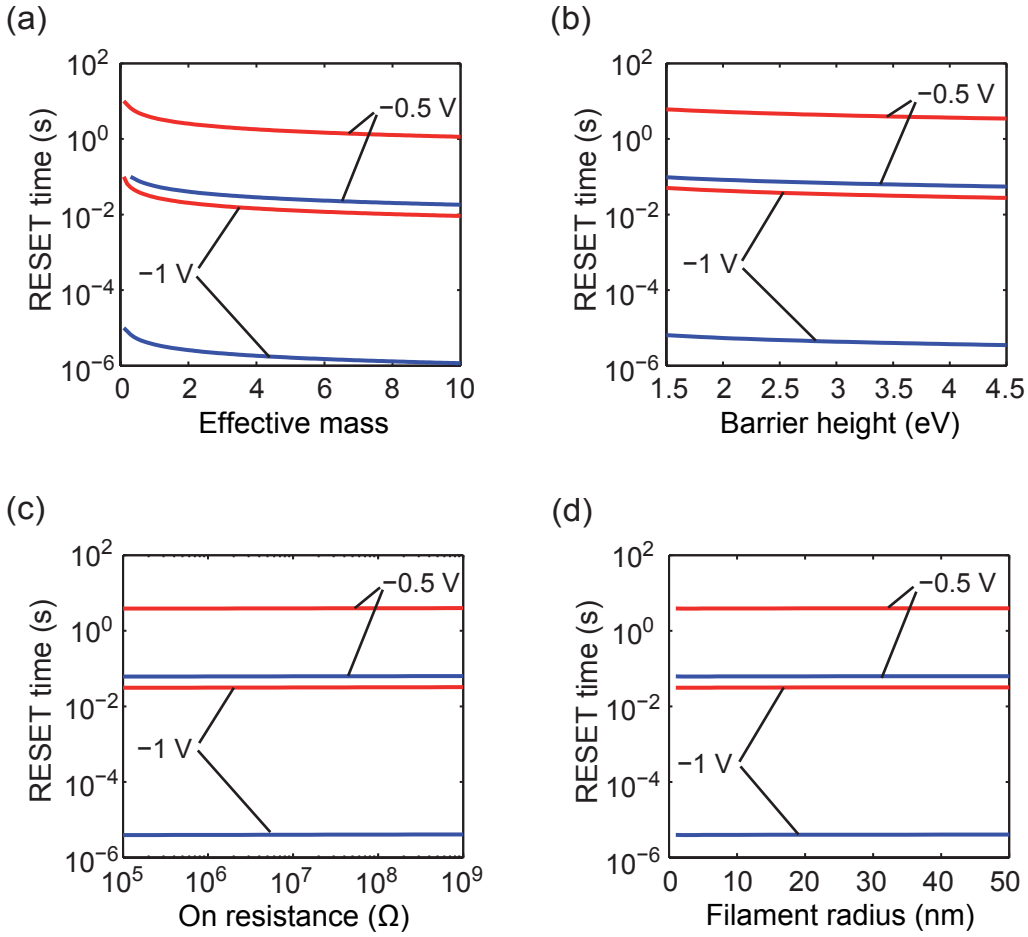

Figure 4.25: Simulated RESET time vs. (a) the effective mass, (b) the effective barrier, (c) the LRS resistance and (d) the filament radius using $z = 1$ (red) and $z = 2$ (blue) and a pulse voltage of $-0.5\,\mathrm{V}$ and $-1\,\mathrm{V}$, respectively.

4.2.1. The SET time defines the point in time when the set current compliance is reached. For this to happen, the filament has to grow several nanometers. On the contrary the RESET time defines the point in time when the current level has dropped at least three orders of magnitude. This is achieved by a modulation of the tunneling gap less than a nanometer. Therefore, the RESET is achieved faster than SET.

To conclude, the parameters predominantly determining the RESET kinetics are the exchange current density, the charge transfer coefficient and the charge number. Here, the former parameter shifts the RESET time-voltage characteristic vertically, whereas the latter two parameters determine the slope of this exponential relation. In contrast the effective electron mass, the barrier height, the initials LRS resistance and the filament area play a minor role for the RESET kinetics. A very important result with respect to multilevel switching is the stable RESET time with varying

LRS resistance. This enables arbitrary switching between different resistance states (see discussion in Section 4.2.5). The simulation of the SET and RESET kinetics show that the electron-transfer reaction leads to a strongly nonlinear SET/RESET time-voltage characteristic. The slope of this characteristic allows for an acceleration of the switching speed of more than 13 order of magnitude by variation of the applied voltage about $1 - 2\,\mathrm{V}$. At fast switching times the SET switching becomes drift limited. In order to enable fast switching times the ionic conductivity needs to be as high as possible. This can be achieved by increasing the ion concentration, which likewise increases the exchange current density value linearly. To meet the criteria for a nonvolatile memory the SET and RESET time should be longer than $1 \cdot 10^{10}\,\mathrm{s}$ while applying a **read** voltage. For this purpose a low value of the exchange current density is required. So a trade-off between long-term stability and fast switching is connected with the variation of ion concentration. Also a reliability issue is related to the ion concentration. If it changes upon switching, a spread in SET voltages would result.

4.2.5 Memristive Switching in ECM Cells

The derived physical model describes a memristive system as defined by Chua [72]. Such systems exhibit a pinched hysteresis loop. Here, pinched means that the $I - V$ characteristic of a memrisitive device must pass through the origin. Mathematically, a memristive system is defined by a state-dependent Ohm's law

$$v = R(p, i, t)i \Leftrightarrow i = G(p, v, t)v \tag{4.36}$$

and the state equation

$$\frac{\mathrm{d}p}{\mathrm{d}t} = f(p, i, t). \tag{4.37}$$

Here, p is the state variable and v and i are the time-dependent voltage and current. For the function $R(p, i, t)$ should hold $R(p, i = 0, t) \geq 0$. In addition the non-volatility criterion

$$f(p, i = 0, t) = 0 \tag{4.38}$$

has to be fulfilled. By comparison of this definition with the derived physical model, the tunneling gap x can be identified as the state variable p. Thus, Faraday's law (4.3) is the state equation. The state-dependent Ohm's law is given by Eq. (4.16) or Eq. (4.13), whereas some further conversion are necessary to achieve the correct form. These are rather tedious and bear no further information so that at this point the conversions are abandoned.

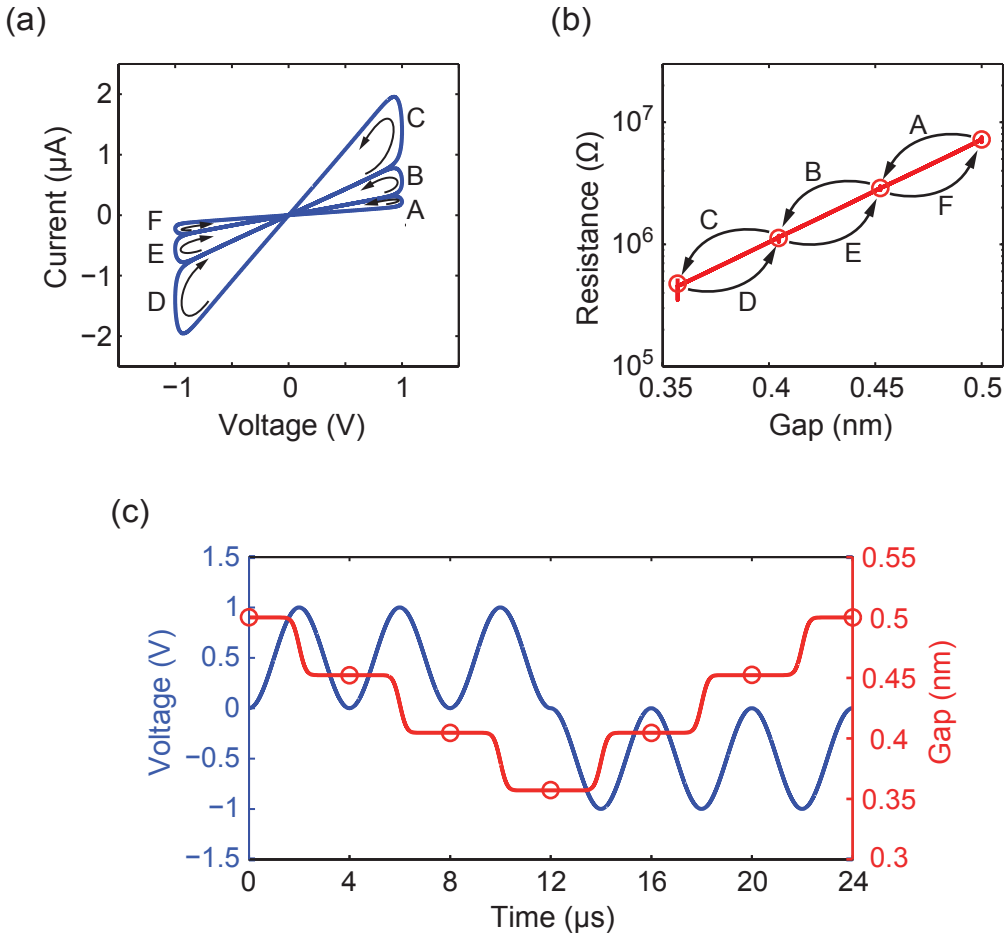

Figure 4.26: (a) Simulated $I-V$ characteristic for three successive SET sweeps (A, B, C) followed by three successive RESET sweeps (D, E, F). (b) Corresponding resistances vs. tunneling gap states after each sweep. The inital gap is 0.5 nm. (c) Applied transient sinusoidal voltage and transient gap. The gaps after each sweep corresponding to (b) are marked as red open circles.

To demonstrate memristive switching behavior, typically a series of sinusoidal voltage sweeps or a series of voltage pulses is applied switching back and forth between different resistance states. As demonstrated in Section 4.2.3 the resistance in an ECM cell is modulated by variation of the tunneling gap within $1.7\,\text{Å} \leq x \leq 12\,\text{Å}$. Thus, the cell needs to be initialized by an appropriate SET operation so that medium resistance is achieved.

In the first simulation an ECM cell with standard parameters and an initial tunneling gap $x_{\text{init}} = 5\,\text{Å}$ is considered. First three successive sinusoidal SET operations are applied followed by three successive RESET operations of the same frequency and amplitude. Thus, the resulting gap is expected to equal the initial gap. **Figure 4.26(a)** shows the resulting $I-V$ characteristics. Apparently, the RESET

operations reverse exactly the SET operations. This becomes more obvious by examining the transient gap, which is illustrated in Figure 4.26(c) along with the applied voltage. For each SET operation the gap is reduced by approximately 0.5 Å and increased by the same distance for each RESET operation. This variation in gap is accompanied with a corresponding resistance modulation (cf. Figure 4.26(b)). The previous simulation revealed, that the tunneling gap can be varied by suitable SET and RESET operations. In a digital circuit SET and RESET pulses with a distinct amplitude would be used. Thus in a further simulation study a pulse series is applied to an ECM cell. Different pulse lengths are used in order to change the resistance state arbitrarily. Thereby, the lengths of a pulse is nT, whereas n is an integer and $T = 2\,\mu s$. Again an ECM cell with standard parameters is considered. The initial tunneling gap is $x_{\text{init}} = 3\,\text{Å}$. In **Figure 4.27(a)** the applied pulse series and the resulting transient gap are shown. These data clearly show that the gap and thus the resistance can be precisely tuned by adjusting the pulse length. If the pulse lengths is doubled, also the gap is changed twice as much. By this gap modulation the resistance changes exponentially due to the tunneling current. The change in resistance states by the voltage pulses is depicted in Figure 4.27(b).

In summary, the derived physical model is a memristive system and shows the typical memristive switching behavior. Within the relevant tunneling distances the gap and thus the resistance state can be modulated arbitrarily by varying the pulse length appropriately. Here, a symmetrical system was considered. Hence, in order to reverse a SET operation, for example, simply a voltage with the same shape and

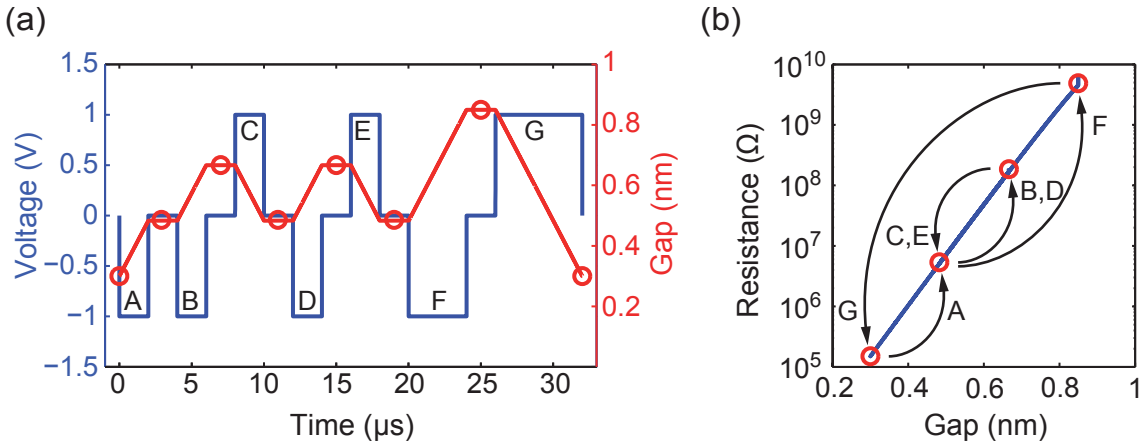

Figure 4.27: Applied transient voltage pulses (A - G) and simulated transient gap. The gaps after each sweep corresponding to (b) are marked as red open circles. (b) Corresponding resistances vs. tunneling gap states after each sweep. The inital gap is 0.3 nm.

inversed polarity has to be applied. If the kinetics of SET and RESET operation are asymmetric as discussed in Section 4.2.1 in contrast, the shape of the SET and corresponding RESET operation would differ. In experiment it might be hard to obtain stable memristive switching, since the change in the tunneling gap is rather small.

4.2.6 Nonlinear Series Resistance

So far only a linear series resistance has been considered. In some material systems exhibiting ECM switching behavior, however, a nonlinear series resistance is present. In Cu:TCNQ based ECM cells, for instance, a thin oxide layer is the active switching layer, whereas the Cu:TCNQ layer serves as an ion source [34]. This Cu:TCNQ layer exhibits a nonlinear hyperbolic sine shaped $I - V$ characteristic. By scaling the area of such an ECM cell this nonlinear series resistance increases and might act as an intrinsic current compliance. Due to the nonlinearity the interaction of current limitation and filamentary growth is more sophisticated and thus worth to investigate.
In order to simulate an ECM cell with a nonlinear series resistance the governing equations for the device current and voltage have to be reformulated. The device comprises the ECM cell itself and the nonlinear series resistance. The corresponding voltages and currents will be termed 'device', 'cell' and 'nl' in the following. Due to the serial connection of the cell and the nonlinar resistor, the device current I_{dev} equals the current through the nonlinear series resistor I_{nl} and the cell current I_{cell} Eq. (4.13). Hence, it is a function of the SL/filament overpotential and the tunneling gap x

$$I_{\mathrm{dev}} = I_{\mathrm{nl}} = I_{\mathrm{cell}} = I_{\mathrm{BV}}\left(\eta_{\mathrm{fil}}\right) + I_{\mathrm{Tu}}\left(V_{\mathrm{Tu}}\right) = f\left(\eta_{\mathrm{fil}}, x\right). \tag{4.39}$$

As current-voltage relation for the nonlinear series resistor a hyberbolic sine function

$$I_{\mathrm{nl}} = J_{\mathrm{nl},0} A_{\mathrm{nl}} \sinh\left(\frac{V_{\mathrm{nl}}}{V_{\mathrm{nl},0}}\right) \tag{4.40}$$

is chosen. Here, $J_{\mathrm{nl},0}$ is a current density prefactor, A_{nl} the cross-sectional area of the series resistor and V_0 a characteristic voltage. If the voltage drop along the

series resistor V_{nl} is lower than the characteristic voltage $V_{\mathrm{nl},0}$, Eq. (4.40) becomes linear and for $V_{\mathrm{nl}} \gg V_{\mathrm{nl},0}$ exponential. Rewriting Eq. (4.40) yields

$$\Rightarrow V_{\mathrm{nl}} = V_{\mathrm{nl},0} \operatorname{arsinh}\left(\frac{I_{\mathrm{BV}}\left(\eta_{\mathrm{fil}}\right) + I_{\mathrm{Tu}}\left(V_{\mathrm{Tu}}\right)}{J_{\mathrm{nl},0} A_{\mathrm{nl}}}\right). \tag{4.41}$$

The device voltage is the sum of the cell voltage and the voltage drop along the series resistor

$$\begin{aligned} V_{\mathrm{dev}} =& V_{\mathrm{cell}} + V_{\mathrm{nl}} \\ =& \eta_{\mathrm{ac}} - \eta_{\mathrm{fil}} + I_{\mathrm{ion}}\left(R_{\mathrm{se}} + R_{\mathrm{fil}} + R_{\mathrm{el}}\right) + I_{\mathrm{Tu}}\left(R_{\mathrm{fil}} + R_{\mathrm{el}}\right) + \\ & V_{\mathrm{nl},0} \operatorname{arsinh}\left(\frac{I_{\mathrm{BV}}\left(\eta_{\mathrm{fil}}\right) + I_{\mathrm{Tu}}\left(V_{\mathrm{Tu}}\right)}{J_{\mathrm{nl},0} A_{\mathrm{nl}}}\right) = f\left(\eta_{\mathrm{fil}}, x\right). \end{aligned} \tag{4.42}$$

It is thus a function of η_{fil} and x. The implicit equations (4.42) and (4.40) have to be solved for η_{fil} in each time step. The growth of the filament is still described by the ordinary differential equation (4.3). The parameters describing the current voltage relation of the series resistor are chosen such as it affects the switching behavior. Here it is $J_{\mathrm{nl},0} = 1 \cdot 10^2\,\mathrm{A/m^2}$ and $V_{\mathrm{nl},0} = 0.15\,\mathrm{V}$. The cylindrical area $A_{\mathrm{nl}} = \pi r_{\mathrm{nl}}^2$ is varied within $1\,\mu\mathrm{m} \leq r_{\mathrm{nl}} \leq 1\,\mathrm{mm}$. Since the device is a vertical stack of the different layers, the electrode resistance changes accordingly. The switching layer thickness is set to 4 nm. For all other parameters the standard values apply. As excitation a voltage sweep with $V_{\mathrm{p}} = 2\,\mathrm{V}$ and $t_{\mathrm{rise}} = 1\,\mathrm{s}$ is used and the current compliance is set to 10 µA.

Figure 4.28(a) shows the simulated $I - V$ characteristics for radii $r_{\mathrm{nl}} = 10\,\mu\mathrm{m}$, 20 µm, 50 µm and 1 mm. For the latter radius the $I - V$ curve has the same shape as for the simulation without load resistor (cf. Figure 4.4). At this radius the nonlinear resistance is too low to influence the switching behavior at all. In contrast, the shape deviates for the other radii. Especially, in LRS the current-voltage relation becomes nonlinear and the LRS resistance value taken at $V_{\mathrm{read}} = 0.2\,\mathrm{V}$ deviates. In these cases the nonlinear series resistance takes effect. As illustrated in Figure 4.28(b) the LRS resistance is predominately determined by the nonlinear series resistance for $r_{\mathrm{nl}} < 100\,\mu\mathrm{m}$. In this regime the LRS resistance converges to $R_{\mathrm{LRS}} \propto A_{\mathrm{nl}}^{-1}$. For large radii the LRS resistance is set by the current compliance and is thus independent of the cell radius as discussed in Section 4.2.3. Interestingly, the remaining gap and thus the cell resistance stays constant upon lateral cell scaling. So it is still adjusted by the current compliance although the nonlinear series resistance should also act as a current limitation. To understand this behavior the transient voltage drops V_{nl}

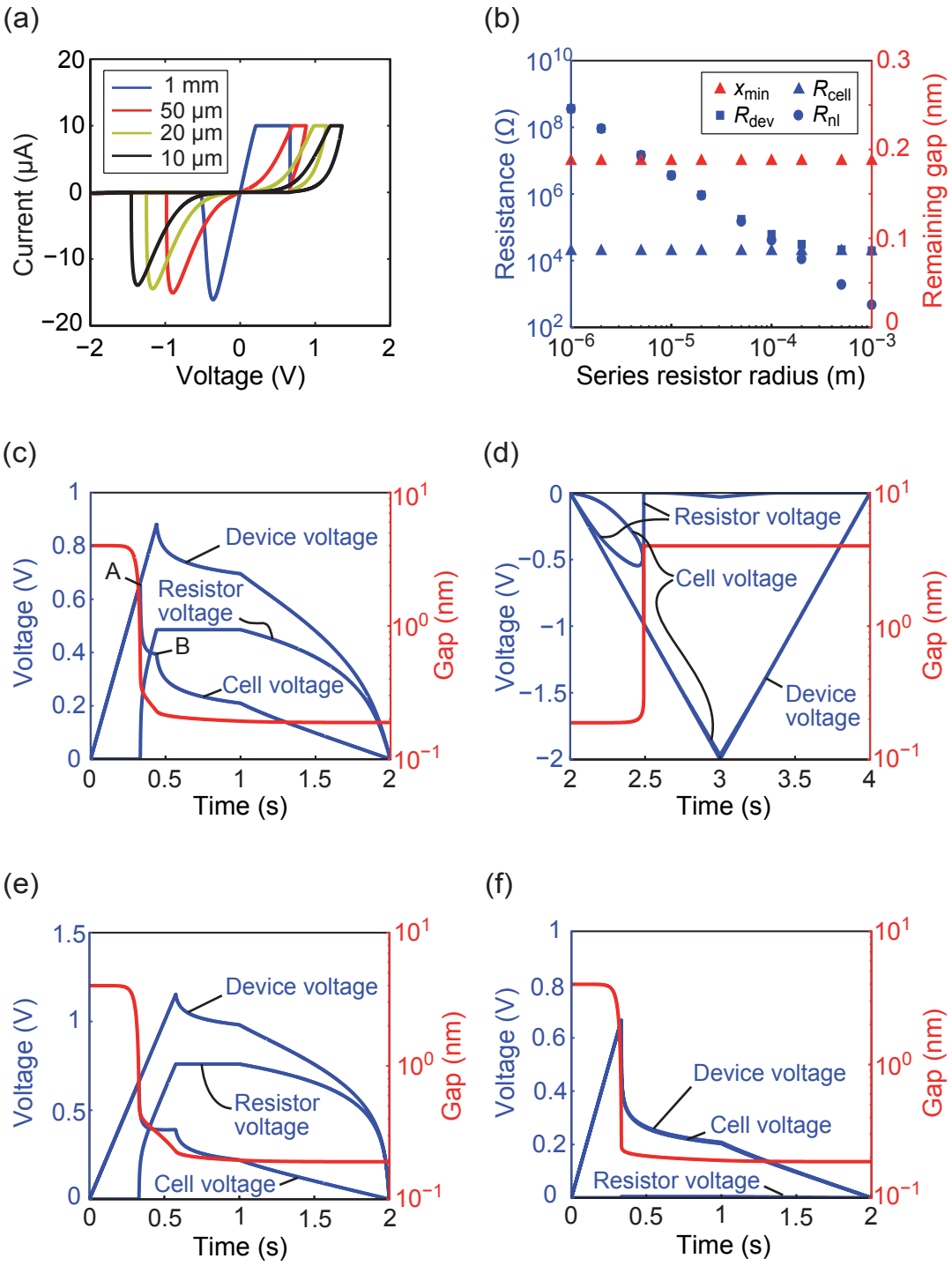

Figure 4.28: (a) Simulated $I - V$ characteristics for four different radii of the nonlinear series resistor. (b) Resistance of the cell (blue triangles) the nonlinear series resistor (blue circles), the whole device resistance (blue squares) and the remaining gap (red triangles) vs. nonlinear series resistor radius. Transient device voltage, cell voltage and series resistor voltage (blue) and the simulated transient gap for (c) SET and (d) RESET. The series resistor radius is 50 µm. Transient device, cell and series resistor voltages (blue) and the simulated transient gap during SET for a series resistor radius of (c) 20 µm and (f) 1 mm.

and V_{cell} as well as the transient gap x have to be considered. The simulated SET transients for $r_{\mathrm{nl}} = 50\,\mu\mathrm{m}$ are illustrated in Figure 4.28(c). The cell voltage exhibits two successive voltage drops (marked with A and B). The first voltage drop A is connected to the current limitation induced by the nonlinear series resistance. In this regime the additional applied voltage drops over the nonlinear series resistor, whereas the cell voltage first drops and then stays constant. The filamentary growth slows down, but it is still significant in contrast to the case of a linear resistor (cf. Figure 4.7). This is caused by the constant cell voltage. Finally, the current compliance is reached and the cell voltage drops again (B) such as the filamentary growth is suppressed. The current compliance can only be reached if the cell resistance and thus the remaining gap is small enough. Therefore, the remaining gap is equal in all cases. For the sake of completeness the RESET transients are given in Figure 4.28(d). The same characteristic SET transients are visible for $r_{\mathrm{nl}} = 20\,\mu\mathrm{m}$ in Figure 4.28(e). For $r_{\mathrm{nl}} = 1\,\mathrm{mm}$, however, only one cell voltage drop occurs (cf. Figure 4.28(f)) caused by the onset of the current compliance. The voltage V_{nl} is negligible and thus the nonlinear series resistor does not influence the SET switching behavior.

The previous simulation study allows for some important implications. For low radii the current-voltage relations in LRS and HRS are dominated by the nonlinear series resistor. A resistive switching effect can therefore only be observed, if the cell resistance in HRS is higher than the resistance of the nonlinear resistor at a given read voltage. A loss of observable resistive switching behavior can therefore occur at small radii. This would limit the cell scaling. On the other hand the series resistor can serve as an inherent selector device superseding a select transistor. At last, the multilevel switching capabilities become limited, if the nonlinear series resistor dominates the LRS resistance.

4.3 Analytical Model

In Section 4.2 a numerical model has been derived to simulate the switching characteristics of an ECM cell. Using this model predictions of the switching behavior with respect to switching speed can be given. It is even more desirable, however, to obtain predictions by the simple use of analytical expressions. The aim of this section is to derive an analytical model for ECM switching based on the simulation results obtained in Section 4.2. In detail, the generic SET and RESET characteristics during voltage sweeps are elucidated in Section 4.3.1 and the material dependence of the switching kinetics is analyzed in Section 4.3.2.

To obtain an analytical model for ECM switching the equation system (4.3) – (4.16) derived in Section 4.2 needs to be simplified. Especially, it is necessary to get rid of the implicit equations for the overpotential η_{fil} (Eq. (4.13) and Eq. (4.16)). A second issue is connected to the calculation of the tunneling current using Eq. (4.15). The voltage V_{Tu} can be only obtained numerically if the gap x and the current I_{Tu} are known. As shown in Section 4.2.1 the ON-state exhibits an ohmic $I-V$ characteristic. Thus, a linear relation for the tunneling current against the voltage is applicable:

$$I_{\mathrm{Tu}} = C\frac{3\sqrt{2m_{\mathrm{eff}}\Delta W_0}}{2x}\left(\frac{e}{h}\right)^2 \exp\left(-\frac{4\pi x}{h}\sqrt{2m_{\mathrm{eff}}\Delta W_0}\right) A_{\mathrm{fil}} V_{\mathrm{Tu}} = G_{\mathrm{Tu}} V_{\mathrm{Tu}}. \quad (4.43)$$

In contrast to Eq. (2.11) in Section 2.4 derived by Simmons [27] an additional factor C is introduced in Eq. (4.43). The value of C is optimized by a least squares method such as the $I-V$ relations of Eq. (4.15) and Eq. (4.43) coincide for the standard set of parameters, which results in $C = 0.29$. Eq. (4.43) can now be solved for x using the Lambert W function $W(\cdot)$, which gives the solution of the equation $xe^x = a$ as $x = W(a)$ [73]. Rewriting Eq. (4.43) to

$$\Leftrightarrow \frac{4\pi x}{h}\sqrt{2m_{\mathrm{eff}}\Delta W_0}\exp\left(\frac{4\pi x}{h}\sqrt{2m_{\mathrm{eff}}\Delta W_0}\right) = C\frac{12\pi m_{\mathrm{eff}}\Delta W_0 e^2 A_{\mathrm{fil}} V_{\mathrm{Tu}}}{h^3 I_{\mathrm{Tu}}} \quad (4.44)$$

and applying the Lambert W function yields:

$$x = \frac{h}{4\pi\sqrt{2m_{\mathrm{eff}}\Delta W_0}} W\left(C\frac{12\pi m_{\mathrm{eff}}\Delta W_0 e^2 A_{\mathrm{fil}} V_{\mathrm{Tu}}}{h^3 I_{\mathrm{Tu}}}\right). \quad (4.45)$$

According to the simulations in Section 4.2 the voltage drops across the electrodes given by $I_{\mathrm{cell}}R_{\mathrm{el}}$ and the ionic conductor $V_{\mathrm{ion}} = I_{\mathrm{ion}}R_{\mathrm{ion}}$ are small compared to the overpotentials η_{fil} and η_{ac}. Thus, the overall cell voltage can be simplified to

$$V_{\mathrm{cell}} \approx V_{\mathrm{Tu}} \approx \eta_{\mathrm{ac}} - \eta_{\mathrm{fil}}. \quad (4.46)$$

This simplification is valid as long as a moderate current compliance $I_{\mathrm{cc}} \leq 10\,\mu\mathrm{A}$ is chosen and the load resistor is $R_{\mathrm{L}} = 0\,\Omega$. In this case the electronic tunneling current can be directly calculated if the cell voltage V_{cell} and the gap x are known. The overpotentials are calculated according to the derivation in Section 4.2 for a

variable α (Eqs. (4.7) – (4.12)). Thus, the overpotential η_{ac} for SET and RESET can be expressed by the overpotential η_{fil} as

$$\eta_{\mathrm{ac,SET}} = -\frac{\alpha}{(1-\alpha)}\eta_{\mathrm{fil,SET}} + \frac{k_{\mathrm{B}}T}{ze}(1-\alpha)\ln\left(\frac{A_{\mathrm{fil}}}{A_{\mathrm{ac}}}\right) \tag{4.47}$$

$$\eta_{\mathrm{ac,RESET}} = -\frac{(1-\alpha)}{\alpha}\eta_{\mathrm{fil,RESET}} - \frac{k_{\mathrm{B}}T}{ze}\alpha\ln\left(\frac{A_{\mathrm{fil}}}{A_{\mathrm{ac}}}\right). \tag{4.48}$$

Substituting Eq. (4.47) and Eq. (4.48) into Eq. (4.46) and rewriting for η_{fil} yields:

$$\eta_{\mathrm{fil,SET}} = -(1-\alpha)V_{\mathrm{cell}} + \frac{k_{\mathrm{B}}T}{ze}\ln\left(\frac{A_{\mathrm{fil}}}{A_{\mathrm{ac}}}\right) \tag{4.49}$$

$$\eta_{\mathrm{fil,RESET}} = -\alpha V_{\mathrm{cell}} - \frac{k_{\mathrm{B}}T}{ze}\ln\left(\frac{A_{\mathrm{fil}}}{A_{\mathrm{ac}}}\right). \tag{4.50}$$

Thus, the overpotential η_{fil} can be directly calculated when the cell voltage is given without solving an implicit equation. The overall current $I_{\mathrm{cell}} = I_{\mathrm{ion}} + I_{\mathrm{Tu}}$ is then an explicit function of cell voltage and the gap. The ordinary differential equation for the SET process under voltage control is now

$$\frac{\mathrm{d}x}{\mathrm{d}t} = -\frac{M_{\mathrm{Me}}}{ze\rho_{\mathrm{m,Me}}}j_0\left(\frac{A_{\mathrm{ac}}}{A_{\mathrm{fil}}}\right)^{\alpha}\exp\left(\alpha(1-\alpha)\frac{ze}{k_{\mathrm{B}}T}V_{\mathrm{cell}}(t)\right), \tag{4.51}$$

where $V_{\mathrm{cell}}(t)$ is an arbitrary function.
Within the current compliance the ionic contribution to the overall current can be neglected for most values of I_{cc}, i.e. $I_{\mathrm{Tu}} \approx I_{\mathrm{cell}} = I_{\mathrm{cc}}$. The cell voltage during current compliance is hence approximated by $V_{\mathrm{cell}} \approx I_{\mathrm{Tu}}R_{\mathrm{Tu}}$ using the linear tunnel equation (4.43). This approximation fails if the current compliance is chosen too low. In this case the ionic contribution to the cell current cannot be neglected. The differential equation under current control now reads

$$\frac{\mathrm{d}x}{\mathrm{d}t} = -\frac{M_{\mathrm{Me}}}{ze\rho_{\mathrm{m,Me}}}j_0\left(\frac{A_{\mathrm{ac}}}{A_{\mathrm{fil}}}\right)^{\alpha}\exp\left(\alpha(1-\alpha)\frac{ze}{k_{\mathrm{B}}T}R_{\mathrm{Tu}}(x)I_{\mathrm{cell}}(t)\right) \tag{4.52}$$

and the differential equation for the voltage driven RESET is

$$\frac{\mathrm{d}x}{\mathrm{d}t} = \frac{M_{\mathrm{Me}}}{ze\rho_{\mathrm{m,Me}}}j_0\left(\frac{A_{\mathrm{ac}}}{A_{\mathrm{fil}}}\right)^{1-\alpha}\exp\left(-\alpha(1-\alpha)\frac{ze}{k_{\mathrm{B}}T}V_{\mathrm{cell}}(t)\right). \tag{4.53}$$

Note that the cell voltage for the RESET operation is negative. In general, these differential equations needs to be solved numerically. This holds in all cases for Eq. (4.52), whereas analytical solutions can be found for Eq. (4.51) and Eq. (4.53) if the excitation is chosen suitably. These cases are discussed in the following sections.

4.3.1 Generic SET and RESET Characteristics

As discussed in Section 4.2.3 different LRS can be programmed using current limitation and the corresponding RESET current depends linearly on the SET current. It is shown that these characteristics are material parameter independent and thus generic for ECM cells. Mathematically, the LRS resistance is given by $R_{\mathrm{LRS}} = V_{\mathrm{ON}}/I_{\mathrm{cc}}$ and for the RESET current the empirical relation $I_{\mathrm{RESET}} = AI_{\mathrm{cc}}$ holds. Here, V_{ON} and A are system inherent constants. These SET and RESET characteristics could be also demonstrated for TCM and VCM systems [74] and hence are quite universal for all types of ReRAMs. A descriptive explanation for this phenomenon can be given based on the nonlinear switching kinetics. As soon as the current compliance level is reached during SET any further decrease in resistance leads to decrease in voltage. As the switching kinetics are highly nonlinear, the driving force for further resistance change decreases drastically. A further resistance change is therefore strongly suppressed. The voltage V_{ON} adjusts accordingly and is very similar for different kind of ReRAMs [22]. Regarding the RESET the empirical relation can be attributed to the linear $I-V$ characteristic of the LRS and again the nonlinear switching kinetics. The driving force for the RESET is strongly voltage-dependent, highly nonlinear and almost independent on R_{LRS}. Hence, the RESET voltage is nearly constant and therefore $I_{\mathrm{RESET}} = V_{\mathrm{RESET}}/R_{\mathrm{LRS}} = V_{\mathrm{RESET}}/V_{\mathrm{ON}} \cdot I_{\mathrm{cc}}$ is only a function of the used current compliance. In the following the empirical relations for SET and RESET are analyzed analytically. Here, the focus lies on the material parameters which control V_{ON} and A and on the $I-V$ curve itself.
In experiment a triangular voltage sweep is commonly used. Thus, the time-dependent cell voltage has to be defined piecewise and the differential equations (4.51) – (4.53) must be solved for each part separately. As a simplification it is assumed that the current compliance is reached before the peak voltage V_{p} is reached, i.e. $t_{\mathrm{SET}} < t_{\mathrm{rise}}$. The corresponding cell voltage in this regime is $V_{\mathrm{cell}} = V_{\mathrm{p}}/t_{\mathrm{trise}} \cdot t = \nu t$. Using this V_{cell} Eq. (4.51) can be solved by partial integration

$$\int_L^x \mathrm{d}x = -\frac{M_{\mathrm{Me}}}{ze\rho_{\mathrm{m,Me}}} j_0 \left(\frac{A_{\mathrm{ac}}}{A_{\mathrm{fil}}}\right)^{\alpha} \int_0^t \exp\left(\alpha(1-\alpha)\frac{ze}{k_{\mathrm{B}}T}\nu t\right) \mathrm{d}t \tag{4.54}$$

where the lower boundaries are given by the initial state of the ECM cell $x(t=0) = L$. Integration yields

$$\Rightarrow x = L - \frac{M_{\mathrm{Me}}}{ze\rho_{\mathrm{m,Me}}} j_0 \left(\frac{A_{\mathrm{ac}}}{A_{\mathrm{fil}}}\right)^{\alpha} \frac{k_{\mathrm{B}}T}{\alpha(1-\alpha)ze\nu} \left(\exp\left(\alpha(1-\alpha)\frac{ze}{k_{\mathrm{B}}T}\nu t\right) - 1\right) \tag{4.55}$$

as an expression for the gap x. Eq. (4.55) gives the solution for x until the current compliance is reached. This upper boundary, which equals the definition of the SET voltage V_{SET} and the SET time t_{SET} (cf. Section 4.2.1), is determined as follows: when the current compliance is reached the gap x_{SET} is calculated by

$$x_{\mathrm{SET}} = L - \frac{M_{\mathrm{Me}}}{ze\rho_{\mathrm{m,Me}}} j_0 \left(\frac{A_{\mathrm{ac}}}{A_{\mathrm{fil}}}\right)^{\alpha} \frac{k_{\mathrm{B}}T}{\alpha(1-\alpha)ze\nu} \exp\left(\alpha(1-\alpha)\frac{ze}{k_{\mathrm{B}}T}V_{\mathrm{SET}}\right). \tag{4.56}$$

Since the current compliance I_{cc} is known, the SET voltage V_{SET} relates to x_{SET} according to Eq. (4.43) as

$$V_{\mathrm{SET}} = \frac{2h^2}{3Ce^2\sqrt{2m_{\mathrm{eff}}\Delta W_0}} x_{\mathrm{SET}} \exp\left(\frac{4\pi}{h}\sqrt{2m_{\mathrm{eff}}\Delta W_0}\, x_{\mathrm{SET}}\right) \frac{I_{\mathrm{cc}}}{A_{\mathrm{fil}}}. \tag{4.57}$$

Inserting Eq. (4.57) into Eq. (4.56) leads to an implicit equation, which is solved numerically for x_{SET}. This gives the upper boundary for the space integral in Eq. (4.54). The upper boundary for the time-integral t_{SET} is calculated using Eq. (4.57) and $V_{\mathrm{SET}} = \nu t_{\mathrm{SET}}$. During the current compliance the current is I_{cc}. Using Eq. (4.43) the ordinary differential equation (4.52) can be rewritten to

$$\begin{aligned}\frac{\mathrm{d}x}{\mathrm{d}t} = &- \frac{M_{\mathrm{Me}}}{ze\rho_{\mathrm{m,Me}}} j_0 \left(\frac{A_{\mathrm{ac}}}{A_{\mathrm{fil}}}\right)^{\alpha} \\ &\cdot \exp\left(\alpha(1-\alpha)\frac{ze}{k_{\mathrm{B}}T}\frac{2h^2}{3Ce^2\sqrt{2m_{\mathrm{eff}}\Delta W_0}} x \exp\left(\frac{4\pi}{h}\sqrt{2m_{\mathrm{eff}}\Delta W_0}\, x\right)\frac{I_{\mathrm{cc}}}{A_{\mathrm{fil}}}\right).\end{aligned} \tag{4.58}$$

Partial integration yields

$$\begin{aligned}\int_{x_{\mathrm{SET}}}^{x} \exp\left(-\alpha(1-\alpha)\frac{ze}{k_{\mathrm{B}}T}\frac{h^2}{e^2 2C\sqrt{2m_{\mathrm{eff}}\Delta W_0}} x \exp\left(\frac{4\pi}{h}\sqrt{2m_{\mathrm{eff}}\Delta W_0}\, x\right)\frac{I_{\mathrm{cc}}}{A_{\mathrm{fil}}}\right)\mathrm{d}x \\ = -\frac{M_{\mathrm{Me}}}{ze\rho_{\mathrm{m,Me}}} j_0 \left(\frac{A_{\mathrm{ac}}}{A_{\mathrm{fil}}}\right)^{\alpha} \int_{t_{\mathrm{SET}}}^{t} \mathrm{d}t.\end{aligned} \tag{4.59}$$

The space integral cannot be solved analytically. For this, the differential equation (4.52) is solved numerically using an advanced Euler method until the end of the SET sweep $t = T$ to obtain the $I - V$ characteristics. For the RESET process the integration has to be conducted separately for $T < t \leq T + t_{\mathrm{rise}}$ and $T + t_{\mathrm{rise}} < t \leq 2T$, respectively. In the former time period the cell voltage reads

$V_{\mathrm{cell}}(t) = -V_{\mathrm{p}}/t_{\mathrm{rise}} \cdot (t-T) = -\nu(t-T)$. Partial integration of Eq. (4.53) with the initial value $x(t=T) = x_{\mathrm{ON}}$ yields

$$\int_{x_{\mathrm{ON}}}^{x} \mathrm{d}x = \frac{M_{\mathrm{Me}}}{ze\rho_{\mathrm{m,Me}}} j_0 \left(\frac{A_{\mathrm{ac}}}{A_{\mathrm{fil}}}\right)^{1-\alpha} \int_{T}^{t} \exp\left(\alpha(1-\alpha)\frac{ze}{k_{\mathrm{B}}T}\nu(t-T)\right) \mathrm{d}t \tag{4.60}$$

and solving for x gives

$$x = x_{\mathrm{ON}} + \frac{M_{\mathrm{Me}}}{ze\rho_{\mathrm{m,Me}}} j_0 \left(\frac{A_{\mathrm{ac}}}{A_{\mathrm{fil}}}\right)^{1-\alpha} \frac{k_{\mathrm{B}}T}{\alpha(1-\alpha)ze\nu} \left[\exp\left(\alpha(1-\alpha)\frac{ze}{k_{\mathrm{B}}T}\nu\,(t-T)\right) - 1\right]. \tag{4.61}$$

For $T + t_{\mathrm{rise}} < t \leq 2T$ the cell voltage is $V_{\mathrm{cell}}(t) = -2V_{\mathrm{p}} + V_{\mathrm{p}}/t_{\mathrm{rise}} \cdot (t-T) = \nu(t-T-2t_{\mathrm{rise}})$. Partial integration and solving for x yields

$$\int_{x_{T+t_{\mathrm{rise}}}}^{x} \mathrm{d}x = \frac{M_{\mathrm{Me}}}{ze\rho_{\mathrm{m,Me}}} j_0 \left(\frac{A_{\mathrm{ac}}}{A_{\mathrm{fil}}}\right)^{1-\alpha} \int_{T+t_{\mathrm{rise}}}^{t} \exp\left(-\alpha(1-\alpha)\frac{ze}{k_{\mathrm{B}}T}\nu(t-T-2t_{\mathrm{rise}})\right) \mathrm{d}t \tag{4.62}$$

$$\begin{aligned} \Rightarrow x = {} & x_{T+t_{\mathrm{rise}}} - \frac{M_{\mathrm{Me}}}{ze\rho_{\mathrm{m,Me}}} j_0 \left(\frac{A_{\mathrm{ac}}}{A_{\mathrm{fil}}}\right)^{1-\alpha} \frac{k_{\mathrm{B}}T}{\alpha(1-\alpha)ze\nu} \\ & \left[\exp\left(\alpha(1-\alpha)\frac{ze}{k_{\mathrm{B}}T}\nu\,(2t_{\mathrm{rise}}+T-t)\right) - \exp\left(\alpha(1-\alpha)\frac{ze}{k_{\mathrm{B}}T}V_{\mathrm{p}}\right)\right], \end{aligned} \tag{4.63}$$

where the initial value $x(T+t_{\mathrm{rise}})$ is calculated according to Eq. (4.61). The complete $I-V$ characteristic of an ECM cell can now be calculated using the analytical equations (4.55), (4.61) and (4.63) and the numerical solution of Eq. (4.52).
As validation of this analytical model an $I-V$ characteristic is calculated with a peak voltage of $V_{\mathrm{p}} = 1\,\mathrm{V}$ and a rise time of $t_{\mathrm{rise}} = 1\,\mathrm{s}$ and compared to the numerical solution of the 1D compact model. As illustrated in **Figure 4.29** the analytical and numerical solutions coincide excellently. The difference in the $R-V$ characteristics in the very low voltage range is caused by the used simplification of the Butler-Volmer equation. Nevertheless, the SET voltage, RESET voltage, RESET current and SET and RESET time are in very good agreement. This demonstrates the validity of the derived analytical model.
To understand the empirical relation between LRS resistance and SET current the growth velocity $v = \mathrm{d}x/\mathrm{d}t$ under current control needs to be analyzed in more detail. In **Figure 4.30(a)** v is plotted against the gap x for different current compliance levels along with the corresponding voltage. Apparently, the $v-x$ as well as the $V-x$ characteristics for different current compliances are shifted parallel to each other by a constant gap. The growth velocity decreases several orders of magnitude,

when the gap is reduced by approximately 0.115 nm. This demonstrates that the LRS resistance can be precisely tuned by a set current compliance. Note, that a growth velocity of 0.2 nm/s is so low, that the growth cannot be considered as continuous. The growth has to be rather described by the deposition of individual atoms. In this regime the growth is statistical.

The calculated SET voltages and ON voltages are marked in Figure 4.30 for different sweep rates ν. For a particular sweep rate the SET voltages are virtually identical for different current compliances. In detail, it increases slightly with the set current compliance. It is for example $V_{\mathrm{SET}}(0.1\,\mathrm{nA}) = 0.7146\,\mathrm{V}$ and $V_{\mathrm{SET}}(100\,\mu\mathrm{A}) = 0.7165\,\mathrm{V}$. This is related to the onset of the current compliance during an $I - V$ sweep. A lower value of the current compliance is reached earlier and thus the SET voltage is lower than for a higher current compliance. In addition the current increase during the switching event is very steep and hence the SET voltages are virtually identical for different current compliances. At the onset of the current compliance also the growth velocities are thus virtually identical. As a consequence of the above considerations an almost identical transient behavior under current control with virtually identical ON voltages (see Figure 4.30) results. In contrast to the SET voltages the ON voltages are slightly decreasing for increasing current compliance, e.g. it is $V_{\mathrm{ON}}(0.1\,\mathrm{nA}) = 0.2078\,\mathrm{V}$ and $V_{\mathrm{ON}}(100\,\mu\mathrm{A}) = 0.2005\,\mathrm{V}$. For increasing sweep

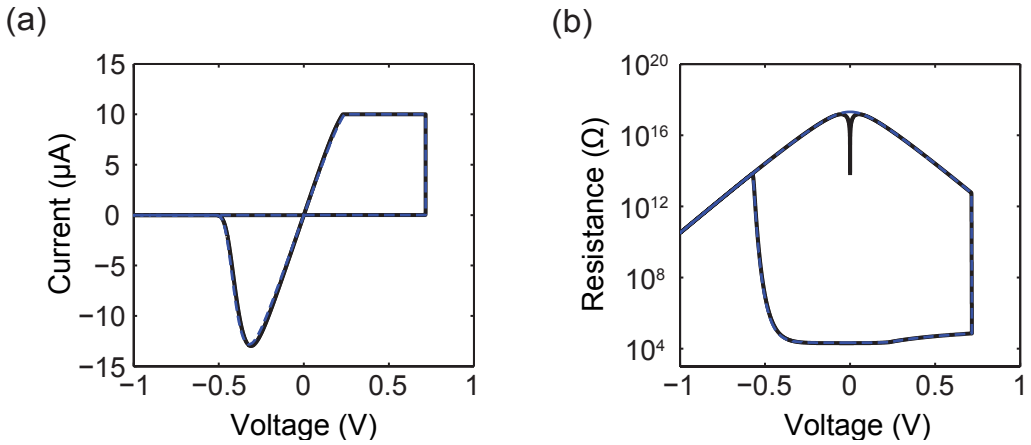

Figure 4.29: Calculated (a) $I - V$ and (b) $R - V$ characteristic for the analytical model (black) compared to the numerical solution of the 1D compact model (blue). The filament radius is $r_{\mathrm{fil}} = 2\,\mathrm{nm}$. The standard values according to Table 4.1 are used for the calculations.

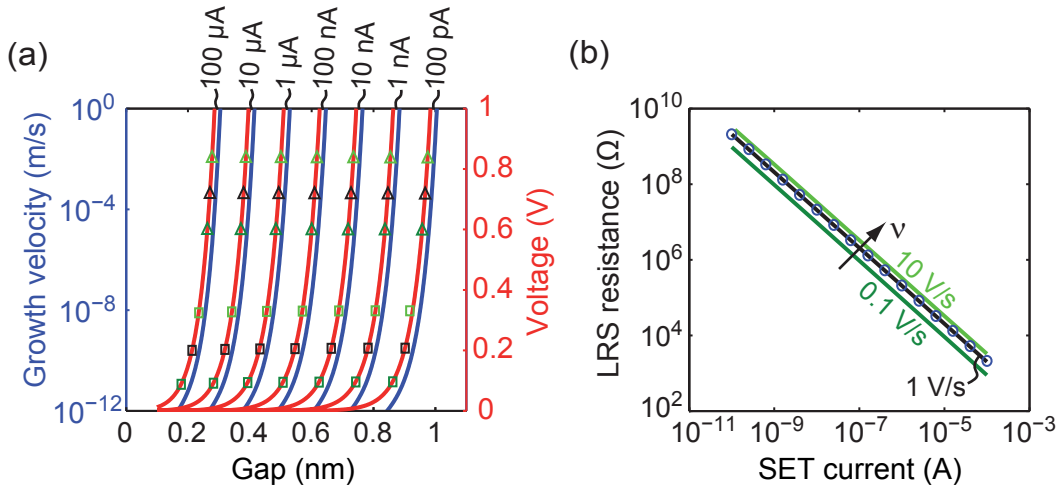

Figure 4.30: (a) Cell voltage (red) and growth velocity (black) vs. gap under current control for different current compliances. In addition, the SET voltages (triangles) and the ON voltages (squares) are shown for sweep rates $\nu = 0.1\,\mathrm{V/s}$ (dark green), $\nu = 1\,\mathrm{V/s}$ (black) and $\nu = 10\,\mathrm{V/s}$ (light green), respectively. (b) On resistance vs. SET current for different sweep rates using the same color code as in (a). The simulation results of the compact model for $\nu = 1\,\mathrm{V/s}$ are illustrated as blue circles. The calculations are performed using $r_{\mathrm{fil}} = 8\,\mathrm{nm}$ and the standard set of parameters.

rates the SET voltages as well as the ON voltages increase (see Figure 4.30(a)). This correlation can be explained mathematically by rewriting Eq. (4.56) to

$$V_{\mathrm{SET}} = \frac{k_{\mathrm{B}}T}{\alpha(1-\alpha)ze} \ln\left(\frac{(L - x_{\mathrm{SET}})z^2e^2\rho_{\mathrm{m,Me}}\alpha(1-\alpha)A_{\mathrm{fil}}^{\alpha}}{M_{\mathrm{Me}}j_0k_{\mathrm{B}}TA_{\mathrm{ac}}^{\alpha}}\nu\right). \tag{4.64}$$

Since $L \gg x_{\mathrm{SET}}$, $L - x_{\mathrm{SET}}$ is almost constant and for the SET voltage $V_{\mathrm{SET}} \propto \ln(\nu)$ holds. Interestingly, the voltage drop during current control $V_{\mathrm{SET}} - V_{\mathrm{ON}} \cong 0.5\,\mathrm{V}$ for all sweep rates. Thus, the set ON resistances depend on the sweep rate as illustrated in Figure 4.30(b). The voltage drop is related to the kinetics under current control and thus a system inherent quantity. The derivation of the exact relations is an important task for further research. Again the results of the analytical model are in very good agreement to the results of the 1D compact model.

To analyze the empirical relation between RESET current and SET current an expression for the RESET current has to be derived. Since the RESET current is defined as the minimum current during the RESET process, this means $\mathrm{d}I/\mathrm{d}t = 0$. As a simplification it is assumed that the RESET event occurs before the peak voltage is reached. Hence, the RESET current is given by Eq. (4.43), where x is given by Eq. (4.61). The current equation can be further simplified by setting the term $1/x$ to a constant value $1/x_{\mathrm{ON}}$. This approximation is valid since the

exponential dependence on x dominates. With these approximation the current now reads

$$\begin{aligned} I &= -\frac{3}{2}C\sqrt{2m_{\mathrm{eff}}\Delta W_0}\left(\frac{e}{h}\right)^2\frac{1}{x}\exp\left(-\frac{4\pi}{h}x\sqrt{2m_{\mathrm{eff}}\Delta W_0}\right)A_{\mathrm{fil}}\nu(t-T) \\ &\approx -\frac{3}{2}C\sqrt{2m_{\mathrm{eff}}\Delta W_0}\left(\frac{e}{h}\right)^2\frac{1}{x_{\mathrm{ON}}}\exp\left(-\frac{4\pi}{h}x\sqrt{2m_{\mathrm{eff}}\Delta W_0}\right)A_{\mathrm{fil}}\nu(t-T) \end{aligned} \tag{4.65}$$

Differentiating Eq. (4.65) with respect to t and setting to zero yields

$$\begin{aligned} \frac{\mathrm{d}I}{\mathrm{d}t} = 0 = &-\frac{3Ce^2\sqrt{2m_{\mathrm{eff}}\Delta W_0}A_{\mathrm{fil}}\nu}{2h^2x_{\mathrm{ON}}}\exp\left(-\frac{4\pi}{h}x\sqrt{2m_{\mathrm{eff}}\Delta W_0}\right) \\ &\left(1-(t_{\mathrm{min}}-T)\frac{4\pi}{h}\sqrt{2m_{\mathrm{eff}}\Delta W_0}\frac{M_{\mathrm{Me}}}{ze\rho_{\mathrm{m,Me}}}j_0\left(\frac{A_{\mathrm{ac}}}{A_{\mathrm{fil}}}\right)^{1-\alpha}\exp\left(\alpha(1-\alpha)\frac{ze}{k_{\mathrm{B}}T}\nu(t_{\mathrm{min}}-T)\right)\right). \end{aligned} \tag{4.66}$$

Eq. (4.66) can be solved for t_{min} with the help of the Lambert W function which gives

$$\Rightarrow t_{\mathrm{min}} = T + \frac{k_{\mathrm{B}}T}{ze\alpha(1-\alpha)\nu}W\left(\frac{\alpha(1-\alpha)\frac{ze}{k_{\mathrm{B}}T}\nu}{\frac{4\pi}{h}\sqrt{2m_{\mathrm{eff}}\Delta W_0}\frac{M_{\mathrm{Me}}}{ze\rho_{\mathrm{m,Me}}}j_0\left(\frac{A_{\mathrm{ac}}}{A_{\mathrm{fil}}}\right)^{1-\alpha}}\right). \tag{4.67}$$

The RESET voltage can now be calculated according to $V_{\mathrm{RESET}} = -\nu(t_{\mathrm{min}} - T)$ as

$$V_{\mathrm{RESET}} = -\frac{k_{\mathrm{B}}T}{ze\alpha(1-\alpha)}W\left(\frac{\alpha(1-\alpha)\frac{ze}{k_{\mathrm{B}}T}\nu}{\frac{4\pi}{h}\sqrt{2m_{\mathrm{eff}}\Delta W_0}\frac{M_{\mathrm{Me}}}{ze\rho_{\mathrm{m,Me}}}j_0\left(\frac{A_{\mathrm{ac}}}{A_{\mathrm{fil}}}\right)^{1-\alpha}}\right). \tag{4.68}$$

Note that the derived equation for the RESET voltage (Eq. (4.68)) is independent of the previous state of the ECM cell and depends only on the material parameters and the sweep rate. Thus under the same sweeping conditions the RESET voltage is constant for a particular ECM cell as stated above. By inserting Eq. (4.67) into Eq. (4.61)

$$\begin{aligned} x_{\mathrm{RESET}} = &x_{\mathrm{ON}} + \frac{M_{\mathrm{Me}}}{ze\rho_{\mathrm{m,Me}}}j_0\left(\frac{A_{\mathrm{ac}}}{A_{\mathrm{fil}}}\right)^{1-\alpha}\frac{k_{\mathrm{B}}T}{ze\alpha(1-\alpha)\nu} \\ &\left[\exp\left(W\left(\frac{\alpha(1-\alpha)\frac{ze}{k_{\mathrm{B}}T}\nu}{\frac{4\pi}{h}\sqrt{2m_{\mathrm{eff}}\Delta W_0}\frac{M_{\mathrm{Me}}}{ze\rho_{\mathrm{m,Me}}}j_0\left(\frac{A_{\mathrm{ac}}}{A_{\mathrm{fil}}}\right)^{1-\alpha}}\right)\right)-1\right] \end{aligned} \tag{4.69}$$

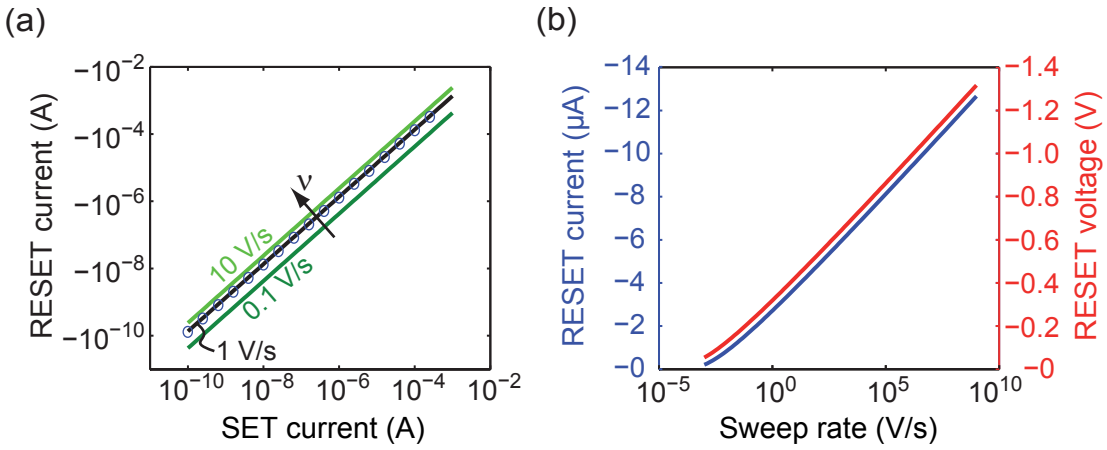

Figure 4.31: (a) Calculated RESET current vs. SET current for three different sweep rates $\nu = 0.1\,\mathrm{V/s}$ (dark green), $1\,\mathrm{V/s}$ (black) and $10\,\mathrm{V/s}$ (light green) as solid lines. The data of the 1D compact model is shown in blue circles. (b) RESET current and RESET voltage vs. sweep rate. The filament radius is $r_{\mathrm{fil}} = 8\,\mathrm{nm}$ in all calculations and the standard set of parameters is used.

results, where the -1 term will be neglected in the following. This equation can be rewritten using the identity $\exp(W(b)) = b/W(b)$ [73] so that

$$x_{\mathrm{RESET}} = x_{\mathrm{ON}} + \frac{h}{4\pi\sqrt{2m_{\mathrm{eff}}\Delta W_0}} W^{-1}\left(\frac{\alpha(1-\alpha)\frac{ze}{k_{\mathrm{B}}T}\nu}{\frac{4\pi}{h}\sqrt{2m_{\mathrm{eff}}\Delta W_0}\frac{M_{\mathrm{Me}}}{ze\rho_{\mathrm{m,Me}}} j_0 \left(\frac{A_{\mathrm{ac}}}{A_{\mathrm{fil}}}\right)^{1-\alpha}}\right). \quad (4.70)$$

The RESET current can now be calculated using Eq. (4.70), Eq. (4.65) and $G_{\mathrm{ON}} = I_{\mathrm{cc}}/V_{\mathrm{ON}}$ as

$$I_{\mathrm{RESET}} = \frac{V_{\mathrm{RESET}}}{V_{\mathrm{ON}}} \exp\left(-W^{-1}\left(\frac{\alpha(1-\alpha)\frac{ze}{k_{\mathrm{B}}T}\nu}{\frac{4\pi}{h}\sqrt{2m_{\mathrm{eff}}\Delta W_0}\frac{M_{\mathrm{Me}}}{ze\rho_{\mathrm{m,Me}}} j_0 \left(\frac{A_{\mathrm{ac}}}{A_{\mathrm{fil}}}\right)^{1-\alpha}}\right)\right) I_{\mathrm{cc}}. \quad (4.71)$$

Hence, the linear dependence of the RESET current on the current compliance is derived. In addition, the prefactor A can be extracted from Eq. (4.71). With this expression the dependencies of the RESET current on the material parameters can be evaluated. **Figure 4.31(a)** shows the calculated RESET currents vs. SET currents using Eq. (4.71) for three different sweep rates ν compared to the numerical simulation results from Section 4.2.3. The same set of parameters is used for both calculations. Apparently, the analytical and the numerical solutions coincide. Moreover, it is illustrated in Figure 4.31(b) that the RESET current and the RESET voltage increase when the sweep rate is faster.

In summary, the analytical model allows for simulating ECM cells within the given conditions. Although it was not possible to derive analytical expressions for the current control, the simplified differential equation in this regime can be solved without solving an implicit equation in each time step. Thus, it is still beneficial over the numerical model. In addition, the empirical relations between ON resistance/RESET current and SET current could be analyzed. Regarding the ON resistance the empirical relation could be demonstrated and explained by analyzing the growth velocity under current control. The derivation of the exact relation needs further research. The analytically derived equation for the RESET current shows the experimentally observed linear dependence on the SET current. Moreover, it enables to evaluate the influence of the material parameters on the RESET current.

4.3.2 Switching Kinetics

In Section 4.2.4 the dynamics of ECM cell have been simulated numerically and the influence of the material parameters on the switching kinetics were shown. Here, analytical expressions for the SET and RESET kinetics are derived and compared to the numerical data. As in Section 4.2.4 ideal voltages pulses are used as excitation.

SET Kinetics

The cell voltage during SET is given by $V_{\mathrm{cell}} = V_{\mathrm{p}}$, where V_{p} correspond to the SET voltage. For solving Eq. (4.51) the integration boundaries have to be defined. The lower boundary for integration is $x(t = 0) = L$. Since the voltage is constant during the SET process the gap x_{SET} corresponding to the preset I_{cc} can be simply calculated according to Eq. (4.43) as

$$x_{\mathrm{SET}} = \frac{h}{4\pi\sqrt{2m_{\mathrm{eff}}\Delta W_0}} W\left(C\frac{12\pi m_{\mathrm{eff}}\Delta W_0 e^2 A_{\mathrm{fil}} V_{\mathrm{SET}}}{h^3 I_{\mathrm{cc}}}\right). \tag{4.72}$$

The partial integration of Eq. (4.51) using the defined integration boundaries is straightforward. Solving for the SET time yields

$$t_{\mathrm{SET}} = \frac{L - x_{\mathrm{SET}}}{\frac{M_{\mathrm{Me}}}{ze\rho_{\mathrm{m,Me}}} j_0 \left(\frac{A_{\mathrm{ac}}}{A_{\mathrm{fil}}}\right)^{\alpha}} \exp\left(-\alpha(1-\alpha)\frac{ze}{k_{\mathrm{B}}T}V_{\mathrm{p}}\right). \tag{4.73}$$

Eq. (4.73) allows for analyzing the parameters controlling the SET time. **Figure 4.32** illustrates this dependence of the SET time on different parameters compared to the numerical simulation results of Section 4.2.4. Overall the analytical

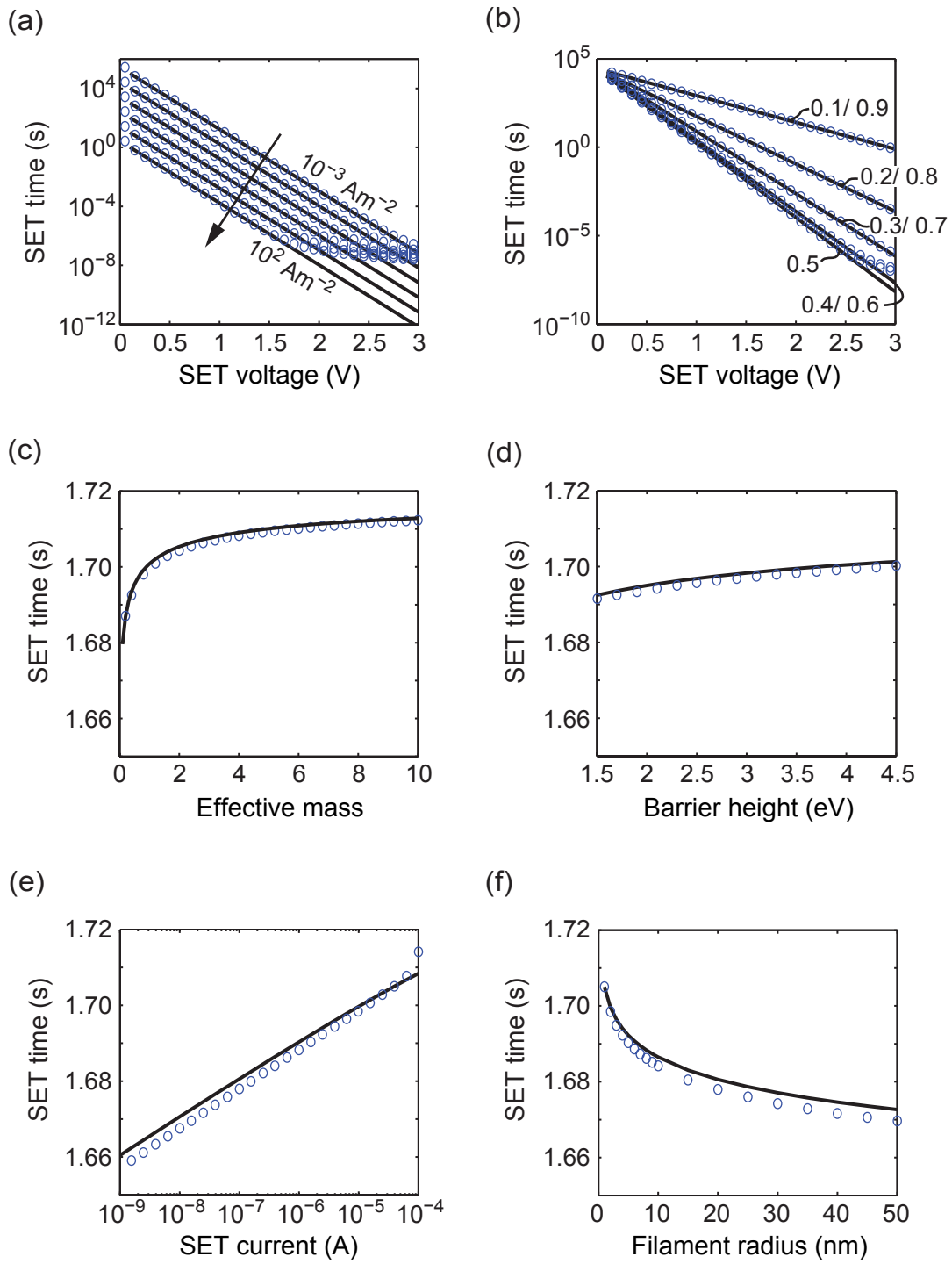

Figure 4.32: Calculated SET times vs. SET voltage for $z = 1$ while varying (a) the exchange current density and (b) the charge transfer coefficient. Calculated SET times vs. (c) the effective mass, (d) the effective barrier, (e) the SET current and (f) the filament radius using $z = 1$ and a pulse voltage of 1 V. As comparison the simulated data from Section 4.2.4 are shown in blue circles. The filament radius is $r_{\mathrm{fil}} = 2\,\mathrm{nm}$.

solutions are in very good agreement to the numerical ones. The SET time depends exponentially on the SET voltage. Here, $t_{\mathrm{SET}} \propto j_0^{-1}$ holds as visible in Figure 4.32(a). The analytical data, however, deviates from the numerical simulation results in the high voltage regime. In this regime the assumption of the analytical model does not hold anymore. As discussed in Section 4.2.4 the switching kinetics become drift limited in the high voltage regime. In the derivation of the analytical model, however, the drift limitation is neglected. This leads to the shown deviation. The slope in the semilogarithmic SET time vs. SET voltage plot corresponds to the term $b = -\alpha(1-\alpha)ze/kT$. Thus, the slope is doubled by changing the charge number from $z = 1$ to 2, which is consistent with the results in Section 4.2.4. The influence of the charge transfer coefficient α (see Figure 4.32(b)) can also be extracted from Eq. (4.73). Let first be $A_{\mathrm{fil}} = A_{\mathrm{ac}}$. Then the charge transfer coefficient influences only the slope b. Obviously, the maximum of b is obtained for $\alpha = 0.5$. Furthermore b is identical for $\alpha = 0.5 \pm X$. When $A_{\mathrm{fil}} \neq A_{\mathrm{ac}}$ this symmetry vanishes. In this case the SET time changes according to $(A_{\mathrm{ac}}/A_{\mathrm{fil}})^{\alpha}$, i.e. it increases for $A_{\mathrm{ac}} > A_{\mathrm{fil}}$. Again the deviation of the numerical simulation results to the analytic ones is correlated to the limits of the assumptions in the derivation of the analytical model.
According to Eq. (4.73) the effective mass m_{eff}, the barrier height ΔW_0 and the SET current I_{cc} only influence the SET time via the gap x_{SET}. This means, the smaller the gap to achieve the set current compliance the longer the SET time. In case of the effective mass $t_{\mathrm{SET}} \propto L - const \cdot W(m_{\mathrm{eff}})/\sqrt{m_{\mathrm{eff}}}$ holds, whereas the square root term dominates. Thus, the SET time decrease for decreasing effective mass as illustrated in Figure 4.32. The same relation applies for the barrier height according to Eq. (4.73). At first glance, this seems to contradict the calculations shown in Figures 4.32(c) and (d). The barrier height, however, is only changed less than one order of magnitude in the calculations in contrast to the effective mass, which is varied two orders of magnitude.
The dependence of the SET time with respect to the SET current is shown in Figure 4.32(e). The SET time increases with increasing SET current which correlates to the fact, that the tunneling current increases for decreasing gap size. Mathematically, this behavior is described by $t_{\mathrm{SET}} \propto L - const \cdot W(const/I_{\mathrm{cc}})$. The dependence of the SET time on the SET current is very week as it only changes 3 % while the SET current changes 5 orders of magnitude. The numerical data seems to increase stronger for SET currents close to 100 µA than the analytical data. For high currents the ionic voltage drop cannot be neglected anymore. Thus, the assumptions in the analytical model derivation are violated and the two models deviate.

In the discussion of the influence of the filament radius two cases need to be distinguished. First of all let $A_{\mathrm{fil}} = A_{\mathrm{ac}}$. In this case the filament radius only affects the SET time via x_{SET}. Then, $t_{\mathrm{SET}} \propto L - const \cdot W(A_{\mathrm{fil}})$ holds. The SET time thus decreases while increasing the filament radius (see Figure 4.32(f)). Is $A_{\mathrm{fil}} \neq A_{\mathrm{ac}}$ an additional proportionality factor appear and it is $t_{\mathrm{SET}} \propto A_{\mathrm{fil}}^{\alpha} \cdot (L - const \cdot W(A_{\mathrm{fil}}))$. As in the case of the effective mass and the barrier height the first term will be the dominating one.

RESET Kinetics

During RESET the cell voltage is given by $V_{\mathrm{cell}} = -V_{\mathrm{p}}$, where $-V_{\mathrm{p}}$ corresponds to the RESET voltage. The lower integration boundary is given by the preset ON state as

$$x_{\mathrm{ON}} = \frac{h}{4\pi\sqrt{2m_{\mathrm{eff}}\Delta W_0}} W\left(C\frac{12\pi m_{\mathrm{eff}}\Delta W_0 e^2 A_{\mathrm{fil}} V_{\mathrm{ON}}}{h^3 I_{\mathrm{cc}}}\right). \tag{4.74}$$

As an ideal voltage pulse is used as excitation, the minimum current during RESET is simply $V_{\mathrm{p}} \cdot R_{\mathrm{ON}}$. The RESET criterion as defined in Section 4.2.1 then reads $I_{\mathrm{RESET}} = 10^{-3} I_{\mathrm{cc}}$. Now the upper boundary can be deduced from as

$$x_{\mathrm{RESET}} = \frac{h}{4\pi\sqrt{2m_{\mathrm{eff}}\Delta W_0}} W\left(C\frac{12\pi m_{\mathrm{eff}}\Delta W_0 e^2 A_{\mathrm{fil}} 10^3 V_{\mathrm{ON}}}{h^3 I_{\mathrm{cc}}}\right). \tag{4.75}$$

By partial integration of Eq. (4.53) an expression for the SET time can be derived:

$$t_{\mathrm{RESET}} = \frac{x_{\mathrm{RESET}} - x_{\mathrm{ON}}}{\frac{M_{\mathrm{Me}}}{ze\rho_{\mathrm{m,Me}}} j_0 \left(\frac{A_{\mathrm{ac}}}{A_{\mathrm{fil}}}\right)^{1-\alpha}} \exp\left(\alpha(1-\alpha)\frac{ze}{k_{\mathrm{B}}T} V_{\mathrm{p}}\right). \tag{4.76}$$

Figure 4.33 shows the calculated RESET time depending on different parameters compared to the numerical simulation results of Section 4.2.4. Again, the results of the compact model and the analytical model are in very good agreement for all parameters. As the derived equation for the RESET is very similar to the one for the SET time, the same considerations regarding the dependence of t_{RESET} on j_0, α, V_{p} and z apply as for the SET time. Thus, for the analysis it is referred to the previous section. Concerning the charge transfer coefficient the case $A_{\mathrm{fil}} \neq A_{\mathrm{ac}}$ and $\alpha \neq 0.5$ is particularly interesting. Here, the RESET time changes according to $(A_{\mathrm{ac}}/A_{\mathrm{fil}})^{1-\alpha}$ and thus the exponent is different as for the SET time. This leads to the asymmetry of the $I - V$ characteristics described in Section 4.2.1.

In contrast to the SET process only a small change in the gap results in a RESET process, whereas for the SET switching the filament has to grow almost completely

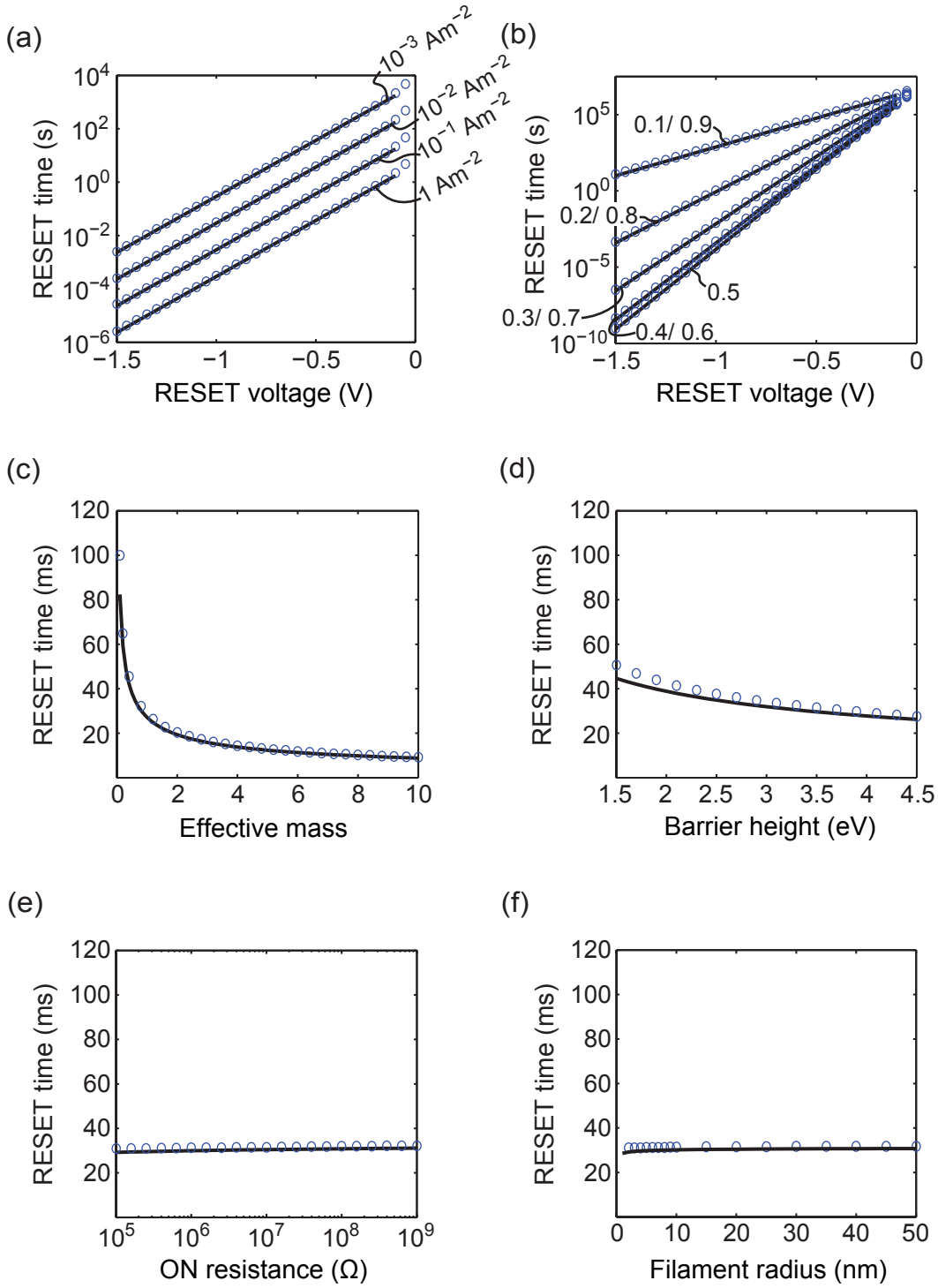

Figure 4.33: Calculated RESET times vs. RESET voltage for $z = 1$ while varying (a) the exchange current density and (b) the charge transfer coefficient. Calculated RESET times vs. (c) the effective mass, (d) the effective barrier, (e) the ON resistance and (f) the filament radius using $z = 1$ and a pulse voltage of $-1\,\mathrm{V}$. As comparison the simulated data from Section 4.2.4 are shown in blue circles. The filament radius is $r_{\mathrm{fil}} = 2\,\mathrm{nm}$.

through the insulating layer. The relative deviation is therefore comparably small for the SET process. Thus, the parameters controlling the gap have a stronger influence on the RESET time than on the SET time. According to Eq. (4.76) the relation between SET time and effective mass is approximately $t_{\mathrm{RESET}} \propto m_{\mathrm{eff}}^{-0.5}$. Thus, the RESET time decreases with increasing effective mass as illustrated in Figure 4.33(c), which is the reversed trend compared to the SET kinetics. The same relation holds for the dependence of the RESET time on the barrier according to Eq. (4.76). Note that in Figure 4.33(d) the barrier height is only changed less than one order of magnitude. Thus, the absolute change is less as in the effective barrier plot, where the effective barrier is varied two orders of magnitude. As shown in Figure 4.33(e) and (f) the RESET time is virtually independent on the ON resistance and the filament area. In case of the filament area, however, it is worth noting that $A_{\mathrm{fil}} = A_{\mathrm{ac}}$ holds in these calculations. If it is $A_{\mathrm{fil}} \neq A_{\mathrm{ac}}$, the RESET time would be proportional to $A_{\mathrm{fil}}^{1-\alpha}$.
Eq. (4.76) implies that the RESET time strongly depends on the RESET criterion. Using the factor 10^{-4} instead of 10^{-3} for the RESET criterion the RESET time would change from 29.1 ms to 39.2 ms at $V_{\mathrm{p}} = -1\,\mathrm{V}$, $z = 1$ and standard parameters apart from that. This is an important issue for comparing the RESET kinetics of different devices.

In summary, analytical expressions for the SET time and the RESET time are found in this section. With these expressions the influence of the switching kinetics could be analyzed in detail. The calculated SET and RESET times are in very good agreement to the numerical results. This proves the validity of the derived analytical expressions. The derived equations are very valuable for predicting the switching kinetics of different ECM cells.

4.4 FEM Model

In the previous sections a one-dimensional model was applied to describe the dynamic behavior of ECM cells. This approach is particularly suited to analyze the general device behavior and for the simulation of more complex networks of devices. In the latter case the computational cost of the simulation is one of the most important issues. The models are only simplifications of a more complex multidimensional case. To investigate the switching behavior in full detail it is necessary to develop a more realistic multidimensional model. Using this approach, phenomena such as polyfilamentary growth or the RESET mechanism in the variable width regime (cf. Section 4.1) can be investigated. In addition, scaling issues, the

influence of spacial inhomogeneities or the optimization of the cell design can be addressed.
Analytical solutions for multidimensional models only exist for some special cases. Therefore, numerical methods have to be applied. Here, the commercial software COMSOL is employed for the simulation (cf. Chapter 3).
To simulate an ECM cell an appropriate FEM model has to account for the electric properties and the growth and dissolution of the metallic filament. In detail, the electrical model has to include the electron transfer reaction at the boundary between electrode and solid electrolyte (cf. Section 2.5), the electron tunneling between the two electrodes (cf. Section 2.4) and the ionic and electronic currents in the electrodes and the insulating layer. To calculate the ionic and electronic currents the continuity equation is solved. Due to the electron transfer reaction at the boundary between ion conductor and electrode a potential drop occurs according to the Butler-Volmer equation (2.14). To account for this discontinuity two continuity equations are used:

$$-\nabla\sigma\nabla V_1 = 0 \tag{4.77}$$

$$-\nabla\sigma\nabla V_2 = 0. \tag{4.78}$$

Here, Eq. (4.77) is solved for in the inert electrode, the filament (Domain I) and the active electrode (Domain III), whereas Eq. (4.78) gives the solution in the insulating layer (Domain II, see **Figure 4.34** for an 2D exemplary case). These two equations are coupled to each other via the boundary conditions. This approach allows for modeling the electron transfer reaction as well as the tunneling current. Especially, the overpotentials η_{fil} and η_{ac} are calculated by the corresponding boundary potentials $V_{1,\mathrm{fil}}$, $V_{2,\mathrm{fil}}$ and $V_{1,\mathrm{ac}}$, $V_{2,\mathrm{ac}}$, respectively, as:

$$\eta_{\mathrm{ac}} = V_{1,\mathrm{ac}} - V_{2,\mathrm{ac}} - V_{\mathrm{ref}} \tag{4.79}$$

$$\eta_{\mathrm{fil}} = V_{1,\mathrm{fil}} - V_{2,\mathrm{fil}} - V_{\mathrm{ref}}. \tag{4.80}$$

The reference potential V_{ref} corresponds to the equilibrium potential for the electron transfer reaction. If the potential drop equals this potential the overpotential is zero. Thus, oxidation and reduction reaction are equally probable and the net current is zero (cf. Section 2.5). Here, it is $V_{\mathrm{ref}} = 0.2\,\mathrm{V}$. Using Eq. (4.79) and Eq. (4.80) the ionic currents at the boundaries can be calculated according to the Butler-Volmer equation (2.14).
The electronic tunneling current for a trapezoidal barrier according to Simmons

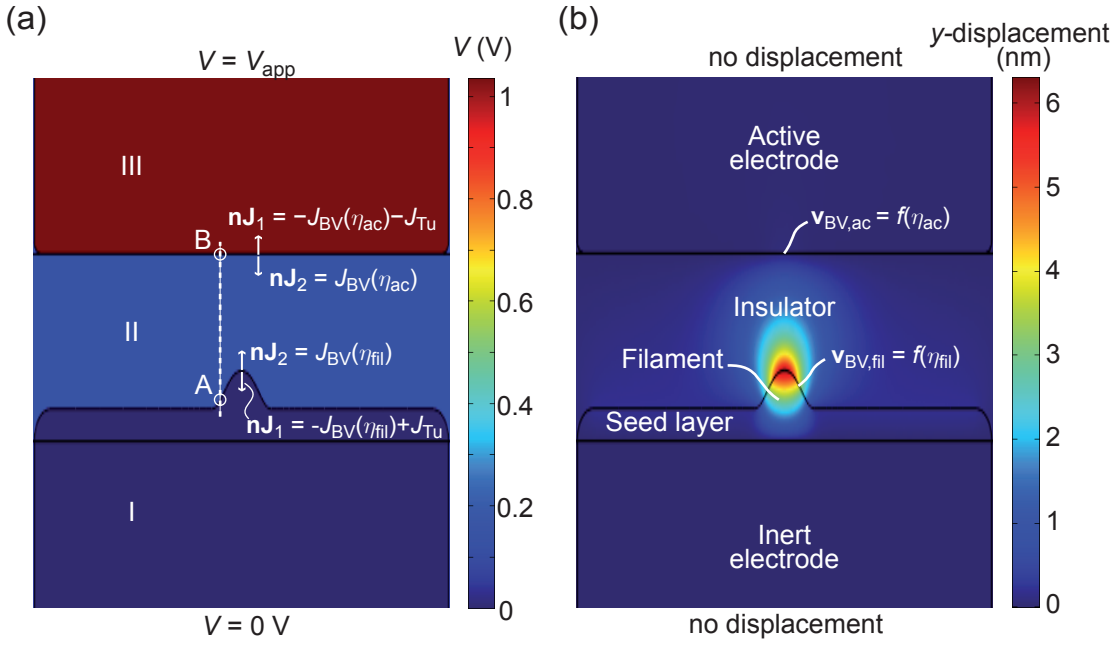

Figure 4.34: (a) Boundary conditions for solving Eq. (4.77) coupled with Eq. (4.78). The former equation is solved for in Domains I and III, whereas the latter is solved for in Domain II. The distance between the points A and B represent the definition of the tunneling gap. In color, a the potential distribution for $V_{\mathrm{app}} = 1\,\mathrm{V}$ is illustrated. Apparently, the voltage drops mainly at the interfaces between domain I + II and II + III, respectively. (b) Boundary conditions for solving for the mesh displacement. In color, the y-displacement is illustrated for the potential profile in (a).

(Eq. (2.12)) depends on the tunneling gap g and the voltage drop across the insulator V_{Tu}. To evaluate both quantities the tunneling current is calculated in vertical (y-) direction as illustrated in Figure 4.34, e.g. from point A to point B. The gap g is thus defined as the distance between the active electrode and the filament in vertical direction. The tunneling voltage V_{Tu} can then be expressed by the corresponding potentials $V_{1,\mathrm{fil}}$ and $V_{1,\mathrm{ac}}$ at the filament and the active electrode boundary as

$$V_{\mathrm{Tu}} = V_{1,\mathrm{ac}} - V_{1,\mathrm{fil}}. \tag{4.81}$$

By these definitions the gap and the tunneling voltage vary in horizontal direction and the tunneling current can be calculated using Eq. (2.12). In addition, it couples the solution of Eq. (4.77) in the Domains I and III. To set up the boundary conditions it has to be distinguished between voltage and current control of the modeled ECM cell. First, the boundary conditions during voltage control are discussed. In Figure 4.34 these boundary conditions are illustrated. The potential at the bottom electrode is set to zero, whereas $V = V_{\mathrm{app}}$ holds at the top electrode. At all

other outer boundaries the normal current density is zero. To model the electron transfer reaction and the electron tunneling at the active electrode/insulator and insulator/filament interface von Neumann boundary conditions are chosen. Since the electrons tunnel through the insulator, the tunneling current is implemented only at the filament (active electrode) side of the corresponding interface. Thus, Eq. (4.78) models only the ionic current. According to these considerations the boundary conditions at the active electrode/insulator interface then read

$$\mathbf{n}\mathbf{J}_1 = -J_{\mathrm{BV}}(\eta_{\mathrm{ac}}) - J_{\mathrm{Tu}}\left(g, V_{1,ac} - V_{1,fil}\right) \tag{4.82}$$

$$\mathbf{n}\mathbf{J}_2 = J_{\mathrm{BV}}(\eta_{\mathrm{ac}}) \tag{4.83}$$

and at the insulator/filament interface

$$\mathbf{n}\mathbf{J}_1 = -J_{\mathrm{BV}}(\eta_{\mathrm{fil}}) + J_{\mathrm{Tu}}\left(g, V_{1,\mathrm{ac}} - V_{1,\mathrm{fil}}\right) \tag{4.84}$$

$$\mathbf{n}\mathbf{J}_2 = J_{\mathrm{BV}}(\eta_{\mathrm{fil}}). \tag{4.85}$$

Note that the normal standard vector $\mathbf{n}$ always points into the interior of the solution domain. This has to be considered by choosing the correct sign in Eqs. (4.82) – (4.85). By using these boundary conditions the differential equations (4.77) and (4.78) are coupled with each other.

This implementation of the electron transfer reaction and the electronic tunneling current imposes constraints on the simulation of current control. Particularly, it is not possible to use von Neumann boundary conditions at the top electrode and the active electrode/insulator interface in a multidimensional simulation. In this case the potential $V_{1,\mathrm{ac}}$ becomes undefined and the tunneling and the Butler-Volmer current cannot be calculated. To model the current limitation a series resistor is included. This additional resistance is modeled as a distributed resistance boundary condition [75] at the top electrode as

$$\mathbf{n}\mathbf{J} = \sigma/d\left(V - V_{\mathrm{app}}\right). \tag{4.86}$$

Here, σ and d are the conductivity and the thickness of the series resistance. These quantities are chosen to match the desired value of the series resistance according to $R_{\mathrm{s}} = d/(\sigma A_{\mathrm{ac}})$, where A_{ac} is the area of the active electrode. In the special case of a 1D simulation it is possible to find suitable boundary conditions since the current

densities at all boundaries are equal. The overpotentials η_{ac} and η_{fil} can thus be calculated by solving the implicit equation system

$$J_{\mathrm{BV,ac}}\left(\eta_{\mathrm{ac}}\right) = -J_{\mathrm{BV,fil}}\left(\eta_{\mathrm{fil}}\right) \tag{4.87}$$

$$J_{\mathrm{cc}} = J_{\mathrm{Tu}}\left(\eta_{\mathrm{ac}} + J_{\mathrm{BV,ac}}\rho_{\mathrm{ion}}\frac{g}{A_{\mathrm{ion}}} - \eta_{\mathrm{fil}}\right) + J_{\mathrm{BV,ac}}\left(\eta_{\mathrm{ac}}\right) \tag{4.88}$$

where ρ_{ion} is the ionic resistivity and A_{ion} the effective area in the insulator. As boundary conditions the potentials can be defined by rewriting Eq. (4.79) and Eq. (4.80). This gives

$$V_{1,\mathrm{ac}} = \eta_{\mathrm{ac}} + V_{2,\mathrm{ac}} + V_{\mathrm{ref}} \tag{4.89}$$

as boundary condition for the potential $V_{1,\mathrm{ac}}$ at active electrode/insulator interface and

$$V_{1,\mathrm{fil}} = \eta_{\mathrm{fil}} + V_{2,\mathrm{fil}} + V_{\mathrm{ref}}, \tag{4.90}$$

$$V_{2,\mathrm{fil}} = V_{1,\mathrm{fil}} - V_{\mathrm{ref}} - \eta_{\mathrm{fil}} \tag{4.91}$$

as boundary conditions for the potentials at the insulator/filament interface. The potential $V_{2,\mathrm{ac}}$ at the active electode/insulator interface is defined as

$$V_{2,\mathrm{ac}} = V_{1,\mathrm{fil}} - V_{\mathrm{ref}} - \eta_{\mathrm{fil}} + J_{\mathrm{BV,ac}}\left(\eta_{\mathrm{ac}}\right) g/\sigma_{\mathrm{ins}}. \tag{4.92}$$

The potentials at these two interfaces are coupled with each other by the implicit equations (4.87) and (4.88). All other boundary conditions are equal to the voltage controlled case.

The growth and dissolution of the metallic filament within the insulating layer is modeled using an moving mesh approach. COMSOL uses an arbitrary Lagrangian-Eulerian (ALE) method to deform the mesh [75]. In the special case of the ECM cell, the filament boundary displacement is propagated throughout the ECM cell to obtain a smooth mesh deformation. This is done by solving appropriate partial differential equations for the mesh displacement. COMSOL employs two different coordinate systems to mathematically describe the moving mesh: a reference coordinate and a spatial coordinate system. In a 2D description the reference coordinates are denoted X and Y and the spatial coordinates x and y. The difference between these coordinate systems is illustrated in **Figure 4.35** by means of an undeformed and a deformed mesh. The formulation of the partial differential equation for the mesh movements depends on the used smoothing method. In COMSOL Laplace

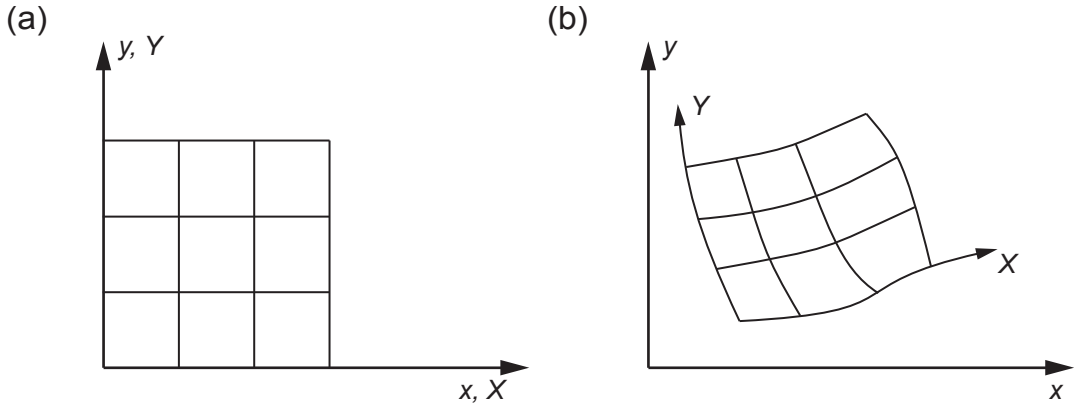

Figure 4.35: (a) An undeformed mesh. The spacial (x, y) and reference coordinates (X, Y) coincide. In contrast, the coordinates do not coincide in a deformed mesh (b)

smoothing or Winslow smoothing can be chosen. For the Laplace smoothing method the governing partial differential equation in x is

$$\frac{\partial^2 x}{\partial X^2}\frac{\partial x}{\partial t} + \frac{\partial^2 x}{\partial Y^2}\frac{\partial x}{\partial t} = 0. \tag{4.93}$$

A corresponding equation is used to solve for the y coordinate. To calculate the mesh deformation using Winslow smoothing, the software solves

$$\frac{\partial^2 X}{\partial x^2} + \frac{\partial^2 X}{\partial y^2} = 0 \tag{4.94}$$

and a corresponding equation for Y. Further details of the ALE method are described in the COMSOL manual [75].

Due to the large mesh deformation it is necessary to divide the filament boundary into several segments. In addition, a seed layer for the filamentary growth has to be introduced (see Figure 4.34). To prevent so called inverted mesh elements during the solution, a remeshing step is conducted if the mesh quality becomes too low. During the remeshing a new geometry is generated from the deformed mesh and subsequently a new mesh is created. The boundary conditions used for the ALE method are illustrated in Figure 4.34(b). The filament boundary displacement $\mathbf{v}$ is modeled consistently to Eq. (4.3) in Section 4.2 and Eq. (4.51) in Section 4.3 as

$$\mathbf{nv} = -\frac{M_{\mathrm{Me}}}{ze\rho_{\mathrm{m,Me}}} J_{\mathrm{BV,fil}}. \tag{4.95}$$

At the outer boundaries the displacement is set to zero. A special case is the active electrode/insulator interface. Here, different boundary conditions are used for 1D,

2D and axisymmetric 2D. In 1D the mesh velocity is set to zero, which is consistent to the 1D compact model in Section 4.2. For the 2D simulations such a constraint leads to numerical instabilities. Therefore, the mesh velocity is calculated similar to Eq. (4.95) using the corresponding Butler-Volmer current. It is, however, divided by 100. This is virtually identical to setting the velocity to zero but it is numerical stable. In fact, the active electrode should dissolve during switching. Due to the asymmetry of the filament area compared to the active electrode, however, this dissolution can be neglected. In addition, a correct model of the dissolution is only possible if complete 3D information is accessible. This is not the case for 1D and 2D simulations. In the axisymmetric 2D simulations (Section 4.4.3) a full 3D information is present and thus the dissolution of the active electrode is modeled according to

$$\mathbf{nv} = -\frac{M_{\mathrm{Me}}}{ze\rho_{\mathrm{m,Me}}} J_{\mathrm{BV,ac}}. \tag{4.96}$$

Apparently, the moving mesh simulation is coupled with the differential equations (4.77) and (4.78) by the Butler-Volmer currents. This FEM model is applied to a 1D case (Section 4.4.1) and compared to the results of the 1D compact model for verification. In Section 4.4.2 polyfilamentary growth is investigated using a 2D model. In these sections the ECM cell is modeled within the variable gap regime, in which the RESET can be simply obtained by reversing the polarity of the applied voltage. If a galvanic contact is present the RESET mechanism is somewhat more complex. To elucidate this process a 2D axisymmetric FEM model is applied and discussed in Section 4.4.2.

4.4.1 1D Simulation

To validate the derived FEM model it is applied to a 1D case and the simulation results are compared to data of the derived 1D compact model (cf. Section 4.2). The mesh deformation due to the filamentary growth is solved for using Laplace smoothing. Thus, the filamentary growth is described by Eq. (4.93) and Eq. (4.96) with the boundary conditions described above. Since the 1D case is considered the second term in Eq. (4.93) is zero. In addition, a remeshing step is not required. To solve for the electric potential the differential equations Eq. (4.77) and Eq. (4.78) are applied. As boundary conditions Eqs. (4.82) – (4.85) hold at the insulator/electrode interfaces during voltage control and Eqs. (4.89) – (4.91) apply during the current compliance. As soon as the set current compliance is reached the boundary conditions are changed from voltage control to current control. Details of the implementation are given in [76].

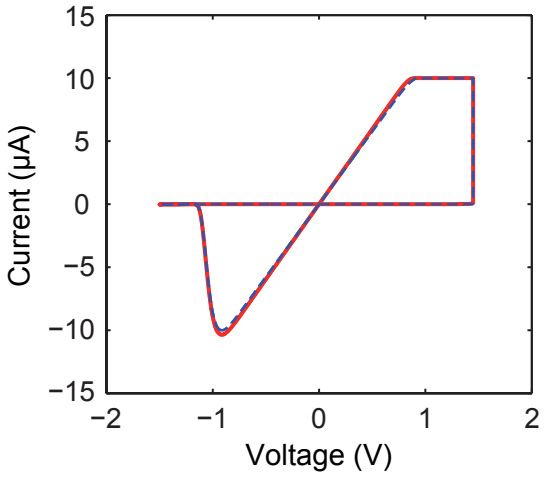

Figure 4.36: Simulated $I-V$ characteristic using the 1D FEM model (red solid line) and the 1D compact model (blue dashed line). As excitation a voltage sweep with a peak voltage $V_\mathrm{p} = 1.5\,\mathrm{V}$ and a rise time $t_\mathrm{rise} = 5\,\mu\mathrm{s}$ is used. The standard simulation parameters according to Table 4.1 apply.

Using the 1D FEM model the $I-V$ characteristic of an ECM cell is simulated. As excitation a triangular voltage sweep with peak voltage $V_\mathrm{p} = 1.5\,\mathrm{V}$ and a rise time of $5\,\mu\mathrm{s}$ is applied. The other simulation parameters are identical to those given in Table 4.1 apart from the filament and switching layer area, which are $A_\mathrm{fil} = A_\mathrm{is} = \pi r^2$ with a radius $r = 2.5\,\mathrm{nm}$. The reference potential is $V_\mathrm{ref} = 0.4\,\mathrm{V}$. A simulation on the basis of the 1D compact model using the same parameters is carried out for comparison. As illustrated in **Figure 4.36** the simulated $I-V$ characteristics based on the FEM and the compact model coincide. Thus, the FEM model is validated and can be used for further simulations.

4.4.2 2D Simulation of Polyfilamentary Growth

In Section 4.2.2 polyfilamentary growth was investigated using a compact model. In this model crosscurrents between adjacent growing filaments are neglected due to numerical simplicity. To address the issue of crosscurrents the derived FEM model is applied to a 2D geometry with two adjacent filaments. In addition, this 2D approach allows for analyzing potential filament broadening by electrodeposition on the sidewalls.

To model the mesh deformation due to the polyfilamentary growth the Winslow smoothing method is used Eq. (4.94). The movement of the filament/insulator boundary is modeled by Eq. (4.95). As discussed above the active electrode/insulator boundary moves for numerical stability according to Eq. (4.96), but the velocity

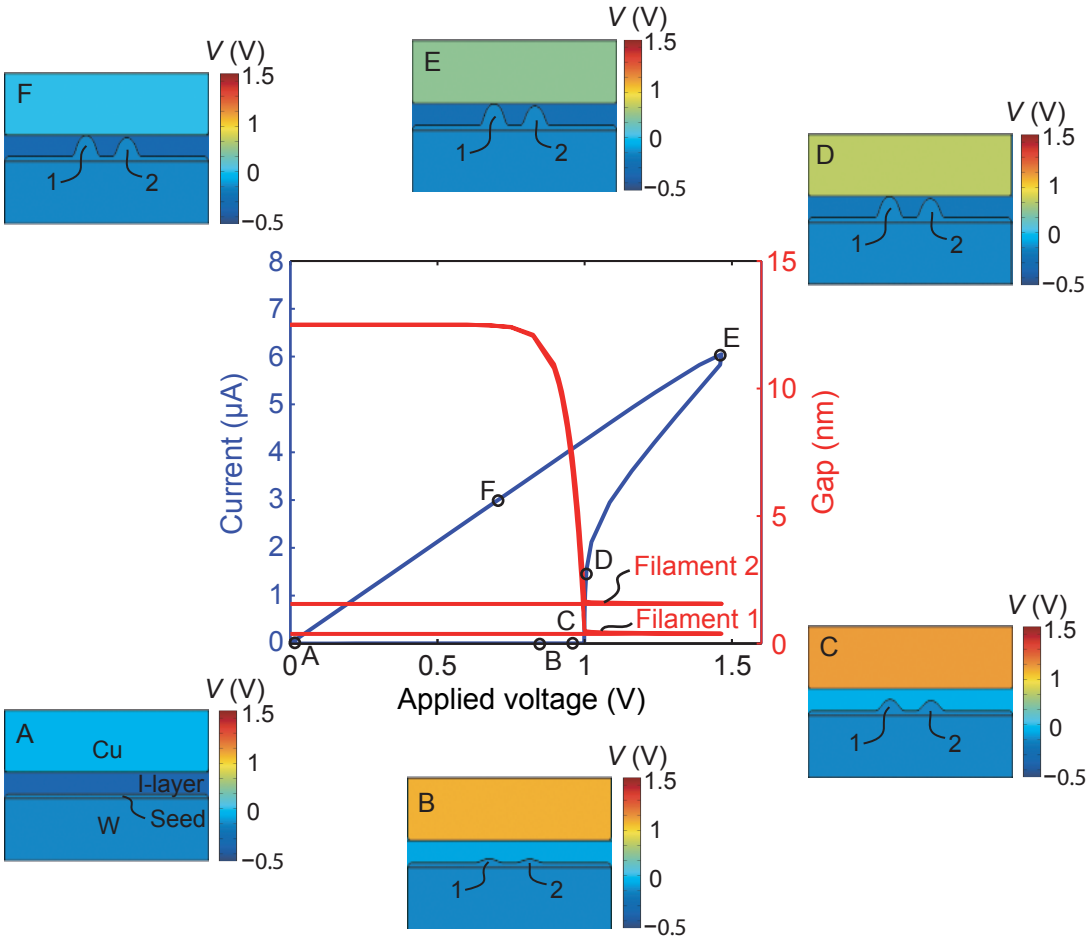

Figure 4.37: Simulated $I-V$ characteristic (blue solid lines) and tunneling gaps – voltage characteristics (red solid lines) for two parallel filaments within the insulating layer. As insets (A-F) the evolution of the filamentary growth is illustrated. As excitation a triangular voltage sweep with a peak voltage of $V_\mathrm{p} = 1.5\,\mathrm{V}$ and a rise time of $t_\mathrm{rise} = 4\,\mathrm{ms}$ is used. The potential distribution is shown in color. Since a distributed resistance boundary condition is used the maximum potential within the solution domains is less than the peak voltage.

is divided by 100. Due to the large deformation of the mesh in the simulation remeshing steps are introduced. The electric potential within the ECM cell is calculated again by solving Eq. (4.77) and Eq. (4.78). To account for a current limitation a series resistor of $R_\mathrm{s} = 150\,\mathrm{k\Omega}$ is used. Thus, the distributed resistance boundary condition Eq. (4.86) applies and hence Eqs. (4.82) – (4.85) are the appropriate boundary conditions for the electrode/insulator interfaces. Further details of the implementation of the 2D FEM model are given in [77].

The considered ECM cell geometry is shown in **Figure 4.37**. It consists of a 20 nm thick Cu top electrode, a 15 nm thick insulating layer including a 2 nm seed layer

and a 20 nm thick W bottom electrode. Two adjacent preferred ionic drift paths are assumed within the insulating layer. These are modeled by a space dependent concentration profile. Both paths are 10 nm wide but differ in their Cu concentrations. In the second path $c_2 = 0.9\,c_1$ applies. Thus, the ionic conductivity and the exchange current density are determined by $j_{0,2} = 0.9\,j_{0,1}$ and $\sigma_{\mathrm{ion},1} = 0.9\,\sigma_{\mathrm{ion},1}$, respectively. Here, it is $j_{0,1} = 1 \cdot 10^{-2}\,\mathrm{A/m^2}$ and $\sigma_{\mathrm{ion},1} = 1 \cdot 10^{2}\,\mathrm{S/m}$. Below the two drift paths two copper seeds are assumed within the seed layer. Mathematically, these seeds are modeled with a space dependent conductivity, where the seeds have the electric conductivity of Cu, whereas the remaining part of the seed layer has the conductivity of W. The W and Cu electric conductivity values are $\sigma_{\mathrm{W}} = 1.8 \cdot 10^{7}\,\mathrm{S/m}$ and $\sigma_{\mathrm{Cu}} = 5.8 \cdot 10^{7}\,\mathrm{S/m}$, respectively. Further simulation parameters are the barrier height $\Delta W_0 = 3.5\,\mathrm{eV}$ and the reference potential $V_{\mathrm{ref}} = 0.37\,\mathrm{V}$. Apart from these values the standard simulation parameters according to Table 4.1 are used.
To simulate the SET characteristic of the ECM cell a triangular voltage sweep with a peak voltage of $V_{\mathrm{p}} = 1.5\,\mathrm{V}$ and a rise time of $t_{\mathrm{rise}} = 4\,\mathrm{ms}$ is used as excitation. The resulting $I - V$ characteristic is shown in Figure 4.37. It exhibits the characteristic shape of a current limitation by a series resistance. After a sharp switching event at about 1 V the current approaches a slope that is determined by $R = R_{\mathrm{s}} + R_{\mathrm{LRS}}$. The insets illustrate the evolution of the filamentary growth during SET. Before the switching event both filaments grow, though filament 1 grows faster than filament 2 as expected (A-D). After the switching event the growth of both virtually stops (E and F). The suppression of further growth within the current limitation is also proven by the plotted gap-voltage characteristics. Furthermore, the simulation results show that the filaments grow only in vertical direction. This means that cross currents in the configuration of the ECM cell with adjacent preferred drift paths can be neglected. Thus, the assumptions of the polyfilamentary compact model in Section 4.2.2 are valid in this case and the results are consistent. Regarding the shape of the simulated filaments, a broadening of the filament tip is not observed after the onset of the current limitation. The maxima of the growth velocity are located at the tips of the filaments during the simulation. In a real device, however, statistical events have to be taken into account which might also lead to a deposition at a less probable site.

4.4.3 2D Axisymmetric Simulation of Nonpolar Switching

In the previous sections ECM switching in the tunneling gap regime has been considered. In this regime the RESET of the cell can be understood as the reversal of the applied voltage since the MIM structure is maintained during switching. If

a galvanic contact is achieved during SET switching, the MIM structure is lost and the RESET mechanism is more complex. A dissolution of the filament for example will occur at the lateral areas of the filament. Thus, a simple 1D approach is not applicable anymore. Here, a 2D axisymmetric geometry is considered, which comprises a full 3D information. Due to the galvanic contact the LRS resistance is very low and a high current will flow through the small filament. Thus, a temperature increase is expected to occur within the filament due to Joule heating. Consequently, also heat generation and transfer have to be considered in the model. Based on these considerations the following equation system is set up. The continuity equations (4.77) and (4.78) are solved for in the metallic regions (filament and electrodes) and in the insulator, respectively. Laplace smoothing (Eq. (4.93)) is used to account for the mesh deformation. To model the Joule heating the heat transfer equation

$$\rho_{\mathrm{m}} C_{\mathrm{P}} \frac{\partial T}{\partial t} - \nabla k \nabla T = \frac{J^2}{\sigma} \tag{4.97}$$

is applied. Here, C_{p} is the heat capacity, k the thermal conductivity, ρ_{m} the mass density and σ the electronic conductivity. The right hand side of Eq. (4.97) corresponds to the local heat generated by the current density J. This set of equations is complemented by appropriate boundary conditions (see **Figure 4.38**). The RESET operation is typically voltage controlled and hence Eqs. (4.83) – (4.85) apply as boundary conditions at the metal/insulator interfaces. The tunneling current, however, is zero, since the filament short-circuits both electrodes. The boundary conditions for solving the heat transfer equation Eq. (4.97) are constant temperature $T = 300\,\mathrm{K}$ at the outer boundaries and thermal insulation at the symmetry axis. The growth and dissolution of the filament and the active electrode are modeled by Eq. (4.95) and Eq. (4.96), respectively. Due to the strong lateral deformation of the filament, the filament insulator boundary is split in several smaller boundaries. In addition, remeshing is required to avoid inverted mesh elements. Further details of the implementation of the model are given in [78].

The highest temperature increase is expected to occur in the filament. Thus, the temperature dependence of the filament material properties has to be considered. Since the diameter of the filament is typically smaller than the mean free path of electrons, the electronic conductivity deviates from its bulk value according to the Fuchs-Sondheimer theory. This is particularly important in the considered case as the dissolution is expected to happen in radial direction. The filament resistance is

therefore also shape-dependent, i. e. r-dependent. The electronic conductivity now reads

$$\sigma_{\mathrm{fil}}(T) = \frac{\sigma_{\mathrm{fil}}(300\,\mathrm{K})}{\nu_{\mathrm{FS}}\,(r)\,(1+\alpha_{\mathrm{el}}(T-300\,\mathrm{K})+\beta_{\mathrm{el}}(T-300\,\mathrm{K})^2)}. \tag{4.98}$$

The first and second order temperature coefficients are $\alpha_{\mathrm{el}} = 3.9 \cdot 10^{-3}\,\mathrm{K}^{-1}$ [79] and $\beta_{\mathrm{el}} = 4 \cdot 10^{-7}\,\mathrm{K}^{-2}$ [79]. The factor $\nu_{\mathrm{FS}}\,(r)$ adjusts the electronic conductivity according to Sondheimer (see Table 2 in [18]) for the surface reflectivity $p = 0.5$. Regarding the thermal conductivity

$$k_{\mathrm{fil}}(T) = \frac{k(300\,\mathrm{K})}{1+\alpha_{\mathrm{th}}(T-300\,\mathrm{K})} \tag{4.99}$$

holds with the first order temperature coefficient $\alpha_{\mathrm{th}} = 2.03 \cdot 10^{-4}\,\mathrm{K}^{-1}$ [79]. The dissolution of the filament described by the Butler-Volmer equation (4.95) is also

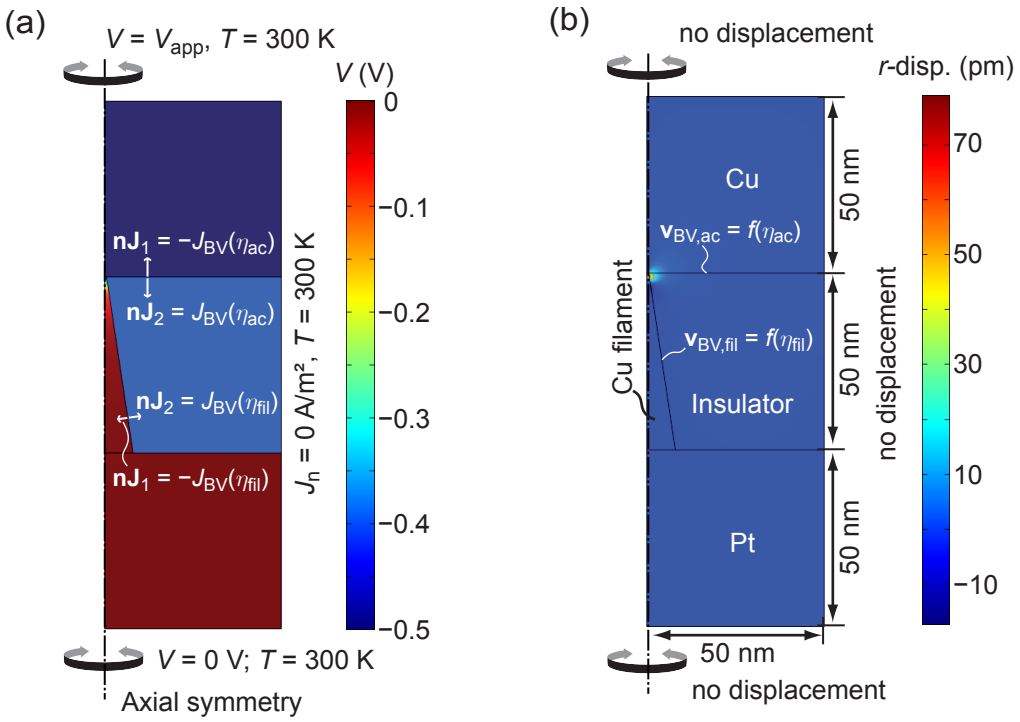

Figure 4.38: (a) Boundary conditions for solving Eq. (4.77) coupled with Eq. (4.78) and Eq. (4.97) in axial symmetry. Eq. (4.77) is solved for in the electrodes and the filament, whereas Eq. (4.78) is solved for in the insulator. In color, a typical potential distribution is illustrated for $V_{\mathrm{app}} = -0.5\,\mathrm{V}$. (b) Boundary conditions for solving for the mesh displacement. In color, the r-displacement is illustrated for the potential profile in (a). The major displacement occurs at the tip of the Cu filament close to the Cu electrode.

Table 4.2: Simulation parameters for $T = 300\,\mathrm{K}$

Symbol	σ (S/m)	k_{th} (W/mK)	C_{p} (J/kg K)	ρ_{m} (kg/m^3)
Pt (TE)	$9.3 \cdot 10^6$ [79]	71.6 [79]	133 [79]	21500 [79]
Cu (Filament,BE)	$5.8 \cdot 10^7$ [79]	401 [79]	384 [79]	8960 [79]
SiO_2 (Insulator)	287 (Ionic)	1.15 [80]	745 [79]	2196 [79]

affected by a temperature increase. As discussed in Section 2.5 the exchange current density is strongly temperature dependent according to

$$j_0(T) = j_0(T = 300\,\mathrm{K}) \cdot \exp\left(-\frac{\Delta W_{\mathrm{a}}}{k}\left(\frac{1}{T} - \frac{1}{300\,\mathrm{K}}\right)\right). \tag{4.100}$$

Here, an activation energy of $\Delta W_{\mathrm{a}} = 1\,\mathrm{eV}$ is assumed. Further material parameters are displayed in **Table 4.2**, whereas the standard parameters according to Table 4.1 apply for the remaining parameters.

To simulate the RESET operation a negative sweep with a sweep rate of $-1\,\mathrm{V}/\mu\mathrm{s}$ is used as excitation. The simulation stops, when the minimum radius along the vertical z-axis is lower than the radius of a copper atom $r_{\mathrm{Cu}} = 1.42\,\text{Å}$. Lower values of the radius might lead to inverted mesh elements and numerical instabilities. The ECM cell is then considered to be reset successfully. Initially, the filament has a conical shape and the LRS cell resistance is $500\,\Omega$. The simulated $I-V$ characteristic is displayed in **Figure 4.39** along with the time evolution of the filament dissolution. Three different regimes can be distinguished. For $0\,\mathrm{V} > V > -0.5\,\mathrm{V}$ the resistance increases slightly with increasing voltage amplitude. A sharp decrease in resistance follows and finally the resistance increases again abruptly. These observations can be attributed to a combination of geometrical and temperature related effects. First, the shape of the filament remains unchanged (A), whereas the current is high enough to cause Joule heating. Thus, the resistance increases due to the temperature dependent electric conductivity of the filament (cf. Eq. (4.98)). At approximately $-0.5\,\mathrm{V}$ the filament dissolution sets in (B). The replating of the Cu, however, does not occur at the Cu electrode as expected from the potential drop. Apparently, a redeposition takes place at the filament right above the location of dissolution (C and D). This surprising phenomenon is related to the temperature dependence of the Butler-Volmer current and in particular the exchange current density. When the temperature increases, the exchange current density increases exponentially. Thus, the Butler-Volmer current density will be highest at the hottest spot along the metal/insulator interface. In addition, the potential drop

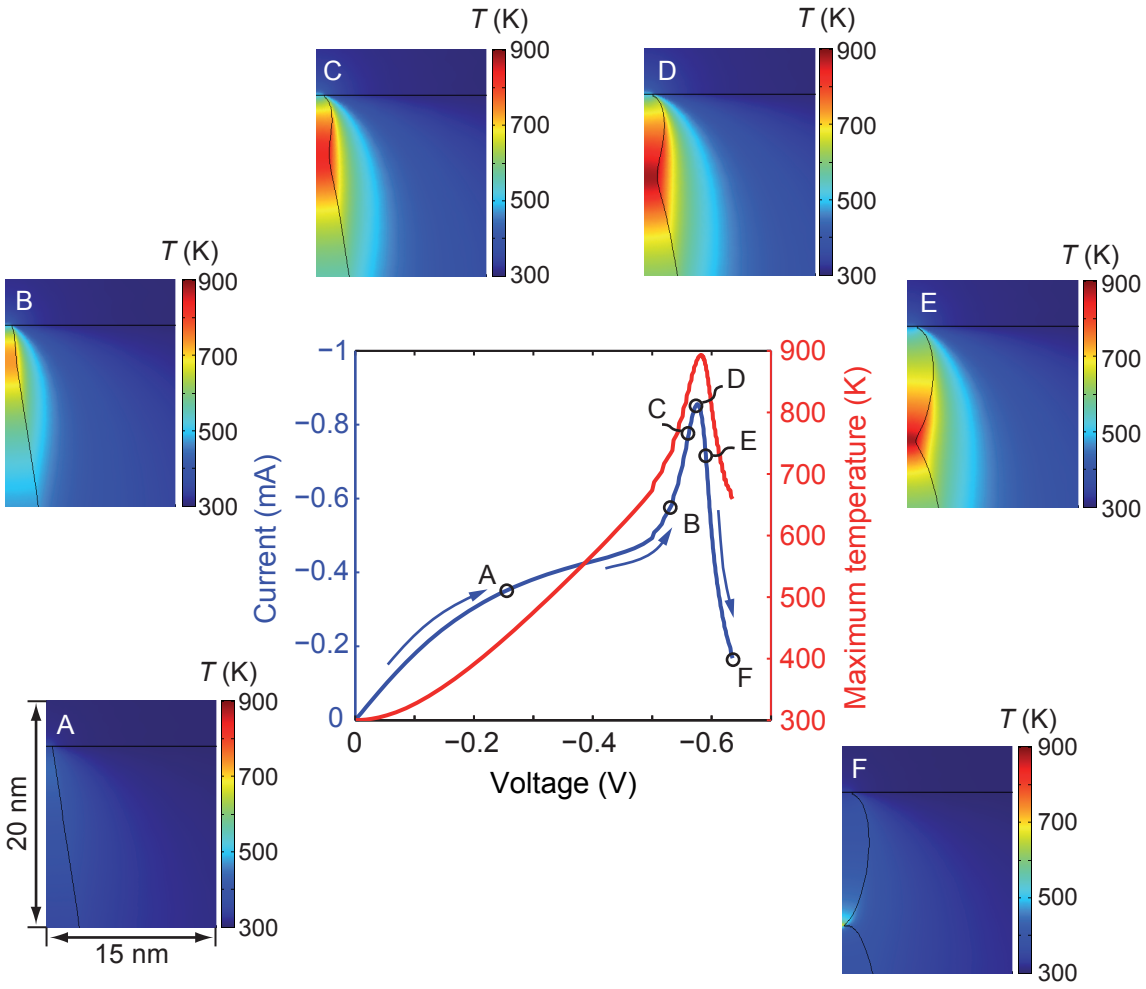

Figure 4.39: Simulated $I - V$ characteristic shown as solid blue line. A voltage sweep with a sweep rate of $\nu = -1\,\mathrm{V}/\mu\mathrm{s}$ is used as excitation. A negative voltage is applied to the top electrode. The transient maximum temperature within the Cu filament is displayed as red solid line. The insets (A-F) illustrate the time evolution of the filament self-dissolution at tip of the filament close to the Cu electrode (cf. Figure 4.38). Cu is redeposited above the evolving constriction, so that the current first increases (B-D) and then drops due to the filament rupture (E and F). The temperature distribution is illustrated in color.

is highest at the constriction of the filament, which will also be the location with the most Joule heating. This combination results in electrochemical dissolution and succeeding redeposition along the the filament close to the hottest spot. In the beginning of this electrochemical process the dissolution takes place at a thicker part of the filament, whereas the Cu is redeposited at a thinner part. Hence, the minimum radius along the filament increases. As a result the local electric conductivity changes according to Fuchs-Sondheimer theory and the cell resistance drops. At the maximum absolute current value (D) the minimum radius along the

filament reaches its maximum and afterwards decreases again (E). Now the location of dissolution becomes the thinnest part of the filament. As a consequence the resistance increases and hence the absolute current value drops. This leads to less Joule heating and the temperature decreases. Finally, the constriction becomes smaller than the atomic radius (F) and the simulation stops. At this point almost the complete voltage drops across the constriction. As soon as the gap opens, an MIM structure is reestablished and a further dissolution occurs as described in the previous sections. Note that the constriction moves slightly downwards during RESET, but it is still located close to the top Cu electrode.

Due to the self-dissolution of the filament, this means dissolution and redeposition take place at the filament, also a dissolution with a positive voltage seems to be conceivable. Thus, the RESET behavior is simulated using a voltage sweep with a sweep rate of $1\,\mathrm{V/\mu s}$. The initial conditions are the same as in the previous simulation. The corresponding simulation results are shown in **Figure 4.40**. The time evolution proofs that a self-dissolution of the filament occurs also for a positive polarity. Again, both processes occur close to the hottest spot in the filament. Thereby, the locations of dissolution and redeposition are inverted compared to the previous simulation in agreement to the applied polarity. The filament dissolutes at its thinnest part and hence the minimum radius only decreases during RESET. As a consequence a decrease in resistance as in the previous simulation is not observed in the $I-V$ characteristics. Here, only two regimes can be distinguished. First, the shape of the filament remains intact and the cell resistance increases due to the temperature increase (A and B). When $V > 0.5\,\mathrm{V}$ the self-dissolution sets in and the resistance increases further and the temperature decreases (C-E). Finally, the constriction close to the Cu electrode becomes smaller than the Cu atomic radius and the filament is ruptured (F). An MIM structure results with the insulating gap close to the Cu electrode. The applied voltage polarity, however, should result in a SET process. Whether the RESET is stable or not, depends therefore on the value of the applied maximum voltage V_{app} with respect to the SET/RESET voltage in the considered time domain. Thereby, three different cases can be identified. Firstly, the RESET is unstable if $V_{\mathrm{RESET}} > V_{\mathrm{SET}}$ and oscillations between a LRS and a HRS resistance might appear. In addition, a strengthening of the filament might occur that could prevent a RESET. Is $V_{\mathrm{RESET}} < V_{\mathrm{SET}} < V_{\mathrm{app}}$, the filament ruptures and at higher voltages a SET process occurs. This might lead to oscillations and the RESET is not stable. Only if $V_{\mathrm{RESET}} < V_{\mathrm{app}} < V_{\mathrm{SET}}$ applies, the RESET is successful. Using this type of unipolar operation, however, the ECM cell is left in a semi-SET state after a RESET. This might lead to instabilities in the following

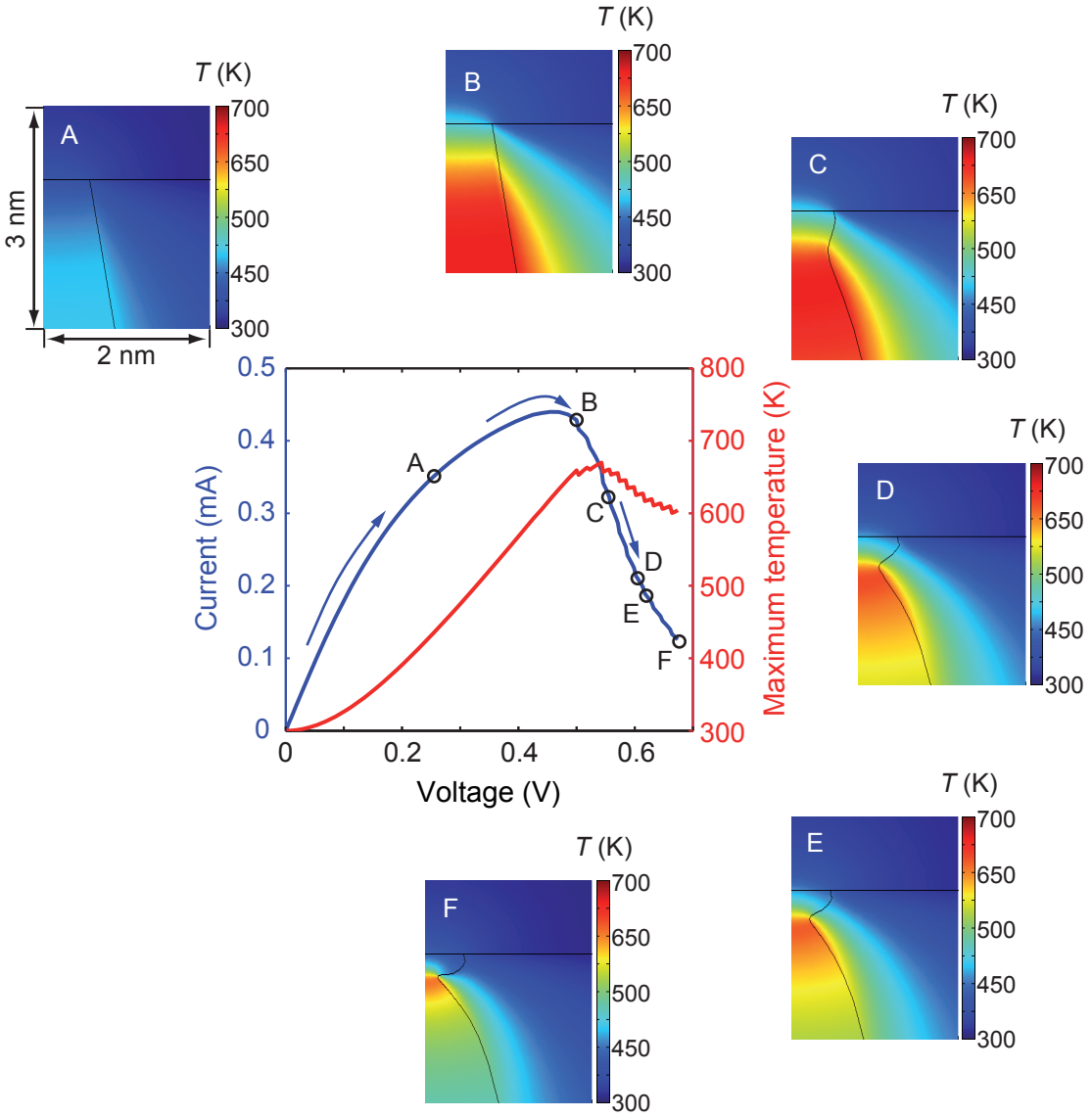

Figure 4.40: Simulated $I - V$ characteristic shown as solid blue line. A voltage sweep with a sweep rate of $\nu = 1\,\mathrm{V}/\mu\mathrm{s}$ is used as excitation. A positive voltage is applied to the top electrode. The transient maximum temperature within the Cu filament is displayed as red solid line. The insets (A-F) illustrate the time evolution of the filament self-dissolution at tip of the filament close to the Cu electrode (cf. Figure 4.38). As soon as the temperature is high enough (B) the dissolution sets in. Cu is redeposited below the evolving constriction (C-F), so that the resistance drops continuously. The temperature distribution is illustrated in color.

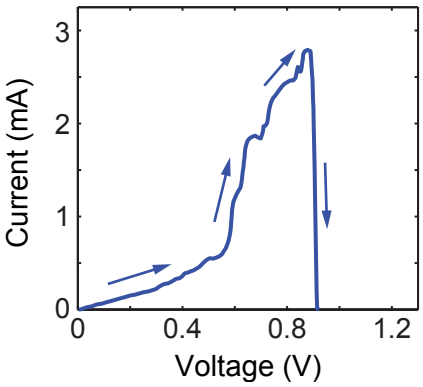

Figure 4.41: Experimental $I-V$ characteristic of unipolar switching in a 12 nm thick Cu/Cu-doped SiO_2/W device. Redrawn from [63].

switching cycles. In a bipolar operation, i.e. a RESET with negative polarity, the ECM cell is reset to a defined value, which should improve the endurance of the cell. This conclusion is consistent to the experimental observation in Cu/Ta_2O_5/Pt cells [54].

As an important implication it results that the shape of the $I-V$ curve depends strongly on the initial shape of the filament. The location of filament rupture is defined by the hottest spot within the filament. Here, a conically shaped filament is assumed and accordingly the hot spot is close to the Cu electrode. By application of a negative voltage bias the dissolution takes place at a thicker part of the filament and the redeposition at a thinner part. As a result a resistance decrease is observed prior to RESET (cf. Figure 4.39). On the other hand the locations of dissolution and redeposition are inverted by application of a positive bias causing a resistance increase during the whole RESET process. To summarize, the occurrence of a resistance decrease prior to RESET is related to the initial shape of the filament. This itself, however, depends strongly on the micro structure of the insulating layer. Thus, also constrictions at different locations of the filament are possible. A resistance decrease prior to RESET is then also conceivable for unipolar operation (positive bias). In fact, such a behavior has been observed in Cu doped SiO_2 based ECM cells (see **Figure 4.41**) by applying a positive voltage to the top electrode. Certainly, a strengthening of the filament and a succeeding RESET could also explain the resistance decrease.

A key parameter of the self-dissolution is the temperature dependent exchange current density and its activation energy. With increasing temperature the exchange current density and thus the Butler-Volmer current is locally enhanced. Dissolution and redeposition will then both take place at the filament close to the hottest spot.

If the temperature dependence of the Butler-Volmer current is less pronounced, the potential gradient becomes more dominating. In that case the locations of dissolution and redeposition get locally separated. The former might occur at the filament and the latter at the Cu electrode and vice versa depending on the applied voltage polarity. The cell operation is then bipolar.
To conclude, the RESET process for a filament bridging the whole insulator can be attributed to an interplay of temperature increase and electrochemical dissolution and redeposition. Due to the temperature increase a self-dissolution of the filament sets in. Thus, a successful RESET can be obtained by either voltage polarity. The operation can be called nonpolar. In fact, this nonpolar RESET behavior at low LRS values has been reported by several groups [54, 62, 63].

4.5 Summary

In this chapter a dynamic simulation model for ECM cells was presented, whose simulation results are in very good agreement to the experimental data. It is based on the electrochemical dissolution and growth of a metallic filament within the insulating matrix. The model accounts for the basic $I - V$ characteristics, the nonlinear switching kinetics as well as the multilevel switching capabilities of ECM cells. This model was implemented as a 1D physical compact model (Section 4.2), an analytical model (Section 4.3) and as a multidimensional FEM model (Section 4.4).
The nonlinear switching kinetics are attributed to kinetics of the electron-transfer reactions occuring at the metal/insulator interfaces. The influence of the material parameters have been analyzed numerically in Section 4.2.4. In Section 4.3.2 analytical expressions for the SET and RESET time could be derived. This enables to predict the switching properties for a set of material parameters.
Multilevel switching is explained by the modulation of a tunneling barrier between the growing filament and the counter electrode. As demonstrated in Section 4.2.3 and Section 4.3.1 this programming of the LRS is a consequence of the interplay between the nonlinear switching kinetics and the SET current compliance. The LRS value is determined by the externally set current compliance level ($R_{\mathrm{LRS}} \propto I_{\mathrm{cc}}^{-1}$) and virtually material independent. It is thus a generic property of ECM cells. This property reveals an important implication. According to the simulations the LRS is independent of the filament area. Thus, it is not possible to decide whether the switching takes place over the whole electrode area or only locally just from experiment. It is therefore not sufficient to analyze the LRS resistance with respect

to the electrode area scaling to identify the filamentary nature of the switching if a current compliance is used.
As a second generic property of ECM cells $I_{\mathrm{RESET}} \propto I_{\mathrm{cc}}$ is identified (cf. Section 4.2.3 and Section 4.3.1). This relation as well as the corresponding proportionality constant could be derived analytically in Section 4.3.1. It is thus possible to predict the RESET current for a chosen sweep rate. The height of the RESET current is especially relevant with respect to power consumption of an ECM cell. The lower the RESET current the less power is consumed.
The possibility of polyfilamentary switching has been investigated using the 1D compact model (cf. Section 4.2.2) and a 2D FEM model in Section 4.4.2. The simulation results demonstrate that only one filament is responsible for the LRS state as long as the current compliance level is well below 1 mA. If the set current compliance level is so high that it is not reached even when the first filament establishes a galvanic contact, further filaments can establish galvanic contacts. The LRS resistance is then inversely proportional to the number of filaments in galvanic contact. With respect to the application as a ReRAM this kind of multilevel switching is irrelevant due to the high currents involved. In the application relevant regime only one filament contributes to the LRS resistance.
It is demonstrated that a galvanic contact can be achieved at long timescales and high current compliances. Both conditions are not relevant for an application as ReRAM, because the operation is either too slow or the power consumption is too high. The RESET operation for such a filament bridging both electrodes was investigated using 2D axisymmetric FEM simulations (cf. Section 4.4.3). The simulation results show that the RESET mechanism in this regime relies on a local temperature increase within the filament and its electrochemical self-dissolution. Due to the thermal nature of this process, RESET switching can be observed by using either voltage polarity. The RESET operation can be thus called nonpolar.

5 Modeling and Simulation of Resistive Switching in VCM Cells

5.1 Resistive Switching Mechanism

The bipolar valence change memory effect (VCM) has been found in complex oxides, e. g. manganites, titanates, and zirconates [11, 13, 81, 82] as well as binary oxides, e. g. TiO_2 and Ta_2O_5 [83, 84, 85, 86]. For bipolar switching an asymmetry is required in these systems, which can be obtained using different electrode materials or by an electroforming step [14]. Often one electrode-oxide interface forms an ohmic contact and the second interface forms a Schottky-type barrier. ReRAMs based on the valence change mechanism show ultrafast switching [87, 88, 89, 2] and very high endurance [2, 90]. The underlying physical and chemical mechanisms and the state of the art in VCM cells have been extensively reviewed by Waser et al. [14]. A more recent review with subject to binary oxides has been given by Akinaga et al. [91]. In the following, the proposed switching mechanism is sketched. Typically, an electroforming step is required to repeatedly switch a VCM cell between HRS and LRS. This can be achieved by current or voltage pulses with positive or negative polarity. In [92] these four different cases were investigated in $Pt/TiO_2/Ti$ crossbar structures. By applying a positive potential to the Pt electrode the cell is formed to the HRS, whereas the cell ends up in the LRS for a negative potential. During electroforming oxygen vacancies are created at the anode by release of oxygen [4, 93]. They migrate in direction of the applied electric field and pile up at the cathode. This enrichment of oxygen vacancies affects the valence state of the transition metal cations and the material becomes highly conducting (cf. Section 2.3). Thus, a virtual cathode forms which grows towards the anode. When it approaches the anode the cell resistance decreases significantly and the electroforming process is terminated (e.g. due to a set current compliance) [14, 93]. The shape of the virtual cathode can be filamentary or more homogeneous. Possibly, locally enhanced ionic mobility along extended defects as well as Joule heating play a significant role in the electroforming process. In TiO_2-based cells a Magnéli phase of Ti_4O_7 forms the virtual cathode [94]. In a $SrTiO_3$ system this can be a highly n-conducting oxygen deficient phase. The actual switching takes place between the virtual cathode and

the anode. Therefore, the anode will be called the active electrode and the virtual cathode the counter electrode in the following. One possible switching scenario is the modification of the electrostatic barrier between the active electrode and the counter electrode by a push and pull of oxygen vacancies [84, 4, 95]. By applying a negative voltage to the active electrode oxygen, vacancies are pulled towards the electrode. Hence, the electronic barrier is reduced and the VCM cell switches to the LRS (cf. Section 2.4). By reversing the voltage, the oxygen vancancies are pushed away from the active electrode and the HRS is restored. However, switching has also been observed with opposite polarities and both polarities within the same sample [96, 97, 98]. The VCM effect may take place at dislocations acting as conducting filaments [4], homogeneously over a somewhat larger interface region [99], or both at the same specimen [96].
To sum up, there are still a lot of open questions concerning the exact switching mechanism. Nevertheless it is widely accepted that a voltage-driven oxygen vacancy movement on the nanoscale and a subsequent electrochemical redox process in the cation sublattice near the active electrode are responsible for the VCM effect [84, 4, 100]. The oxygen vacancy migration within the oxide material is thus the driving force of the switching event. In the following sections the role of this transport is investigated with respect to the origin of the switching kinetics (cf. Section 5.2) and the scaling potential of VCM cells in Section 5.3.

5.2 Origin of the Switching Kinetics

To fulfill the requirements of a suitable nonvolatile memory a single cell should be scalable down to a few nanometers. As a further important requirement a write voltage of a few volts must be sufficient to switch a cell within less than 100 ns and a read voltage of a few tenths of a volt should leave the resistance state unchanged for 10 years, also known as the voltage time dilemma [14]. VCM cells show a strongly nonlinear dependence between switching time and applied voltage and can thus potentially fulfill this requirement. It is therefore crucial to understand the physical mechanism behind this nonlinearity so that it can be actively tuned to solve the voltage-time dilemma. The nonlinearity in most VCM systems exhibits a single exponential slope, which means that there is one single mechanism limiting the switching speed. In VCM cells the limiting factor is supposed to be the mobility of oxygen vacancies due to its low value at room temperature and at low electric fields. This mobility, however, increases dramatically at high electric fields or at high temperatures, which can be achieved by Joule heating (cf. Eq. (2.2) in Section 2.3).

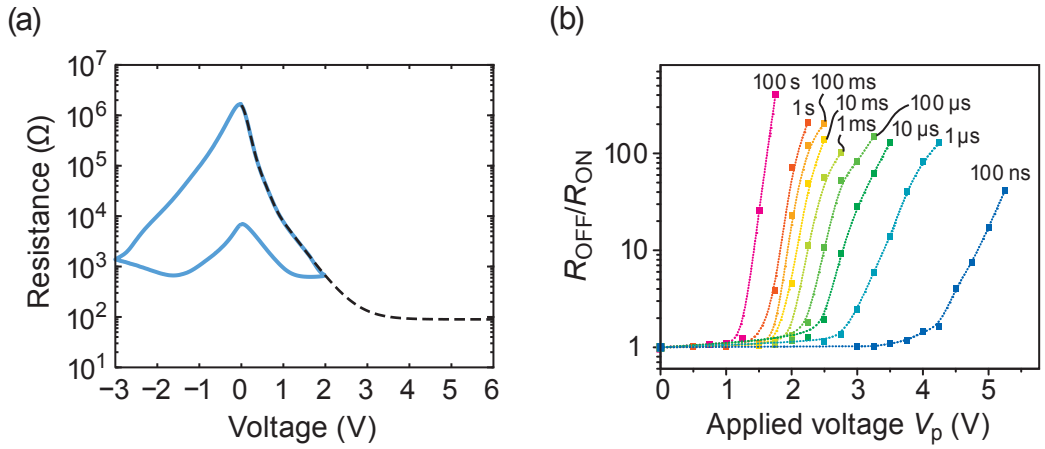

Figure 5.1: R-V characteristic of a measured cell (blue curve) and in the simulation (black dashed curve). Above 3 V the simulated resistance saturates since the disc region becomes very well conducting and the cell resistance is given by the series resistance of the plug. (b) Switching dynamics of SET processes for different pulse amplitudes and pulse widths, shown as the R_{OFF}/R_{ON} ratio as a function of the applied voltage amplitude of the pulse and the pulse duration. The pulse length-pulse voltage measurements were all performed on the same sample as in (a) (redrawn from [101]).

So both temperature and field enhancement can explain the nonlinear switching kinetics. Based on experimental data of $SrTiO_3$-based VCM cells both possibilities are discussed with the aid of electro-thermal FEM simulations.

In [101] thin film devices consisting of an epitaxially $SrTiO_3$ thin film sandwiched between a single-crystalline Nb-doped $SrTiO_3$ (STO:Nb) bottom electrode and a Ti top electrode are investigated. The quasi-static resistance-voltage (R-V)) curve of this device is depicted in **Figure 5.1(a)**. A quasi-static resistance ratio $R_{OFF}/R_{ON} > 300$ was observed for moderate SET and RESET voltages of 2 V and −3 V. Pulse measurements on the same sample with a pulse duration Δt_p ranging from 100 ns to 100 s and a pulse amplitude V_p ranging from 0.5 to 5 V were performed. The resulting resistance change is depicted in Figure 5.1(b). While reducing V_p by a factor of 5, the Δt_p required to change the resistance increases over nine orders of magnitude. This clearly indicates the extremely high nonlinearity of the switching kinetics mentioned above. For Δt_p below 100 ns a resistance change for V_p below 6 V was not observed [101].

To simulate the temperature and field distribution within the device its geometry, morphology and the material properties need to be known. For the analysis of the experimental data, an oxygen deficient n-conducting cylindrical region in the STO film which rises from the bottom electrode and comes into the close vicinity of the Ti top electrode (cf. Figure 5.3(b)) is considered. In the following, this region is

termed the "conducting plug". It is created during the electroforming process and has been directly observed in the considered films by local conduction atomic force microscopy (LC-AFM) after peeling off the top electrode [96]. For the switching polarity depicted in Figure 5.1, it has been shown that switching takes place locally in a slightly extended, disc-shaped region at the electrode interface [96]. Therefore, this region between the front of the plug and the Ti electrode is called the "disc" in the following. The kinetics of the switching is thus determined by the drift velocity of the oxygen vacancies within this disc region. It has been proven by transmission electron microscopy analysis that the perovskite structure remains unchanged in the conducting region of the samples [102]. In addition, experimental data show that the perovskite lattice is still stable at huge oxygen vacancy concentrations of 10 % and more [103, 104]. Thus, phase transitions as in the TiO_2 system are not expected here.

$SrTiO_3$ (STO) is known to be a mixed electronic-ionic conductor. Its transport properties can be precisely tuned during fabrication and described well in terms of point defect chemistry [105, 106, 107]. The investigated sample exhibits n-conduction due to self-doping by donor-type oxygen vacancies during fabrication and the subsequent electroforming step [108]. The temperature dependence of the electron mobility μ_n can be described by

$$\mu_\mathrm{n,p}\,(T) \propto (T/\mathrm{K})^{-\beta} \tag{5.1}$$

with $\beta = 2.23$ [109]. It is negligibly small compared to that of the oxygen vacancy mobility

$$\mu_\mathrm{V\ddot{O}}\,(T) \propto (T/\mathrm{K})^{-1} \exp\left(-E_\mathrm{A}/kT\right) \tag{5.2}$$

with an activation energy $E_\mathrm{A} = 1.01\,\mathrm{eV}$ [110]. This value of the activation energy even holds if a phase transformation into SrO and TiO_{2-x} occurs upon forming. The calculated activation energies of oxygen vacancy migration in TiO_{2-x} (which is the relevant phase) are also in the order of 1 eV [111].

The absolute value of μ_n is higher than $\mu_\mathrm{V\ddot{O}}$ in the whole temperature range. For highly n-conducting $SrTiO_3$, this results in a weak temperature dependence of the total sample conductivity, although the ionic partial conductivity increases by many orders of magnitude within a temperature range of some hundred degrees due to the increase of oxygen vacancy mobility, cf. **Figure 5.2**.

To calculate the thermal and field enhancement of the oxygen vacancy movement in the disc, the mean temperature of the disc T_disc and the electric field in the disc E_disc need to be evaluated as a function of the applied voltage. Based on these quantities,

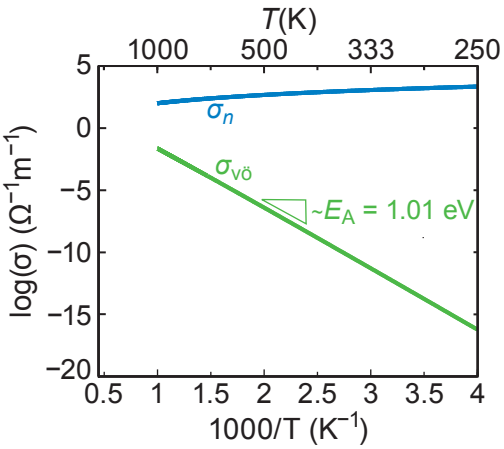

Figure 5.2: Temperature dependence of the electronic partial conductivity and the ionic partial conductivity. Doubly positively charged oxygen vacancies and electrons are the majority carriers in n-conducting $SrTiO_3$. A constant oxygen vacancy concentration of $8.3 \cdot 10^{18}\,\mathrm{cm}^{-3}$ has been assumed and the values $\beta = 2.23$ [109] and $E_\mathrm{A} = 1.01\,\mathrm{eV}$ [110] were used (redrawn from Menzel et al. [101]).

the SET switching time can be estimated as follows: The oxygen vacancies are assumed to move over a certain distance in the range of the disc thickness l_disc to result in a SET process. On the one hand the SET time Δt_SET is thus related to the oxygen vacancy drift velocity by

$$v_\mathrm{drift} = \frac{l_\mathrm{disc}}{\Delta t_\mathrm{SET}}. \tag{5.3}$$

On the other hand the drift velocity depends on the mobility and the electric field. Here, it is discriminated between a purely linear dependence

$$v_\mathrm{drift} = \mu\left(T_\mathrm{disc}\right) E_\mathrm{disc} \tag{5.4}$$

and an exponential dependence

$$v_\mathrm{drift} = \mu\left(T_\mathrm{disc}\right) E_0 \sinh\left(\frac{E_\mathrm{disc}}{E_0}\right) \tag{5.5}$$

at very high electric fields [112]. At electric fields well below the characteristic field E_0 Eq. (5.5) turns into Eq. (5.4). Combining Eq. (5.3) with Eq. (5.4) or Eq. (5.5) and setting $E_\mathrm{disc} = V_\mathrm{disc}/l_\mathrm{disc}$ an expression for the SET time Δt_SET can be derived in case of linear field-dependent drift velocity to

$$\Delta t_\mathrm{SET} = \frac{l_\mathrm{disc}^2}{\mu\left(T_\mathrm{disc}\right) V_\mathrm{disc}} \tag{5.6}$$

and in case of exponential field-dependent drift velocity according to

$$\Delta t_{\mathrm{SET}} = \frac{l_{\mathrm{disc}}}{\mu\left(T_{\mathrm{disc}}\right) E_0} \left(\sinh\left(\frac{V_{\mathrm{disc}}}{l_{\mathrm{disc}} E_0}\right)\right)^{-1}. \tag{5.7}$$

Here, V_{disc} corresponds to the voltage drop across the disc, $E_0 = 1\,\mathrm{MV/cm}$ to the characteristic field [113, 112] and $\mu\left(T_{\mathrm{disc}}\right)$ is calculated using Eq. (5.2). The characteristic field is related to the hopping distance of ions a as $E_0 = 2k_{\mathrm{B}}T/(ea)$. For $1\,\mathrm{MV/cm}$ a is approximately $0.5\,\mathrm{nm}$, which is in the range of interatomic distances. Eq. (5.6) and Eq. (5.7) lead to four different cases. Firstly, based on Eq. (5.6) Δt_{SET} can be estimated with a constant temperature $T_{\mathrm{disc}} = 300\,\mathrm{K}$ (called "no acc."), and, secondly, it can be thermally accelerated using the calculated mean temperature T_{disc} (T-acc.). Thirdly, with Eq. (5.7) Δt_{SET} can be calculated either with field acceleration at constant disc temperature $T_{\mathrm{disc}} = 300\,\mathrm{K}$ (E-acc.) or with both field and temperature acceleration (T- and E-acc.). The values V_{disc} and T_{disc}, which determine the switching time, are extracted from electro-thermal FEM simulations. In these simulations the transient heat equation

$$\rho_{\mathrm{m}} C_{\mathrm{p}} \frac{\partial T}{\partial t} - \nabla k \nabla T = \frac{J^2}{\sigma} \tag{5.8}$$

is solved along with the continuity equation

$$-\nabla J = -\nabla \sigma \nabla V = 0. \tag{5.9}$$

Here, ρ_{m} denotes the mass density, C_{p} the heat capacity, k the thermal conductivity, and σ the electric conductivity. Due to the small device dimensions it is expected that the equilibrium temperature distribution is reached within a few nanoseconds. Thus, in the time frame of our switching experiments ($> 100\,\mathrm{ns}$), the thermal and electronic conductivities can be regarded as the decisive parameters of the switching kinetics. The electronic conductivity of the disc region is extracted from the experimental $I - V$ characteristic for voltages up to $1\,\mathrm{V}$ assuming a plug radius of $300\,\mathrm{nm}$ and a plug conductivity of $\sigma_{\mathrm{plug},0} = 4 \cdot 10^3\,\mathrm{S/m}$. The chosen plug radius is comparable to experimental observations [96]. Above $1\,\mathrm{V}$, the electronic conductivity is extrapolated using an exponential fit

$$\sigma_{\mathrm{disc}} = \sigma_{\mathrm{disc},0} \exp\left(V_{\mathrm{disc}}/V_0\right) \tag{5.10}$$

with $\sigma_{\mathrm{disc},0} = 0.18\,\mathrm{S/m}$ and $V_0 = 0.39\,\mathrm{V}$. The exponential relation is chosen to account for the nonlinear $I - V$ characteristic.

Table 5.1: Simulation parameters for $T = 300\,\mathrm{K}$

Symbol	Ti	Cu	Nb:STO	STO (plug)	STO (matrix)	SiO_2
$\sigma\,(\mathrm{S/m})$	$2.5 \cdot 10^6$ [114]	$5.8 \cdot 10^7$ [79]	$1.0 \cdot 10^6$	$4.0 \cdot 10^3$	$< 10^{-2}$	$1 \cdot 10^{-16}$ [80]
$k\,(\mathrm{W/m\,K})$	21.9 [79]	401 [79]	12 [115]	12 [115]	12 [115]	1.2 [80]
$C_\mathrm{p}\,(\mathrm{J/kg\,K})$	522 [79]	384 [79]	538 [116]	538 [116]	538 [116]	745 [79]
$\rho_\mathrm{m}\,(\mathrm{kg/m^3})$	4506 [79]	8960 [79]	5130 [117]	5130 [117]	5130 [117]	2200 [79]

A comparison between the measured and the modeled $R - V$ curve is shown in Figure 5.1(a). In the high voltage regime, the cell resistance and thus the cell current are dominated by the resistance of the conducting plug. Hence, the conductivity of the plug has a key influence on the temperature distribution in this voltage regime. The highest temperature increase is expected to be in the highly n-conducting plug and the disc region. Therefore, it is crucial to account for the temperature dependence of the electronic conductivity in the plug. Using Eq. (5.1) it can be modeled as

$$\sigma_\mathrm{plug}\,(T) = \sigma_\mathrm{plug,0}\,(T/T_0)^{-\beta}\,. \tag{5.11}$$

The material parameters are given in **Table 5.1** and are considered temperature-independent, except for the conductivity of the plug (cf. Eq. (5.11). For the disc thickness $l_\mathrm{disc} = 5\,\mathrm{nm}$ applies. Due to the symmetry of the investigated cell it is sufficient to solve the equation system Eq. (5.8) to Eq. (5.11) in 2D axial symmetry, for which the commercial finite element software COMSOL is employed. This set of equations is complemented by suitable boundary conditions shown in **Figure 5.3(b)** along with the geometry. It is solved until a steady state is reached.
In a first simulation a 5 V voltage pulse of 10 ns duration with rise and fall times of 2 fs is applied to investigate the transient temperature evolution. **Figure 5.3(a)** shows the simulated mean temperature of the disc region. The equilibrium temperature distribution is reached within 2 ns, which proves that the decisive parameters are the electronic and thermal conductivities. Likewise the temperature drops immediately after pulse application and the initial temperature is reached after approximately 5 ns. Thus, resistance relaxation due to oxygen vacancy diffusion at elevated temperatures after pulse application can be excluded. In Figure 5.3(b) the corresponding equilibrium temperature distribution is illustrated. It is evident that the highest temperatures are reached in the plug and in the disc close to the plug. This distribution is typical for this kind of geometry. Since the equilibrium temper-

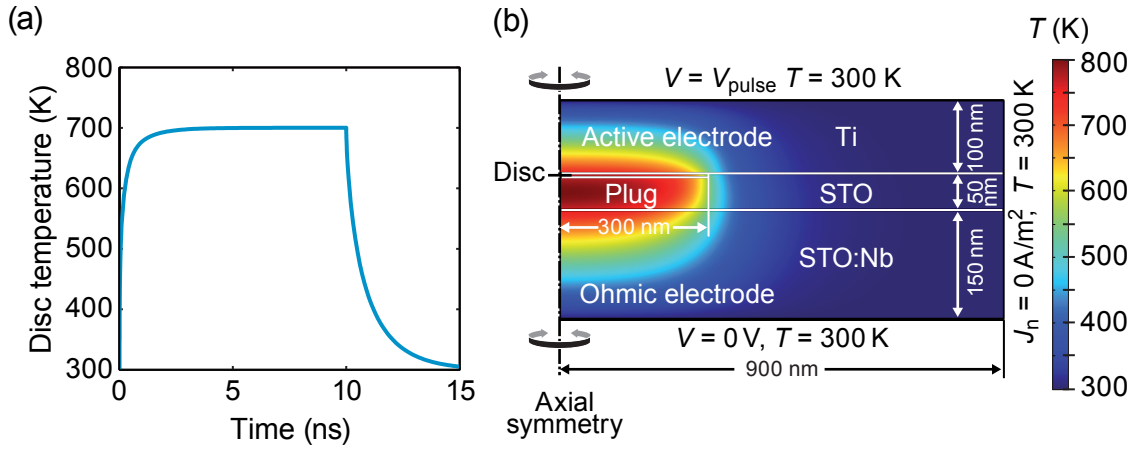

Figure 5.3: (a) Time-dependent disc temperature for a 10 ns voltage pulse of 5 V with 2 fs rise/fall time. (b) Cross section of the simulated cell with boundary conditions. The equilibrium temperature distribution for $V_\mathrm{p} = 5\,\mathrm{V}$ is shown in color (redrawn from Menzel et al. [101]).

ature is established almost instantaneously, the mean equilibrium disc temperature will be used to estimate the switching time according to Eq. (5.6) and Eq. (5.7), respectively.

Simulations were performed for a plug radius of 300 nm and different potentials V_p between 0.1 V and 6 V. To calculate the SET time the mean disc temperature as well as the disc voltage drop are evaluated from the simulation results. **Figure 5.4** shows the calculated SET times resulting from the four different cases deduced from equations Eq. (5.6) and Eq. (5.7) compared to the experimental SET time. The experimental data are extracted from Figure 5.1(b) for a resistance ratio $R_\mathrm{HRS}/R_\mathrm{LRS} = 30$. It becomes apparent that the temperature-accelerated drift of oxygen vacancies plays a major role in interpreting the exponential dependence of the switching kinetics on the SET voltage, leading to a switching speed acceleration of more than ten orders of magnitude. The underlying temperature increase originates from the nonlinear $I - V$ characteristic of the disc region. As soon as a certain voltage (about 1 V) is reached, the current is high enough (above 100 µA) to bring about a significant temperature increase (cf. Figure 5.4), which is consistent with the derivations of a recent study [55]. Below this voltage there is no Joule heating effect and, thus, the switching speed is very low (because of the very low mobility of oxygen vacancies at room temperatures). Above this voltage the disc temperature increases with the applied voltage and due to the exponential temperature dependence of $\mu_\mathrm{V\ddot{O}}$ the switching speed increases exponentially. In contrast, field acceleration only leads to a switching speed acceleration of less than two orders

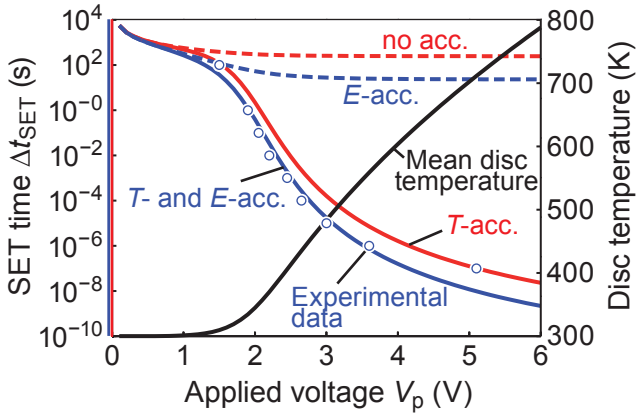

Figure 5.4: Calculated SET time depending on the applied voltage for the four different cases in red and blue. The black line corresponds to the mean disc temperature used for the calculations. The experimental data are extracted from Figure 5.1(b) for a resistance ratio $R_{OFF}/R_{ON} = 30$ and shown as open circles. The data point at 100 ns must be regarded with caution because it may be affected by the RC time of the setup (redrawn from Menzel et al. [101]).

of magnitude and saturates around $2-3$ V. This is caused by the field-dependent conductivity of the disc region (cf. Eq. (5.10)), leading to a redistribution of the voltage drops across the disc and the plug at high applied voltages.

In the previous simulation study optimized values for the disc thickness, the characteristic field and the plug diameter were used. Thus, it is necessary to discuss how a variation of theses parameters affects the simulation results. Especially, it should be evaluated if an alternative scenario can explain the experimental data. For this a corresponding fit should not result in unphysical values of the hopping distance or the activation energy of oxygen vacancy mobility. According to the literature the hopping distance in ionic crystals should be within interatomic distances. Hopping distances over a few nanometers are impossible due to the intrinsic energy landscape [20]. As motivated before the activation energy is about 1 eV and thus values that clearly deviate from this value are considered as unphysical for the considered STO cell.

The calculated SET time based on field enhancement shows a strong dependency on the disc thickness. Therefore, a simulation series with different disc thicknesses was performed for voltages between 0.1 V and 6 V. In all simulations the thickness of the insulation layer remains 50 nm. The conductivity of the disc has to be adjusted for each disc thickness to match the experimental $R-V$ characteristic. To discriminate between temperature and field acceleration the cases T-acc. and E-acc. are considered to calculate the SET time. In **Figure 5.5(a)** the simulated mean

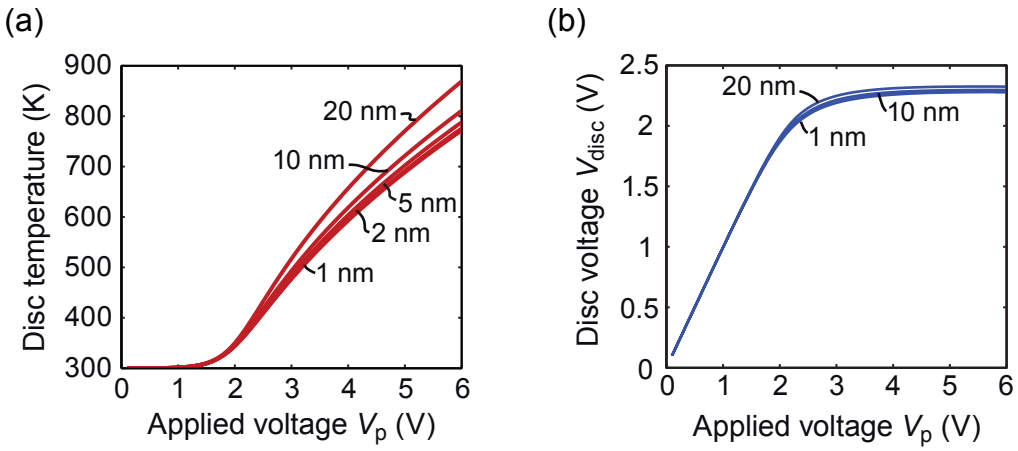

Figure 5.5: (a) Mean disc temperature against the applied voltage for different disc thicknesses. (b) Corresponding voltage drops across the disc (redrawn from Menzel et al. [101]).

disc temperature is shown. The temperature increase is less for a thinner disc than for a thicker disc, but it is still significant. This increase is attributed to the volume of the disc. The bigger the volume the more Joule heating occurs, since Joule heating is proportional to the electric resistivity. The voltage drop on the other hand shows only a slight increase with increasing disc thickness (cf. Figure 5.5(b)), which is caused by the different temperature profiles. For all disc thicknesses a saturation of the voltage drop at approximately 2.3 V is observed. This is caused by the redistribution of the electric potential according to the nonlinear voltage dependence of the disc conductivity.

With these findings the calculated SET times can be easily understood. **Figure 5.6(a)** shows the calculated SET times for temperature acceleration and Figure 5.6(b) for field acceleration. Below 1.5 V the temperature increase is very low, and the difference in SET time for the case T-acc. is directly linked to the different thicknesses. For higher voltages the difference is less pronounced since the temperature increase is higher for thicker discs. Moreover, the calculated SET times deviate from the experimental data only within one to two orders of magnitude for each voltage. For the case E-acc. a strong impact of the disc thickness on the switching speed is observed. The thinner the disc the higher is the electric field, which modifies the switching speed exponentially. Due to field saturation the switching speed also saturates at voltages above 2 V. The calculated SET times can be well below 100 ns, which is also observed in experiment. In order to achieve the correct slope of the first five data points for purely electric-field enhanced migration at $E_0 = 1\,\mathrm{MV/cm}$, the disc thickness should be 0.75 nm. However, calculated and

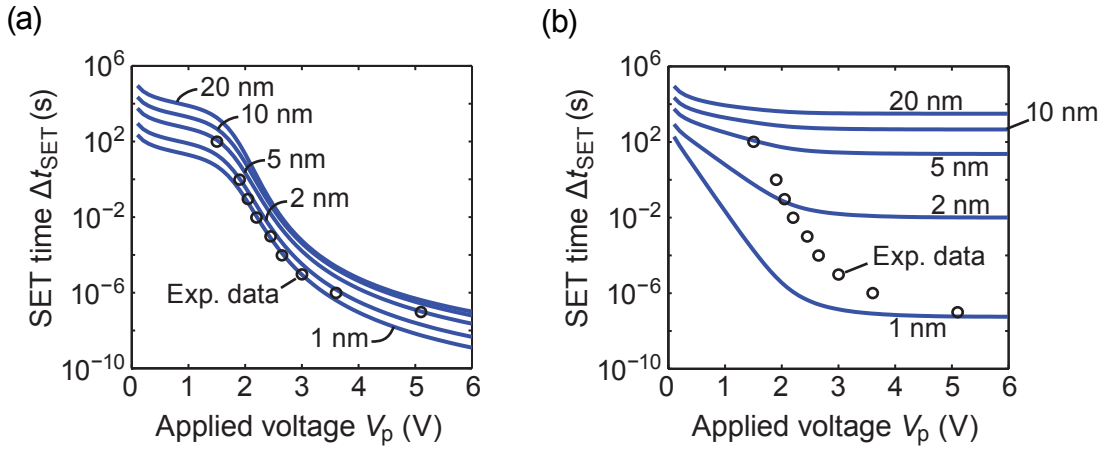

Figure 5.6: (a) SET time vs. applied voltage for different disc thicknesses. The SET time is calculated using Eq. (5.6) (T-acc.). (b) Corresponding SET times calculated using Eq. (5.7) and a constant temperature $T_{\mathrm{disc}} = 300\,\mathrm{K}$ (E-acc.) (redrawn from Menzel et al. [101]).

experimental data then deviate tremendously in the low voltage regime, which is related to the low field mobility at 300 K. To match the experimental data this mobility has to be reduced unrealistically by eight orders of magnitude compared to the bulk data. This can only be accommodated by an increase in the activation energy of oxygen vacancy migration to 1.4 eV, which is unphysically high compared to the reported experimental value of 1.0 eV. Therefore, this scenario does not lead to a self-consistent set of parameters and smooth fitting results. The best fit to the experimental data is achieved as a combination of the temperature and field enhanced case using a disc thickness of 5 nm.

According to Eq. (5.7) the calculated SET times are very sensitive against the characteristic field E_0. Here, it is $E_0 = 1\,\mathrm{MV/cm}$ and $a = 0.5\,\mathrm{nm}$ holds for the ionic hopping distance. To study the influence of the characteristic field, the simulation data of the previous simulation study for a 5 nm thick disc and the SET time is recalculated according to Eq. (5.7) with $T_{\mathrm{disc}} = 300\,\mathrm{K}$. As can be seen in **Figure 5.7** a reduction of E_0 and thus an increase in a leads to a significant acceleration of switching speed. However, the calculated SET times do not fit to the experimental data at all. An optimal fit for a purely electric-field enhanced migration could be obtained for $E_0 = 0.16\,\mathrm{MV/cm}$ and an activation energy for oxygen vacancy migration of 1.4 eV. This value of E_0 corresponds to an unphysical high hopping distance of $a = 3\,\mathrm{nm}$. Note that such large hopping distances are impossible for ions due to the intrinsic landscape in ionic crystals [20]. So this scenario can also be eliminated.

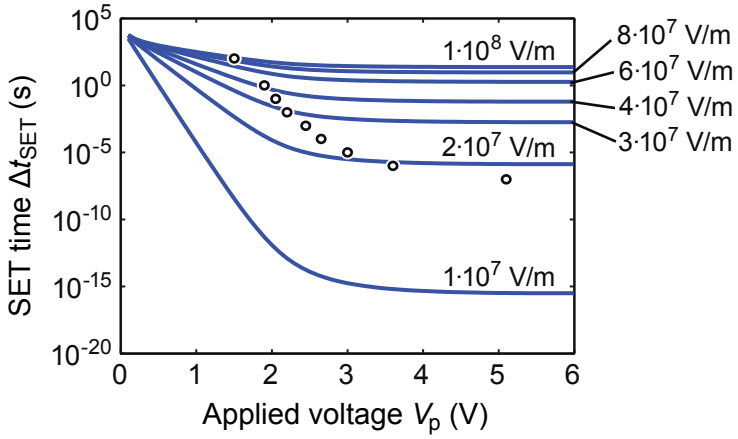

Figure 5.7: (a) SET time vs. applied voltage for different characteristic fields. The SET time is calculated using Eq. (5.7) and a constant temperature $T_{\mathrm{disc}} = 300\,\mathrm{K}$. The disc thickness is 5 nm (redrawn from Menzel et al. [101]).

Finally, the variation of the plug radius is discussed. Since the conductivities of the plug and the disc region are fitted to the experimental data (cf. Figure 5.1(a)), the absolute value of the current stays constant. By varying the plug radius the current density and thus the local Joule heating change accordingly. For a smaller radius this leads to an increased heating and higher temperatures. In an extreme case the local temperatures can become unphysically high. On the other hand the temperature increase can be insignificant for very large radii. In this case only a field enhancement would be possible, but a fit to the experimental data leads again to unphysical values of the hopping distance and/or the activation energy of the oxygen vacancy mobility. The chosen radius of 300 nm is a result of these considerations.

In summary, the simulations reveal that the nonlinear switching kinetics is predominantly caused by a temperature-accelerated drift of oxygen vacancies rather than by field acceleration. For all other reasonable alternative scenarios the fitting procedure fails dramatically or unphysical parameter values have to be used.

5.2.1 Ultrafast Switching in Titanium Oxide

In the previous section a $SrTiO_3$-based VCM cell was considered as a model system. Here, experimentally observed ultrafast switching of a TiO_2-based VCM cell in the nanosecond regime is analyzed using electrothermal FEM simulations. This way it can be proven that thermal enhancement is also likely to occur in TiO_2 cells. Recently, ultrafast switching below 10 ns was demonstrated in bipolar

Table 5.2: Simulation parameters

Symbol	Ti	Pt	Ti_4O_7	TiO_2
σ (S/m)	$2.5 \cdot 10^6$ [114]	$1.0 \cdot 10^7$ [79]	$2.0 \cdot 10^4$ [118]	$1.0 \cdot 10^{-6}$ [119]
k (W/m K)	21.9 [79]	71.6 [79]	3.15 [118]	5.18 [119]
C_p (J/kg K)	522 [79]	133 [79]	700 [120]	700 [120]
ρ_m (kg/m^3)	4506 [79]	21450 [79]	4240	4082

Pt/Ti/TiO_2/Pt nanocrossbar devices [87]. A SET voltage of about 2 V and a RESET voltage about −1.5 V are reported for quasistatical $I-V$ sweeps. In a 5 ns pulse mode, however, the observed switching voltages are considerably higher with $V_{SET} = 4\,V$ and $V_{RESET} = -5\,V$, respectively. This discrepancy in the switching voltages demonstrates the strongly nonlinear switching kinetics. The observed transient peak currents during switching are 200 µA for the SET processes and about −230 µA for the RESET process [87]. Also for non-switching events, which were probed with the opposite polarity compared to the switching polarity, the reported peak currents are about 200 µA (cf. **Figure 5.8(a) and (b)**). Such high currents are likely to generate significant Joule heating within the device. To simulate the temperature distribution in the LRS and HRS for the reported cell, the transient heat equation (5.8) is solved along with the continuity equation (5.9). Due to the symmetry of the device this equation system is solved in 2D axial symmetry. For the reported switching polarity the actual switching is considered to take place in a disc-shaped region in front of a Magnéli phase Ti_4O_7 filament at the Pt bottom electrode, which has grown during electroforming [94]. The resulting device geometry is shown in Figure 5.8(c) along with the used boundary conditions. A filament diameter of 5 nm is assumed as reported in literature [94]. The electric conductivity of the disc region and the filament are fitted to match the experimental current data of the non-switching events (cf. Figure 5.8(a) and (b)), whereas it is assumed to be field-dependent in the disc region to account for the nonlinear $I-V$ characteristic. The slight time shift between experimental and simulated data might be attributed to the measurement setup. The remaining material parameters are given in **Table 5.2**. The electrical and thermal conductivities of TiO_2 and Ti_4O_7 are taken from [118, 119].

Time-dependent simulations are performed with the same 5 ns voltage pulse as excitation for the LRS and the HRS state as in the experiment (cf. Figure 5.8(a) and (b) solid and dashed blue lines). Figure 5.8(c) shows a typical simulated temperature distribution for the HRS state with the hottest spot located within the

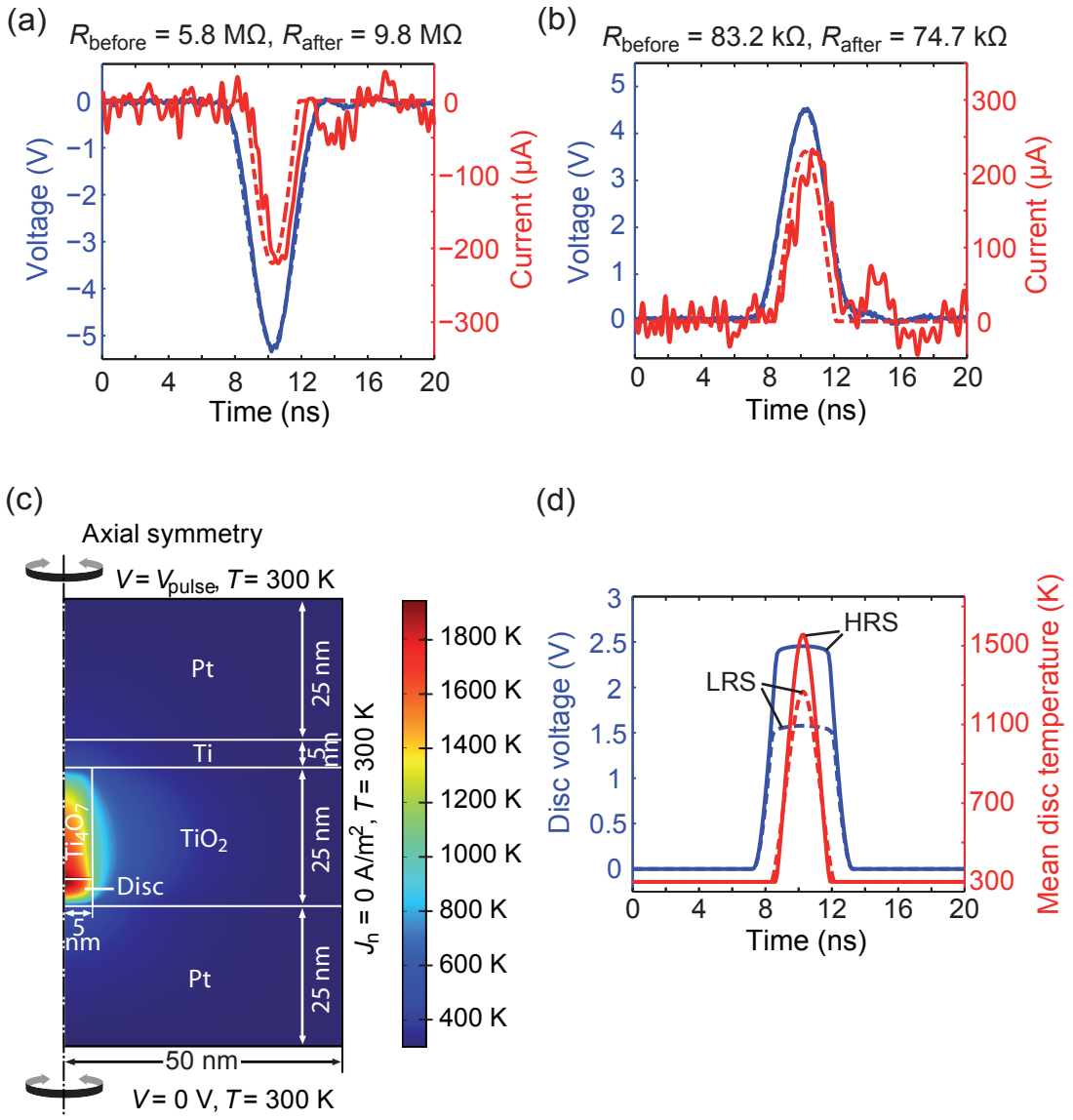

Figure 5.8: Experimental (solid lines) and simulated (dashed lines) $V(t)$ and $I(t)$ data of non-switching events after (a) a successful RESET and (b) a succesful SET operation. Note that the experimental and the simulated voltage pulses are virtually identical. (c) Cross section of the simulated cell with boundary conditions. The color represents the temperature distribution 2.5 ns after the beginning of a voltage pulse (defined amplitude and shape) applied to the device. (d) Voltage dropping across the disc not across the complete device (blue) and mean disc temperature (red) for LRS (dashed lines) and HRS (solid lines) as a function of time (published in [87])

disc region. Since switching takes place in the disc region, the mean temperature within this region is evaluated for each time step (Figure 5.8(d)). In the HRS and the LRS mean temperatures above 1000 K are reached, which could explain a high vacancy mobility and thus switching taking place in the nanosecond regime. The highest temperature is reached in the HRS state, whereas the peak currents of both states are equal. This is directly linked to the voltage drop across the disc as shown in Figure 5.8(d).Due to the nonlinear electric conductivity of the disc region, the disc voltage saturates and the exceeding applied voltage drops along the Magnéli phase filament. The disc voltage is higher for the HRS state than the LRS state leading to increased Joule heating. Based on the simulation results the higher voltage needed for RESET operation than for SET operation can be explained. To switch within the same time frame similar mean temperatures are needed for SET and RESET, which requires a higher current in the LRS state. This is consistent with the findings of the switching experiments (cf. Fig. 3 in [87]).
The calculated activation barrier of oxygen vacancy migration is about 1 eV [111]. The simulated temperature increase of about $700 - 1000$ K can therefore account for an increase in drift velocity of over twelve orders of magnitude. Thus, also for the TiO_2 cell the predominant mechanism is supposed to be the temperature enhanced drift of oxygen vacancies. This shows that the model derived in the previous section is generic in nature. It holds for all insulating oxides which become highly *n*-conducting when reduced to lower cation valences and which show highly temperature-activated ion mobility. This is true for the majority of transition metal oxides.

5.3 Scaling of VCM Cells

In Section 5.2 the thermal origin of the switching kinetics has been revealed. This thermal effect has to be considered for scaling purposes and optimization of the cell design. To deduce essential design rules for scaling the $SrTiO_3$-based VCM cells are considered again while the dimensions are scaled.
To study the influence of the plug diameter, a series of electro-thermal simulations is performed, in which the disc and the plug radius are varied within the range of 750 nm to 6.25 nm. The SET time is estimated using Eq. (5.7). The resulting SET time-voltage characteristics are shown in **Figure 5.9(a)**. With decreasing radius the SET time increases up to seven orders of magnitude. This increase can be attributed to a decreasing mean disc temperature with decreasing radius (cf. Figure 5.9(b)). At a first glance this decrease of the disc temperature may appear

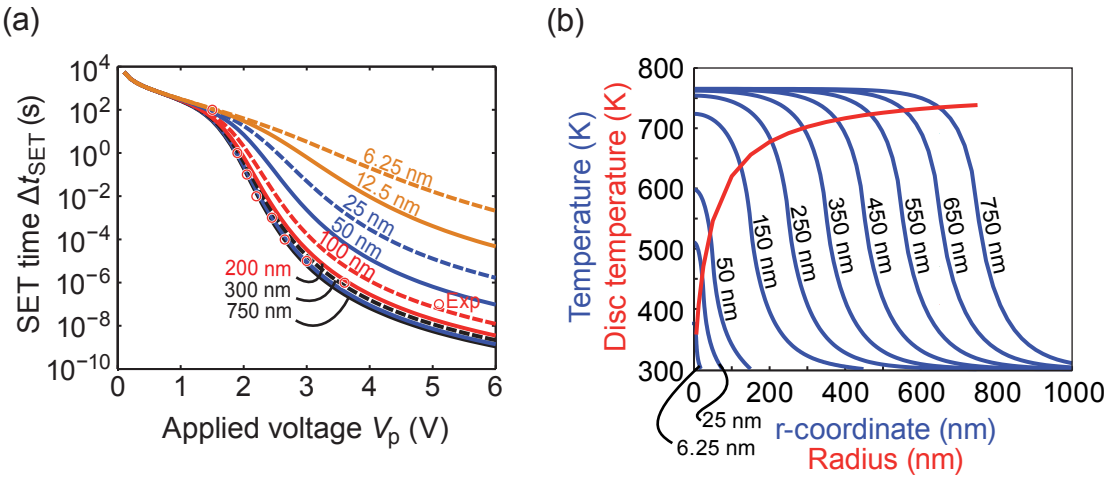

Figure 5.9: (a) SET time vs. applied voltage for different radii of the conducting disc and plug. As a comparison the experimental data is pictured in open circles. (b) The blue lines show the temperature distribution through a cross section of the disc in r-direction for different radii. The red curve represents the mean temperature in the disc region for these radii (redrawn from Menzel et al. [101]).

counter-intuitive, since the heating power density ($p = J^2/\sigma$) remains constant in the voltage driven simulation. However, it can be explained by interpreting the cross-sectional temperature distribution within the disc as shown for different radii in Figure 5.9(b). For large radii, the temperature distribution has a saturated maximum temperature of approximately 760 K in the plug center. Within a region of ±250 nm around the outer disc boundary the temperature decreases to approximately 300 K. If the disc radius is smaller than 250 nm, this maximum temperature is not achieved anymore. This results in a lower mean disc temperature and, hence, a longer SET time. The temperature decrease would be a limiting factor for lateral cell size scaling.

The influence of the switching layer thickness has been simulated in the range from 10 nm to 100 nm, while the plug radius is kept at 300 nm and the disc thickness at 5 nm. The resulting SET time-voltage characteristics are shown in **Figure 5.10(a)**. Here, the SET time decreases with decreasing thickness. A shorter plug corresponds to a lower overall resistance of the cell, resulting in a higher current and, hence, heating power density (cf. Figure 5.10(b)). Therefore, the mean disc temperature is raised and the switching speed is enhanced. In conclusion, thinner resistive switching layers boost the switching performance of the resistive switching cell.

As a result of these simulations the following design rules for scaling can be deduced: While the cell area is reduced, the thickness of the resistive switching layer has to be reduced, too. Hence, the decrease in switching speed for thinner

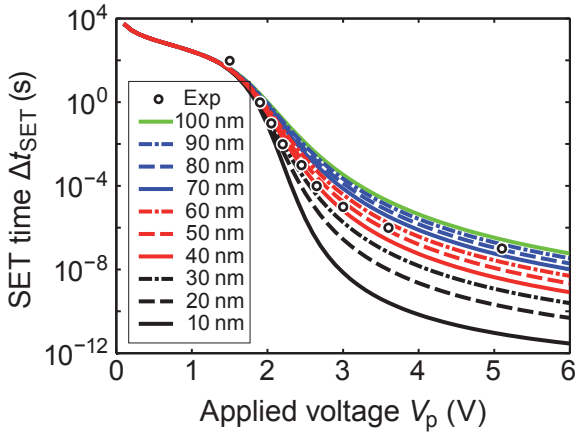

Figure 5.10: (a) SET time vs. applied voltage for different thicknesses of the switching layer. The radius is kept at 200 nm and the thickness of the disc at 5 nm. The experimental data are shown as black circles (redrawn from Menzel et al. [101]).

diameters of the plug can be compensated by shortening the plug. This enables fast cell operation in the nanosecond regime.

In order to obtain the limit for cell scaling, simulations for integrated nano-sized cells are conducted. The corresponding cell geometry is shown as an inset in **Figure 5.11(a)**. The MIM cell is now sandwiched between two Cu electrodes representing interconnects. A SiO_2 insulating layer is introduced between adjacent cells. The feature size F is varied between 100 nm and 20 nm in 20 nm steps. For $F = 20$ nm the diameters of the top and bottom electrodes equal the constant plug diameter. Further downscaling leads to a shrinking of the plug diameter and is not considered here. For each feature size the temperature distribution for different applied voltages is simulated and Δt_{SET} is calculated according to Eq. (5.7). With decreasing feature size, the switching speed increases considerably and SET times in the nanosecond regime become feasible (cf. Figure 5.11(a)). This acceleration is directly related to the reduction of the plug length and, hence, an increase in the current (cf. Figure 5.11(b)). The biggest decrease in switching speed occurs as the feature size is reduced from 40 nm to 20 nm. Note, that for the 20 nm feature size the plug and disc are surrounded by SiO_2 rather than by STO as for larger feature sizes. Due to the lower thermal conductivity of SiO_2 the heat dissipation through the surroundings is reduced, leading to higher temperatures within the disc. Here, a limitation in switching speed results from the time the disc needs to heat up. This heating time is below 2 ns for the geometries under consideration according to the simulations. Figure 5.11(b) shows the corresponding switching energy and cell current, where the switching energy is calculated as $E = V_{\mathrm{p}} I_{\mathrm{cell}} \Delta t_{\mathrm{SET}}$. Interestingly,

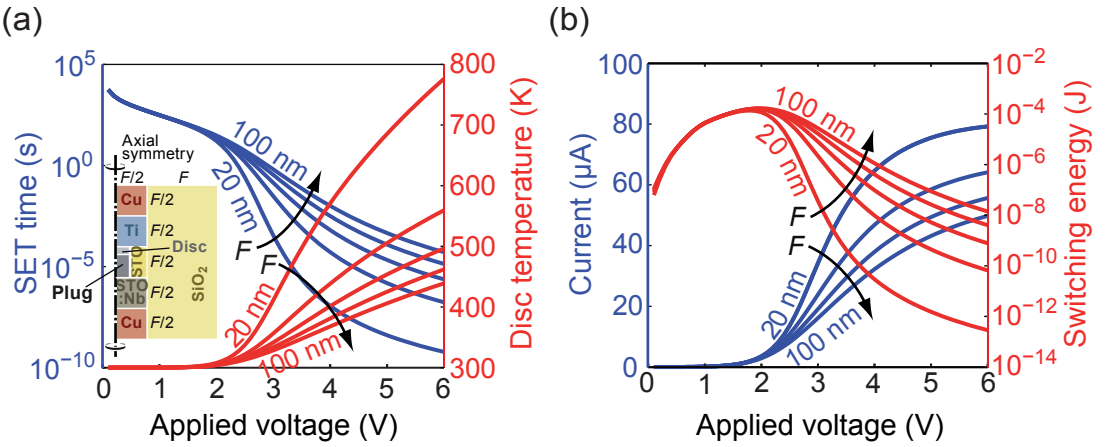

Figure 5.11: (a) SET time (blue) and disc temperature vs. applied voltage for different feature sizes F. Inset: geometry of a nano-sized cell. (b) Corresponding switching energy and cell current vs. applied voltage. The plug diameter is 20 nm and the disc thickness 5 nm in all simulations. All other dimensions scale with F (redrawn from Menzel et al. [101]).

the switching energy first increases and then decreases tremendously for higher voltages. This is consistent with the onset of switching speed acceleration due to local Joule heating. For low voltages there is no Joule heating and the switching energy is mainly determined by the increasing current and voltages. As soon as the temperature acceleration sets in the switching energy decreases according to the SET time. For a cell with $F = 20\,\text{nm}$ a switching time of 10 ns is achieved at an applied voltage of approximately 3 V. According to Figure 5.11(b) this corresponds to a write current and a switching energy of approximately 25 µA and 100 nJ, respectively. This current is still higher than the 10 µA target (cf. Section 2.2), but significantly lower than that in the large cell in Section 5.2. By proper cell design with respect to thermal confinement this goal seems to be attainable.

5.4 Summary

In summary, switching time-voltage data of SET pulse studies on interface-type $SrTiO_3$-based VCM cells were presented and an electro-thermal model was introduced which, despite simplifications, allows a remarkably good description of the data. The simulations reveal that the nonlinear switching kinetics is predominantly caused by a temperature-accelerated drift of oxygen vacancies in the low nanometer range rather than by field acceleration. This result is further supported by electro-

thermal simulations of TiO_2-based VCM cells. The voltage-time dilemma [14] can thus be overcome to a large extent by thermal accelerated ionic drift in this cell type. It should be mentioned that this model is generic in nature and holds for all insulating oxides which become highly n-conducting when reduced to lower cation valences and which show highly temperature-activated ion mobility. This applies to the majority of transition metal oxides. Furthermore, the model explains the close relationship of bipolar VCM and unipolar TCM, shown by the fact that one can toggle between the two mechanisms by adjusting the current. Typically, the bipolar mode turns into a unipolar mode at higher currents [83, 121, 122, 123]. In addition to physics-based design rules for the material selection, the model permits scaling rules to be estimated. The influence of geometrical variations was simulated and the results show that nano-sized VCM cells are feasible without any deterioration of the switching performance. Due to the origin of the switching kinetics the cell design can be optimized with respect to thermal confinement. In addition, thermal properties should be considered while selecting proper materials.

6 Conclusions and Outlook

In this chapter the simulations results of the ECM and VCM cells are briefly summarized and compared to each other. Especially, it is discussed if the results of the ECM switching are transferable to VCM switching. Moreover, the simulation results are discussed with respect to application as ReRAM. In addition, an outlook on further model development and simulations is presented.

6.1 Summary and Conclusions

In Chapter 4 a dynamic model for ECM cells was presented which is in very good agreement to the experimental data. The model accounts for the quasistatic $I - V$ characteristics, the nonlinear switching kinetics and the multilevel programming capabilities. It is based on the electrochemical dissolution and growth of a metallic filament within the insulating layer. It is shown that different LRS are realized by a variation of the tunneling gap between the growing filament and its counter electrode. For high current compliance levels the metallic filament can establish a galvanic contact. In this case the RESET mechanism becomes a combination of a local temperature increase and a subsequent self-dissolution of the metallic filament. Due to the self-dissolution the RESET can be obtained by application of either voltage polarity. This differs from the mere bipolar operation, where a tunneling gap remains in the LRS. Based on the simulation results a challenge for the application as ReRAM emerges from the asymmetry of the switching voltages. Typically, the RESET voltage is lower than the SET voltage. To define suitable switching voltage and read voltage windows, the RESET voltage should be typically higher than the read voltage by a factor of ten. Using the analytically derived expressions for the RESET switching a set of parameters can be possibly identified which satisfies this demand.

In Chapter 5 the origin of the nonlinear switching kinetics in VCM cells has been identified with the aid of electro-thermal FEM simulations. It is dominated by temperature-accelerated drift of oxygen vacancies rather than by field-acceleration. The thermal nature of the switching process allows for optimization of the VCM cell design. At the same time the high current necessary to achieve significant Joule

heating poses an issue for ReRAM realization. In an integrated memory the select transistor cannot drive currents higher than a few ten µA while the dimensions are in the nanometer regime. Thus, the cell design has to be optimized with respect to thermal confinement in order to bring down the switching currents.

Both, ECM and VCM cells rely on the drift of ions in an electric field. Mobile cations (typically Ag, Cu) are responsible for the switching effect in ECM cells, whereas the movement of oxygen vacancies triggers the resistance change in VCM cells. As the Cu/Ag cations are typically smaller than oxygen vacancies a higher mobility is anticipated. In VCM cells Joule heating is necessary to obtain a fast drift of oxygen vacancies, whereas the mobility in ECM cells is already high enough at room temperature. In contrast, the ECM kinetics are electron-transfer limited. The different origins of the switching kinetics result in differing switching voltages. Typically, the switching voltages for ECM cells are lower than for VCM cells in the same time regime. The difference in switching voltage and ion mobility causes that ECM-type switching predominates in a specific oxide thin film if Cu or Ag electrodes are used. In oxides, showing typically VCM-type of switching, as TiO_2 [52], Ta_2O_5 [54] or $SrTiO_3$[124], ECM-type switching emerges using Cu and Ag electrodes, respectively.

Both types of switching exhibit a similar structure and switching location. In ECM cells the variation of a tunneling gap between a growing filament and its counter electrode is responsible for the resistive switching effect. The complement to the metallic filament in VCM cells is the oxygen-deficient well conducting plug, which has evolved during electroforming. Typically, the resistance of the plug in VCM cells is higher than the corresponding filament resistance in ECM cells. The actual switching takes place in the disc region close to the active electrode in analogy to the tunneling gap in ECM cells. Also in VCM cells the resistance change can be considered as the modulation of the electronic barrier in the disc region. The oxygen vacancies accumulating in this region causes a modulation of the width and the height of the electrostatic barrier. In contrast, only a modulation of the width occurs in ECM cells.

The RESET operation of ECM cells can become nonpolar when the filament establishes a galvanic contact at low LRS values. A transition from bipolar VCM-type switching to unipolar TCM-type switching has been observed in TiO_2 [83], $Ba_{0.7}Sr_{0.3}TiO_3$ [122] or $SrTiO_x$ [123] based ReRAMs. Typically, the bipolar VCM mode turns into the unipolar TCM mode at high current levels. The LRS in the unipolar mode exhibits an ohmic current-voltage relation. By comparing this transition to the transition in ECM cells it can be reasoned that the conductive

plug bridges the insulating layer and the disc region vanishes. In this case the cell is rather symmetric and high currents (and temperatures, respectively) are required to enable a RESET. Thus, the thermal driving force prevails over the electrochemical driving force and the switching operation becomes unipolar.
In Section 4.3.1 two generic properties of ECM switching were investigated. On the one hand the LRS can be precisely tuned by variation of the current compliance according to $R_{\mathrm{LRS}} \propto I_{\mathrm{cc}}^{-1}$. On the other hand the RESET current depends linearly on the SET current (current compliance) as $I_{\mathrm{RESET}} \propto I_{\mathrm{cc}}$. These characteristics have also been demonstrated for VCM and TCM systems [74] and are hence possibly generic for all kind of ReRAMs. The tuning of the LRS is caused by the nonlinear switching kinetics of the resistive switching effects. As soon as the set current compliance level is reached, the cell voltage drops and the driving force for resistive switching decreases dramatically due to the nonlinear switching kinetics. As prerequisite the current compliance has to be fast enough to prevent current overshoots. The linear relation between the SET and RESET current can be also led back to the nonlinear switching kinetics. The latter leads to an almost constant RESET voltage for a specific sweep rate. In combination with an ohmic LRS this RESET characteristic is obtained. Note that not all VCM cells exhibit a linear $I-V$ characteristic. For these cells the linear relation between RESET current and SET current has to be proven.

6.2 Outlook

Regarding the 1D modeling of ECM cells the ionic transport can be described in more detail using the Mott-Gurney law for ion hopping. Especially, in the high voltage regime the simulation results showed that the switching kinetics become drift-limited. In this regime the electric field within the insulating layer may become so high that the ionic transport gets electric field accelerated. Considering both cases enables to analyze the impact on the switching kinetics in different voltage regimes. It is particularly interesting to investigate the impact of the material parameters on the transition between drift and electron transfer limitation. A following step would be to implement the nucleation process into the model to include all possible processes limiting the switching process. The implementation of the nucleation process will provide valuable information about the first stages of the electroforming process in ECM cells.
Furthermore, the 1D model should be extended to account for a step wise resistance change induced by deposition/dissolution of single cations. A possibility for

implementation is to compare the continuous Faradaic current integrated over an observation period to the charge of a single transfer reaction. If the integrated charge is lower, the decrease is regarded step wise. By this method single events should be covered.
The FEM simulations of ECM cells should be extended to 2D axisymmetry to get full 3D information about the switching process. This will allow for investigation of the asymmetry in SET and RESET switching. Using the 1D compact model it was shown that a geometrical asymmetry accompanied with a charge transfer coefficient $\alpha \neq 0.5$ results in such an asymmetric switching behavior. Using 2D axisymmetric FEM simulations this behavior can be investigated in more detail. The obtained results will provide information to improve the 1D physical compact model.
A next step would be to allow for concentration gradients within the insulating layer. In this case the drift-diffusion equation for Cu/Ag ions has to be solved using FEM methods. The Butler-Volmer equation has to be changed accordingly to account for a variable cation concentrations. In addition, as for the 1D model implementation the nucleation process should be incorporated. This enables a better insight into the first stages of the electroforming process.
Regarding the nonpolar switching further simulations with varying material parameters will be conducted. Especially, changing the activation energy of the exchange current density may inform about the conditions under which nonpolar switching occurs. A gedankenexperiment suggests that only bipolar switching is obtained for a low temperature dependence of the exchange current density. These simulations can also be extended by considering cation concentration gradients within the insulating layer as discussed above. Furthermore, the simulations of the self-dissolution should be extended to a full simulation of the RESET to investigate the dissolution after the filament rupture.
Further simulation studies should be carried out to investigate the reliability of ECM cells. At a first stage different assumed starting conditions can be employed and the impact on switching parameters as SET/RESET voltage can be analyzed. In a second step the derived ECM model can be simulated using a more statistical approach as Monte-Carlo simulations.

Concerning the simulation of the VCM switching the development of the models is still in the beginning. Nevertheless, temperature accelerated drift as the origin of the nonlinear switching kinetics could be identified. Using the derived electro-thermal simulation model the cell design might be optimized. Furthermore, it should be applied to other VCM cells (e.g. Ta_2O_5) to investigate the switching kinetics. Based on the electro-thermal simulations a methodology can be developed which allows

for extracting the activation energy of the ionic transport and the ionic mobility at $T = 300\,\mathrm{K}$ from experimental data.

The FEM model can be extended by using a more sophisticated description of the electronic barrier transport. This allows to investigate the influence of different electrode and insulator materials in more detail. Especially, the nonlinearity of the $I - V$ characteristic will influence the switching kinetics dramatically. Furthermore, the temperature dependence of the $I - V$ characteristics in LRS and HRS can be studied in depth.

To understand the electroforming process in VCM cells dynamic simulations including the ionic transport, Joule heating, possible redox reactions and the electronic barrier transport are required. This will tell how the virtual cathode evolves. At a first stage different oxygen vacancy concentration profiles can be assumed which resemble a distinct stage of the electroforming process. Simulating the electronic properties of such a structure will help to understand this process. The model can then be further extended to the switching case.

A 1D compact model similar to the ECM model should be developed. In a first approximation, a triangular barrier instead of the rectangular one can be assumed. The oxygen vacancy transport will then modulate the width of the barrier. To account for the nonlinear switching kinetics the temperature at the plug/disc boundary can be calculated using a simplistic model. The ionic current density at this point gives the change of the barrier width. Different $I - V$ relations should be used for the forward and reverse direction. As conduction mechanisms thermionic emission, thermionic field emission and field emission should be considered. In addition, barrier lowering due to the Schottky effect has to be taken into account. The obtained simulation results need to be compared to experimental data to further improve the model.

List of Figures

Bibliography

[1] I. I. T. R. for Semiconductors, "Edition 2010," *http://www.itrs.net/*, 2010.

[2] M. J. Lee, C. B. Lee, D. Lee, S. R. Lee, M. Chang, J. H. Hur, Y. B. Kim, C. J. Kim, D. H. Seo, S. Seo, U. I. Chung, I. K. Yoo, and K. Kim, "A fast, high-endurance and scalable non-volatile memory device made from asymmetric Ta(2)O(5-x)/TaO(2-x) bilayer structures," *Nat. Mater.*, vol. 10, no. 8, pp. 625–630, 2011.

[3] A. C. Torrezan, J. P. Strachan, G. Medeiros-Ribeiro, and R. S. Williams, "Sub-nanosecond switching of a tantalum oxide memristor," *Nanotechnology*, vol. 22, p. 485203, 2011.

[4] K. Szot, W. Speier, G. Bihlmayer, and R. Waser, "Switching the electrical resistance of individual dislocations in single-crystalline $SrTiO_3$," *Nat. Mater.*, vol. 5, no. 4, pp. 312–20, 2006.

[5] K. Terabe, T. Hasegawa, T. Nakayama, and M. Aono, "Quantized conductance atomic switch," *Nature*, vol. 433, no. 6, pp. 47–50, 2005.

[6] J. Borghetti, G. S. Snider, P. J. Kuekes, J. J. Yang, D. R. Stewart, and R. S. Williams, "'Memristive' switches enable 'stateful' logic operations via material implication," *Nature*, vol. 464, no. 7290, pp. 873–876, 2010.

[7] R. Rosezin, E. Linn, C. Kügeler, R. Bruchhaus, and R. Waser, "Crossbar Logic Using Bipolar and Complementary Resistive Switches," *IEEE Electron Device Lett.*, vol. 32, no. 6, pp. 710–712, 2011.

[8] G. Dearnaley, A. M. Stoneham, and D. V. Morgan, "Electrical phenomena in amorphous oxide films," *Rep. Prog. Phys.*, vol. 33, no. 33, p. 1129, 1970.

[9] D. P. Oxley, "Electroforming, switching and memory effects in oxide thin films," *Electrocomponent Science and Technology, UK*, vol. 3, no. 4, pp. 217–24, 1977.

[10] H. Pagnia and N. Sotnik, "Bistable switching in electroformed metal-insulator-metal devices," *Phys. Stat. Sol.*, vol. 108, no. 1, pp. 11–65, 1988.

[11] A. Asamitsu, Y. Tomioka, H. Kuwahara, and Y. Tokura, "Current switching of resistive states in magnetoresistive manganites," *Nature*, vol. 388, no. 6637, pp. 50–2, 1997.

[12] M. N. Kozicki, M. Yun, L. Hilt, and A. Singh, "Applications of programmable resistance changes in metal-doped chalcogenides," in *Proceedings of Solid-State Ionic Devices, Seattle, WA, USA, 02/05/1999-07/05/1999*, pp. 298–309, Center for Solid State Electron Res, Arizona State Univ, Tempe, AZ, USA, J. Electrochem. Soc, 1999.

[13] A. Beck, J. G. Bednorz, C. Gerber, C. Rossel, and D. Widmer, "Reproducible switching effect in thin oxide films for memory applications," *Appl. Phys. Lett.*, vol. 77, no. 1, pp. 139–41, 2000.

[14] R. Waser, R. Dittmann, G. Staikov, and K. Szot, "Redox-Based Resistive Switching Memories - Nanoionic Mechanisms, Prospects, and Challenges," *Adv. Mater.*, vol. 21, no. 25-26, pp. 2632–2663, 2009.

[15] I. Valov, R. Waser, J. R. Jameson, and M. N. Kozicki, "Electrochemical metallization memories-fundamentals, applications, prospects," *Nanotechnology*, vol. 22, no. 25, pp. 254003/1–22, 2011.

[16] D. Ielmini, R. Bruchhaus, and R. Waser, "Thermochemical resistive switching: materials, mechanisms, and scaling projections," *Phase Transit.*, vol. 84, no. 7, pp. 570–602, 2011.

[17] E. Linn, R. Rosezin, C. Kuegeler, and R. Waser, "Complementary Resistive Switches for Passive Nanocrossbar Memories," *Nat. Mater.*, vol. 9, no. 5, pp. 403–406, 2010.

[18] E. H. Sondheimer, "The mean free path of electrons in metals," *Adv. Phys.*, vol. 1, no. 1, pp. 1–42, 1952.

[19] V. V. Zhirnov, R. K. Cavin, S. Menzel, E. Linn, S. Schmelzer, D. Braeuhaus, C. Schindler, and R. Waser, "Memory Devices: Energy-Space-Time Tradeoffs," *Proc. IEEE*, vol. 98, no. 12, pp. 2185 – 2200, 2010.

[20] J. O'Dwyer, *The Theory of Electrical Conduction and Breakdown in Solid Dielectrics, Clarendon Press, Oxford*. Clarendon Press, Oxford, 1973.

[21] N. F. Mott and R. W. Gurney, *Electronic processes in ionic crystals*. Oxford Univ. Press, London, U.K., 1948.

[22] R. Waser, S. Menzel, and R. Bruchhaus, *Nanoelectronics and Information Technology (3rd edition)*, ch. 30. Wiley-VCH, 2012.

[23] H. Bethe, "Theory of the Boundary Layer of Crystal Rectifiers," *Radiation Laboratory, Massachusetts Institute of Technology*, vol. 185, 1942.

[24] S. M. Sze and K. K. Ng, *Physics Of Semiconductor Devices*. Wiley, 3 ed., 2007.

[25] W. Schottky, "Vereinfachte und erweiterte Theorie der Randschichtgleichrichter," *Zeitschrift für Physik A Hadrons and Nuclei*, vol. 118, no. 9, pp. 539–592, 1942.

[26] F. A. Padovani and R. Stratton, "Field and thermionic-field emission in Schottky barriers," *Solid State Electronics*, vol. 9, no. 7, pp. 695–707, 1966.

[27] J. G. Simmons, "Generalized Formula for the Electric Tunnel Effect between Similar Electrodes Separated by a Thin Insulating Film," *J. Appl. Phys.*, vol. 34, pp. 1793–1803, 1963.

[28] J. G. Simmons, "Electric Tunnel Effect between Dissimilar Electrodes Separated by a Thin Insulating Film," *J. Appl. Phys.*, vol. 34, p. 2581, 1963.

[29] C. H. Hamann, A. Hamnett, and W. Vielstich, *Electrochemistry*. Wiley-VCH, Weinheim, 2 ed., 2007.

[30] K. Szot, M. Rogala, W. Speier, Z. Klusek, A. Besmehn, and R. Waser, "TiO_2 - a prototypical memristive material," *Nanotechnology*, vol. 22, no. 25, p. 254001, 2011.

[31] *COMSOL Multiphysics Reference Guide*, 3.5a ed., 2008.

[32] K.-J. Bathe, *Finite-Elemente-Methoden*. Wiley-VCH, Weinheim, 2 ed., 2002.

[33] W. Dahmen and A. Reusken, *Numerik für Ingenieure und Naturwissenschaftler*. Springer, 2 ed., 2008.

[34] T. Kever, U. Boettger, C. Schindler, and R. Waser, "On the origin of bistable resistive switching in metal organic charge transfer complex memory cells," *Appl. Phys. Lett.*, vol. 91, no. 8, pp. 083506–1–3, 2007.

[35] R. Müller, C. Krebs, L. Goux, D. J. Wouters, J. Genoe, P. Heremans, S. Spiga, and M. Fanciulli, "Bipolar Resistive Electrical Switching of CuTCNQ Memories Incorporating a Dedicated Switching Layer," *IEEE Electron Device Lett.*, vol. 30, no. 6, pp. 620–622, 2009.

[36] R. Mueller, J. Genoe, and P. Heremans, "Bipolar resistive electrical switching of silver tetracyanoquinodimethane based memory cells with dedicated silicon dioxide switching layer," *Appl. Phys. Lett.*, vol. 95, no. 13, pp. 133509/1–3, 2009.

[37] M. Meier, C. Schindler, S. Gilles, R. Rosezin, A. Rudiger, C. Kuegeler, and R. Waser, "A Nonvolatile Memory With Resistively Switching Methyl-Silsesquioxane," *IEEE Electron Device Lett.*, vol. 30, no. 1, pp. 8–10, 2009.

[38] C. Schindler, *Resistive switching in electrochemical metallization memory cells.* PhD thesis, RWTH Aachen, 2009.

[39] M. Aono and T. Hasegawa, "The Atomic Switch," *Proc. IEEE*, vol. 98, no. 12, pp. 2228–2236, 2010.

[40] Y. Hirose and H. Hirose, "Polarity-dependent memory switching and behaviour of Ag dendrite in Ag-photodoped amorphous As_2S_3 films," *J. Appl. Phys.*, vol. 47, no. 6, pp. 2767–72, 1976.

[41] X. Guo, C. Schindler, S. Menzel, and R. Waser, "Understanding the switching-off mechanism in Ag+ migration based resistively switching model systems," *Appl. Phys. Lett.*, vol. 91, no. 13, pp. 1–3, 2007.

[42] Y. C. Yang, F. Pan, Q. Liu, M. Liu, and F. Zeng, "Fully Room-Temperature-Fabricated Nonvolatile Resistive Memory for Ultrafast and High-Density Memory Application," *Nano Lett.*, vol. 9, no. 4, pp. 1636–1643, 2009.

[43] C. Schindler, G. Staikov, and R. Waser, "Electrode kinetics of Cu-SiO_2-based resistive switching cells: Overcoming the voltage-time dilemma of electrochemical metallization memories," *Appl. Phys. Lett.*, vol. 94, no. 7, p. 072109, 2009.

[44] U. Russo, D. Kamalanathan, D. Ielmini, A. L. Lacaita, and M. N. Kozicki, "Study of Multilevel Programming in Programmable Metallization Cell (PMC) Memory," *IEEE Trans. Electron Devices*, vol. 56, no. 5, pp. 1040–1047, 2009.

[45] Y. Bernard, V. T. Renard, P. Gonon, and V. Jousseaume, "Back-end-of-line compatible Conductive Bridging RAM based on Cu and SiO_2," *Microelectron. Eng.*, vol. 88, no. 5, pp. 814–816, 2011.

[46] S. Yu and H.-S. Wong, "Compact Modeling of Conducting-Bridge Random-Access Memory (CBRAM)," *IEEE Trans. Electron Devices*, vol. 58, no. 5, pp. 1352–1360, 2011.

[47] J. R. Jameson, N. Gilbert, F. Koushan, J. Saenz, J. Wang, S. Hollmer, and M. N. Kozicki, "One-dimensional model of the programming kinetics of conductive-bridge memory cells," *Appl. Phys. Lett.*, vol. 99, no. 6, pp. 063506–063506, 2011.

[48] S. Menzel, B. Klopstra, C. Kügeler, U. Böttger, G. Staikov, and R. Waser, "A Simulation Model of Resistive Switching in Electrochemical Metallization Memory Cells," *Mater. Res. Soc. Symp. Proc.*, vol. 1160, pp. 101–106, 2009.

[49] S. Tappertzhofen, S. Menzel, I. Valov, and R. Waser, "Redox Processes in Silicon Dioxide Thin Films using Copper Microelectrodes," *Appl. Phys. Lett.*, vol. 99, no. 20, pp. 203103–203106, 2011.

[50] C. Schindler, M. Weides, M. N. Kozicki, and R. Waser, "Low current resistive switching in Cu-SiO_2 cells," *Appl. Phys. Lett.*, vol. 92, no. 12, p. 122910, 2008.

[51] C. Schindler, M. Meier, R. Waser, and M. N. Kozicki, "Resistive switching in Ag-Ge-Se with extremely low write currents," in *Non-Volatile Memory Technology Symposium 2007*, pp. 82–85, Inst. of Solid State Res., Julich, Germany, Proceedings of NVMTS, 2007.

[52] K. Tsunoda, Y. Fukuzumi, J. R. Jameson, Z. Wang, P. B. Griffin, and Y. Nishi, "Bipolar resistive switching in polycrystalline TiO_2 films," *Appl. Phys. Lett.*, vol. 90, no. 11, pp. 113501/1–3, 2007.

[53] V. V. Zhirnov, R. Meade, R. K. Cavin, and G. Sandhu, "Scaling limits of resistive memories," *Nanotechnology*, vol. 22, no. 25, pp. 254027/1–, 2011.

[54] T. Tsuruoka, K. Terabe, T. Hasegawa, and M. Aono, "Forming and switching mechanisms of a cation-migration-based oxide resistive memory," *Nanotechnology*, vol. 21, no. 42, pp. 425205/1–, 2010.

[55] D. B. Strukov and R. S. Williams, "Intrinsic constrains on thermally-assisted memristive switching," *Appl. Phys. A - Mater. Sci. Process.*, vol. 102, no. 4, pp. 851–855, 2011.

[56] D. Ielmini, F. Nardi, and C. Cagli, "Physical models of size-dependent nanofilament formation and rupture in NiO resistive switching memories," *Nanotechnology*, vol. 22, no. 25, pp. 254022/1–12, 2011.

[57] N. Derhacobian, S. C. Hollmer, N. Gilbert, and M. N. Kozicki, "Power and Energy Perspectives of Nonvolatile Memory Technologies," *Proc. IEEE*, vol. 98, no. 2, pp. 283–298, 2010.

[58] S. Menzel, U. Böttger, and R. Waser, "Simulation of multilevel switching in electrochemical metallization memory cells," *J. Appl. Phys.*, vol. 111, no. 1, p. 014501, 2012.

[59] J. Xiang, B. Liu, B. Liu, B. Ren, and Z. Tian, "A self-terminated electrochemical fabrication of electrode pairs with angstrom-sized gaps," *Electrochemistry Communications*, vol. 8, no. 4, pp. 577–580, 2006.

[60] E. Scheer, N. Agrait, J. Cuevas, A. Yeyati, B. Ludoph, A. Martin-Rodero, G. Bollinger, J. van Ruitenbeek, and C. Urbina, "The signature of chemical valence in the electrical conduction through a single-atom contact," *Nature*, vol. 394, no. 6689, pp. 154–157, 1998.

[61] A. Nayak, T. Tsuruoka, K. Terabe, and T. H. . M. Aono, "Switching kinetics of a Cu_2S-based gap-type atomic switch," *Nanotechnology*, vol. 22, p. 235201, 2011.

[62] W. Guan, S. Long, Q. Liu, M. Liu, and W. Wang, "Nonpolar Nonvolatile Resistive Switching in Cu Doped ZrO2," *IEEE Electron Device Lett.*, vol. 29, no. 5, pp. 434–437, 2008.

[63] C. Schindler, S. C. P. Thermadam, R. Waser, and M. N. Kozicki, "Bipolar and unipolar resistive switching in Cu-doped SiO_2," *IEEE Trans. Electron Devices*, vol. 54, no. 10, pp. 2762–2768, 2007.

[64] M. Faraday, "Experimental researches in electricity," *Phil. Trans. Roy. Soc. London*, vol. 124, pp. 77–122, 1834.

[65] L. Chua, "Resistance switching memories are memristors," *Appl. Phys. A-Mater. Sci. Process.*, vol. 102, no. 4, pp. 765–783, 2011.

[66] S. Zafar, K. Conrad, Q. Liu, E. Irene, G. Hames, R. Kuehn, and J. Wortman, "Thickness and effective electron mass measurements for thin silicon dioxide films using tunneling current oscillations," *Appl. Phys. Lett.*, vol. 67, no. 7, pp. 1031–1033, 1995.

[67] Y. C. Yang, C. Chen, F. Zeng, and F. Pan, "Multilevel resistance switching in Cu/TaOx/Pt structures induced by a coupled mechanism," *J. Appl. Phys.*, vol. 107, no. 9, pp. 93701/1–, 2010.

[68] Y. Lu, S. Long, Q. Liu, Q. Wang, M. Zhang, H. Lv, L. Shao, Y. Wang, S. Zhang, Q. Zuo, S. Liu, and M. Liu, "Nonvolatile multilevel memory effect in Cu/WO_3/Pt device structures," *Phys. Status Solidi-Rapid Res. Lett.*, vol. 4, no. 5-6, pp. 124–126, 2010.

[69] C. Chen, Y. C. Yang, F. Zeng, and F. Pan, "Bipolar resistive switching in Cu/AlN/Pt nonvolatile memory device," *Appl. Phys. Lett.*, vol. 97, no. 8, pp. 83502/1–, 2010.

[70] L. Nielen, "Fabrication, Electrical Characterization and Macro-Modeling of Complementary Resistive Switches (CRS)," 2011.

[71] Q. Liu, C. Dou, Y. Wang, S. Long, W. Wang, M. Liu, M. Zhang, and J. Chen, "Formation of multiple conductive filaments in the Cu/ZrO2:Cu/Pt device," *Appl. Phys. Lett.*, vol. 95, no. 2, pp. 23501/1–, 2009.

[72] L. Chua and S. Kang, "Memristive devices and systems," *Proc. IEEE*, vol. 64, no. 2, pp. 209–223, 1976.

[73] R. Corless, G. Gonnet, D. Hare, D. Jeffrey, and D. Knuth, "On the Lambert W function," *Advances in Computational Mathematics*, vol. 5, no. 4, pp. 329–359, 1996.

[74] D. Ielmini, F. Nardi, and C. Cagli, "Universal Reset Characteristics of Unipolar and Bipolar Metal-Oxide RRAM," *IEEE Transactions on Electron Devices*, vol. 58, no. 10, pp. 1–8, 2011.

[75] *COMSOL Multiphysics Modeling Guide*, 3.5a ed., 2008.

[76] A. Wille, "Simulation der Schaltkinetik von ECM-Speicherzellen in Abhängigkeit des Materialsystems," 2010.

[77] J. Müller, "FEM-Simulation des Schaltvorgangs in ECM-Speicherzellen," 2011.

[78] N. Adler, "Modellierung und Simulation des Reset-Vorgangs in ECM-Speicherzellen," 2010.

[79] D. R. Lide, ed., *CRC Handbook of Chemistry and Physics*. CRC Press, 84 ed., 2003.

[80] J. S. W. Alexander, ed., *CRC Materials Science and Engeneering Handbook*. CRC Press, 3 ed., 2001.

[81] S. Q. Liu, N. J. Wu, and A. Ignatiev, "Electric-pulse-induced reversible resistance change effect in magnetoresistive films," *Appl. Phys. Lett.*, vol. 76, no. 19, pp. 2749–51, 2000.

[82] Y. Watanabe, J. G. Bednorz, A. Bietsch, Gerber-Ch, D. Widmer, A. Beck, and S. J. Wind, "Current-driven insulator-conductor transition and nonvolatile memory in chromium-doped $SrTiO_3$ single crystals," *Appl. Phys. Lett.*, vol. 78, no. 23, pp. 3738–40, 2001.

[83] D. S. Jeong, H. Schroeder, and R. Waser, "Coexistence of bipolar and unipolar resistive switching behaviors in a $Pt/TiO_2/Pt$ stack," *Electrochem. Solid State Lett.*, vol. 10, no. 8, pp. G51–G53, 2007.

[84] J. J. Yang, M. D. Pickett, X. Li, D. A. A. Ohlberg, D. R. Stewart, and R. S. Williams, "Memristive switching mechanism for metal/oxide/metal nanodevices," *Nat. Nanotechnol.*, vol. 3, no. 7, p. 429, 2008.

[85] Z. Wei, Y. Kanzawa, K. Arita, Y. Katoh, K. Kawai, S. Muraoka, S. Mitani, S. Fujii, K. Katayama, M. Iijima, T. Mikawa, T. Ninomiya, R. Miyanaga, Y. Kawashima, K. Tsuji, A. Himeno, T. Okada, R. Azuma, K. Shimakawa, H. Sugaya, T. Takagi, R. Yasuhara, H. Horiba, H. Kumigashira, and M. Oshima, "Highly Reliable TaOx ReRAM and Direct Evidence of Redox Reaction Mechanism," *IEEE Tech. Dig.*, 2008.

[86] J. H. Hur, M.-J. Lee, C. B. Lee, Y.-B. Kim, and C.-J. Kim, "Modeling for bipolar resistive memory switching in transition-metal oxides," *Phys. Rev. B*, vol. 82, pp. 155321–, 2010.

[87] C. Hermes, M. Wimmer, S. Menzel, K. Fleck, G. Bruns, M. Salinga, U. Boettger, R. Bruchhaus, T. Schmitz-Kempen, M. Wuttig, and R. Waser, "Analysis of transient currents during ultra fast switching of TiO_2 nanocrossbar devices," *IEEE Electron Device Lett.*, vol. 32, no. 8, pp. 1116 – 1118, 2011.

[88] C. Nauenheim, C. Kuegeler, S. Trellenkamp, A. Ruediger, and R. Waser, "Phenomenological considerations of resistively switching TiO_2 in nano crossbar arrays," in *Proceedings of 10th International Conference on Ultimate Integration of Silicon, March 18-20, Aachen*, pp. 135–138, Proceedings of 10th International Conference on Ultimate Integration of Silicon, 2009.

[89] C. H. Cheng, C. Y. Tsai, A. Chin, and F. S. Yeh, "High Performance Ultra-Low Energy RRAM with Good Retention and Endurance," in *International Electron Devices Meeting (IEDM), San Francisco, CA*, 2010 international electron devices meeting - technical digest, 2010.

[90] J. J. Yang, M. Zhang, J. P. Strachan, F. Miao, M. D. Pickett, R. D. Kelley, G. Medeiros-Ribeiro, and R. S. Williams, "High switching endurance in TaO_x memristive devices," *Appl. Phys. Lett.*, vol. 97, no. 23, pp. 232102/1–3, 2010.

[91] H. Akinaga and H. Shima, "Resistive Random Access Memory (ReRAM) Based on Metal Oxides," *Proc. IEEE*, vol. 98, no. 12, pp. 2237–2251, 2010.

[92] C. Nauenheim, C. Kuegeler, A. Ruediger, and R. Waser, "Investigation of the electroforming process in resistively switching TiO_2 nanocrosspoint junctions," *Appl. Phys. Lett.*, vol. 96, no. 12, p. 122902, 2010.

[93] J. J. Yang, F. Miao, M. D. Pickett, D. A. A. Ohlberg, D. Stewart, C. N. Lau, and R. S. Williams, "The mechanism of electroforming of metal oxide memristive switches," *Nanotechnology*, vol. 20, no. 21, p. 215201, 2009.

[94] D.-H. Kwon, K. M. Kim, J. H. Jang, J. M. Jeon, M. H. Lee, G. H. Kim, X.-S. Li, G.-S. Park, B. Lee, S. Han, M. Kim, and C. Hwang, "Atomic structure of conducting nanofilaments in TiO_2 resistive switching memory," *Nat. Nanotechnol.*, vol. 5, no. 2, pp. 148–153, 2010.

[95] A. Sawa, "Resistive switching in transition metal oxides," *Mater. Today*, vol. 11, no. 6, pp. 28–36, 2008.

[96] R. Muenstermann, T. Menke, R. Dittmann, and R. Waser, "Coexistence of Filamentary and Homogeneous Resistive Switching in Fe-doped $SrTiO_3$ Thin-Film Memristive Devices," *Adv. Mat.*, vol. 22, no. 43, p. 4819, 2010.

[97] F. Miao, J. J. Yang, J. Borghetti, G. Medeiros-Ribeiro, and R. S. Williams, "Observation of two resistance switching modes in TiO2 memristive devices electroformed at low current," *Nanotechnology*, vol. 22, no. 25, pp. 254007/1–7, 2011.

[98] R. Bruchhaus, C. R. Hermes, and R. Waser, "Memristive Switches with Two Switching Polarities in a Forming Free Device Structure," *MRS Online Proceedings Library*, vol. 1337, 2011.

[99] A. Sawa, T. Fujii, M. Kawasaki, and Y. Tokura, "Interface resistance switching at a few nanometer thick perovskite manganite active layers," *Appl. Phys. Lett.*, vol. 88, no. 23, pp. 232112–1–3, 2006.

[100] Y. B. Nian, J. Strozier, N. J. Wu, X. Chen, and A. Ignatiev, "Evidence for an oxygen diffusion model for the electric pulse induced resistance change effect in transition-metal oxides," *Phys. Rev. Lett.*, vol. 98, no. 14, pp. 146403/1–4, 2007.

[101] S. Menzel, M. Waters, A. Marchewka, U. Böttger, R. Dittmann, and R. Waser, "Origin of the Ultra-nonlinear Switching Kinetics in Oxide-Based Resistive Switches," *Adv. Funct. Mater.*, vol. 21, no. 23, pp. 4487–4492, 2011.

[102] R. Muenstermann, R. Dittmann, T. Menke, I. Krug, D. Park, J. Mayer, A. Besmehn, F. Kronast, C. M. Schneider, and R.Waser, "Scaling Potential of local redox-processes in memristive $SrTiO_3$ thin film devices," *Phase Transit.*, 2011.

[103] M. Kestigian, J. G. Dickinson, and R. Ward, "Ion-deficient Phases in Titanium and Vanadium Compounds of the Perovskity Type," *J. Am. Chem. Soc.*, vol. 79, no. 21, pp. 5598–5601, 1957.

[104] M. A. A. Franco and M. V. Regi, "Anion deficiency in strontium titanate," *Nature*, vol. 270, no. 5639, pp. 706–707, 1977.

[105] D. M. Smyth, "The role of impurities in insulating transition metal oxides," *Progress in Solid State Chemistry*, vol. 15, no. 3, pp. 145–71, 1984.

[106] D. M. Smyth, "Defect structure in perovskite titanates," *Current Opinion in Solid State & Materials Science*, vol. 1, no. 5, pp. 692–697, 1996.

[107] R. Moos and K. H. Haerdtl, "Defect Chemistry of Donor-Doped and Undoped Strontium Titanate Ceramics between 1000° and 1400°C," *J. Am. Cer. Soc.*, vol. 80, no. 10, pp. 2549–62, 1997.

[108] T. Menke, P. Meuffels, R. Dittmann, K. Szot, and R. Waser, "Separation of bulk and interface contributions to electroforming and resistive switching

behavior of epitaxial Fe-doped $SrTiO_3$," *J. Appl. Phys.*, vol. 105, p. 066104, 2009.

[109] G. M. Choi, H. L. Tuller, and D. Goldschmidt, "Electronic-transport behavior in single-crystalline $Ba_{0.03}Sr_{0.97}TiO_3$," *Physical Review B (Condensed Matter)*, vol. 34, no. 10, pp. 6972–9, 1986.

[110] R. Waser, "Bulk conductivity and defect chemistry of acceptor-doped strontium titanate in the quenched state," *J. Am. Cer. Soc.*, vol. 74, no. 8, pp. 1934–40, 1991.

[111] H. Iddir, S. Ogut, P. Zapol, and N. D. Browning, "Diffusion mechanisms of native point defects in rutile TiO_2: Ab initio," *Phys. Rev. B: Condens. Matter*, vol. 75, no. 7, p. 073203, 2007.

[112] D. B. Strukov and R. S. Williams, "Exponential ionic drift: fast switching and low volatility of thin-film memristors," *Appl. Phys. A-Mater. Sci. Process.*, vol. 94, no. 3, pp. 515–519, 2009.

[113] R. Meyer, L. Schloss, J. Brewer, R. Lambertson, W. Kinney, J. Sanchez, and D. Rinerson, "Oxide Dual-Layer Memory Element for Scalable Non-Volatile Cross-Point Memory Technology," *Proc. NVMTS*, pp. 54–58, 2008.

[114] G. K. White and S. B. Woods, "ELECTRICAL AND THERMAL RESISTIVITY OF THE TRANSITION ELEMENTS AT LOW TEMPERATURES," *Philosophical Transactions of the Royal Society of London Series a-Mathematical and Physical Sciences*, vol. 251, no. 995, pp. 273–302, 1959.

[115] Y. Suemune, "THERMAL CONDUCTIVITY OF $BATIO_3$ AND $SRTIO_3$ FROM 4.5 DEGREES TO 300 DEGREES K," *Journal of the Physical Society of Japan*, vol. 20, no. 1, p. 174, 1965.

[116] D. deLigny and P. Richet, "High-temperature heat capacity and thermal expansion of SrTiO3 and SrZrO3 perovskites," *Physical Review B*, vol. 53, no. 6, pp. 3013–3022, 1996.

[117] A. Moses, *Optical Material Properties: Handbook of Electronic Materials*, vol. 1. Plenum, New York, 1971.

[118] S. Harada, K. Tanaka, and H. Inui, "Thermoelectric properties and crystallographic shear structures in titanium oxides of the Magneli phases," *J. Appl. Phys.*, vol. 108, no. 8, pp. 83703/1–, 2010.

[119] D. B. Rogers, R. D. Shannon, A. W. Sleight, and J. L. Gillson, "Crystal Chemistry of Metal Dioxides with rutile-related Structures," *Inorganic Chemistry*, vol. 8, no. 4, pp. 841–9, 1969.

[120] F. Birch, J. F. Schairer, and H. C. Spicer, *Handbook of physical constants.* 36, The Society, 1 ed., 1942.

[121] S. Yu and H. Wong, "A Phenomenological Model for the Reset Mechanism of Metal Oxide RRAM," *IEEE Electron Device Lett.*, vol. 31, no. 12, pp. 1455–1457, 2010.

[122] W. Shen, R. Dittmann, and R. Waser, "Reversible alternation between bipolar and unipolar resistive switching in polycrystalline barium strontium titanate thin films," *J. Appl. Phys.*, vol. 107, no. 9, pp. 94506/1–4, 2010.

[123] S. B. Lee, J. S. Lee, S. H. Chang, H. K. Yoo, B. S. Kang, B. Kahng, M. Lee, C. J. Kim, and T. W. Noh, "Interface-modified random circuit breaker network model applicable to both bipolar and unipolar resistance switching," *Appl. Phys. Lett.*, vol. 98, no. 3, pp. 33502/1–, 2011.

[124] X. B. Yan, K. Li, J. Yin, Y. D. Xia, H. X. Guo, L. Chen, and Z. G. Liu, "The Resistive Switching Mechanism of Ag/SrTiO3/Pt Memory Cells," *Electrochem. Solid State Lett.*, vol. 13, no. 3, pp. H87–H89, 2010.